Measurement of Neutrino Oscillation with a High Intensity Neutrino Beam

Keigo Nakamura

Kyoto University

December 20, 2018

Abstract

We report the measurement of the neutrino oscillation with the high intensity proton beam in the T2K experiment.

The T2K experiment is a long baseline neutrino oscillation experiment in Japan. Almost pure muon neutrino and antineutrino beams are produced by a proton beam from J-PARC Main Ring and are detected at the ND280 near detector and the Super-Kamiokande far detector. The T2K experiment measures muon neutrino disappearance and electron neutrino appearance in the neutrino and antineutrino beams and determines neutrino oscillation parameters. To measure the neutrino oscillation parameters precisely, it is important to reduce both systematic and statistical uncertainties.

A high intensity neutrino beam is required since the current uncertainty in the T2K oscillation analysis is dominated by the statistical uncertainty, therefore, the intensity upgrade of J-PARC Main Ring is necessary. The beam loss limits the proton beam power in high intensity proton accelerators. In J-PARC Main Ring, beam instabilities and mis-control of the proton beam are the main sources of the beam loss. To reduce the beam loss, we developed an intra-bunch feedback system which damps the oscillation caused by the beam instabilities and a beta function measurement method during acceleration to correct the beam control. With these developments, a 480 kW operation was achieved.

It is also important to understand the neutrino-nucleus interaction modeling and its uncertainty precisely since the interaction uncertainty is one of the largest systematic uncertainties in the T2K oscillation analysis. There are various neutrino-nucleus interaction models and the predicted neutrino event rates at Super-Kamiokande depend on the choice of the interaction model. A wrong prediction of the event rates at Super-Kamiokande directly affects the determination of the oscillation parameters. Therefore, it is required to check whether the oscillation analysis is robust against the possible variation of the interaction models. We performed the oscillation analysis with various simulated data and found the current oscillation analysis makes a bias by more than 100% on Δm^2_{32} relative to the total uncertainty in some of the interaction model variations. We developed a method to loosen the bias and succeeded in reducing the bias to below 50%.

We performed the oscillation analysis with these improvements, and we obtained $\sin^2\theta_{13} = 0.0917^{+0.0063}_{-0.0049}$, $\sin^2\theta_{23} = 0.517^{+0.036}_{-0.035}$, $|\Delta m^2_{32}| = 2.457^{+0.065}_{-0.064} \times 10^{-3}$ eV^2, $\delta_{CP} = -1.70^{+0.87}_{-0.88}$. Using the constraint on $\sin^2\theta_{13}$ from reactor experiments, we got $\sin^2\theta_{23} = 0.536^{+0.027}_{-0.037}$, $|\Delta m^2_{32}| = 2.455^{+0.067}_{-0.066} \times 10^{-3}$ eV^2, $\delta_{CP} = -1.70^{+0.64}_{-0.62}$. This is the indication of the CP violation in the lepton sector at 2σ significance.

Acknowledgments

This thesis would not have been possible without the time and support given by a number of people. First of all, I would like to thank my supervisor, Tsuyoshi Nakaya for his help and support throughout my Ph.D. course.

I also would like thank J-PARC Main Ring group, especially, Tadashi Koseki, Takeshi Toyama, Masayuki Okada, Makoto Tobiyama, Chin Yong Ho, Yoshihiro Shobuda, Yoichi Sato, Yoshinori Kurimoto, Tetsuji Shimogawa, Hiroaki Harada, Susumu Igarashi. I am very impressed by their hard work for the realization of the high intensity beam operation at J-PARC Main Ring.

Although I couldn't touch anything about neutrino beam line work in this thesis, I enjoyed R&D of MUMON and the neutrino beam line commissioning. I want to thank KEK neutrino group and MUMON colleagues: Takashi Kobayashi, Takeshi Nakadaira, Ken Sakashita, Taku Ishida, Megan Friend, Tetsuro Sekiguchi, Yoshiaki Fujii, Hajime Kubo, Takahiro Hiraki, Yosuke Ashida, Yoshie Nakanishi, Wataru Uno.

For the oscillation analysis, I want to thank Mark Hartz and Claudio Giganti for their strong leadership in the oscillation analysis group. I also want to thank BANFF group: Mark Scott, Simon Bienstock, Christine Nielsen, P-theta group: Christophe Bronner, Simon, Taichiro Koga, Wing Ma, Benjamin Quilain and NIWG group: Yoshinari Hayato. Without their persistent help, I could not finish my study.

I am particularly grateful for the proofreading of my thesis given by Tatsuya Kikawa and Ken Sakashita.

I would like to express my gratitude to T2K fellow: Tatsuya Hayashino, Kento Yoshida, Miao Jiang, Mika Yamamoto, Ayami Hiramoto, Kenji Yasutome, Akutsu Ryosuke, Naruhiro Chikuma, Faminao Hosomi, Tomoyo Yoshida, Lukas Berns, Riku Tamura, Keiju Wakamatsu, Kenichi Kin, Jun Harada, Tsubasa Inoue, Yuma Azuma, Kei Ieki, Huang Kunxian, Seiko Hirota, Shota Takahashi, Kento Suzuki, Akihiro Minamino, Atsuko Ichikawa and Roger Wendell. I really enjoyed Tokai and Kamioka life with them.

I would also like to give many thanks to the members in our laboratory: Osamu Tajima, Toshi Sumida, Masaya Ishino, Hajime Nanjo, Eriko Hayashi, Saki Yamashita, Ichinori Kamiji, Takuto Kunigo, Kota Nakagiri, Shigeto Seki, Takuya Tashiro, Satoshi Shinohara, Sei Ban, Shunichi Akatsuka, Shunsuke Tanaka, Yohei Noguchi, Yuta Okazaki, Kazuhiro Nakamura, Masamitsu Mori, Masashi Yoshida, Keisuke Kondo, Koichiro Kuniyoshi, Junta Komine, Tomofumi Abe, Takuji Ikemitsu, Takahiro Odagawa, Soichiro Kuribayashi, Masanori Tajima, Masayuki Hatano, Yuya Mino, Yosuke Maeda, Saori Yanagida, Ryutaro Monden, Daichi Naito, Son Cao, Yuki Ishiyama, Naoki Kawasaki, Kiseki Nakamura and Ina Sanjana.

Finally, I would like to thank my parents, Kazuo Nakamura and Kumi Nakamura and Yuki Maeda for supporting my Ph.D life.

Contents

List of Figures

List of Tables

Part I

Introduction

Chapter 1

Neutrino Physics

In this chapter, we briefly summarize the properties of neutrinos.

1.1 Neutrino in the Standard Model

In the standard model of particle physics, neutrino is an elementary particle which has spin 1/2, no electric charge, no color and no mass, and interacts only through the weak interaction. Neutrino has three flavors: ν_e, ν_μ, ν_τ associated with charged leptons: electron, muon and tau, and the lepton number of each generation is conserved.

The first suggestion of the existence of neutrino came from β decay ($n \to p + \nu + e^-$) experiments. The β decay seemed to violate the energy conservation law because of its continuous electron spectrum [1]. Pauli predicted the existence of neutrinos in 1930 [2] and the theory was extended by Enrico Fermi in 1934 [3]. In the Fermi theory, current-current interaction was introduced on the analogy of quantum electrodynamics. His model has succeeded in reproducing the shape of the beta spectra perfectly and has extended to describe muon decay and muon capture by nucleus. After thirty years later, neutrino was first detected by Reines and Cowan in 1953 by observing inverse β decay ($\nu + p \to e^+ + n$) from the nuclear reactor with delayed coincidence method [4]. A few years later in 1959, Davis and Harmer showed that the neutrino and antineutrino were distinct particles [5].

The Fermi theory was modified to account for the new experimental results. In 1956, Lee and Yang noticed that the parity is not always conserved in the processes governed by the weak interaction [6]. In 1957, the parity violation was confirmed experimentally by Wu [7] and several experimentalists [8]. An experiment by Goldhaber showed that the same helicity of the neutrino are always emitted in the β decay [9]. In 1958, Sudarshan and Marshak, Feynman and Gell-Mann proposed V-A theory to account for these experimental results [10, 11]. From these developments, the massless left-handed neutrino was established.

In 1967, the electroweak theory was established by Abdus Salam, Sheldon Glashow and Steven Weinberg [12–14]. A theory combining the electroweak theory and Quantum Chromodynamics (QCD) [15, 16] is referred to as the "standard model" in these days. In the standard model, the weak interaction obeys $SU(2)_L \times U(1)_Y$ gauge theory where the subscript L indicates that the $SU(2)$ transformations are only on left-handed particles, and Y is hypercharge. The gauge invariant theory should have mass-less boson. In the standard model, the massive gauge boson is obtained by Higgs mechanism [17–19] of spontaneous symmetry breaking [20]. In their theory, three gauge bosons ($W^\pm$, Z^0) which cooperate to weak interaction are predicted. Interactions via the $W^\pm$ bosons are called Charged Current (CC) interaction, which has charged particles in the final state. While interactions via the Z boson are called Neutral Current (CC) interaction, where neutrino just transfers the mo-

mentum to the other particles (Fig. 1.1). The couplings for the neutrino and lepton field Ψ_ν, Ψ_l to the $W^\pm$ and Z^0 are described as follows:

$$-\frac{g_W}{2\sqrt{2}}(\bar{\Psi}_\nu\gamma_\mu(1-\gamma^5)\Psi_l)W^\mu \tag{1.1}$$

$$-\frac{g_W}{4\cos\theta_W}(\bar{\Psi}_\nu\gamma_\mu(1-\gamma^5)\Psi_\nu)Z^\mu. \tag{1.2}$$

where θ_W is the weak mixing angle (so called Weinberg angle) and g_W is the coupling constant to $W^\pm$. The existence of the neutral current was confirmed in 1973 in a neutrino experiment in the Gargamelle bubble chamber at CERN [21] and the direct observation of $W^\pm$ and Z^0 was done in 1983 in the $p\bar{p}$ collider at CERN [22, 23]. The masses of the gauge bosons were measured $m_{W^\pm} = 80.385$ GeV/c^2 and $m_{Z^0} = 91.1876$ GeV/c^2, which agree with the predicted values from the neutrino cross-section measurement. In 2012, the last piece of the standard model, Higgs boson was finally discovered in the experiments at Large Hadron Collider (LHC) [24].

Until 1962, neutrino theories assumed that all neutrinos were the same except the distinction between neutrino or anti-neutrino. An experiment by L.M. Lederman, M. Schwartz and J. Steinberger at AGS (Alternating Gradient Synchrotron) showed that the neutrinos from pion decay ($\pi^+ \to \mu^+ + \nu_\mu$) only produce muons rather than electrons in 1962 [25]. This indicates that there are more than one neutrino generation. Once τ was discovered in 1975 [26], the existence of the neutrino related to τ was suggested, and the direct observation of third generation neutrino ν_τ was done by DONUT in FermiLab in 2000 [27]. So far, the existence of the forth generation neutrinos is disfavored from the Z^0 decay width measurement at CERN in 1989 [28] [1] and the cosmic microwave background measurement [29].

The standard model successfully describes almost all the experimental results up to ~ 14 TeV. However, the standard model should be modified so that the neutrino mass is taken into account.

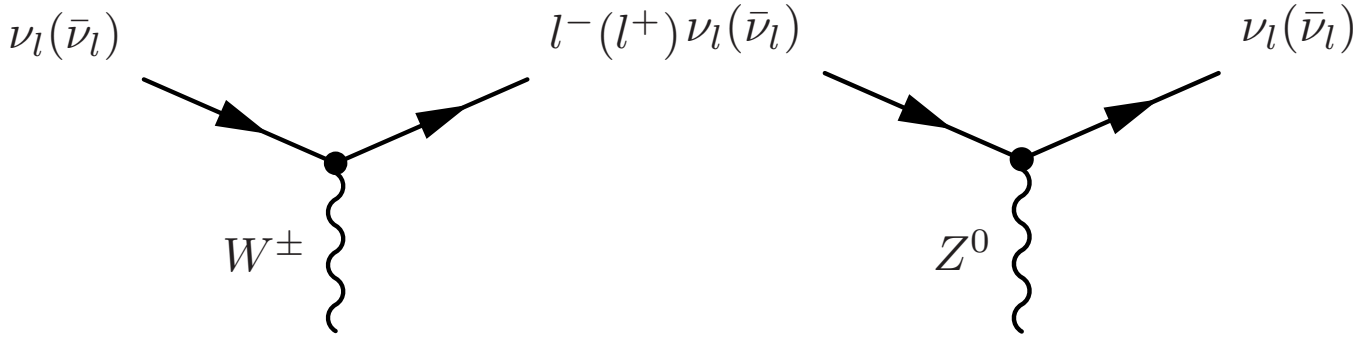

(a) Charged Current interaction

(b) Neutral Current interaction

Figure 1.1: Feynman diagrams of weak interactions

1.2 Neutrino Oscillation

The fact that neutrino has tiny mass is known to be a phenomenon "beyond the standard model" since the standard model assumes exactly zero mass. The evidence of neutrino mass came from neutrino oscillation.

[1] This measures the number of neutrinos that can couple to the Z^0 boson.

1.2.1 Evidence of Neutrino Oscillation

First indication was obtained from "solar neutrino problem". In 1967, Davis [30] measured the neutrino coming from the sun with ^{37}Cl and found the neutrino flux was 1/3 of expected value from standard solar model [31]. This deficit was also observed by Kamiokande [32], GALLEX (GALLium EXperiment) [33], GNO (Gallium Neutrino Observatory) [34] and SAGE (Soviet American Gallium Experiment) [35] at the end of 1980s. The first evidence of the oscillation of solar neutrinos was brought from Super-Kamiokande [36] and SNO (Sudbury Neutrino Observatory) [37] in 2001, after the strong evidence from the atmospheric neutrinos. Super-Kamiokande measured neutrino by Charged current (CC) interaction while SNO measured both charged and neutral current interaction using a D_2O target. Only ν_e is measured with CC interaction due to the low energy of solar neutrino, while NC interaction is sensitive to the other flavor neutrinos. SNO results showed that the electron neutrino flux was 1/3 of expected value, on the other hand, the absolute flux agreed with the standard solar model combined with Super-Kamiokande electron scattering data.

Another indication of the neutrino oscillation came from "atmospheric neutrino anomaly" observed by Kamiokande. When a cosmic ray interacts with the nucleus in the atmosphere, neutrinos are produced via pion decay and muon decay. The neutrino flux ratio $(\nu_\mu + \bar{\nu}_\mu)/(\nu_e + \bar{\nu}_e)$ is estimated about two. However, Kamiokande experiment reported the data-simulation ratio of this flux ratio was measured 0.6 [38, 39]. Similar results were obtained by IMB and Soudan-2 experiments [40, 41]. In 1998, the Super-Kamiokande observed a zenith angle dependent deficit in atmospheric muon neutrino flux, which was consistent with the two-flavor $\nu_\mu \to \nu_\tau$ oscillation [42], which is known to be the discovery of neutrino oscillation. The first demonstration of $\nu_\mu \to \nu_\mu$ oscillation using artificially produced neutrinos was done by K2K experiment [43]. The muon neutrinos were produced at KEK-PS in Tsukuba, Japan and detected at Super-Kamiokande. K2K observed muon neutrino deficits the as with the atmospheric neutrino oscillation. The direct confirmation of $\nu_\mu \to \nu_\tau$ oscillation was achieved by OPERA experiment in 2014 [44].

1.2.2 Theory of Neutrino Oscillation

Neutrino Oscillation occurs when the mass eigenstate and the flavor eigenstate are not identical. The relationship between flavor and mass eigenstates can be written with a unitary Matrix called Pontecorvo-Maki-Nakagawa-Sakata (PMNS) Matrix U introduced by Z. Maki, M. Nakagawa and S. Sakata [45] [2]:

$$|\nu_i\rangle = \sum_j U_{ij} |\nu_j\rangle \tag{1.3}$$

PMNS matrix U can be written with three mixing angles: θ_{12},θ_{13},θ_{23} and CP-violating phase δ_{CP}:

$$U = \begin{pmatrix} 1 & 0 & 0 \\ 0 & c_{23} & s_{13} \\ 0 & -s_{23} & c_{23} \end{pmatrix} \begin{pmatrix} c_{13} & 0 & s_{13}e^{-i\delta_{CP}} \\ 0 & 1 & 0 \\ -s_{13}e^{i\delta_{CP}} & 0 & c_{13} \end{pmatrix} \begin{pmatrix} c_{12} & s_{12} & 0 \\ -s_{12} & c_{12} & 0 \\ 0 & 0 & 1 \end{pmatrix} \tag{1.4}$$

where s_{ij} and c_{ij} denote $\sin\theta_{ij}$ and $\cos\theta_{ij}$ respectively. The time revolution of mass eigenstate $|\nu_j\rangle$ when a neutrino travels distance L in vacuum is given:

$$|\nu_j(t)\rangle = e^{-i(E_j t - p_j L)} |\nu_j(0)\rangle \,. \tag{1.5}$$

Assuming ultrarelativistic limit $p >> m_j$ where the m_j is mass of neutrino:

[2] B. Pontecorvo predicted neutrino oscillation first, however he predicted $\nu \to \bar{\nu}$ oscillation which is not the same as the flavor mixing [46]

$$E_j = \sqrt{p_j^2 + m_j^2} = p_j + \frac{m_j^2}{2E} \tag{1.6}$$

The time evolution of mass eigenstate after traveling $t = L$ is given as follows.

$$|\nu_j(t)\rangle = \exp\left(-i\frac{m_j^2 L}{2E}\right)|\nu_j(0)\rangle \tag{1.7}$$

Therefore, the time evolution of the flavor eigenstate $|\nu_\alpha\rangle$ is given:

$$|\nu_\alpha(t)\rangle = \sum_j U_{\alpha j} \exp\left(-i\frac{m_j^2 L}{2E}\right)|\nu_j(0)\rangle\,. \tag{1.8}$$

The oscillation probability $P(\nu_\alpha \to \nu_\beta)$ is then given:

$$P(\nu_\alpha \to \nu_\beta) = |\,\langle\nu_\beta(t)|\nu_\alpha(0)\rangle\,|^2 \tag{1.9}$$

$$= \delta_{\alpha\beta} - 4\sum_{i>j} Re(U_{\alpha i}U_{\beta i}^* U_{\alpha j}^* U_{\beta j}) \sin^2\left(\frac{\Delta m_{ij}^2 L}{4E}\right) \tag{1.10}$$

$$+ 2\sum_{i>j} Im(U_{\alpha i}U_{\beta i}^* U_{\alpha j}^* U_{\beta j}) \sin\left(\frac{\Delta m_{ij}^2 L}{2E}\right) \tag{1.11}$$

where $\Delta m_{ij}^2 = m_i^2 - m_j^2$.

Matter Effects

When the neutrinos travel through a dense medium such as the Earth, neutrinos interact with the electrons in the matter. ν_μ and ν_τ interacts with the electrons via neutral current interaction, on the other hand, ν_e interacts with the electron via both charged and neutral current interaction. Therefore, electron neutrinos feel different potential from the other flavor neutrinos and changes the neutrino oscillation probabilities. This effect is referred to as Mikheyev-Smirnov-Wolfenstein (MSW) effect [47, 48]. The matter effect is described as an effective potential for the Schödinger equation of neutrinos in vacuum.

$$V \equiv \sqrt{2} G_F n_e \tag{1.12}$$

where G_F denotes the Fermi constant and n_e denotes the density of electrons.

Oscillation Probabilities of $\nu_\mu \to \nu_e$ Oscillation and $\nu_\mu \to \nu_\mu$ Oscillation

The oscillation probability for the $\nu_\mu \to \nu_e$ and $\nu_\mu \to \nu_\mu$ with the first order of the matter effects is written as follows [49]:

$$\begin{aligned}
P(\nu_\mu \to \nu_e) &= 4c_{13}^2 s_{13}^2 s_{23}^2 \left(1 + \frac{2a}{\Delta m_{31}^2}(1 - 2s_{13}^2)\right)\sin^2\Phi_{31} \\
&+ 8c_{13}^2 s_{12}s_{13}s_{23}(c_{12}c_{23}\cos\delta_{CP} - s_{12}s_{13}s_{23})\cos\Phi_{32}\sin\Phi_{31}\sin\Phi_{21} \\
&- 8c_{13}^2 c_{12}c_{23}s_{12}s_{13}s_{23}\sin\delta_{CP}\sin\Phi_{32}\sin\Phi_{31}\sin\Phi_{21} \\
&+ 4s_{12}^2 c_{13}^2(c_{12}^2 c_{23}^2 + s_{12}^2 s_{23}^2 s_{13}^2 - 2c_{12}c_{23}s_{12}s_{13}\cos\delta_{CP})\sin\Phi_{21} \\
&- 2c_{13}^2 s_{13}^2 s_{23}^2 \frac{aL}{E}(1 - 2s_{13}^2)\cos\Phi_{32}\sin\Phi_{31}
\end{aligned} \tag{1.13}$$

$$
\begin{aligned}
P(\nu_\mu \to \nu_\mu) &= 1 - 4c_{13}^2 s_{23}^2 (c_{12}^2 c_{23}^2 + s_{12}^2 s_{13}^2 s_{23}^2) \sin^2 \Phi_{32} \\
&- 4c_{13}^2 s_{23}^2 (s_{12}^2 c_{23}^2 + c_{12}^2 s_{13}^2 s_{23}^2) \sin^2 \Phi_{31} \\
&+ c_{13}^2 s_{13}^2 s_{23}^2 (1 - 2c_{13}^2 s_{23}^2) \frac{8a}{\Delta m_{31}^2} \sin \Phi_{31} (\sin \Phi_{31} - \Phi_{31} \sin^2 \Phi_{31}) \\
&- 8 c_{12} c_{13}^2 c_{23} s_{12} s_{13} s_{23}^3 \cos \delta_{CP} (\sin^2 \Phi_{31} - \sin^2 \Phi_{32}) \\
&- 4 \left((c_{12}^2 c_{23}^2 + s_{12}^2 s_{13}^2 s_{23}^2)(s_{12}^2 c_{23}^2 + c_{12}^2 s_{13}^2 s_{23}^2) \right. \\
&+ \left. 2 c_{12} c_{23} s_{12} s_{23} (c_{23}^2 - s_{13}^2 s_{23}^2)(c_{12}^2 - s_{12}^2) \cos \delta_{CP} - 4 c_{12}^2 c_{23}^2 s_{12}^2 s_{13}^2 s_{23}^2 \cos^2 \delta_{CP} \right) \sin^2 \Phi_{21}
\end{aligned}
\tag{1.14}
$$

where

$$
\Phi_{ij} \equiv \frac{\Delta m_{ij}^2 L}{4E} \tag{1.15}
$$

$$
a \equiv 2\sqrt{2} G_F n_e \tag{1.16}
$$

and s_{ij} and c_{ij} denote $\sin\theta_{ij}$ and $\cos\theta_{ij}$. The oscillation probability for the anti-neutrinos $\bar{\nu}_\mu \to \bar{\nu}_e$ and $\bar{\nu}_\mu \to \bar{\nu}_\mu$ are obtained by just replacing δ_{CP} and a with $-\delta_{CP}$ and $-a$. Figure 1.2 shows the oscillation probabilities of $\nu_\mu \to \nu_e$ and $\bar{\nu}_\mu \to \bar{\nu}_e$ assuming $L = 295$ km and $\sin^2 2\theta_{13} = 0.1$ for various δ_{CP} values. The $\nu_\mu \to \nu_\mu$ oscillation doesn't violate CP symmetry, on the other hand, $\nu_\mu \to \nu_e$ violate CP symmetry if $\sin\delta_{CP}$ has non-zero value.

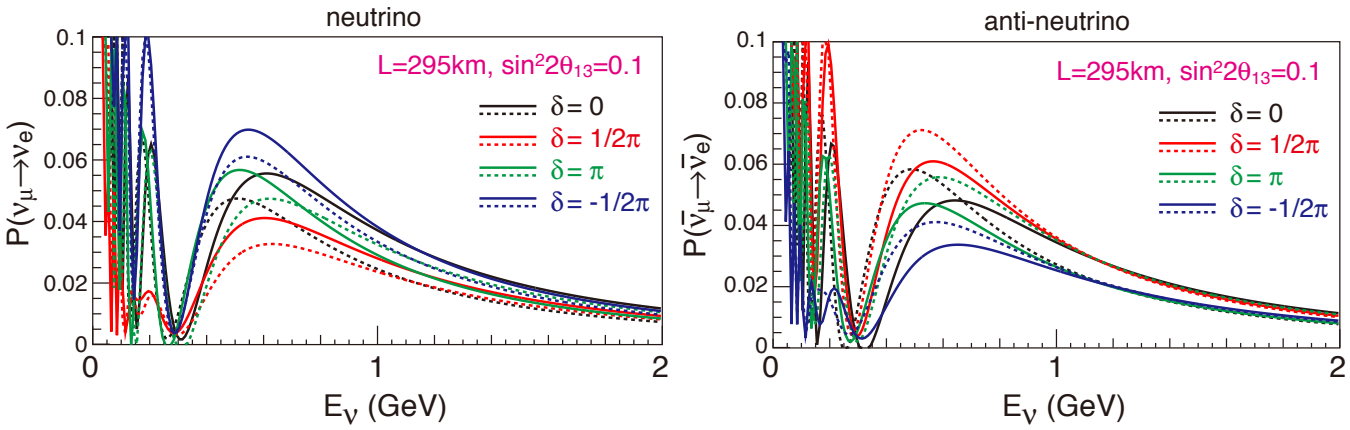

(a) $\nu_\mu \to \nu_e$ (b) $\bar{\nu}_\mu \to \bar{\nu}_e$

Figure 1.2: The $\nu_\mu \to \nu_e$ and $\bar{\nu}_\mu \to \bar{\nu}_e$ oscillation probabilities with L=295km and $\sin^2 2\theta_{13} = 0.1$ Solid line and dotted line correspond to the normal and inverted hierarchy respectively [50]. The mass hierarchy will be explained later.

1.2.3 Measurements of Neutrino Oscillation Parameters

The mixing parameters θ_{23}, θ_{12}, θ_{13} and the mass splitting Δm_{32}^2 and Δm_{12}^2 are measured by various neutrino oscillation experiments.

θ_{12}, Δm^2_{12}

These parameters are related to the solar neutrino oscillation. They are obtained from electron neutrino disappearance measured by solar neutrino experiments [33–35, 37, 51–53] and KamLAND experiment [54]. The KamLAND (Kamioka Liquid Scintillator Anti-Neutrino Detector) collaboration measures these values with reactor neutrino. They measure $\bar{\nu}_e \to \bar{\nu}_e$ oscillation for the $\mathcal{O}(1)$ MeV neutrinos, which is the same energy region as solar neutrinos. The best fit values from the global fit [55] are $\sin^2\theta_{12} = 0.307^{+0.013}_{-0.012}$ and $\Delta m^2_{21} = 7.40^{+0.21}_{-0.20} \times 10^{-5}$ eV^2.

θ_{23}, Δm^2_{32}

These parameters are related to the atmospheric neutrino oscillation. Atmospheric neutrino experiments (Super-Kamiokande [56], IceCube [57]) and accelerator neutrino experiments (T2K [58–60], NOνA [61–63] currently, and K2K [43], MINOS/MINOS+ [64, 65] in the past) measured these values with muon neutrino disappearance of $\mathcal{O}(100)$ MeV neutrinos. The best fit values from the global fit [55] are $\sin^2\theta_{23} = 0.538^{+0.033}_{-0.069}$ and $\Delta m^2_{32} = 2.494^{+0.033}_{-0.031} \times 10^{-3}$ eV^2 for normal hierarchy and $\sin^2\theta_{23} = 0.554^{+0.023}_{-0.033}$ and $\Delta m^2_{32} = -2.465^{+0.032}_{-0.031} \times 10^{-3}$ eV^2 for inverted hierarchy. The mass hierarchy is explained later.

θ_{13}

The first indication of non-zero θ_{13} was reported in 2011 by T2K accelerator neutrino oscillation experiment [66]. In 2012, reactor neutrino experiments Daya Bay [67], RENO [68] and Double Chooz [69] reported their first measurements of θ_{13} with $\bar{\nu}_e$ disappearance. In 2014, T2K established non-zero θ_{13} at more than 7σ with accelerator neutrinos [70]. The best fit value from the global fit [55] is $\sin^2\theta_{13} = 0.02206^{+0.00075}_{-0.00075}$ for Normal hierarchy and $\sin^2\theta_{13} = 0.02227^{+0.00074}_{-0.00074}$ for inverted hierarchy.

δ_{CP}

The value of δ_{CP} has never been measured yet precisely. The first hint of δ_{CP} was reported by T2K in 2014 [70]. The $\nu_\mu \to \nu_e$ probability was slightly greater than the expected value assuming $\sin\delta_{CP} = 0$ and the reactor neutrino θ_{13} value. Combining reactor results and T2K results, constraint on δ_{CP} was obtained. The T2K experiment also reported the δ_{CP} measurement in 2016 combining antineutrino oscillation results [71]. As described later in this thesis, T2K reported an updated result in 2017. $\delta_{CP} = -1.70^{+0.64}_{-0.62}$ was obtained and CP-conservation was excluded with 2σ significance. Another complementary accelerator neutrino oscillation experiment, NOνA reported updated ν_e appearance results in 2017, and showed that $\delta_{CP} = \pi/2$ is strongly disfavored [63]. The best fit value from the global fit is $\delta_{CP} = -2.20^{+0.75}_{-0.54}$ for Normal hierarchy and $\delta_{CP} = -1.43^{+0.45}_{-0.51}$ for inverted hierarchy.

1.3 Open Question About Neutrinos

Since 1998, the great experimental progress has been achieved by the various neutrino oscillation experiments. Further understanding of the pattern of neutrino masses and neutrino mixing, of their origins and of the status of CP symmetry in the lepton sector is required to understand the nature of neutrinos. There are unsolved questions about neutrinos as follows.

1.3.1 The Values of δ_{CP} and θ_{23}

As described in Section 1.2, δ_{CP} has never been measured yet. θ_{23} was measured however, the uncertainty is still large. The importance of these measurements is described in the next section.

1.3.2 Mass Hierarchy

The sign of Δm^2_{32} is not known yet. The both mass ordering $m_3 > m_2 > m_1$ and $m_2 > m_1 > m_3$ is possible with the current precision of the measurement. The former case is called "normal hierarchy" and latter case is called "inverted hierarchy". T2K and NOνA experiments are sensitive to the mass hierarchy through the matter effect of the $\nu_\mu \to \nu_e$ oscillation. NOνA is more sensitive to the mass hierarchy than T2K because the baseline is longer (L$\sim$ 810 km) and the matter effect is more significant. Super-Kamiokande experiment is also trying to determine the mass hierarchy using atmospheric neutrino [56]. All the oscillation measurement results prefer the normal hierarchy, however, the significance is still small. The other experiments such as $0\nu\beta\beta$ decay experiments and cosmological observation are also sensitive to the mass hierarchy [72].

1.3.3 Absolute Mass

Neutrino oscillation measurement measures only the squared mass difference of each mass eigenstate but not absolute mass. The absolute masses are not measured yet. The upper limit of electron neutrino mass $m_{\nu_e} < 2.05$ eV is obtained by the precise measurement of tritium decay spectrum by Troitzk experiment [73] and similar results was obtained in the Mainz experiment [74]. The upper limit of sum of the neutrino mass $\sum m_\nu < 0.12$ eV is obtained by the cosmological observation (Cosmic microwave background and large scale structure survey) [29]. It is important to know the mass scale of neutrino since several Grand Unified Theory (GUT) models predict massive neutrinos.

1.3.4 Sterile Neutrinos

As shown in Section 1.1, the Z^0 decay width measurement showed that there are only three neutrino generations that interact with Z^0. However, it is possible there is fourth generation neutrino which does not interact via weak interaction. Such a neutrino is called sterile neutrino. In 1996, LSND experiment reported the short baseline (30 m) $\bar{\nu}_\mu \to \bar{\nu}_e$ oscillation with $\Delta m^2 = 0.05 - 1$ eV^2 [75]. Several experiments excluded the LSND some allowed region [76, 77], however the existence of sterile neutrinos is still under investigation.

1.3.5 Majorana Neutrino or Dirac Neutrino ?

A spin 1/2 particle which is its own antiparticle is called Majorana particle [78], and a spin 1/2 particle which its antiparticle is a different particle is called Dirac particle. Neutrino in the standard model is assumed to be the Dirac particle. Once massive neutrino is established, right-handed neutrino should be introduced to the standard model to conserve gauge invariance if neutrinos are Dirac particles. The neutrino mass term of Dirac neutrino is given as follows:

$$\mathcal{L}_{Dirac\ mass} = m_{D\nu}(\bar{\nu}_R \nu_L + \bar{\nu}_L \nu_R) \tag{1.17}$$

where $m_{D\nu}$ is neutrino Dirac mass, R and L are right-handed and left-handed, respectively. Since only left-handed particles are participated the weak interaction, therefore, the right-handed neutrino

is sterile in this case. In the standard model, particles obtain their mass by Higgs mechanism. It is unnatural that the Higgs boson couples the particles from $\mathcal{O}(1)$ meV to $\mathcal{O}(100)$ GeV mass range.

On the other hand, if neutrinos are Majorana particles, the mass term is given as follows:

$$\mathcal{L}_{Majorana\ mass} = m_{M\ \nu}(\bar{\nu}_R^C \nu_R + \bar{\nu}_L^C \nu_L) \tag{1.18}$$

In the standard model, only neutrino can be Majorana particle. If neutrinos are Majorana particle, the light mass of neutrino may be explained. The Dirac and Majorana mass term are rewritten as follows:

$$\mathcal{L}_{mass} = (\bar{\nu}_L, \bar{\nu}_R^C) \begin{pmatrix} m_L & m_D \\ m_D & m_R \end{pmatrix} \begin{pmatrix} \nu_L^C \\ \nu_R \end{pmatrix} \tag{1.19}$$

where m_L and m_R are left-handed and right-handed Majorana neutrino mass, and m_D is Dirac mass. The observable masses are the eigenvalues of the mass matrix. Assuming $m_L = 0$ and $m_R >> m_D$, the eigenvalues are obtained.

$$m_\nu \sim \frac{m_D^2}{m_R},\ m_N = m_R \tag{1.20}$$

We take m_ν neutrino is actually observed neutrino. If the m_R is heavy, m_ν can be light, and another heavy neutrino is predicted. This mechanism is called (Type-I) seesaw mechanism [79–83].

If the neutrino is Majorana particle, lepton number violation is predicted. The $0\nu\beta\beta$ decay is a possible process for the observation of the lepton number violation. Several $0\nu\beta\beta$ decay searches such as GERDA [84] KamLAND-zen [85] are ongoing. There are also many heavy neutrino and lepton number violation process searches in collider experiments [86, 87].

It is also important to note that if the neutrino is Majorana particle, additional CP-violating phases can be introduced [3]. These CP phases are also important to understand the baryon asymmetry in the universe which is described later.

1.4 Motivation of δ_{CP} Measurement

1.4.1 Physics Behind the Mixing Angle

The theoretical framework of flavor mixing of neutrino oscillation is similar to the Cabibbo-Kobayashi-Maskawa (CKM) Matrix [88] which describes the mixing in the quark sector. However, the matrix elements are totally different. The values of CKM matrix element from PDG 2018 [89] are:

$$V_{CKM} = \begin{pmatrix} 0.97446 \pm 0.00010 & 0.22452 \pm 0.00044 & 0.0365 \pm 0.00012 \\ 0.22438 \pm 0.00044 & 0.97359^{+0.00010}_{-0.00011} & 0.04214 \pm 0.00076 \\ 0.00896^{+0.00024}_{-0.00023} & 0.04133 \pm 0.00074 & 0.999105 \pm 0.000032 \end{pmatrix} \tag{1.21}$$

In contrast, the 3σ ranges for the magnitude of the entries of the PMNS matrix is written [55]:

$$V_{PMNS} = \begin{pmatrix} 0.799 - 0.844 & 0.516 - 0.582 & 0.141 - 0.156 \\ 0.242 - 0.494 & 0.467 - 0.678 & 0.639 - 0.774 \\ 0.284 - 0.521 & 0.490 - 0.695 & 0.615 - 0.754 \end{pmatrix} \tag{1.22}$$

The diagonal part of the CKM matrix is almost one, in contrast, the PMNS matrix has relatively small diagonal part. The best fit value of the mixing angle is close to $\sin\theta_{23} = 1/\sqrt{2}$, $\sin\theta_{12} = 1/\sqrt{3}$ and $\delta_{CP} = -\pi/2$, which indicates the physics behind the mixing angle.

[3] This Majorana CP phase doesn't affect the neutrino oscillation.

In recent years, several theories with the discrete non-Abelian symmetry are proposed to account for the mixing angle and the difference between quark and lepton. One model called *tri-bimaximal* mixing model [90], for example, predicted $\theta_{13} = 0$, however it was ruled out since the non-zero θ_{13} was established. Some theorists are trying to modify this model to account for the non-zero θ_{13} and predict δ_{CP} value. An extension model called *tri-bimaximal-Cabibbo* mixing model [91] gives following matrix using the relationship between Cabibbo angle and mixing parameter $\theta_{13} \sim \theta_C/\sqrt{2} \sim 9.2$:

$$V_{TBC} = \begin{pmatrix} \sqrt{\frac{2}{3}}(1-\frac{1}{4}\lambda^2) & \frac{1}{\sqrt{3}}(1-\frac{1}{4}\lambda^2) & \frac{1}{\sqrt{2}}\lambda e^{-i\delta} \\ -\frac{1}{\sqrt{6}}(1+\lambda^2 e^{i\delta}) & \frac{1}{\sqrt{3}}(1-\frac{1}{2}\lambda e^{i\delta}) & \frac{1}{\sqrt{2}}(1-\frac{1}{4}\lambda^2) \\ \frac{1}{\sqrt{6}}(1-\lambda e^{i\delta}) & -\frac{1}{\sqrt{3}}(1+\frac{1}{2}\lambda e^{i\delta}) & \frac{1}{\sqrt{2}}(1-\frac{1}{4}\lambda^2) \end{pmatrix} \tag{1.23}$$

where $\lambda = 0.2253 \pm 0.0007$ [89] is the Wolfenstein parameter. This model predicts $\delta_{CP} = \pm\pi/2$.

In order to identify whether the mixing matrix is given based on the discrete symmetry or different mechanism (anarchy model for example [92]), it is necessary to measure the mixing angles precisely including δ_{CP}.

1.4.2 Baryon Asymmetry in the Universe

More than fifty years ago, Sakharov has studied the conditions in which a matter-antimatter asymmetry is generated [93]. These basic conditions are:

- The theory should violate baryon number.
- The theory should violate both C and CP.
- The processes of a baryon-number generation should have a non-thermal equilibrium dynamics.

It is known that the standard model cannot explain the observed baryon asymmetry in the universe. The quarks can violate C and CP, however the size of CP violation is not sufficient to explain the baryon asymmetry in the universe [94]. To account for the baryon asymmetry in the universe, various scenarios "beyond the standard model" have been considered. A scenario where the matter-antimatter asymmetry is first generated in the lepton sector is called *leptogenesis*. In the scenario, lepton asymmetry is generated by heavy neutrino decay, thereafter the lepton asymmetry is converted into baryon asymmetry by sphaleron process [95]. The CP phase in the PMNS matrix does not always contribute to every leptogenesis scenario, however the CP violation in the lepton sector will be a strong evidence for the leptogenesis and it is important to measure the CP phase in PMNS matrix to constrain the scenario.

1.5 Problems on the δ_{CP} Measurement

The δ_{CP} measurement is done by $\nu_\mu \to \nu_e$ long baseline neutrino oscillation measurement. As shown in Fig. 1.2, the oscillation probability changes depending on the δ_{CP} value. Therefore, precise measurement of $\nu_\mu \to \nu_e$ oscillation enables us to obtain δ_{CP}. Two experiments: T2K and NOνA which can measure $\nu_\mu \to \nu e$ oscillation are currently operating. The latest results of these experiments will be discussed in Section 13.4.

Figure 1.3 shows the systematic and statistical uncertainties of T2K and NOνA presented in NEUTRINO 2018 conference [96, 97]. In both experiments, statistical uncertainties are dominant error sources. For the systematic uncertainties, the neutrino-nucleus cross-section uncertainties (For T2K, E_b, NC1γ and NCOther are also related to the cross-section) are one of the largest uncertainties in both experiments.

	1Rμ		1Re	
Error Source	FHC	RHC	FHC	RHC
SK Detector	2.40	2.01	2.83	3.79
SK FSI+SI+PN	2.20	1.98	3.02	2.31
w/ ND280 const. flux & xsec	2.88	2.68	3.02	2.86
E_b	2.43	1.73	7.26	3.66
NC1γ	0.00	0.00	1.07	2.58
NC Other	0.25	0.25	0.14	0.33
Syst. Total	4.91	4.28	8.81	7.03
Stat. Error	6.41	9.90	11.5	25.8

(a) The percentage of the T2K uncertainties for muon-like and electron-like sample

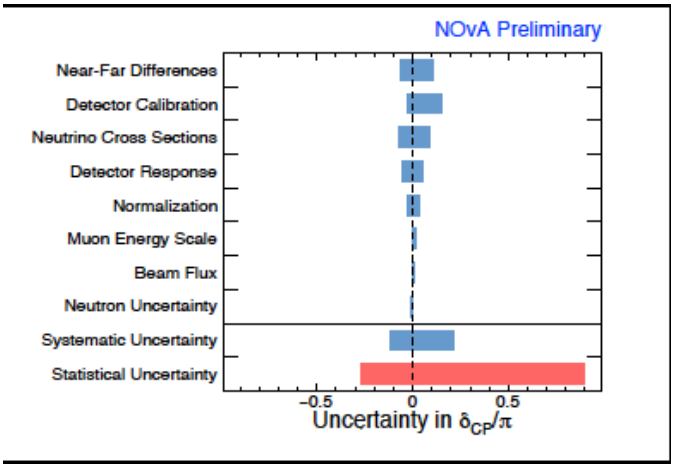

(b) NOνA uncertainties for δ_{CP} measurement

Figure 1.3: The uncertainties of T2K and NOνA. The value of the table for T2K and the plot for NOνA are taken from [96, 97].

1.5.1 Statistical Uncertainties

Neutrino rarely interacts with the other particles since it interacts only via weak interaction. Furthermore, in the long baseline neutrino oscillation experiments we shoot the neutrino beam to a target detector $\mathcal{O}(100)$ km away from the neutrino source. Therefore, large amount of neutrino is necessary for the precise measurement. It is important to achieve high intensity neutrino beam and high efficiency neutrino detection with large volume target. As will be discussed in Chapter 2, neutrino beam is produced from proton beam and its intensity depends on that of the proton beam. Thus, an achievement of high intensity proton beam is one of the most important keys for the precise measurement of δ_{CP}.

Systematic Uncertainties from Neutrino-Nucleus interaction

As will be described in Chapter 6, the neutrino-nucleus interaction model is required to predict the event rates and spectrum at the near detector and the far detector in the long baseline neutrino experiments. Over many years, neutrino cross-section has been measured with various detector techniques, target nucleus and neutrino energy. Figure 1.4a shows the CC inclusive ($\nu + X \to \mu + X'$) measurement from various experiments. At high energy region the inclusive cross section is dominated by deep inelastic scattering (DIS) which will be discussed in Chapter 8. DIS describes the interaction with point-like scattering of neutrino with quarks, therefore, the cross-section becomes almost linear to the neutrino energy.

In most of the accelerator neutrino experiment, they utilize the neutrinos with energy around a few GeV. The neutrino interaction below 1 GeV is dominated by CC quasi-elastic (CCQE) interaction.

$$\begin{aligned} \nu_l + n &\to l^- + p \\ \bar{\nu}_l + p &\to l^+ + n \end{aligned} \tag{1.24}$$

Figure 1.4b shows the current status of existing measurements of CCQE interaction cross section as a function of neutrino energy. Solid line corresponds to the prediction from neutrino event generator NUANCE [98]. There are some discrepancies between theoretical prediction and observations. This difference affects the neutrino oscillation measurement since it directly affects the event rate prediction at the far detector. Therefore, it is important to understand the neutrino-nucleus interaction and estimate its uncertainty precisely.

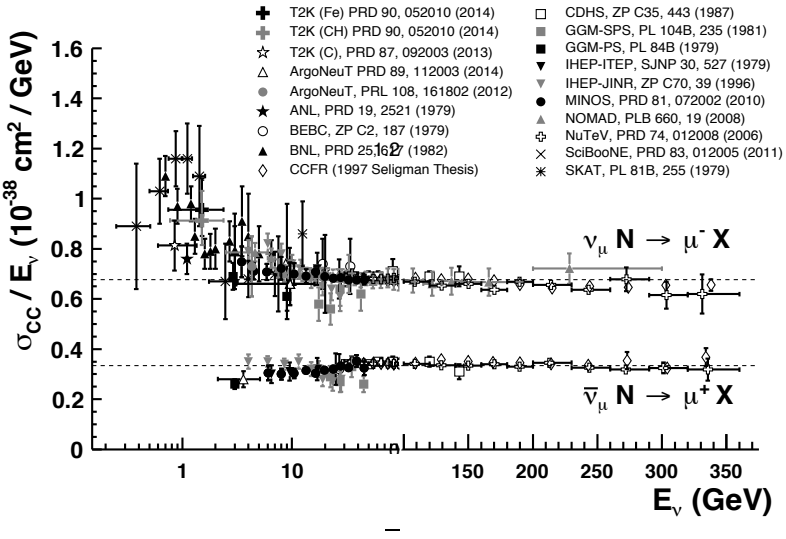

(a) CC inclusive interaction cross-section measurements

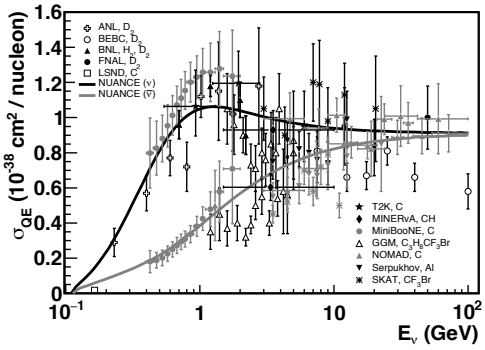

(b) CC quasi elastic scattering cross-section measurements

Figure 1.4: Current status of neutrino-nucleus interaction measurements. The plots are taken from [89]

In recent years, various theoretical works has been proposed to solve this discrepancy. Each model uses different description of the nuclear effects or different parameters. They predict different cross-section and kinematics however, the measurements are not yet so accurate that constraint the models. It is still uncertain which interaction model should be chosen and the choice of interaction model also affects the oscillation analysis. Therefore, it is important to understand how the interaction model affect the oscillation analysis.

1.6 Outline of This Thesis

We report the updated T2K oscillation analysis using the neutrino beam data collected from Jan. 2010 to Apr. 2017. First, the overview of the T2K experiment is shown in Chapter 2. To improve the statistics, the J-PARC proton accelerator upgrade is necessary. In Chapter 3, the overview of the J-PARC accelerator is described. The developments toward the higher beam intensity are shown in Chapter 4. A summary of collected data is shown in Chapter 5.

From Chapter 6 to Chapter 13, the details of neutrino oscillation analysis in T2K are described. As shown in Section 1.5, the neutrino-nucleus interaction is not known well and various models are proposed. In this thesis, we focus on the investigation of the effects on the oscillation parameters coming from the neutrino-nucleus interaction modeling. The overview of the analysis is given in Chapter 6. The details of the flux simulation and the neutrino-nucleus interaction model are given in Chapter 7 and Chapter 8. In Chapter 9, we describe the near detector analysis to reduce the systematic uncertainties. In Chapter 10 and Chapter 11, the details of the far detector analysis and the fit procedure for the oscillation parameter determination are described. The effects of the neutrino-nucleus cross-section modeling on the oscillation parameters are discussed in Chapter 12. The results of oscillation parameter measurement are shown in Chapter 13. The conclusion is given in Chapter 14.

Chapter 2

T2K Experiment

2.1 Introduction of T2K Experiment

T2K (Tokai to Kamioka) is a long baseline neutrino oscillation experiment in Japan [99]. An almost pure ν_μ beam is produced with J-PARC (Japan Proton Accelerator Research Complex) Main Ring in Tokai, Japan and is detected at ND280 near detector and Super-Kamiokande far detector 295 km away from J-PARC.

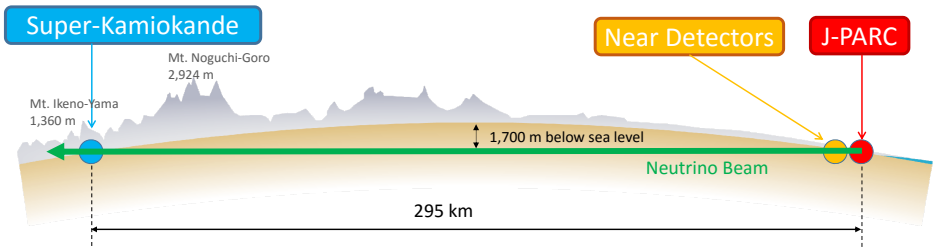

Figure 2.1: Overview of the T2K experiment

2.1.1 Physics Goal of the T2K experiment

The main goal of the T2K experiment is to measure the CP violating phase δ_{CP} in the PMNS matrix by observing following neutrino oscillation.

Precise Measurement of $\nu_\mu \to \nu_e$ Oscillation

In 2013, T2K observed $\nu_\mu \to \nu_e$ oscillation with 7.3σ significance [70]. This is the first observation of this oscillation. It is important to measure $\nu_\mu \to \nu_e$ oscillation more precisely since this oscillation is sensitive to δ_{CP}.

Precise Measurement of $\nu_\mu \to \nu_\mu$ Oscillation and $\bar{\nu}_\mu \to \bar{\nu}_\mu$ Oscillation

Current best fit value for $\sin\theta_{23}$ is close to 0.5, which indicates the maximal mixing. However, NOνA claimed non-maximal mixing in [100] [1]. Therefore, it is important to resolve this discrepancy. For δ_{CP} measurement, a precise measurement of θ_{23} is also important since the CP violation term in $\nu_\mu \to \nu_e$ oscillation is proportional not only to $\sin\theta_{13}$ and $\sin\delta_{CP}$ but also to $\sin\theta_{23}$. Our goal is to determine the values of θ_{23} and Δm^2_{32} with an accuracy of 1% and 3%, respectively.

Discovery of $\bar{\nu}_\mu \to \bar{\nu}_e$ Oscillation

The $\bar{\nu}_\mu \to \bar{\nu}_e$ has never been observed before 2018. [2]. The oscillation probability is same as $\nu_\mu \to \nu_e$ except the sign of CP violation term. However, the $\bar{\nu}$ cross-section at the T2K neutrino energy is 1/3 of that of ν and has larger uncertainties, therefore, it is more difficult to observe than $\nu_\mu \to \nu_e$ oscillation. Observation of $\bar{\nu}_\mu \to \bar{\nu}_e$ is also important to determine δ_{CP} since the oscillation probability difference between ν and $\bar{\nu}$ directly indicates the CP violation in the lepton sector.

2.2 J-PARC Accelerator and Neutrino Beamline

2.2.1 J-PARC Accelerator

J-PARC (Japan-Proton Accelerator Research Complex) is placed at Tokai, Japan. The proton beam is accelerated up to 30 GeV and extracted from Main Ring to the neutrino beamline. The details of J-PARC are explained in Chapter 3.

2.2.2 Neutrino Beamline

Figure 2.2 shows the illustration of the neutrino beamline in T2K. The neutrino beamline consists of two parts: primary beamline which delivers the proton beam to the target, and secondary beamline which generates the neutrino beam. In the primary beamline, there are 11 normal conducting magnets (preparation section) to tune the proton beam, 14 superconducting magnets [101] (Arc section) to bend the beam to the Super-Kamiokande direction, and 10 normal conducting magnets (Final focusing section) to transport the beam to the neutrino production target. The proton beam is monitored by beam monitors which are shown later. The proton beam from the primary beamline enters the beam window made of Titanium, and impinges on the target through the beam baffle which is a collimator to protect the magnetic horns in the secondary beamline. Various mesons such as pions and kaons are produced by the proton beam in the target. The outgoing mesons from the target are focused to the forward direction by three magnetic horns excited by a 250 kA (designed for up to 320 kA) current pulse. Thereafter, the pions decay into muons and neutrinos ($\pi \to \mu\nu_\mu$) during traveling in a 94 m long decay volume. The remaining particles are absorbed by the beam dump placed at the end of the decay volume. The neutrino beam intensity and direction are monitored by measuring the profile of muons associated with the neutrinos with Muon Monitor (MUMON) on bunch-by-bunch basis, and by measuring the neutrino beam profile directly with INGRID.

[1] NOνA reported updated results in Jan. 2018. The results became consistent with the maximal mixing [63]. NOνA also updated their results in NEUTRINO2018 conference, and reported their results prefers the upper octant ($\sin^2\theta_{23} > 0.5$) [97].

[2] NOνA claimed the observation of $\bar{\nu}_\mu \to \bar{\nu}_e$ oscillation at more than 4σ in the NEUTRINO 2018 conference [97].

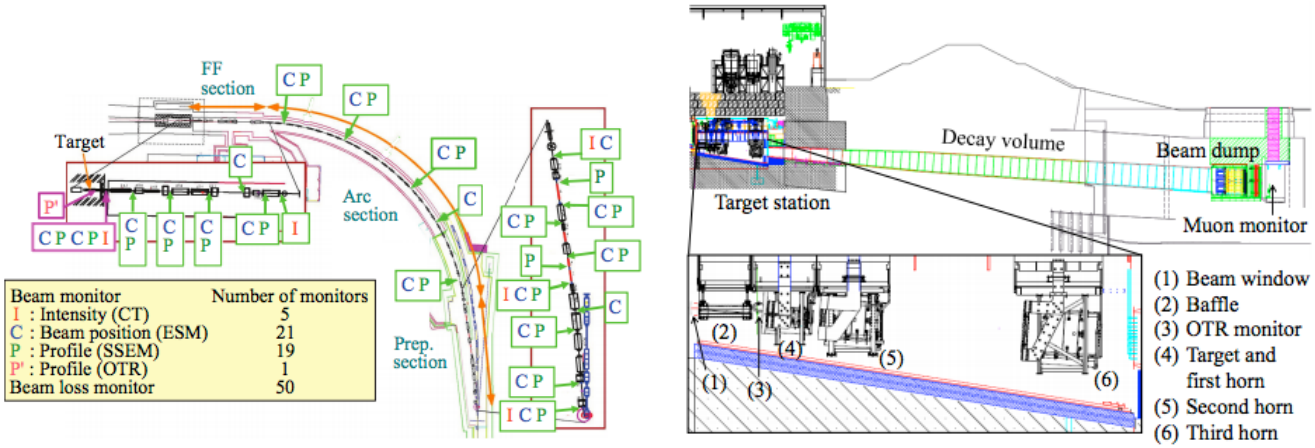

(a) primary beamline

(b) secondary beamline

Figure 2.2: Overview of the T2K beamline

Graphite Target

T2K uses a 91.4 cm long, 2.6 cm diameter graphite target. The temperature at the center of the target is expected to reach 700 °C, therefore the target is cooled by helium gas. The target is supported inside the inner conductor of the first horn with a positional accuracy of 0.1 mm.

Magnetic Horn

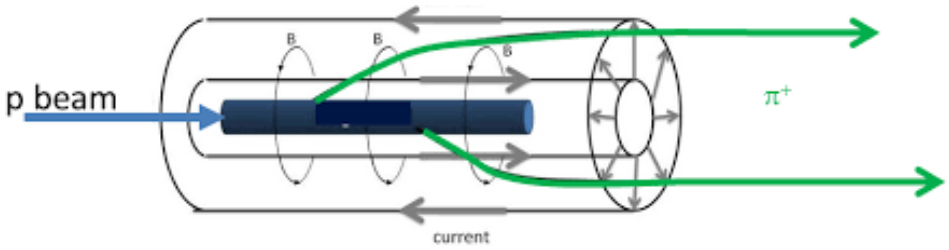

Figure 2.3: Schematic view of the T2K magnetic horn

Figure 2.3 shows the schematic view of the magnetic horn. A toroidal magnetic field is generated with co-axial structures. Charged mesons (mainly pions) are focused to the forward direction with the magnetic field [102]. The currents are measured by four Rogowski coils. Measurement uncertainty of the absolute current is less than 2%. The neutrino flux at Super-Kamiokande is increased by a factor of 16 (compared to the flux at 0 kA) at the spectrum peak energy ($\sim$ 0.6 GeV) [103, 104]. The polarity of the horn can be changed when the current direction is reversed. When the inner conductor current flows along the beam direction, the positive pions are focused and negative pions are defocused. This condition is referred to as "Forward Horn Current" (FHC) mode. On the other hand, when the current flows opposite direction, negative pions are focused. This mode is referred to as "Reverse Horn Current" (RHC) mode. Positive pions decay into positive muons and neutrinos, and negative pions decay into negative muons and anti-neutrinos. Therefore, neutrino-enriched beam is produced in the FHC mode, while anti-neutrino-enriched beam is produced in the RHC mode.

Beam Monitors

To monitor the condition of the proton beam, several beam monitors are equipped around the beamline. Figure 2.2 shows the position of the beam monitor in the primary beamline and secondary beamline. Each alphabet denotes:

- I: Current Transformer (CT)
  CT is a 50-turn toroidal coil around a cylindrical ferromagnetic core. CT measures the intensity of the proton beam with a 2% accuracy.

- C: Electro-Static Monitor (ESM)
  ESM has four segmented cylindrical electrodes surrounding the proton beam orbit. ESM measures the proton beam center position by measuring top-bottom and left-right asymmetries of the beam-induced current on the electrodes. The measurement precision of the beam position is less than 450 μm.

- P: Segmented Secondary Emission Monitor (SSEM)
  SSEM has two thin (5 μm) titanium foils stripped horizontally and vertically, and an anode high voltage foil between them. When the proton beam hits the strips, secondary electrons are emitted. The electrons then drift along the electric field and induce currents on the strips. The proton beam profile is reconstructed from the corrected charge distributions of the strips. The systematic uncertainty of the beam width measurement is 200 μm.

- Beam Loss Monitor (BLM)
  To monitor the beam loss, 50 BLMs are installed in the T2K beamline. BLM (Toshiba Electron Tubes & Devices E6876-400) is a wire proportional counter filled with an Ar-CO_2 mixture [105]. When the BLM signal exceeds a threshold, a beam abort interlock signal is fired. The BLM has a sensitivity down to a 16 mW beam loss.

- Optical Transition Radiation Monitor (OTR)
  The OTR measures the beam profile just upstream of the target. The OTR has an eight-position carousel holding four titanium-alloy foils, an aluminum foil, a fluorescent ceramic foil of 100 μm thickness, a calibration foil and an empty slot [106]. As the beam enters and exits the foil, visible light (transition radiation) is produced in a narrow cone around the beam. The light is transported to an area with lower radiation levels then measured by a camera to reconstruct the beam profile.

- Muon Monitor (MUMON)
  The muon monitor consists of two types of detector arrays: ionization chambers and silicon PIN photodiodes [107,108]. Each silicon PIN photodiode (Hamamatsu S3590-08) has an active area of $10 \times 10\ mm^2$ and a depletion layer thickness of 300 μm. The photodiodes are operated with 80 V high voltage. The ionization chamber consists of two parallel plate electrodes on alumina-ceramic plates with an active volume of $75 \times 75 \times 3$ mm. Between the electrodes, 200-270 V is applied. Two kinds of gas are used for the ionization chambers according to the beam intensity: Ar with 2 % N_2 for low intensity, and He with 1 % N_2 for high intensity. The 2D muon profile is reconstructed in 7×7 arrays from the distributions of the observed charges. The intrinsic resolution of the muon monitor is less than 0.1 % for the intensity and less than 0.3 cm for the profile center.

The optics parameters of the proton beam (Twiss parameters and emittance) are reconstructed from the profiles measured by the SSEMs, and are used to estimate the profile center, width and divergence at the target. The photographs of beam monitors are shown in Fig. 2.4 and the muon beam profile measured by MUMON is shown in Fig. 2.5.

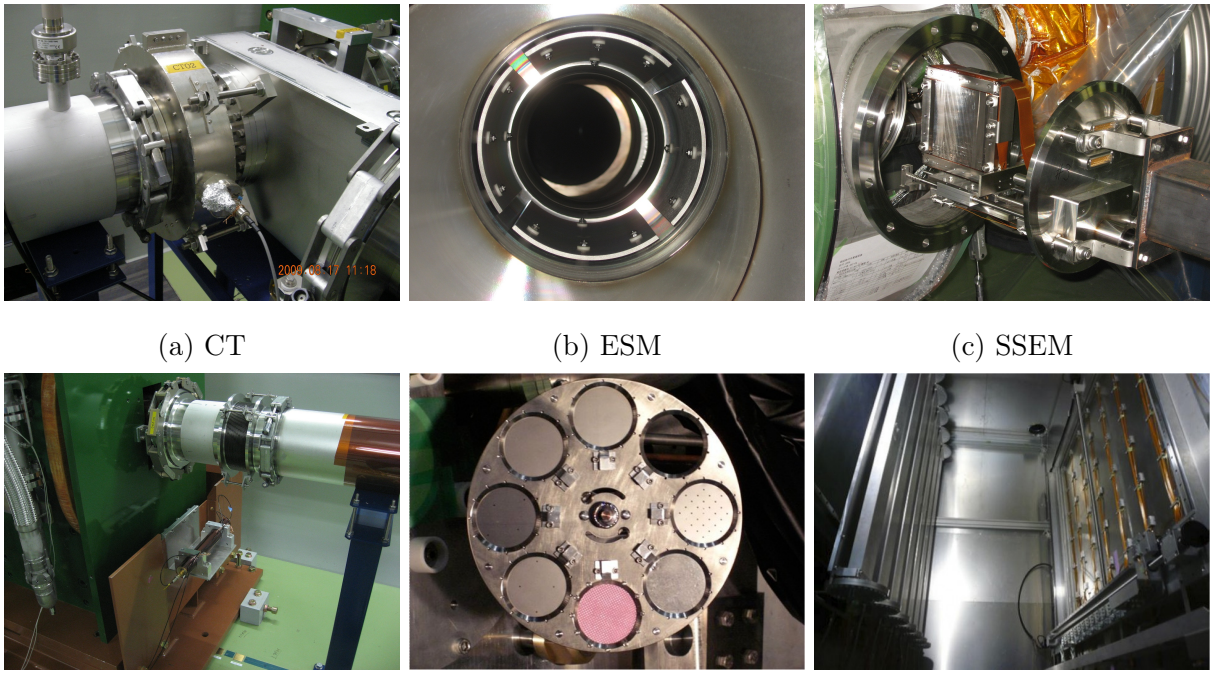

(a) CT (b) ESM (c) SSEM

(d) BLM (e) OTR (f) MUMON

Figure 2.4: Beam monitors

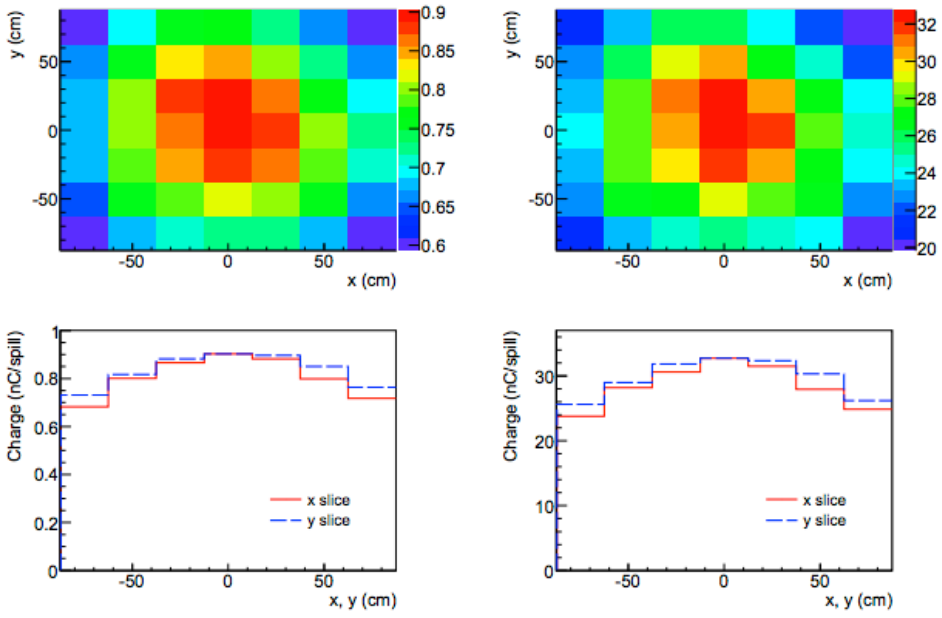

Figure 2.5: Muon beam profile measured by MUMON. Left plots are for Si PIN photo-diode and Right plots are for ionization chamber.

2.2.3 Off-Axis Method

T2K adopted off-axis configuration to achieve a narrow-band neutrino beam [109]. In the off-axis configuration, the neutrino beam axis is displaced from the far detector. The bottom plot of Fig. 2.6 shows the neutrino flux for different off-axis angles as a function of neutrino energy. With a non-zero off-axis angle, the high energy neutrinos reduce and the neutrino flux is centered around a peak in the low energy region. As described in Section 1.5.1, non-CCQE events are dominant in the high energy region. The neutrino energy is reconstructed by the lepton momentum assuming CCQE as described in Chapter 10. The non-CCQE interaction has different kinematics from CCQE and the energy reconstruction will be biased. The off-axis angle method therefore reduces the background events. T2K adopts 2.5° off-axis angle. The off-axis angle was determined to have a peak around the oscillation maximum as shown in second and third plots in Fig. 2.6. The neutrino flux spectrum is largely affected by the off-axis angle, which may cause large uncertainty of the neutrino flux. The neutrino direction is thus monitored by the INGRID detector which is described later.

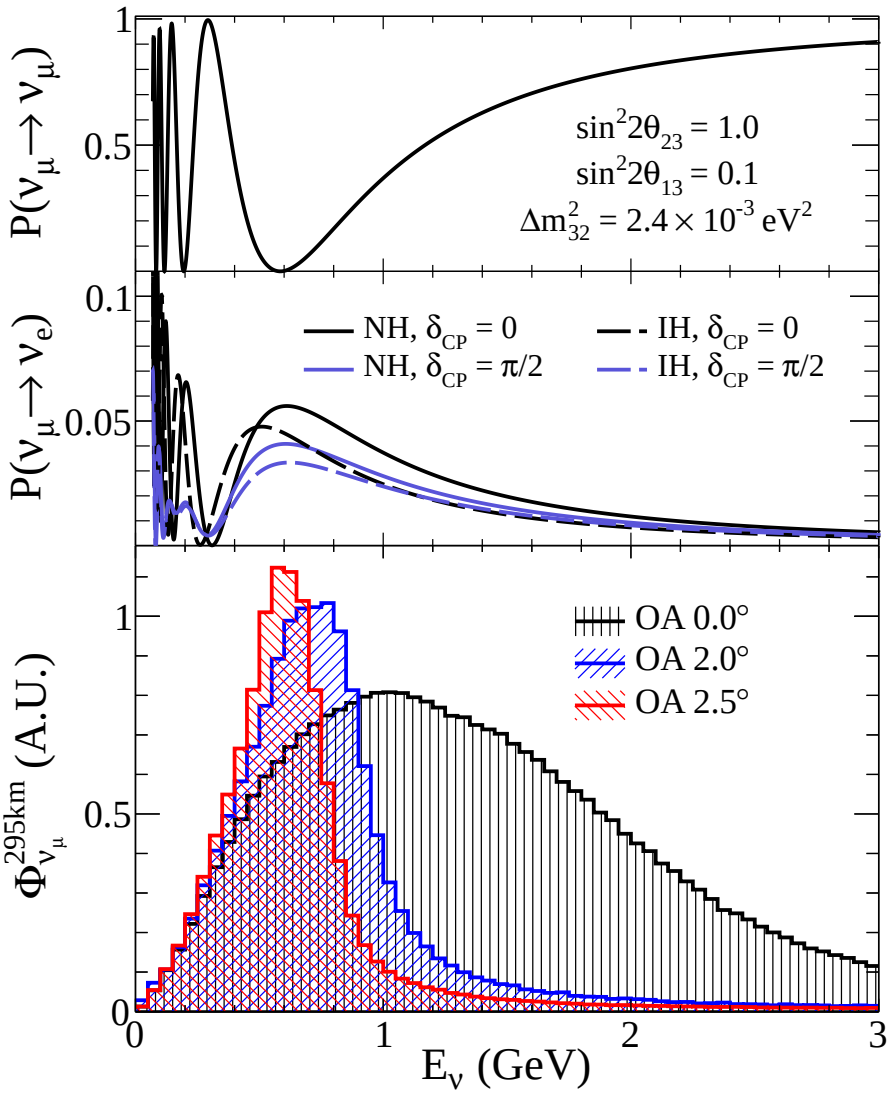

Figure 2.6: Neutrino oscillation probability and flux as a function of neutrino energy for different off-axis angles.

2.3 Near Detector

T2K measures the neutrino events before oscillations with two near detectors. They are located at 280 m downstream from the neutrino target. One detector called INGRID is placed on the beam axis and the other detector called ND280 is placed at 2.5 degree off-axis.

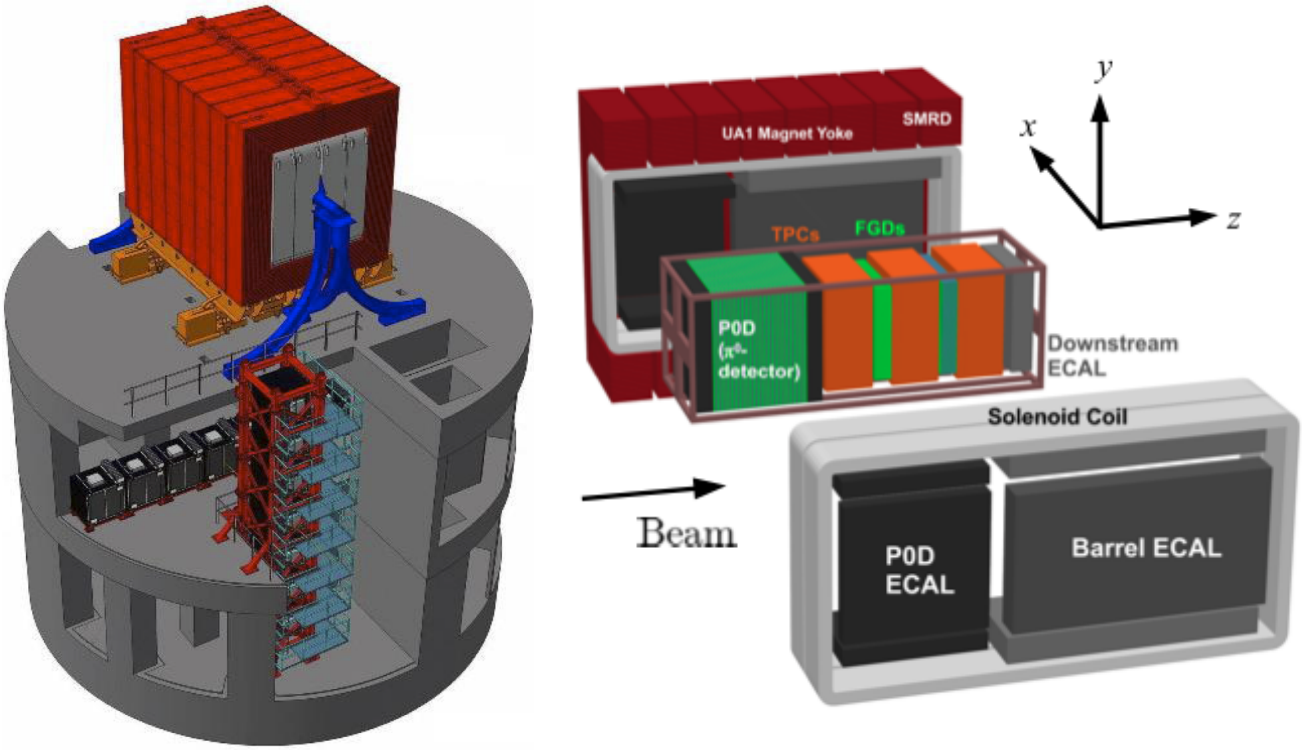

Figure 2.7: The Overview of Left: Near detector hall, Right: ND280 detector.

2.3.1 Off-Axis Near Detector: ND280

ND280 (Near Detector at 280 m) (Fig. 2.7) is a complex detector which consists of several sub-detectors. It measures the neutrino beam flux and energy spectrum before the oscillation and the neutrino-nucleus cross section for several target nuclei. Sub-detectors are placed in a dipole magnet which was used in the UA1 experiment. The dimensions of the inner volume of the magnet are 7.0 m $\times$ 3.5 m $\times$ 3.6 m.

- Pi-zero Detector (P0D)
  Pi-zero detector (P0D) is designed to measure the neutral current interaction (NCπ^0 production). P0D is composed of scintillator modules alternated with water target bags and lead and bronze sheets [110].

- Time Projection Chamber (TPC)
  The Time Projection Chambers (TPCs) provide 3-D tracking for charged particles. Using energy deposit and curvature of the track, TPC also provides particle identification and momentum measurement of the particles. There are three TPCs, all the same design. The TPCs are placed upstream of FGD 1 (TPC 1), between FGD 1 and FGD 2 (TPC 2) and downstream of FGD 2 (TPC 3) [111].

- Fine Grained Detector (FGD)
  The Fine Grained Detectors (FGDs) are used as the main target of ND280 and measures the

vertex and tracks for the events. There are two FGDs: FGD 1, which has the carbon-only target volume, and FGD 2, which has both carbon and oxygen targets [112].

- Electromagnetic CALorimeter (ECAL)
  The Electromagnetic calorimeter (ECAL) is a sampling electromagnetic calorimeter which surrounds the TPCs, FGDs and the P0D. The ECAL is made up of various configurations of layers of scintillator bars and layers of lead, which provide a neutrino-interaction target and additionally act as a radiator to produce electromagnetic showers. There are three types of modules in the ECAL: six Barrel ECAL modules, which are placed around the sides of the FGD and TPC parallel to the beam axis, one Downstream ECAL module, positioned downstream at the exit of the FGD and TPC and six P0D-ECAL modules around the P0D parallel to the beam axis [113].

- Side Muon Range Detector (SMRD)
  The Side Muon Range Detector (SMRD) is not a part of the inner detectors in ND280, but instead is incorporated with the magnet yoke that surrounds the rest of ND280. It serves mainly cosmic ray trigger and veto for particles entering the ND280 volume and neutrino interactions from the surrounding magnet and the detector [114].

- UA1 Magnet
  This magnet provides a 0.2 T dipole magnetic field for ND280, which is near constant in the detector volumes.

For the oscillation analysis, FGD and TPC events are used to constrain flux and cross-section uncertainties. The details of the ND280 analysis are described in Chapter 9.

2.3.2 On-Axis Detector : INGRID

INGRID (Interactive Neutrino GRID) is a neutrino detector centered on the neutrino beam axis [115]. This on-axis detector was designed to monitor the neutrino beam direction and intensity by neutrino interactions on iron. The INGRID detector has 14 identical modules arranged as a cross of two identical groups along the horizontal and vertical axes as shown in Fig. 2.8 [3]. Each INGRID module consists of a sandwich structure of nine iron plates and 11 tracking scintillator planes as shown in Fig. 2.8. Using the number of observed neutrino events in each module, the beam center is measured to a precision better than 3 cm. Figure 2.9 shows the neutrino profile for the vertical and horizontal directions measured by INGRID.

2.4 Super-Kamiokande Detector

Super-Kamiokande [116] is a 50 kton water Cherenkov detector in Hida-city, Japan located 295 km away from the beam source (J-PARC). Super-Kamiokande serves as the far detector in the T2K experiment. The geometry of the Super-Kamiokande detector consists of two major volumes, an inner and an outer detector which are separated by a cylindrical stainless steel structure. In the inner detector (ID), 11,129 50 cm diameter Photo Multiplier Tubes (PMTs) are installed with 40% PMT coverage, and it is filled with 50 kton of pure water. The outer detector (OD) contains 1,885 outward-facing 20 cm diameter PMTs along the inner walls. When a neutrino interacts with a nucleus in the target, a Cherenkov light is emitted by produced charged particles. The Cherenkov light produces a ring-shaped hit pattern which is used to extract information about the interaction

[3] The remaining two non-diagonal modules are removed for different purposes.

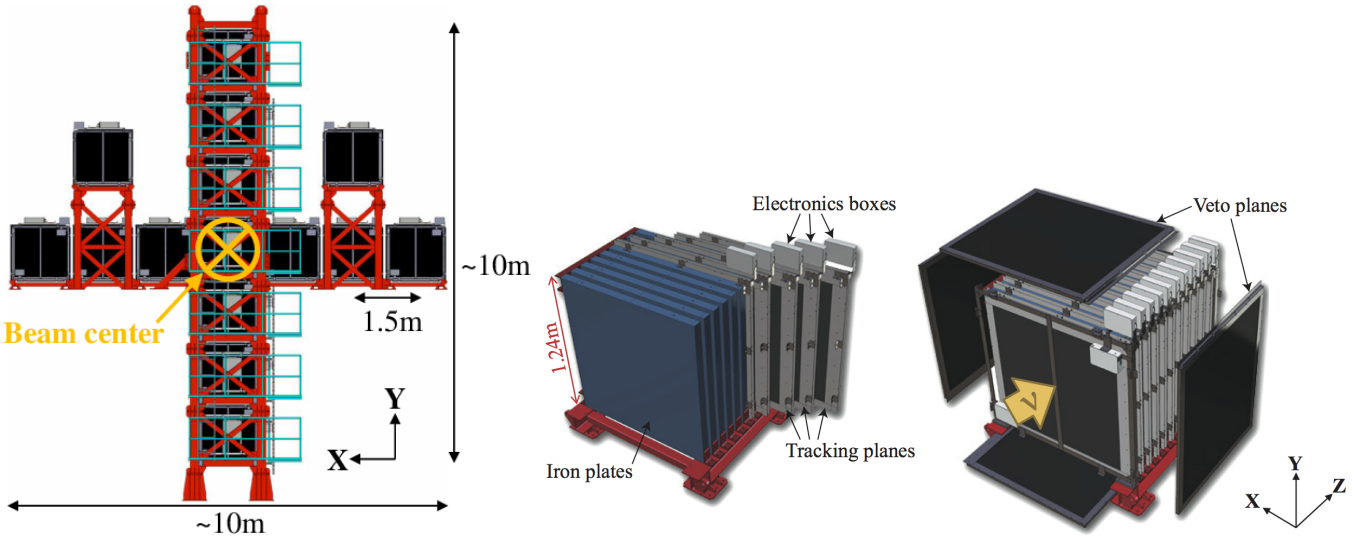

(a) INGRID view from the beam source.

(b) INGRID module

Figure 2.8: Overview of INGRID detector

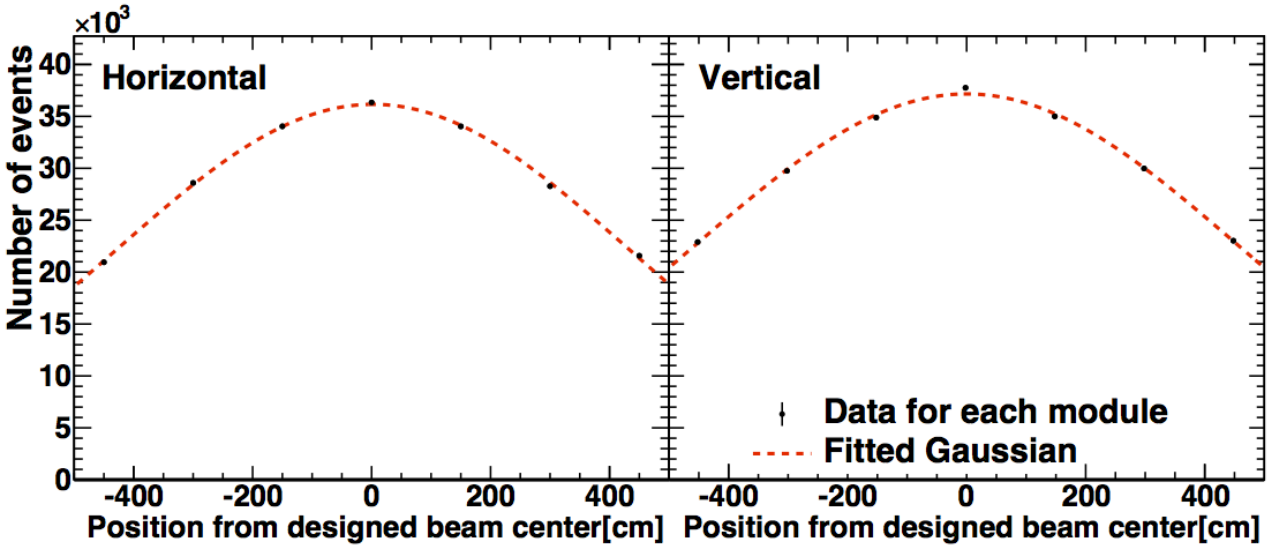

Figure 2.9: Neutrino Beam Profile measured by the INGRID detector

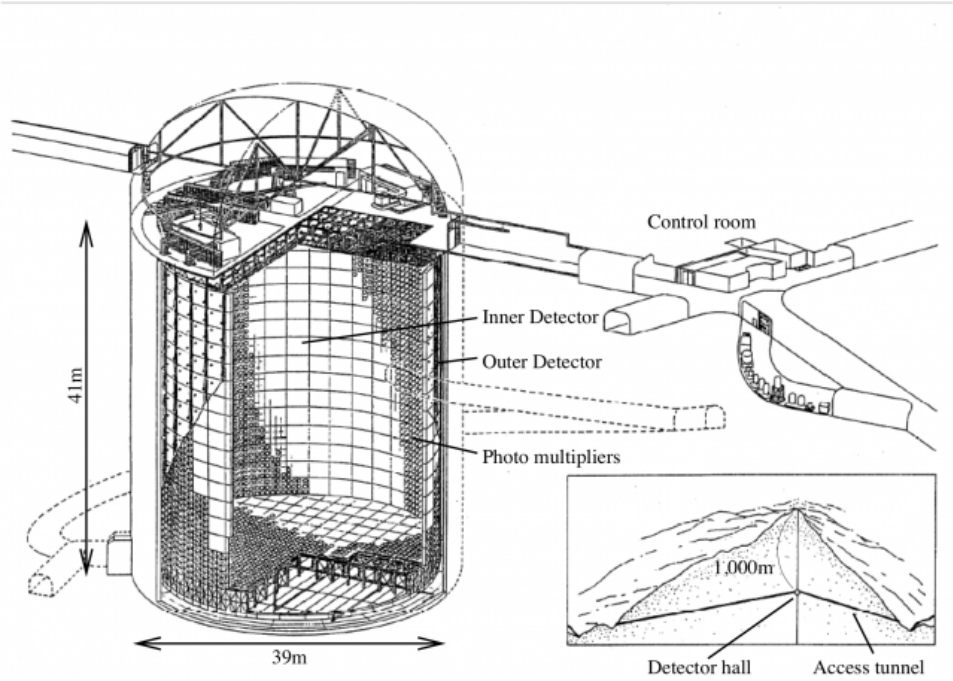

Figure 2.10: Overview of Super-Kamiokande

such as the event vertex position and momenta of product particles. When a muon travels through the detector, a clear and sharp ring of PMT hits is seen on the detector wall. In contrast, when an electron travels through the detector, a "fuzzy" ring of PMT hits is seen due to multiple scattering and generation of electromagnetic shower. Figure 2.11 shows the event display of the electron-like and muon-like Cherenkov ring. The details of the analysis are discussed in Chapter 10.

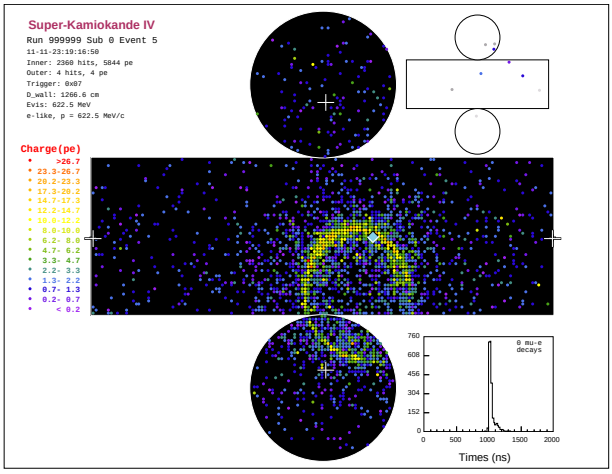

(a) Event display of electron-like ring

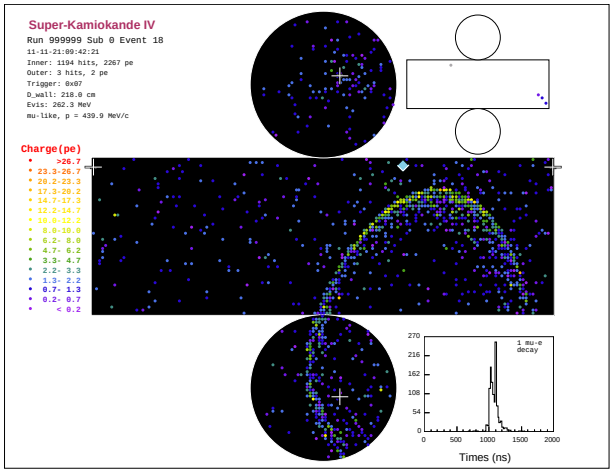

(b) Event display of muon-like ring

Figure 2.11: Event display of the Super-Kamiokande

Part II

Neutrino Beam Intensity Improvement

Chapter 3

J-PARC Accelerator

In this chapter, the overview of the J-PARC accelerator complex and the strategy of the intensity improvement are described. The details of the improvement will be explained in the next chapter.

3.1 J-PARC Overview

J-PARC (Japan Proton Accelerator Research Complex) is composed of three accelerators: 400 MeV LINAC (LINear ACcelerator), 3 GeV RCS (Rapid Cycling Synchrotron) and 30 GeV Main Ring Synchrotron. J-PARC is one of the highest intensity proton accelerators in the world. J-PARC produces various secondary particle beams from the high intensity proton beam such as kaons, muons, neutrons and neutrinos. J-PARC has three experimental facilities: Neutrino facility which utilizes the neutrino beam for a long baseline neutrino oscillation experiment, Hadron Hall which utilizes the various beam to explore the nuclear and particle physics, and Material and Life science Experimental Facility (MLF) which utilizes the neutrons and muons to mainly study the structures of martials (Fig. 3.1).

In high intensity accelerators, beam loss is a main issue in order to operate the accelerators stably and safely. Accelerator equipment is radioactivated when the lost particles hit it. The radioactivated equipment causes the serious problems on maintenance and safety. Therefore, it is important to reduce the beam loss as small as possible. To minimize the beam loss, we consider various strategies. In a synchrotron, charged particles oscillate around the designed orbit in a transverse direction [1]. This oscillation is referred to as betatron oscillation and the number of such oscillation per turn is defined as betatron tune or simply tune. When the tune is integer or simple fraction such as 1/2, the particle repeats its path in the accelerator and feels the same field. The resonance then grows and the particle is lost. Therefore, the tune is set to avoid such values, however, various effects such as the momentum deviation spread the tune from the setting value and the tune of some particles become integer or simple fraction. Therefore, it is important to understand the tune spread and to take care of the spread for high intensity accelerators. The details of the source of the tune spread are described in Appendix A.

In this chapter, we describe the overview of each accelerator and the J-PARC Main Ring strategy for intensity improvement.

[1] In accelerators, Frenet-Serret coordination is commonly used. We take the axis along to the beam direction (s) as "longitudinal" and the axis for plane perpendicular to the beam direction (x,y) is "transverse". The detail of coordination is shown in Appendix A

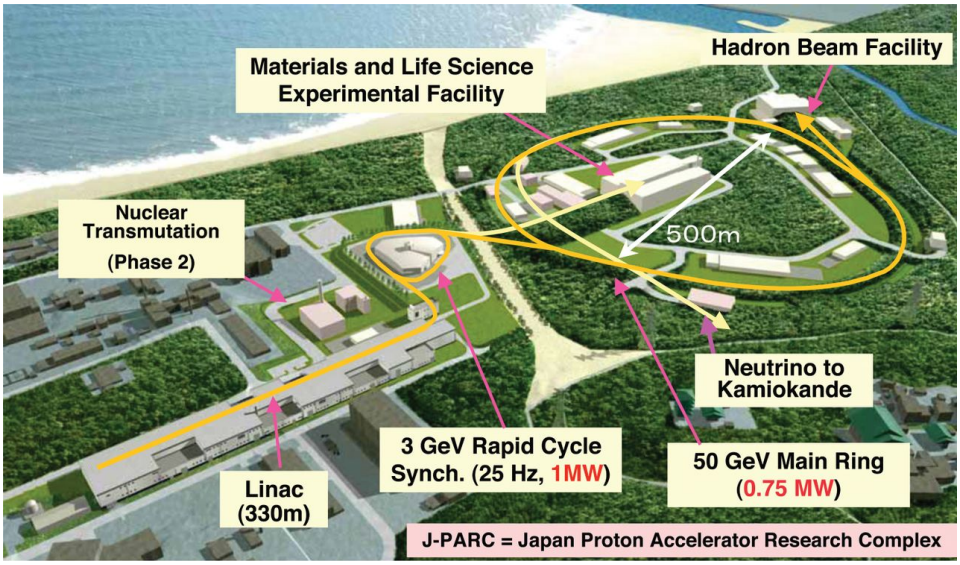

Figure 3.1: Overview of J-PARC

3.1.1 LINAC

LINAC has four types of cavities to accelerate H^- ions effectively as shown in Fig. 3.2. There are Radio Frequency Quadrupole (RFQ), Drift Tube LINAC (DTL), Separated-type DTL (SDTL) and Annular-ring Coupled Structure LINAC (ACS) which accelerates H^- ions to 3 MeV, 50 MeV, 181 MeV and 400 MeV, respectively. The main parameters of LINAC are shown in Table 3.1. RFQ, DTL, STDL are operated with 324 MHz RF frequency while ACS is operated with 972 MHz RF frequency to get higher acceleration efficiency.

Figure 3.3 shows the overview of the pulse structure of LINAC. LINAC generates the pulse beam of 500 μs (called macro pulse) at the 25 Hz repetition rate. In the macro pulse, there are micro pulses of 3.1 ns repetition period since LINAC is operated with 324 MHz RF frequency. As shown in later, RCS is operated with 1.2-1.6 MHz, which is much lower frequency than LINAC. When the macro pulses are directly injected to RCS, some micro pulses are not captured by the RF bucket (see Appendix A) and cause unnecessary beam loss. To reduce such a beam loss, the macro pulses are thinned to make intermediate pulse by the RF chopper system to be captured by the RCS RF buckets effectively at the injection [117].

3.1.2 RCS

Figure 3.4 shows the overview of RCS. RCS has three arc sections and three straight lines. The functions of three straight lines are injection and collimation, RF acceleration, and extraction. H^- ions from LINAC is converted to protons at the injection point by carbon foils [119]. RCS accelerates the proton beam from 400 MeV to 3 GeV with the magnetic alloy RF system which has high accelerating gradient (more than 20kV/m) [120] with 25 Hz repetition rate. The intermediate pulses from LINAC are merged into two pulses during the injection. This merged pulse is called a bunch. RCS provides the proton beam to MLF and to injects the beam to Main Ring. RCS delivers about 95% of the proton beam to MLF to produce muon and neutron beams. The rest of 5% is delivered to Main Ring.

The main parameters of RCS are listed in Table 3.2. RCS is designed to have higher transition energy than the extraction energy to avoid the beam loss at the transition (see Appendix A). The main source of the beam loss in RCS is a space charge effect which occurs due to the repulsive force

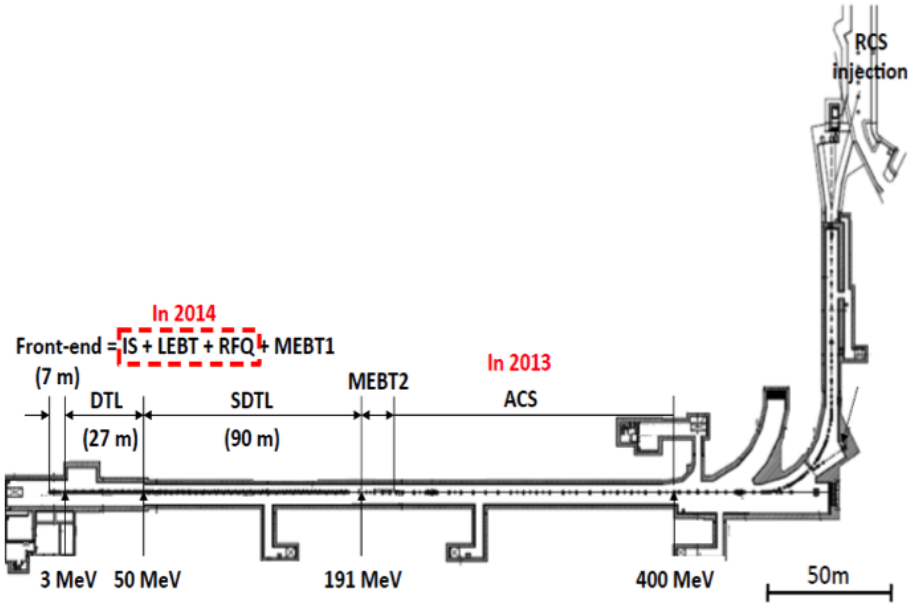

Figure 3.2: J-PARC LINAC

Table 3.1: Parameters of J-PARC LINAC

Parameter	Current value (2018)
Ion source	H^-
Energy	400 MeV
Length (including transport line)	248 m
RF frequency (RFQ, DTL, SDTL)	324 MHz
RF frequency (ACS)	972 MHz
Repetition cycle	25 Hz (50Hz for ADS [118])
Peak current	$\sim$ 40 mA (designed 50 mA)
Macro pulse length	500 μs

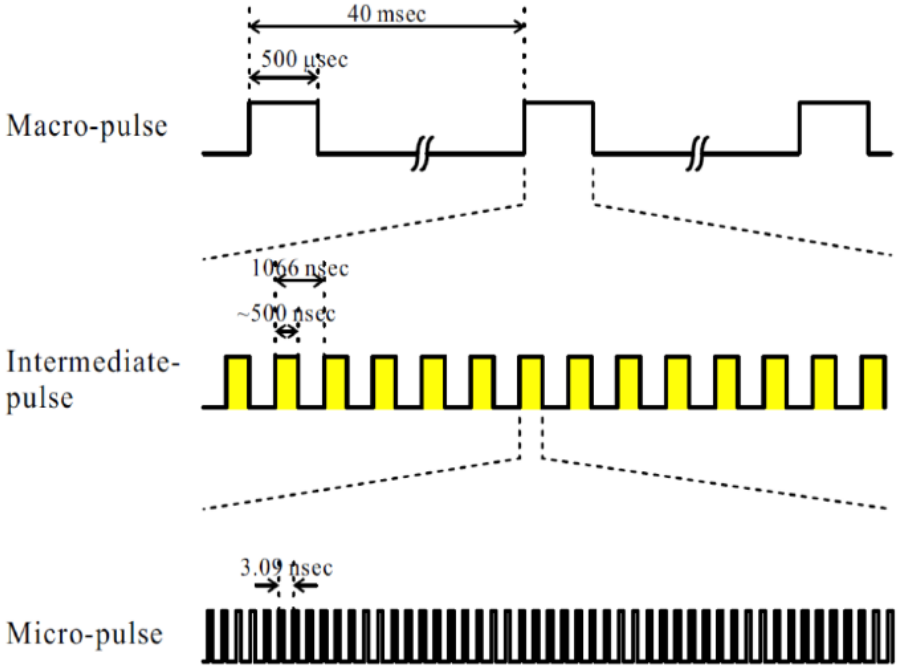

Figure 3.3: The bunch structure of LINAC

of the electromagnetic field in a high charge density circumstance (see Appendix A). To mitigate this effect, RCS adopts the transverse and longitudinal injection painting in order to distribute the injection particles on the large phase space area [121]. The details and recent commissioning results are described in [122].

3.1.3 Main Ring

Figure 3.5 shows the overview of Main Ring. Main Ring also has three arc sections and three straight lines. Three straight lines are used for injection and collimation, RF acceleration and fast extraction, and slow extraction. The parameters of Main Ring are shown in Table 3.3. Main Ring accelerates eight bunches of the proton beam while RCS accelerates two bunches beam. Thus, RCS injects the proton beam to Main Ring four times (Fig. 3.6). Thereafter, Main Ring accelerates the beam from 3 GeV to 30 GeV with the same RF system as RCS, operating at 1.67-1.72 MHz. The repetition period is 2.48 second for the fast extraction. Main Ring is designed to have imaginary transition energy (i.e. negative momentum compaction factor) to avoid the beam loss at the transition (See Appendix A).

Main Ring provides the proton beam to two experimental facilities: Neutrino facility and Hadron Hall. Each facility requires different types of the beams. The neutrino facility requires the bunched beam to identify the neutrinos from the accelerator and backgrounds using timing information. On the other hand, the Hadron Hall requires DC-like beam. For the neutrino facility, J-PARC extracts all the eight bunch proton beam to the neutrino beamline in a single extraction (fast extraction). For the Hadron Hall, proton beams are de-bunched and extracted gradually to the Hadron beamline throughout extraction period (slow extraction). In this thesis, we focus on the fast extraction. More details of Main Ring are found in [123].

Figure 3.4: J-PARC Rapid Cycle Synchrotron

Table 3.2: Parameters of the J-PARC RCS

Parameters	Current value (2018)
Circumference	348.333 m
Energy	3 GeV
Protons per bunch	$\sim 2.5 \times 10^{13}$ (designed 8.3×10^{13})
Repetition frequency	25 Hz
Typical tune	(6.45, 6.42)
Momentum compaction factor	0.0085 (designed 0.012)
Transition Energy	9.21 GeV (designed 9.17 GeV)
Harmonic number	2
RF frequency	1.23 ∼1.67 MHz
RF voltage	400 kV (designed 412 kV)

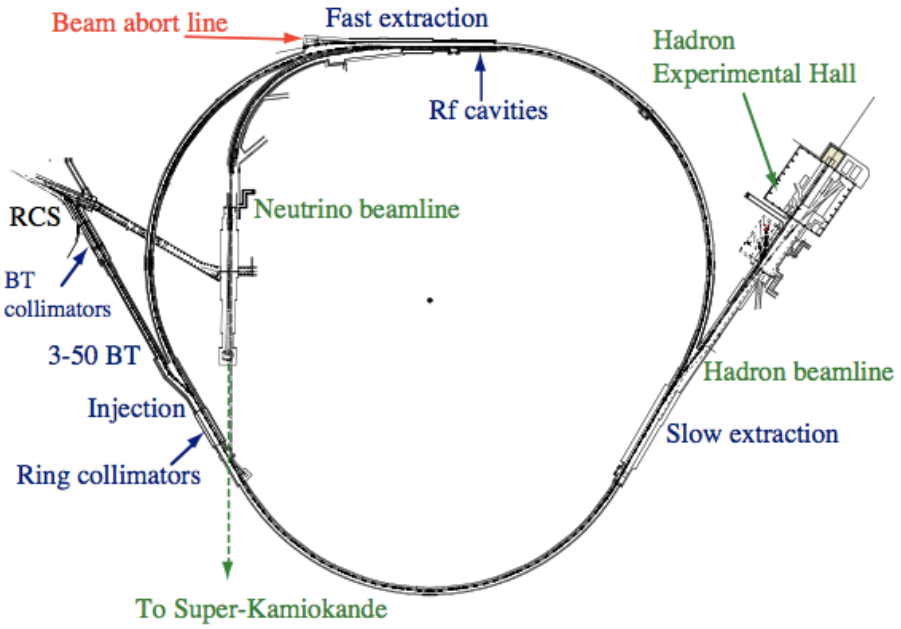

Figure 3.5: J-PARC Main Ring Synchrotron

Table 3.3: Main parameters of Main Ring

Parameter	Current value (2018)
Circumference	1567.5 m
Energy	30 GeV (designed 50 GeV)
Protons per pulse	$\sim 1.4 \times 10^{14}$ (designed 3.3×10^{14})
Repetition period	$\sim$ 0.4 Hz (1.0/2.48s)
Average beam current	8.7 μA (designed 15 μA)
Beam power	$\sim$ 0.48 MW (designed 0.75 MW)
Typical tune	(21.35, 21.45)
Momentum compaction factor	-0.001
Transition energy	31.6i GeV
Harmonic number	9
RF frequency	1.67 $\sim$1.72 MHz

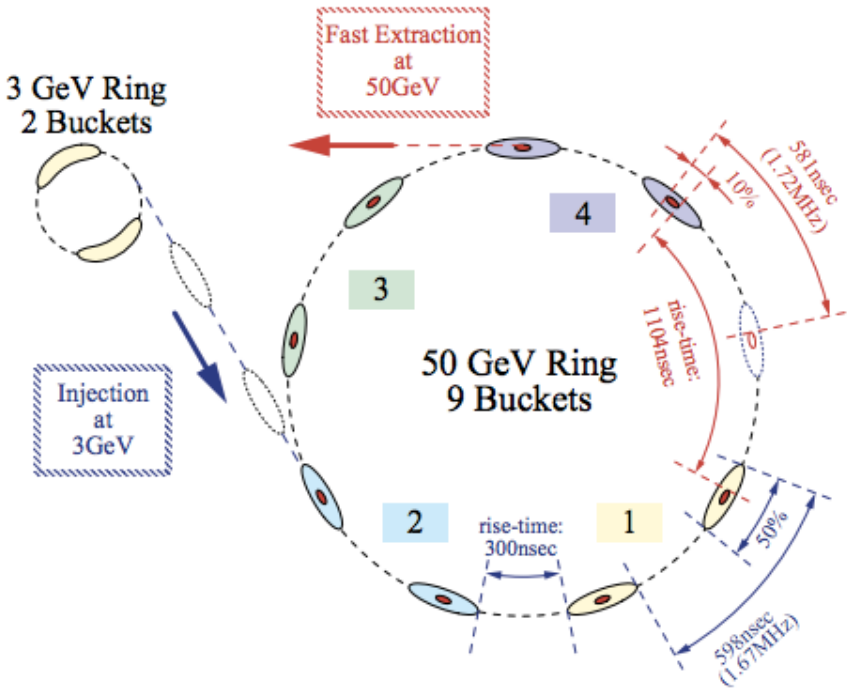

Figure 3.6: The bunch structure of Main Ring

3.2 Beam Power Upgrade Strategy in Main Ring

Current beam power of Main Ring is 480 kW as of 2018, about 60% of the designed beam power 750 kW. It is desired to achieve the designed beam power or higher. The beam power of the accelerator is given by the product of the average current of the beam and the beam energy. It is a natural way to increase the protons per pulse to achieve the designed beam power. However, we found it is almost impossible to accelerate designed proton per pulse (3.3×10^{14}) with the current configuration due to the limited dynamic aperture. Therefore, J-PARC has changed the scenario to shorten the repetition period to increase the beam current effectively. To shorten the repetition period from 2.48 s to 1.3 s, new power supplies will be installed and J-PARC will reach the designed beam power.

Furthermore, it plays a critical role to reduce the beam loss for higher beam power than the designed value. It is also important to get higher beam power before the power supply installation to run experiments more smoothly. In J-PARC Main Ring, we have made various efforts to reduce five main sources of the beam loss described below [124]:

1. Quality of the beam from RCS and injection
   The condition of the beam from RCS largely affects the beam loss in Main Ring. When the beam from RCS has large halo, it can be a source of the beam loss. We are trying to optimize the condition by using the OTR halo monitor [125] and improving the injection matching.

2. Beam capture and acceleration by RF system
   Space charge effect depends on the bunching factor which is the ratio of the peak current to the average current. Larger bunching factor mitigates the space charge effect. We introduced second harmonic RF [126] to make a flatter RF bucket. Main Ring adopts the beam loading compensation [127] to avoid the distortion of the RF buckets due to the space charge effect.

3. Beam instabilities
   The beam interacts with the components via electromagnetic force when the beam passes

through the accelerator. The field called wake field is emitted when the beam is accelerated or decelerated as a result of the interaction. In a certain condition, the beam makes a resonance with the wake field and the amplitude of the oscillation blows up. As a result of this resonance, beam particles are lost. This beam loss is called beam instabilities. Figure 3.7 shows the oscillation amplitudes of the beam and the beam intensity when the beam instabilities occurred in J-PARC Main Ring.

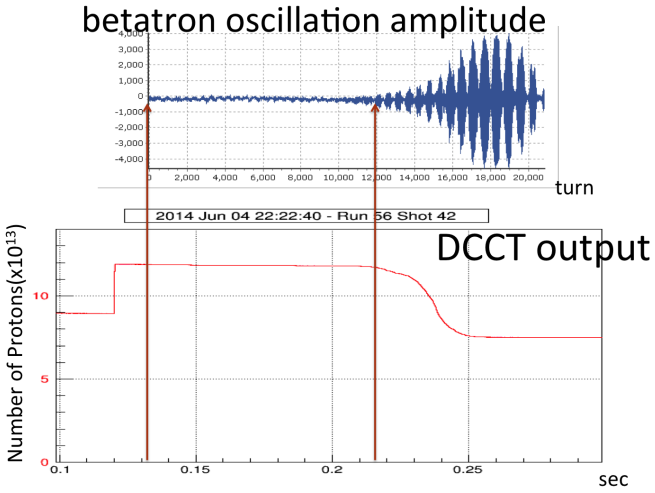

Figure 3.7: The betatron amplitudes and beam intensity when the beam instabilities occurred in J-PARC Main Ring

The wake field emission depends on the electromagnetic properties of the accelerator equipment. Normally, it is difficult to calculate the wake field from each equipment in the accelerator. This means that it is also difficult to remove the source of the wake field itself, sometimes it is impossible. Hence, we should suppress the beam instabilities with an additional way. Tuning chromaticity (see Appendix A for more details) mitigates the beam instabilities, however larger chromaticity makes a larger tune spread and becomes a potential beam loss source related to the next point. Therefore, we are developing feedback systems which are described in the next chapter.

4. Crossing betatron resonance lines
   Betatron tune in horizontal and vertical direction (ν_x, ν_y) is one of the most important parameters for accelerators. The tune determines the frequency of the transverse oscillation of the beam in the accelerator (see Appendix A for more details) and are controlled by quadruple magnets. The tunes are set to avoid "resonance line" where the beam becomes unstable. Figure 3.8 shows the resonance line around the operation point of Main Ring. Even though the operation points are set correctly, the tunes spread due to various mechanisms such as space charge effect. When particles in the beam cross a resonance line, they are lost. Figure 3.8 also shows the simulated tune spread at 380 kW beam power. The red circle is the operation point used until 2014. The tune spread crosses the several resonance lines. Some of the dotted lines can be canceled by using correction magnets [128]. However, $\nu_y = 20.5$ resonance line is not avoidable in this operation point. To avoid crossing line, we are searching for new operation points (like blue point in Fig. 3.8) where the crossing lines are less than the present operation point. Such operation points require larger voltage operation than design value to the equipment, thus, we must investigate the feasibility of the operation carefully.

5. Accurate control of beam optics
   Related to the fourth point, it is important to control the beam optics as we want to reduce

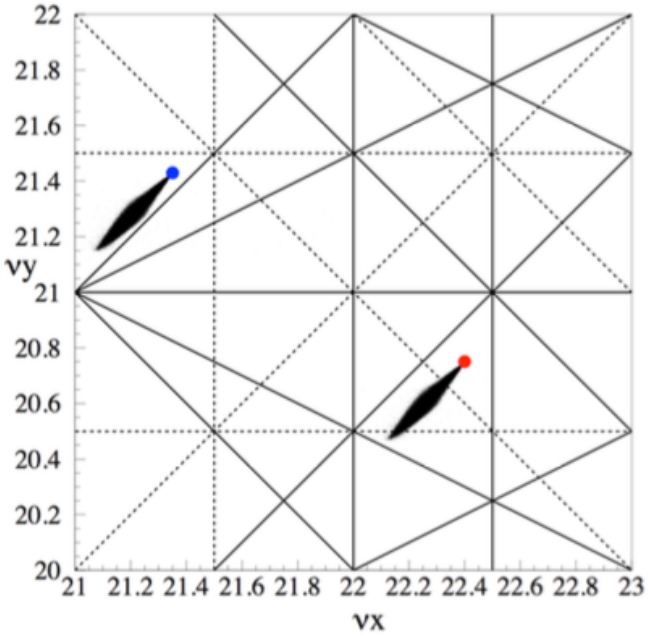

Figure 3.8: Simulated tune spread for the beam power of 380 kW. Black lines are the resonance lines. Red point shows the typical tune of Main Ring until 2014 and Blue point shows the current one.

the unexpected beam loss. The beam optics is largely affected by setting of the accelerator equipment. However, the equipment sometimes outputs deviated value from its setting. If each equipment is not well controlled, the beam optics will be distorted. This distortion will bring the shift of the tune, narrowing the dynamic aperture, which results in the beam loss. We are trying to understand the properties of the equipment by using the actual beam.

In the next chapter, we show the details of the development of the feedback system which improves the third point, and betatron function measurement which addresses to the forth and fifth points.

Chapter 4

Improvement of J-PARC Main Ring Performance

In this chapter, we will describe the details of the development of the intra-bunch feedback system for the beam instability improvement and the betatron function measurement.

4.1 Transverse Intra-bunch Feedback System

As discussed in the previous chapter, beam instability is one of the main sources of the beam loss in Main Ring. Beam instabilities occur by interactions between beams and accelerator components. Thus, it is sometimes inevitable to happen, and what is worse, the beam instabilities sometimes limit the beam intensity of the accelerator. To avoid the beam instabilities, the transverse feedback system is widely used in accelerators around the world.

The transverse feedback system consists of mainly three components: a Beam Position Monitor (BPM), a signal processing module and a stripline kicker. First, BPM measures the position of the beam and BPM signals are then sent to the signal processing module. The module first digitizes the BPM signals and calculates the magnitude of the kick and its phase to suppress the beam instabilities. Afterward, the output signals are sent to the kicker through the power amplifier with an appropriate timing to kick back the beam to the correct position before the beam instabilities grow (Fig. 4.1).

In J-PARC, the transverse feedback system was introduced in 2014 [129] and it successfully has damped the beam instabilities. This feedback system detects the beam position and applies the external kick every bunch as shown in Fig. 4.2. This system is called bunch-by-bunch feedback system.

Although the bunch-by-bunch feedback system is available, we require a wider-band feedback system to suppress the beam instabilities more effectively. The bunch-by-bunch feedback system in J-PARC is operated at 1.72 MHz, which is the same frequency as the RF frequency. We have observed head-tail motion in a bunch which may cause additional beam instabilities [130]. Figure 4.3 shows the BPM signals observed in J-PARC Main Ring overlaid every five turns [1]. The frequency of the motion is estimated to be $\sim$ 10 MHz, which indicates that this motion cannot be suppressed by the bunch-by-bunch (BxB) feedback system. It is possible to suppress this motion by applying the feedback kicks of higher frequency. Therefore, we have developed a wideband feedback system called intra-bunch feedback system.

[1] In an accelerator, monitors are placed in fixed positions. Thus, a beam monitor measures the beam turn by turn.

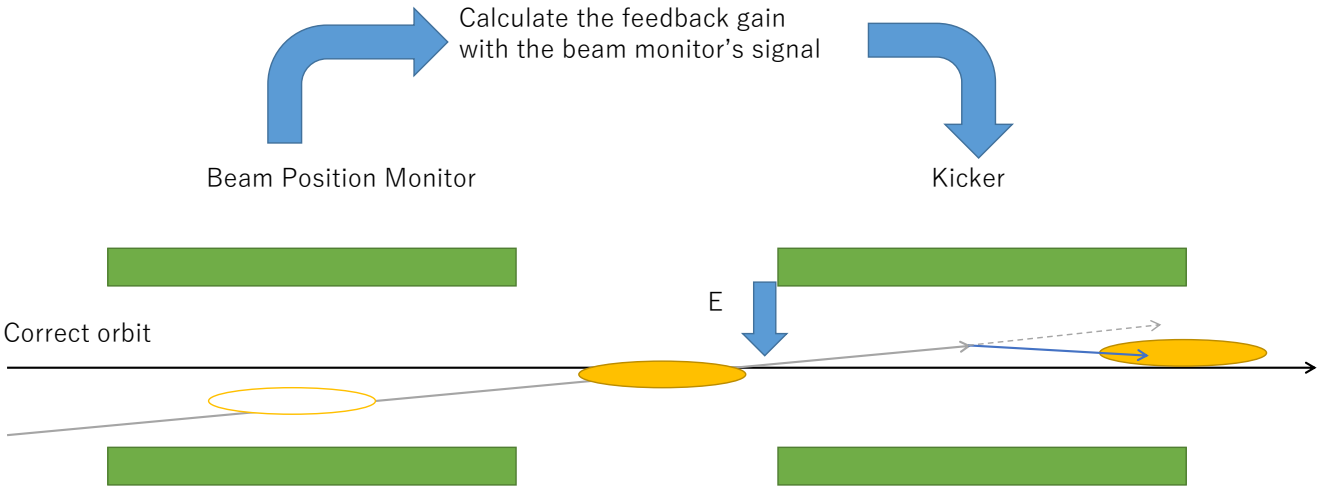

Figure 4.1: Illustration of the transverse feedback systems

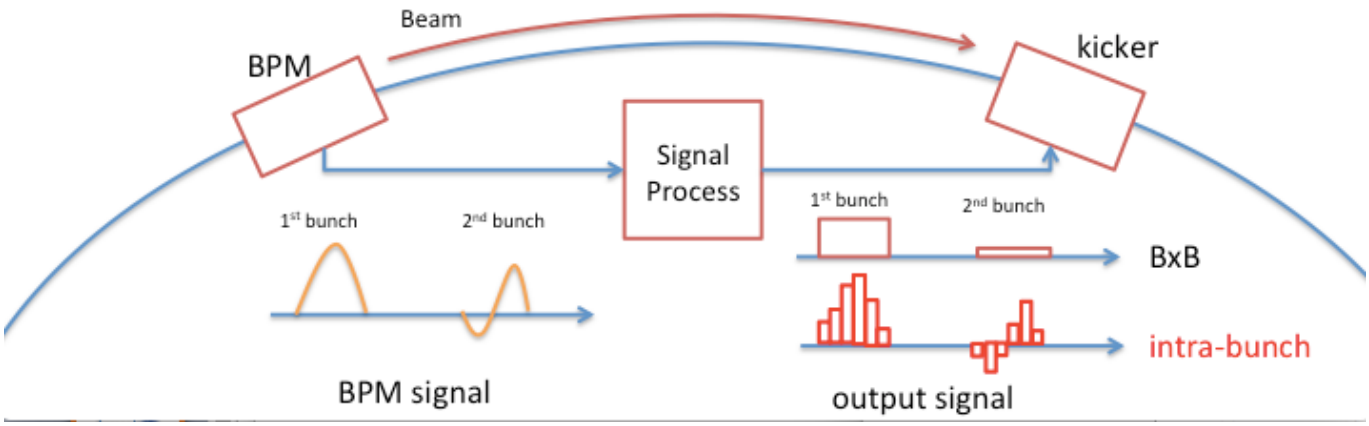

Figure 4.2: Overview of the transverse feedback systems in J-PARC. "BxB" corresponds to bunch-by-bunch feedback system and "intra-bunch" corresponds to intra-bunch feedback system.

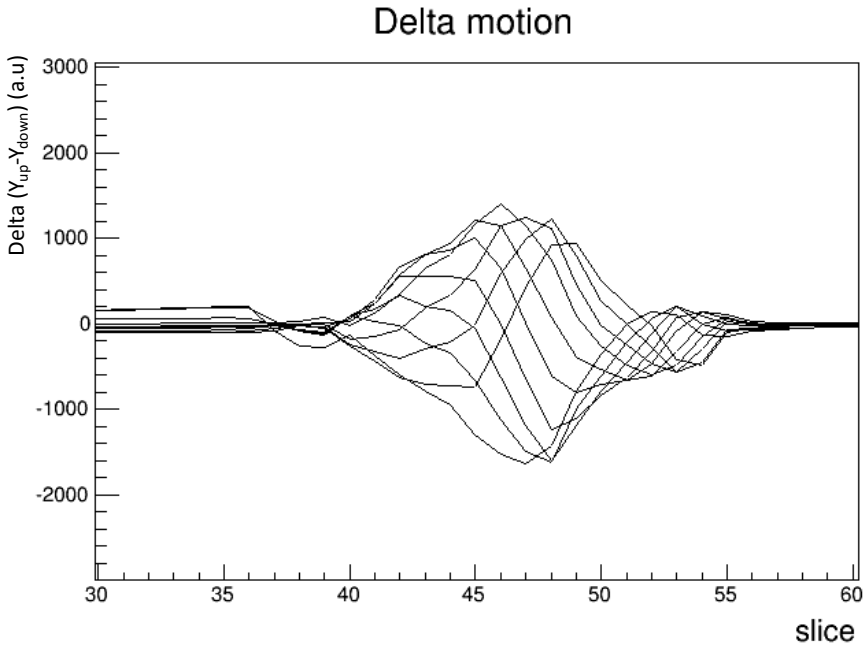

Figure 4.3: Internal-bunch oscillation observed in J-PARC Main Ring by strip-line BPM. The plots are overlaid every five turns. "slice" corresponds to 10 ns. Delta shows the unbalance of the BPM signal.

Figure 4.4 shows the overview of the intra-bunch feedback system in J-PARC. We fabricated a new BPM and a new strip-line kicker, and installed a new signal processing module for this system.

4.1.1 Components of the Intra-bunch Feedback System

We installed the BPM and kicker near the neutrino extraction point in Main Ring. We selected this point for two reasons. One reason is that we want to set this system at the straight line to avoid the dispersion effect. Another reason is that the beta function at this point is small, therefore the kicker can kick the beam effectively.

Beam Position Monitor

BPM has four electrodes inside the beam ducts and measures the beam position with the unbalance of the electrode signals. The BPM for the intra-bunch feedback system should have a wideband detection capability to detect internal motion of the bunch. A good candidate is a stripline type BPM which has a wider response than other types of BPM. Nevertheless, the stripline BPM has notches in the frequency response as shown in blue line in Fig. 4.5. To avoid these notches, exponentially tapered stripline BPM (exponentially tapered coupler : ETC) [131] is fabricated for the intra-bunch feedback system [132] as shown in Fig. 4.5.

We have measured the frequency and position response with a wire method [133] to calibrate this BPM. The measured position and frequency response agree with the calculation up to 1 GHz with 7% and 15% systematic error respectively. Right plot in Fig. 4.5 shows the frequency response of the calculated response of ETC (Green line) and measured frequency response of ETC (Red line). More

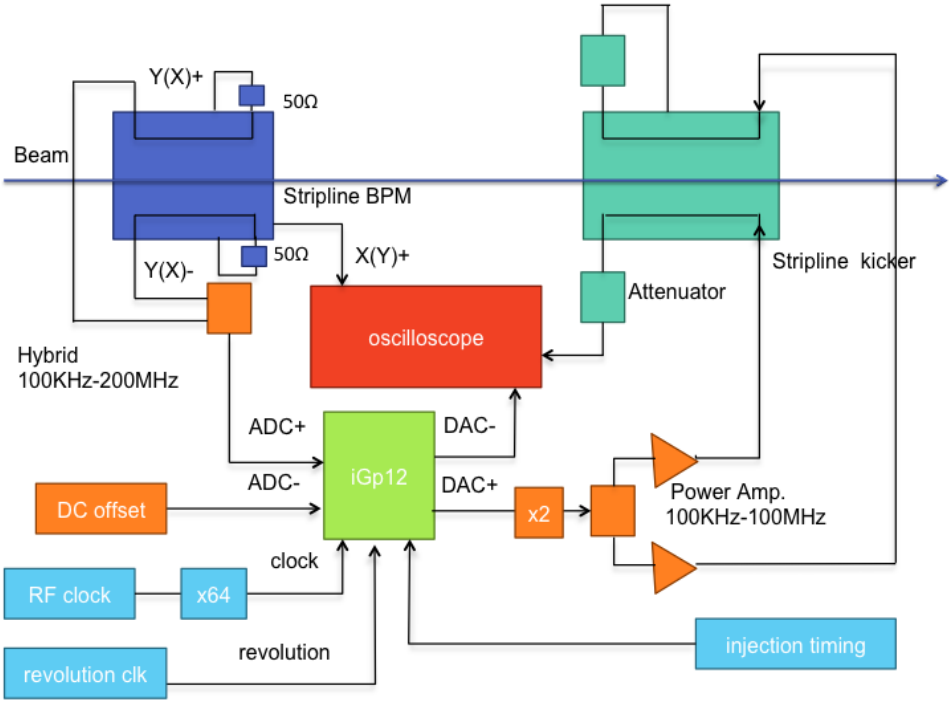

Figure 4.4: Schematic diagram of the Intra-bunch feedback system

details are found in [134] and [132].

We also investigated the optimized shape of the electrode with respect to the flatter frequency response and better fabrication. The exponentially tapered electrodes have difficulties in impedance matching and precise fabrication. This mechanical limitation may cause unexpected distortion at high frequency response (over 2 GHz in Fig. 4.5). We concluded that the linearly tapered electrode is the most suitable for both fabrication and frequency response [135], [136].

Signal Processing Module

We introduced iGp12 digital signal processing module developed by Dimtel Inc [137]. It was originally developed for the bunch-by-bunch feedback in electron storage rings such as Super-KEKB [138] and SIRIUS Light Source [139]. These accelerators have much shorter bunch length ($\sim$ 5 mm) than that of J-PARC Main Ring ($\sim$ 10 m), therefore much higher frequency feedback system is required compared to the J-PARC bunch-by-bunch feedback system. Such a high frequency feedback system is suitable for J-PARC Main Ring as an intra-bunch feedback system.

The module consists of 12 bit ADC (Analog to Digital Converter), FPGA (Field-Programmable Gate Array) and high-speed 12 bit DAC (Digital to Analog Converter). In FPGA, the signals pass through a 0-32 tap FIR (Finite Impulse Response) filter to extract information of oscillation of the beam. The module has several I/O ports to control it. It is driven by “RF clock” which is input of operating clock, “fiducial” which controls the start timing of the feedback, and “external trigger” which changes settings of the module. We drive this module with 106.8-110.0 MHz RF clock which is sixty-four multiplied the original RF frequency of Main Ring. This means that we divide the RF bucket into sixty-four slices and apply the feedback kick in each slice. We also set “fiducial” as the injection timing (called "p0"). For the external trigger, we make arbitrary timings to change the setting of the parameters as the beam is accelerated. The details of the module can be found in [137].

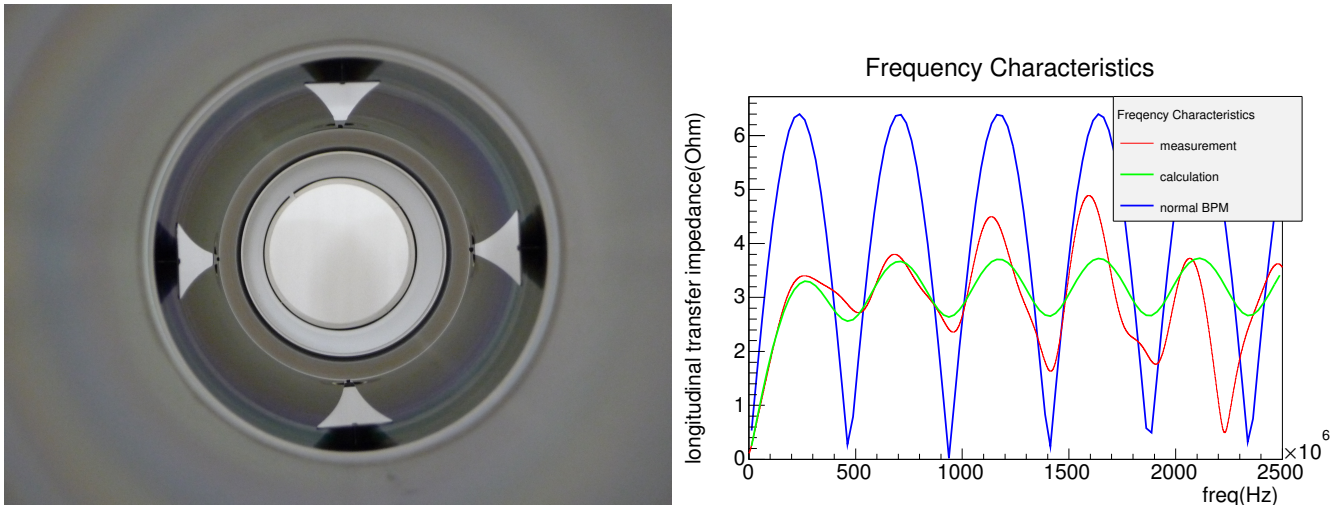

Figure 4.5: Left: Cross-sectional view of the ETC from the upstream. Right: The frequency response of normal stripline type BPM (Blue line), calculated response of ETC (Green line) and measured frequency response of ETC (Red line)

Stripline Kicker

Figure 4.6 shows the cross-sectional view of the stripline kicker. The stripline kicker has two electrodes. In each electrode, different polarity of the currents flow to make a dipole electromagnetic field. The electrode's length characterizes the frequency response of the kicker. If the electrode is short, the frequency response becomes wider, while the kick strength becomes weaker. We fabricated 110 cm long strip-line kicker, which is half-length of that used in the bunch-by-bunch feedback system. The frequency response of the kicker was calculated as shown in Fig. 4.6.

The details of the kicker performance are described in [140] and [141].

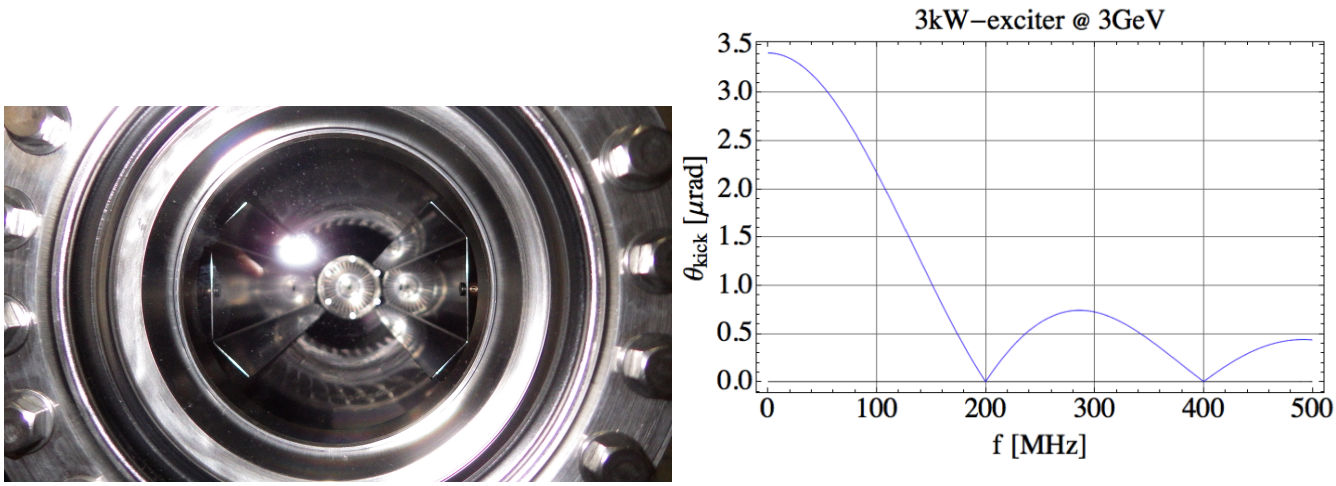

Figure 4.6: Left: Cross-sectional view of stripline kicker, Right:Calculated frequency response of stripline kicker

4.1.2 Operation of the Intra-bunch Feedback System

Performance Evaluation of the Feedback System

We performed the evaluation of the intra-bunch feedback system using 3 GeV DC beam. To evaluate the feedback system, we examined the damping time of the oscillation excited by another kick. We observed the additional kick due to the reflection current of the injection kicker magnet. This kick causes the additional beam loss [142], which was the one of the main beam loss sources at the injection period. We used this kick for the evaluation[2].

We set the chromaticity to almost zero to see the effects of the feedback system clearly, and the tune to the normal operation point (ν_x, ν_y)=(22.41, 20.75) in 2014. We used a beam with 2.7×10^{13} protons per bunch, which was one fifth of the maximum intensity. We compared the damping time of oscillation in three conditions; all feedback systems are off, the bunch-by-bunch feedback system is on, and the intra-bunch feedback system is on. The details of the test are shown in [134].

Figure 4.7 shows the betatron oscillation amplitude observed by the ETC in each condition. Figure 4.8 also shows the time evolution of the spectrum of the beam. Each signal is split into 200 turns and Fast Fourier Transformation (FFT) is applied. The betatron oscillation continues $\sim$ 6000 turns when the feedback system is off. On the other hand, the betatron oscillations are damped within 2000 turns and 100 turns when the bunch-by-bunch and intra-bunch feedback systems are on [144], respectively.

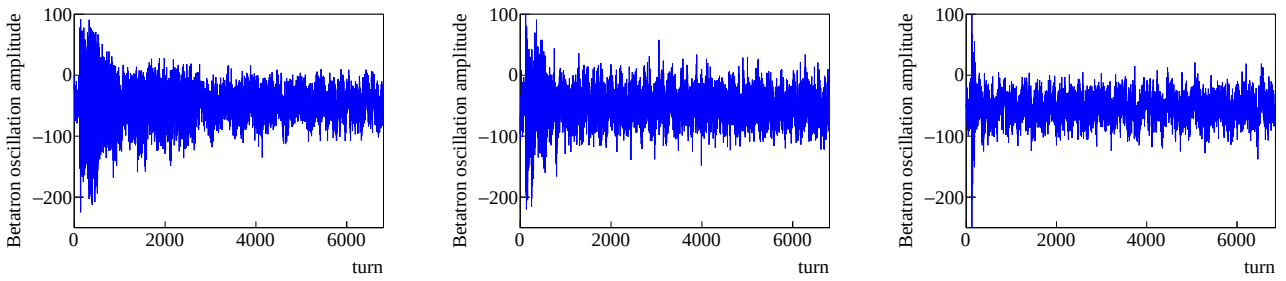

(a) feedback off (b) bunch-by-bunch feedback on (c) Intra-bunch feedback on

Figure 4.7: Time evolution of the Betatron oscillation measured by ETC used in the intra-bunch feedback system

Figure 4.9 shows the internal bunch motion starting just after the additional kick. In each plot, the waveforms for every four turns are overlaid ten times. The internal oscillation is effectively damped within 100 turns by the intra-bunch feedback system while the internal oscillation still remains even after 300 turns when the bunch-by-bunch feedback is on.

We performed a simulation with macro particle tracking to confirm the properties of the intra-bunch feedback system. We succeeded in reproducing the experimental results with the same order of magnitude and confirmed the intra-bunch feedback system damped the oscillation faster than the bunch-by-bunch feedback system by a factor of $\sim$30. The details are described in [145] and [134].

So far, we explained the evaluation for horizontal direction. We observed the beam instabilities in vertical direction. Thus, we also applied the intra-bunch feedback system to the instabilities in the vertical direction. We succeeded in suppressing the beam instabilities in vertical direction. The details are shown in [134].

[2]This additional kick was weakened by the correction kicker installed in 2016 [143] which kicks back the beam to the correct orbit.

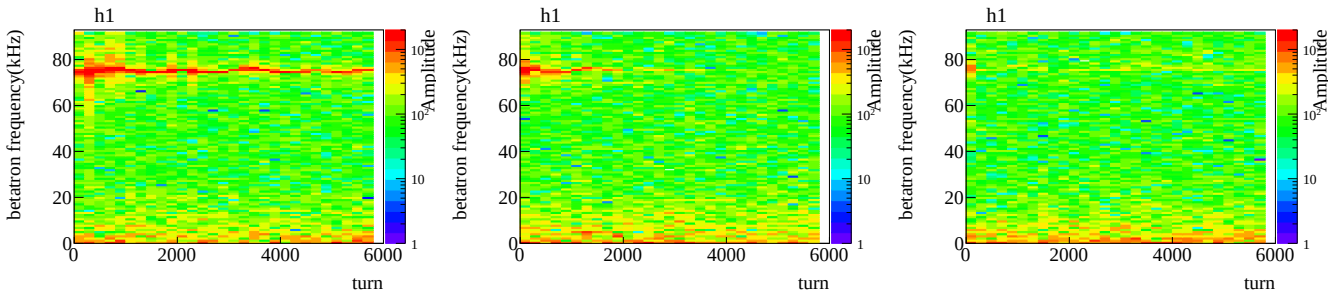

(a) feedback off (b) bunch-by-bunch feedback on (c) Intra-bunch feedback on

Figure 4.8: Time evolution of the Betatron amplitude spectrum measured by ETC used in the intra-bunch feedback system

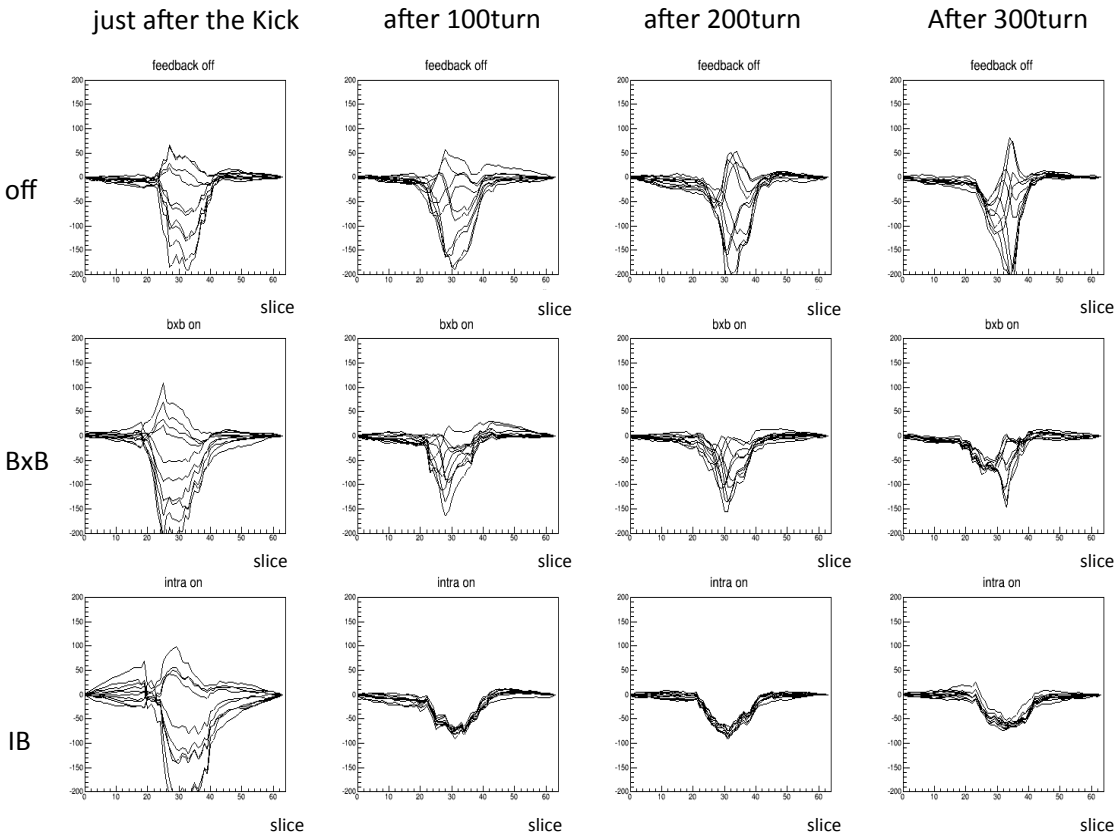

Figure 4.9: Internal bunch motion observed by ETC. Ten waveforms for every four turns is overlaid after the external kick is applied. (Top) all feedback systems are off, (Middle) the bunch-b-bunch feedback system is on, (Bottom) the intra-bunch feedback system is on. In each plot, the y-axis denotes the oscillation amplitude (arbitrary unit).

Feedback System in the Operation for the Neutrino Beamline

As discussed so far, the intra-bunch feedback system reduced the beam loss at the injection due to the beam instabilities. We also introduced the intra-bunch feedback system to the neutrino beam operation. Figure 4.10 shows the beam current stored in Main Ring at the third injection period. The intra-bunch feedback system successfully reduced the beam loss caused by the injection kicker.

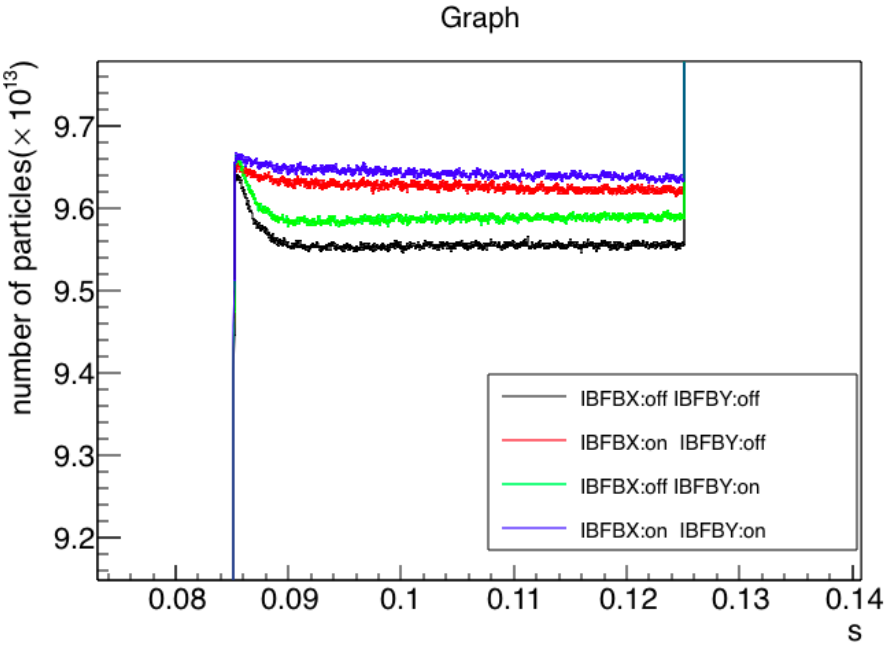

Figure 4.10: Time evolution of the beam current from the third injection period when the additional kick is applied. IBFB: denotes the intra-bunch feedback system, and X and Y correspond to the horizontal and vertical feedback systems.

We also tried to tune the feedback system during acceleration. The iGp12 changes the setting of the parameters ("state" in Fig. 4.11) with the external triggers. We changed the state at appropriate timing and tuned the parameters for each state. We tuned the state up to 0.1s and succeeded in suppressing the beam instabilities which occurred during the acceleration as shown in Fig. 4.11 [146].

4.2 Beta Function Measurement During Acceleration

4.2.1 HIll's Equation and Beta Function

In an accelerator, electromagnetic fields are applied to the beam to change its orbit. Dipole and quadruple magnets are commonly used to bend and to focus (defocus) the beam, respectively. The arrangement of these magnets is called lattice which characterizes all the properties of the beam in the accelerator.

The general equation of motion of transverse linear motion $x(s)$ is described by Hill's equation.

$$x''(s) + k(s)x(s) = 0 \tag{4.1}$$

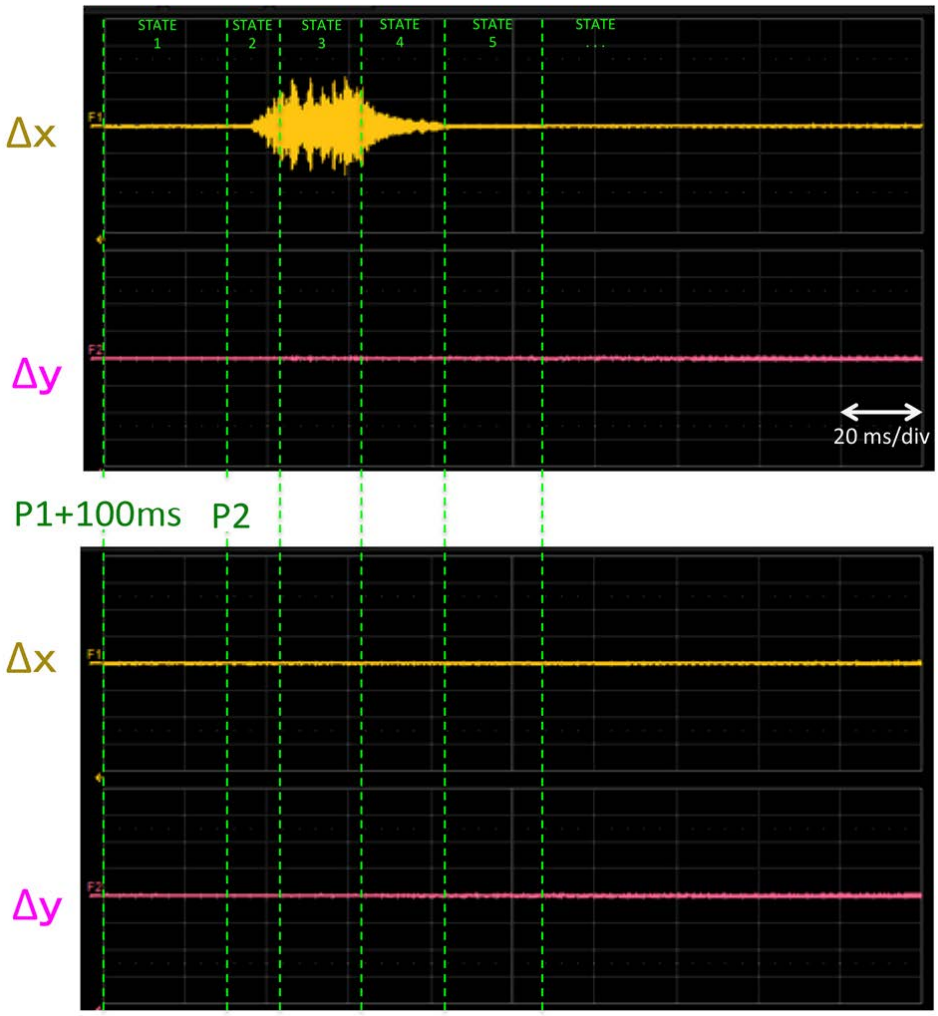

Figure 4.11: The horizontal (Δx) and vertical (Δy) betatron oscillation amplitude from 100 ms after the first injection period taken by oscilloscope. Upper plot shows the betatron amplitude before the feedback system optimization and lower plot shows one that after the application of the intra-bunch feedback system.

where $k(s)$ corresponds to the focusing or defocusing strength at s [3]. The general solution of the Hill's equation Eq. (4.1) is given as:

$$x(s) = \sqrt{\beta(s)\epsilon}\cos[\psi(s) - \psi_0]. \tag{4.2}$$

where ψ_0 is the constant phase determined by the initial condition, ϵ is the emittance of the beam. The $\beta(s)$ and $\psi(s)$ are related to each other:

$$\psi(s) = \int \frac{ds}{\beta(s)} \tag{4.3}$$

This $\beta(s)$ is called betatron amplitude function or beta function, which describes the oscillation amplitude at position s. The beta function is controlled by the strength of the quadruple magnets in a synchrotron. The magnetic field is ramped up in proportion to the particle momentum so that the beam optics keeps constant during a whole acceleration period. Imperfection of the setting of magnetic field distorts the optics and causes the beam loss. Especially, narrowing the dynamic aperture is one of the main issues. Therefore, it is necessary to measure the beta function during beam acceleration and correct the magnet ramping patterns based on the measurement especially for high intensity beams.

To measure the beta function, we excite the betatron oscillation coherently and measure the amplitude of the betatron oscillation since beta function of a single particle is related to the amplitudes of the oscillation as described in Eq. (4.2). At injection period, we excite the betatron oscillation by making offset at the injection [147]. However, we could not measure the beta function during acceleration since we had no way to excite it. We have developed a new method to excite coherent motion by applying the electromagnetic field gradually with the stripline kicker. With this new method, we measured the beta function during the acceleration period up to 406 ms from the injection [148], [149].

4.2.2 Setup of the Beta Function Measurement

Figure 4.12 shows the schematic view of the beta function measurement. The setup is similar to the feedback system described in Section 4.1. In this measurement, the signal processing module just sends signals to the kicker. The module generates sinusoidal signals to excite the betatron oscillation. The output signal is written as :

$$y_i = A\sin\frac{2\pi(N+\delta\nu)}{T_{rev}}\frac{i}{f_{clk}} \tag{4.4}$$

where i is the index of the output signal, A is the amplitude of the signal, N is an arbitrary integer, $\delta\nu$ is fractional tune, T_{rev} is the revolution time ($\sim 5.3\mu s$) and f_{clk} is reference clock frequency ($\sim$ 106 MHz). As the reference clock, a clock having 64 times higher frequency than RF is used. The module sends the signal at an arbitrary timing and width. We set these parameters by PC via USB port. The signal is sent to the stripline kicker which is used in the intra-bunch feedback system. The excited betatron oscillation is measured by 189 BPMs equipped around Main Ring. BPM has diagonal cut electrodes which has a linear response to the position [150].

Figure 4.13 shows the timing chart of J-PARC Main Ring. The start timing of the measurement and width of the signal are referred to as "start" and "interval" in Fig. 4.13. Parameters and measurement time of each measurement are shown in Table 4.1. "start", "interval" and "measurement time" are set as follows. The module receives a reference trigger "p0" in Fig. 4.13 at the beginning of the synchrotron cycle. The data acquisition system can take only $\sim$ 15 ms due to the limited memory

[3] For horizontal direction, bending is also included in $k(s)$. See Appendix A for the coordinates.

resources. Before data taking, the betatron oscillation should be excited largely. Thus, we set "interval" to around 50 ms to excite the oscillation largely, and set "start" just before the measurement time we want. We set the tune as (22.40, 20.75), which is the same as the normal operation point in 2014. However, the tune is occasionally displaced from its value due to the incorrect setting of the magnet and ripples of the magnet power supply. Therefore, we optimized the tune parameter to kick the beam effectively at each timing.

Table 4.1: Setting parameters of each timing

Measurement time	start (ms)	interval (ms)	$(\delta\nu_x, \delta\nu_y)$	N	$p(GeV/c)$
p0+100ms	50	45	(0.400,0.750)	20	3.82
p0+201ms	150	45	(0.390,0.740)	20	4.19
p0+303ms	250	50	(0.395,0.750)	20	6.11
p0+405ms	350	50	(0.405,0.750)	20	8.20
p0+510ms	450	50	(0.404,0.760)	20	10.28

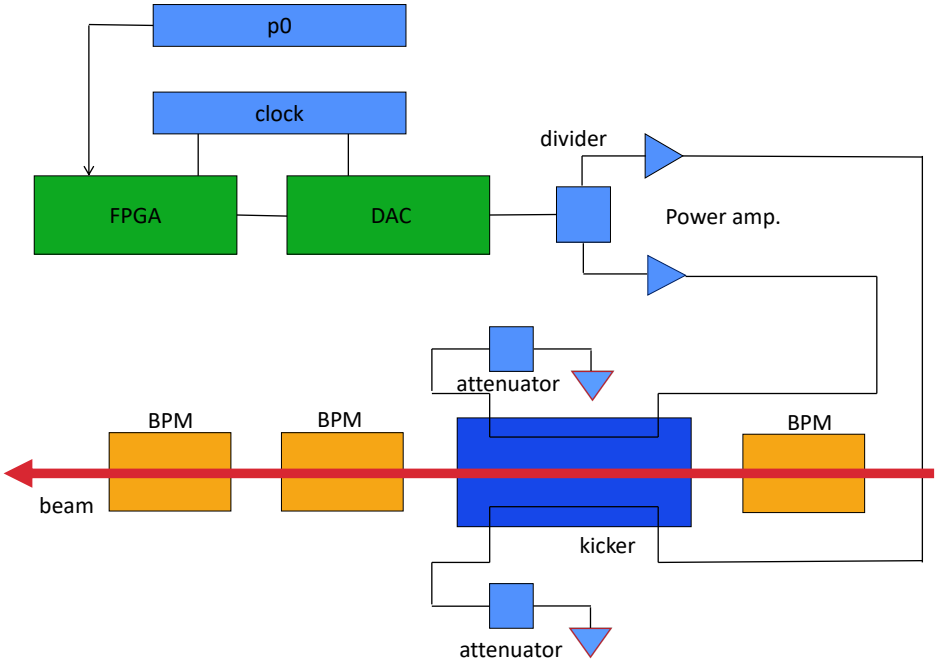

Figure 4.12: Schematic diagram of the beta function measurement

4.2.3 Measurement and Analysis of Beta Function

Figure 4.14 shows the measured horizontal betatron oscillation of the beam by one BPM and its Fourier spectrum of the oscillation. In the spectrum, the peak exists in the point which corresponds

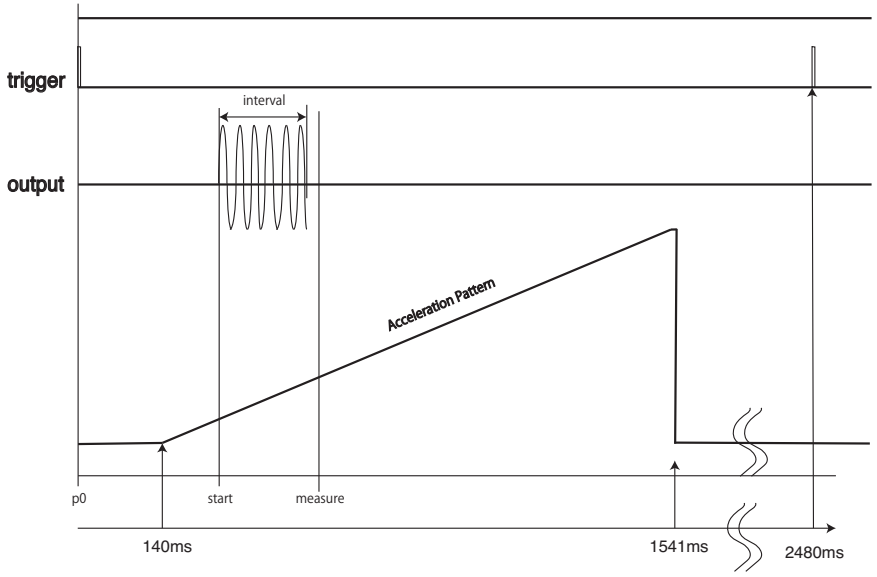

Figure 4.13: Timing chart of the beta function measurement

to the fractional tune $\delta\nu_x = 0.4$. This indicates that we could excite the betatron oscillation with this method.

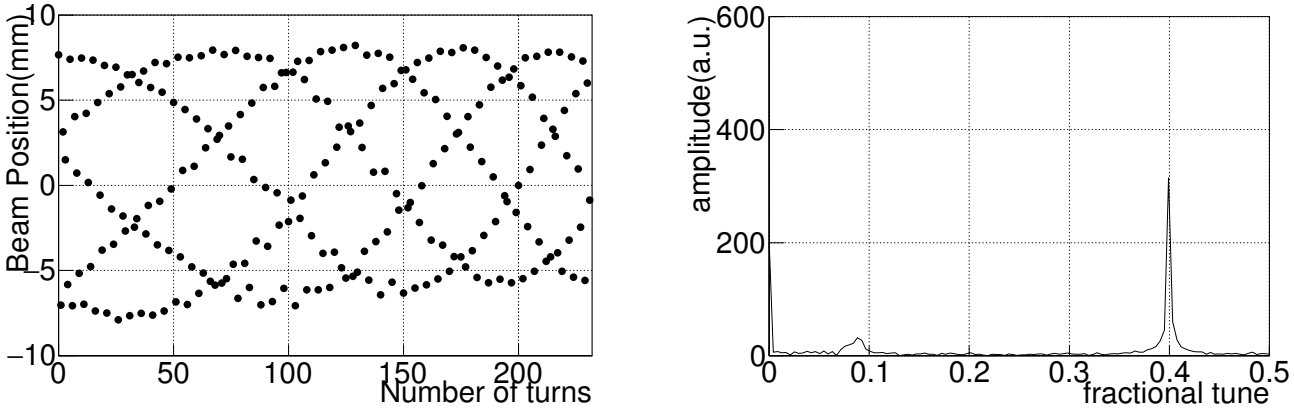

Figure 4.14: The measured (Left) waveform and (Right) the Fourier spectrum of one of the BPMs

We chose the amplitude of the peak in Fig. 4.14 as the amplitude of the betatron oscillation. We extracted the betatron oscillation amplitude from all BPMs. To make a comparison with our simulation model, we normalized the amplitude with the scaling factor calculated as:

$$\frac{\Sigma_{i=0}^{N_{BPM}} \beta_{i,meas.}}{\Sigma_{i=0}^{N_{BPM}} \beta_{i,model}} \tag{4.5}$$

where N_{BPM} is the total number of BPMs (189), $\beta_{i,model}$ and $\beta_{i,meas.}$, are beta functions at the ith BPM obtained by the simulation model and measurement, respectively.

The measured beta function at "p0+405ms" is shown in the first, third and fifth plots of Fig. 4.15[4]. We had several measurements in each timing and plotted the mean of the measurements in these

[4]As shown in Chapter 3, J-PARC Main Ring has a three-fold symmetry shape (triangle), and each section has the same beam optics.

plots. The second, fourth and sixth plots describe the fractional deviation of the measurement values from the simulation model. The beta function deviates largely from the model, which means that the magnet is not set correctly.

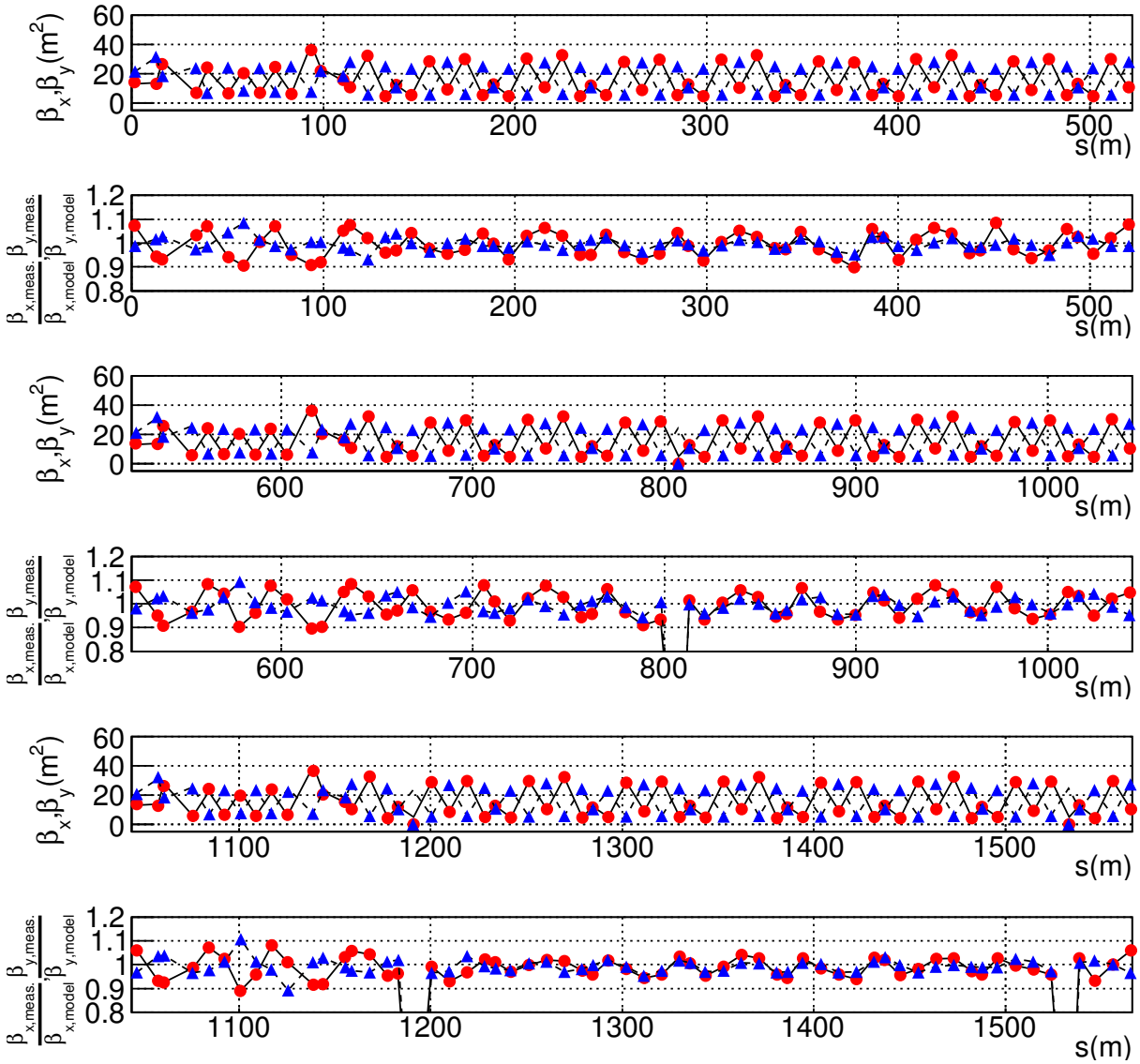

Figure 4.15: The first, third and fifth plots show the measured beta functions of J-PARC MR before the optics correction. The second, fourth and sixth plots describe the fractional deviation of the measurement values from the simulation model. The circles correspond to the horizontal beta function and the triangles correspond to those of vertical. In this plot, the circumferential length of Main Ring is divided into three parts.

The optics of J-PARC Main Ring is controlled by eleven families of the quadruple magnets. Each family of the magnets is controlled by a single power supply. We fitted the measured beta functions to the simulation model with parameters for the focusing strengths of the quadruple magnet families simultaneously with the measured dispersion functions. Since we measured the beta functions at five different timings, we performed the fit at each timing.

The fitted parameters were used as the correction factors to correct the power supply output so that it matches the simulation model. After the correction, the beta functions were measured again

and the results at "p0+405 ms" are shown in Fig. 4.16. It is seen that the measured values match the simulation model after the correction. Figure 4.17 shows the tune measurement before and after the optics correction. The tunes are largely shifted during the acceleration before the correction while they stay around the constant value after the optics correction.

This is the first measurement of the beta function during the beam acceleration. This measurement also contributes to the beam loss reduction with the optics correction during the acceleration period.

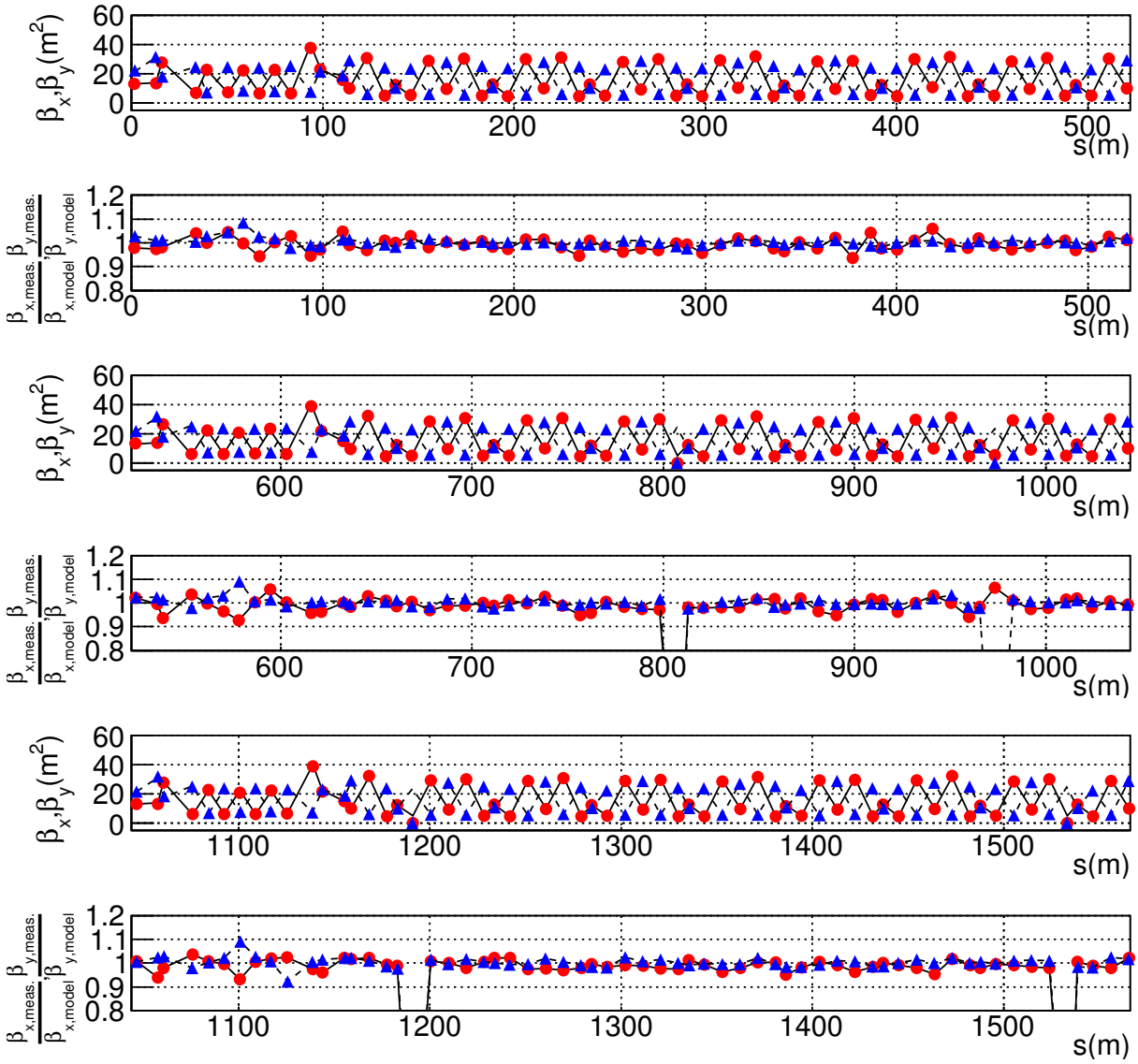

Figure 4.16: The first, third and fifth plots show measured beta functions of J-PARC MR after optics correction. The second, fourth and sixth plots describe the fractional deviation of the measurement values from the simulation model. The circles correspond to horizontal beta function and the triangles correspond to those of vertical. In this plot, the circumferential length of Main Ring is divided into three part.

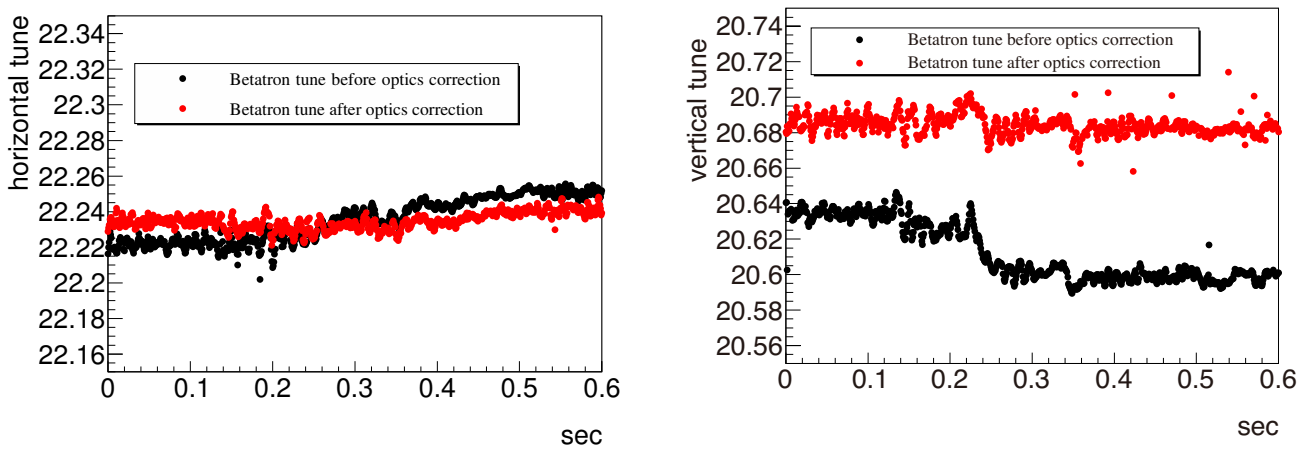

(a) horizontal tune

(b) vertical tune

Figure 4.17: The time evolution of vertical and horizontal tunes. Black circle corresponds to the measurement before the optics correction and red corresponds to that after the correction.

4.3 Discussion

It is difficult to estimate the effects of these developments on the beam intensity qualitatively since the improvement of the accelerator is related closely each other. However, the intra-bunch feedback system and the beta function measurement are still indispensable for the intensity improvement of J-PARC Main Ring [151].

4.3.1 Impact of the Intra-bunch Feedback System

As discussed in Chapter 3, the beam instability was one of the main issues for the J-PARC Main Ring operation and the intra-bunch feedback system effectively dumped the beam instability as shown in this chapter. Since the beam loss would cause serious problems on the maintenance and safety, an interlock system called MPS is triggered when the abnormal sign (such as large beam loss, unusual output of the power supply and so on) is detected [152]. When the beam instability is occurred, a large amount of the beam are lost, and the beam operation is interrupted. Therefore, the accelerator tuning was done so that the beam instability would not occur, which meant that the beam instability limited the beam intensity until 2014. Therefore, damping the beam instability directly improves the limit of the beam intensity.

Until now, the beam instability which cannot be suppressed by the intra-bunch feedback system is not yet observed. However, the strength of wake field emission depends on the beam intensity [153], therefore, an unexpected beam instability may occur in the high power beam operation in the future. Hence, it is important to understand the beam instability itself and the properties of the feedback system to predict whether the beam instability is critical or not and to know whether current intra-bunch feedback system can damp such a beam instability in the future. To estimate this, a more precise macro particle simulation including wake field effects and the construction of the more precise impedance model of the accelerator are required.

4.3.2 Impact of the Beta Function Measurement

The beginning of the acceleration is one of the largest loss points due to the poor properties of the power supplies in J-PARC. For accelerators, the tracking error, the deviation between command value and measured value of the power supplies and the fluctuation called ripple affect the beam operation. The control precision of the transverse motion of the beam depends on the accuracy of the output current of the power supplies. The absolute error of the output is the same in the whole acceleration period, while the effects on the beam control is larger at the beginning of the acceleration since the relative error to the command value is larger [5]. Measuring the beta function during the acceleration enables us to estimate the tracking error size in actual situation, and we succeeded in reducing the beam loss at that period.

As described in Chapter 3, new power supplies will be installed in the future. The new power supply is motivated by not only for the high reputation rate operation, but also for the high precision control of the beam. Especially, the ripple is one of the main issues for the beam quality in the slow extraction operation. We have been developing the new FPGA-based control system which is also used for this beta function measurement [154]. We installed a new power supply in 2017 and evaluated. A low ripple level operation is already achieved and we are waiting for the mass production. However, even with these developments, the tracking error may still exist due to the unexpected error source. Therefore, this beta function measurement will also help to understand the beam optics in the future.

4.3.3 Summary

In this chapter, we described the development of the intra-bunch feedback system and the new method for the beta function measurement. Both developments have succeeded in reducing the beam loss, and became indispensable for the intensity improvement of J- PARC Main Ring. The effects on the T2K data taking is summarized in the next chapter.

[5] For this reason, beta function measurement up to 405 ms was enough to suppress the beam loss.

Chapter 5

Data Taking

5.1 History of the Beam Intensity of J-PARC Main Ring

5.1.1 Achievement of 480kW Operation

As described in the previous chapter, we established the intra-bunch feedback system for the beam instabilities and the beta function measurement for the beam optics control. We succeeded in reducing the beam loss with these improvements and introduced them to the neutrino beam operation.

Figure 5.1 shows the beam power delivered to the T2K beamline and accumulated Protons On Target (POT). The beam power of J-PARC Main Ring has been gradually increased. The intra-bunch feedback system was installed in May 2014, and beta function measurement method was established in 2015 May. Since 2016, we have succeeded to operate the accelerator at the new operation point with (ν_x, ν_y)=(21.35, 21.45) (blue point in Fig. 3.8) and succeeded to deliver the proton beam to the neutrino beam line with 480kW (2.44×10^{14} protons per pulse (PPP)) beam power in 2017. In 2018, the beam power of single shot reached to 520kW [151]. We are planning to install new power supplies in 2019 or later. After the installation, the beam power will reach to the designed value or higher.

5.1.2 Toward 1.3 MW Operation

We also demonstrated that the two-bunch acceleration of 3.5×10^{13} proton per bunch with current operation point (ν_x, ν_y)=(21.24, 21.31) in 2015. This proton per bunch is equivalent to 520 kW with eight bunches, and we already achieved this beam power in 2018. If the new power supply is installed, the beam power would reach to 1 MW. This is a big milestone for both J-PARC and T2K toward higher beam power operation in the future. Furthermore, if we could increase the number of protons up to 4.0×10^{13} and shorten the repetition period from 1.3 s to 1.16 s, the beam power will reach to 1.3 MW [155]. To achieve this beam power, further reduction of the beam loss is necessary.

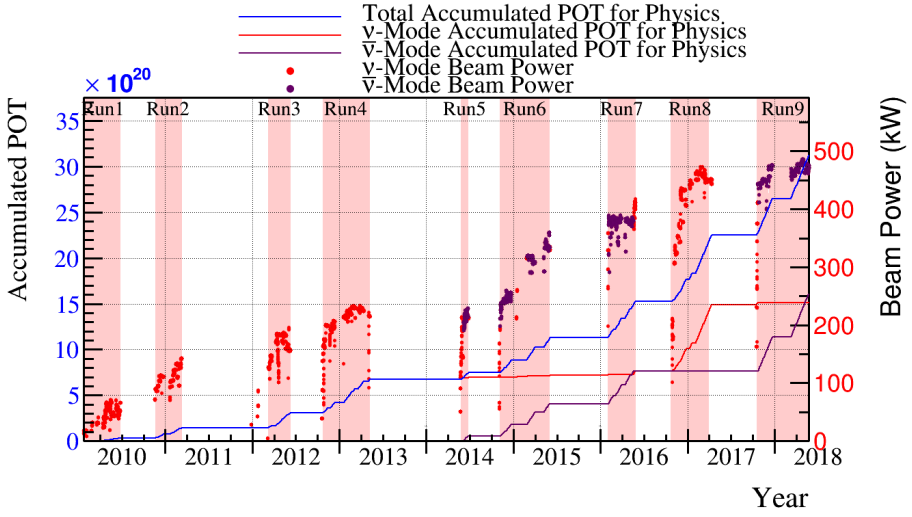

Figure 5.1: POT and beam power history of T2K. Solid lines show the accumulated POT (Red:FHC mode, Purple: RHC mode, Blue: total). Red and Purple dots show the achieved beam power at that point (Red: FHC mode, Purple: RHC mode).

5.2 T2K Data Taking

5.2.1 Data Taking Until 2018

T2K started physics data taking in 2010 and accumulated the data for seven years with interruptions by Earthquake (Mar. 2011) and an accident at Hadron Hall (May. 2013). There are nine data taking period called Run1-9 as shown in Fig. 5.1. The accumulated POT so far is 3.16×10^{21} POT. This is 40% of the approved POT. We accumulated 1.51×10^{21} and 1.65×10^{21} POT data for FHC and RHC mode. In this thesis, we use the data until Run8, collected 2.25×10^{21} POT (1.49×10^{21} POT for FHC mode and 7.62×10^{20} POT for RHC mode).

5.2.2 Quality of the Neutrino Beam

Figure 5.2 shows the history plot of the neutrino event rate measured by INGRID and the neutrino beam direction measured by INGRID and MUMON. The neutrino event rate per POT is stable within 0.7 %, except for the period in the beginning of Run 3. Due to the troubles in the horn power supply, the magnetic horn was operated with 205 kA in the beginning of Run 3 while the nominal value is 250 kA. The stability of the beam direction is much better than the requirement (1 mrad) during whole run period.

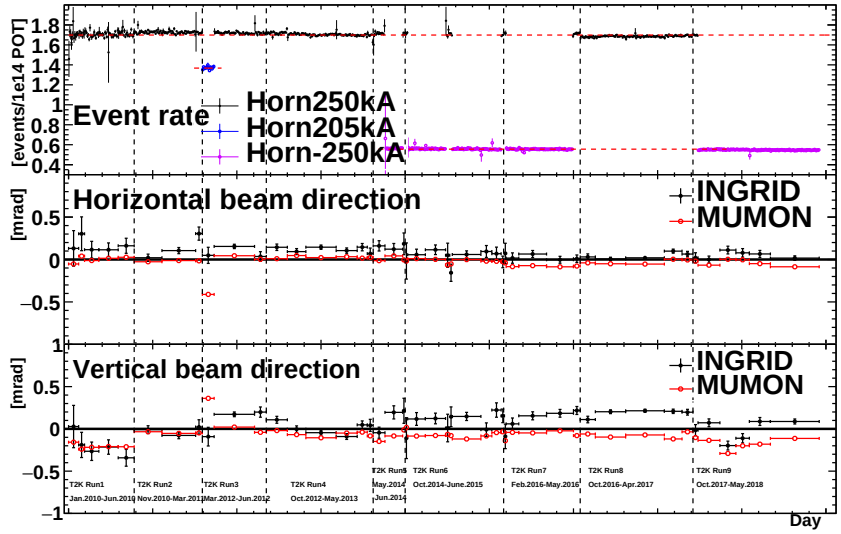

Figure 5.2: Event rate, beam direction stability measured by INGRID and MUMON

Part III

Measurement of Neutrino Oscillation Parameters

Chapter 6

Overview of the T2K Neutrino Oscillation Analysis

In this chapter, we introduce the oscillation analysis in T2K.

6.1 Oscillation Analysis Strategy in the T2K Experiment

Oscillation parameters are measured by comparing the measured energy spectrum and event rates to the predicted ones at Super-Kamiokande. The predicted event rate of ν_β oscillated from ν_α with neutrino energy E_ν at Super-Kamiokande is written:

$$N_{SK}(E_\nu) = \phi_{SK}(E_\nu)\sigma(E_\nu)\epsilon_{SK}(E_\nu)P(\nu_\alpha \to \nu_\beta, E_\nu) \tag{6.1}$$

where $\phi_{SK}(E_\nu)$ is the neutrino flux, $\sigma(E_\nu)$ is the neutrino-nucleus interaction cross-section, $\epsilon_{SK}(E_\nu)$ is the detection efficiency of Super-Kamiokande, and $P(\nu_\alpha \to \nu_\beta, E_\nu)$ is the oscillation probability at E_ν. We use Monte Carlo simulation with JNUBEAM [156] for the flux, NEUT generator [157] for neutrino interaction, and GEANT4 [158] and SKdetsim [159] for the detector simulation of ND280 and Super-Kamiokande to predict the energy spectrum and event rates.

The parameters of interest are related to $P(\nu_\alpha \to \nu_\beta)$, and the other parameters should be taken as nuisance parameters. Thus, it is necessary to understand the flux, cross-section and the detector efficiency precisely and reduce their uncertainties to measure the oscillation parameters. Especially, neutrino flux and cross-section have large uncertainties of about 10 % which will be discussed later. To reduce the flux and cross-section uncertainties, we measure the neutrino events at ND280 and give constraints on these parameters.

We fit the data to the prediction by maximum likelihood method in Super-Kamiokande. The likelihood for the parameters of flux $\vec{b}$, cross-section $\vec{x}$ and oscillation $\vec{o}$, given the ND280 (M_{ND}) and Super-Kamiokande (M_{SK}) data is written as follows:

$$\mathcal{L}(\vec{b}, \vec{x}, \vec{o}|M_{ND}, M_{SK}) = \mathcal{L}(\vec{b}, \vec{x}|M_{ND}) \times \mathcal{L}(\vec{b}, \vec{x}, \vec{o}|M_{SK}) \tag{6.2}$$

The flux and cross-section parameters are constrained by external experiments such as NA61/SHINE for the flux and various experiments such as MINERνA, MiniBooNE for the cross-section. These information is added to the likelihood as prior constraints for the fit. The systematic uncertainties are modeled as multivariate Gaussian distributions here:

$$\pi(\vec{y}) = (2\pi)^{\frac{n}{2}} |V_y|^{\frac{1}{2}} \exp(-\frac{1}{2}\Delta\vec{y}V_y^{-1}\Delta\vec{y}) \tag{6.3}$$

where $\vec{y}$ is the vector of parameter values, n is the number of parameters, V_y is the covariance matrix of the parameters and $\Delta\vec{y}$ is the difference between current parameter values and nominal parameter values. Taking the natural log, considering prior constraints of the flux and cross-section parameters, and dropping constant terms, the log-likelihood is given as :

$$\ln \mathcal{L}(\vec{b}, \vec{x}, \vec{o}|M_{ND}, M_{SK}) = \ln P(M_{ND}|\vec{b}, \vec{x}) + \ln P(M_{SK}|\vec{b}, \vec{x}, \vec{o}) - \frac{1}{2}\Delta\vec{b}(V_b^{-1})\Delta\vec{b}^T - \frac{1}{2}\Delta\vec{x}(V_x^{-1})\Delta\vec{x}^T. \tag{6.4}$$

The T2K oscillation analysis maximizes this log-likelihood with two steps [1]. We maximize the log-likelihood for the ND280 data first then propagate the fit results to the oscillation fit at Super-Kamiokande as prior constraints. The log-likelihood for the near detector fit $\mathcal{L}(\vec{b}, \vec{x}|M_{ND})$ is given by adding near detector systematic parameters $\vec{d}$:

$$\ln \mathcal{L}(\vec{b}, \vec{x}|M_{ND}) = \ln P(M_{ND}|\vec{b}, \vec{x}) - \frac{1}{2}\Delta\vec{b}(V_b^{-1})\Delta\vec{b}^T - \frac{1}{2}\Delta\vec{x}(V_x^{-1})\Delta\vec{x}^T - \frac{1}{2}\Delta\vec{d}(V_d^{-1}(\vec{b}, \vec{x}))\Delta\vec{d}^T. \tag{6.5}$$

The log-likelihood Eq. (6.5) is maximized by changing of $\vec{b}$ and $\vec{x}$ marginalizing over the ND280 detector systematic parameters $\vec{d}$. Using the best fit parameters of the near detector fit $\vec{f} = (\vec{b}_{best}, \vec{x}_{best})$, the likelihood Eq. (6.4) is given:

$$\mathcal{L}(\vec{b}, \vec{x}, \vec{o}|M_{SK}) = P(M_{SK}|\vec{f}, \vec{o}) - \frac{1}{2}\Delta\vec{f}(V_f^{-1})\Delta\vec{f}^T \tag{6.6}$$

We then maximize this log-likelihood again with respect to the oscillation parameters $\vec{o}$. The summary of the oscillation analysis is shown in Fig. 6.1.

In the following chapter, we show the details of the oscillation analysis. First, we describe the neutrino flux simulation and cross-section models used in the Monte Carlo simulation to predict the energy spectrum and event rates at Super-Kamiokande and at ND280 in Chapter 7 and Chapter 8. In Chapter 9, we describe the detail of the near detector fit and the fit results. In Chapter 10, we show the details of the Super-Kamiokande event selection. We also describe the detail of the oscillation fit, which maximizes the Eq. (6.6) in Chapter 11. In Chapter 12, we show the investigation of the additional uncertainties which are not considered in the near detector fit and inclusion of them into the fit with simulated data studies. In Chapter 13, we show the results of the oscillation analysis.

[1] There are three independent oscillation analysis frameworks in T2K. One of them maximizes the likelihood directly with the Markov Chain Monte Carlo method [160].

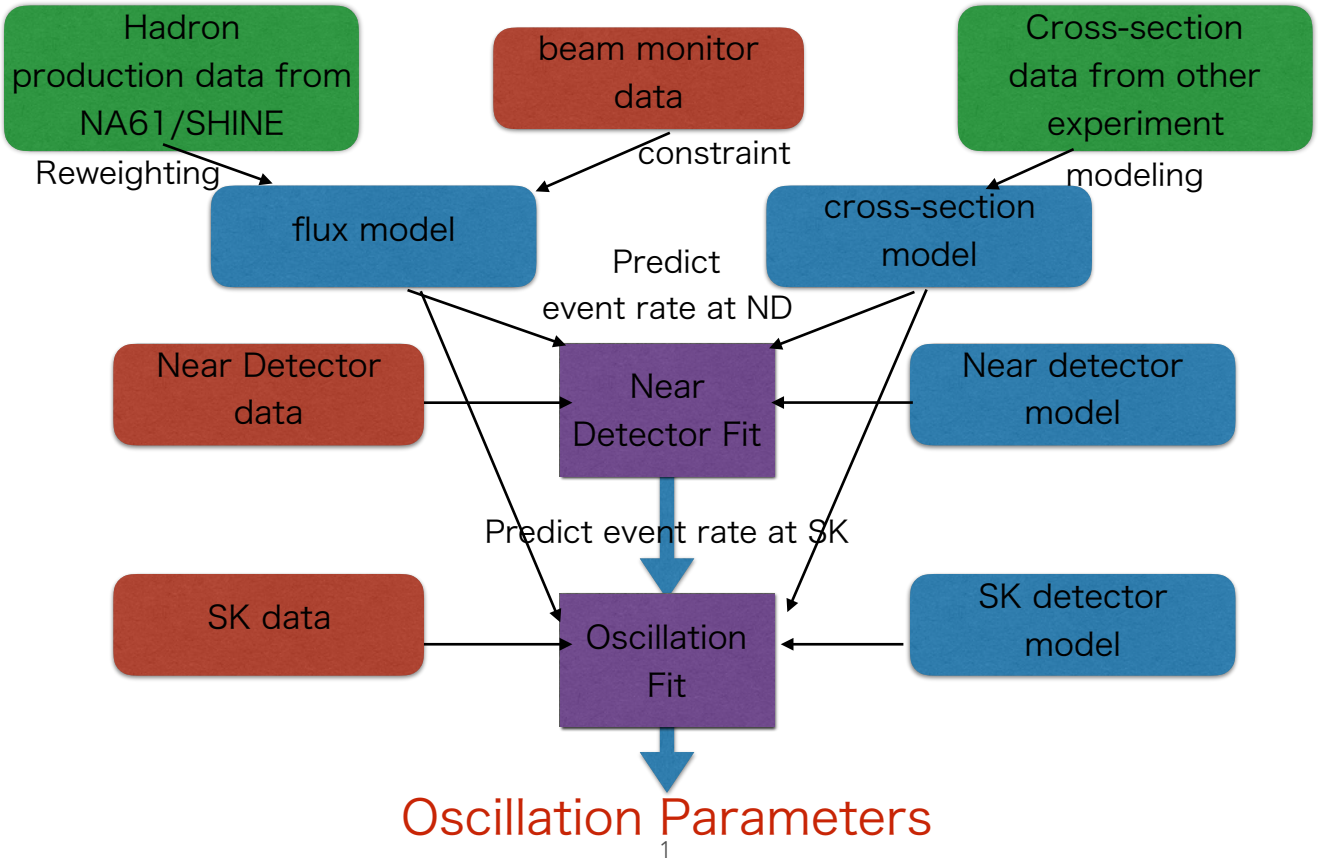

Figure 6.1: Overview of the T2K oscillation analysis

Chapter 7

Neutrino Flux Prediction

In this chapter, we summarize the neutrino flux prediction.

7.1 Procedure of the Neutrino Flux Simulation

As described in Section 2.2.2, neutrinos are produced from meson decays which are produced from following nucleon-Carbon interaction.

$$\begin{aligned} p(n) + C \rightarrow & \pi^{\pm} + X \\ & \hookrightarrow \mu^{\pm} + \nu_{\mu}(\bar{\nu}_{\mu}) \end{aligned} \tag{7.1}$$

$$\begin{aligned} p(n) + C \rightarrow & K^{\pm} + X \\ & \hookrightarrow \mu^{\pm} + \nu_{\mu}(\bar{\nu}_{\mu}) \\ & \hookrightarrow e^{\pm} + \nu_{e}(\bar{\nu}_{e}) \end{aligned} \tag{7.2}$$

$$\begin{aligned} p(n) + C \rightarrow & K^{0} + X \\ & \hookrightarrow \pi^{\pm} + e^{\mp} + \bar{\nu}_{e}(\nu_{e}) \\ & \hookrightarrow \pi^{\pm} + \mu^{\mp} + \bar{\nu}_{\mu}(\nu_{\mu}) \end{aligned} \tag{7.3}$$

The neutrino flux at ND280 and Super-Kamiokande (SK) is predicted by simulations starting from the proton beam. The neutrino flux is simulated with three steps. First, we simulate the hadron production in the target by FLUKA [161]. Second, we track the particles exiting from the target and simulate meson decays by JNUBEAM [156] developed based on GEANT3 [162]. Finally, we tune the neutrino flux with external experiments including NA61/SHINE [163] to improve the accuracy of the flux simulation and reduce the systematic uncertainties coming from hadron production uncertainties.

FLUKA Simulation

FLUKA simulates hadron production in the target. The proton beam in the simulation starts from the end of the baffle. The center, width and emittance of the proton beam are measured by ESM, SSEM and OTR as described in Chapter 2. The proton beam properties at the baffle are extrapolated from these measurements and used as the input of the FLUKA simulation. The information of the exiting particles from the target are transferred to JNUBEAM.

JNUBEAM

JNUBEAM is a Monte Carlo simulation code of the baffle, target, horn magnets, helium vessel, decay volume, beam dump, and muon monitor. JNUBEAM tracks the particles exiting from the target in a magnetic field generated by magnetic horns and simulates meson decays. In JNUBEAM, hadron interactions outside the target are simulated by GCALOR [164]. For the meson decays, we consider $\pi^{\pm}$, $K^{\pm}$, K^0_L and $\mu^{\pm}$ decays as the neutrino sources.

Hadron Production Tuning

Hadron production is the dominant source of the neutrino flux uncertainty. The NA61/SHINE experiment measures the hadron production cross-section at the same proton energy as Main Ring (30 GeV) with T2K replica target [165, 166]. We calculate the data-prediction ratio for each hadron production mode and tune the neutrino flux with this ratio to improve the neutrino flux prediction.

Figure 7.1 shows the predicted neutrino flux of the FHC and RHC mode at ND280 and Super-Kamiokande.

The energy spectrum is similar in ND280 and Super-Kamiokande, it is peaked around 0.6 GeV in both FHC mode and RHC mode. For RHC mode, the wrong-sign component is larger than that of FHC mode due to the difference of the parent meson multiplicity.

7.2 Systematic Uncertainties of the Neutrino Flux

The fractional errors of ν_μ flux in FHC and $\bar{\nu}_\mu$ flux in RHC at ND280 and Super-Kamiokande are shown in Fig. 7.2. The dominant uncertainty is the hadron production modeling as mentioned. The total uncertainties are estimated about 10% at the peak energy. The errors of the other neutrino flux are shown in Appendix B.

There is a strong correlation between the predicted flux at ND280 and Super-Kamiokande. Figure 7.3 shows the ND280/SK flux correlation matrix and covariance matrix which is used in the fit.

The binning of the covariance matrix is as follows:

- 1 - 25 : ND280 FHC mode
- 26 - 50 : ND280 RHC mode
- 51 - 75 : SK FHC mode
- 76 - 100 : SK RHC mode

In each mode, the flux for each neutrino species are arranged in the following order: (ν_μ, $\bar{\nu}_\mu$, ν_e, $\bar{\nu}_e$) and following binning of the neutrino energy:

- ν_μ in FHC/$\bar{\nu}_\mu$ in RHC : 0.0, 0.4, 0.5, 0.6, 0.7, 1.0, 1.5, 2.5, 3.5, 5.0, 7.0, 30.0 (GeV)

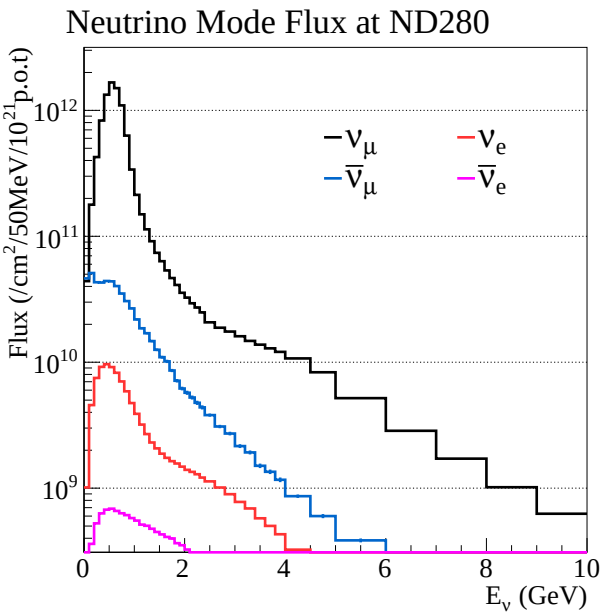

(a) FHC at ND280

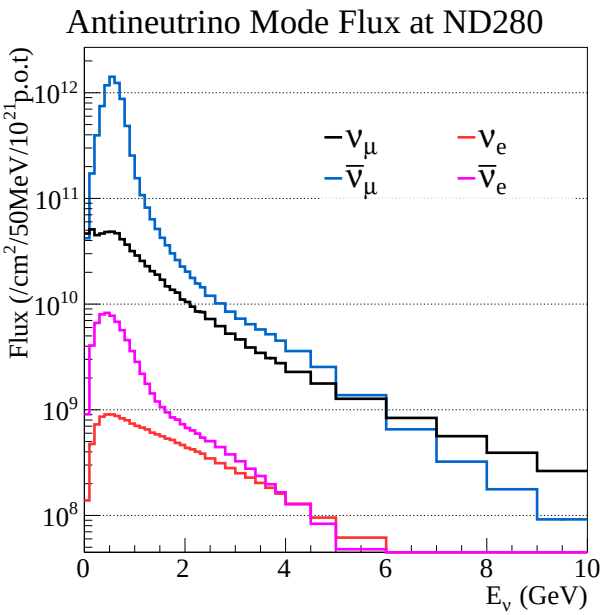

(b) RHC at ND280

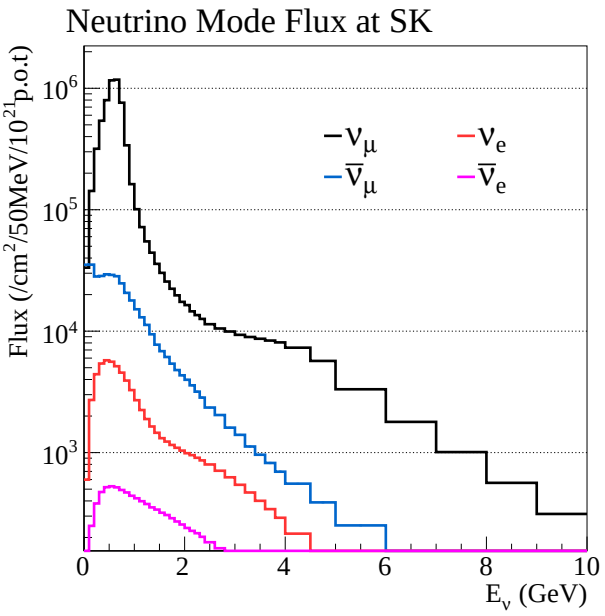

(c) FHC at Super-Kamiokande

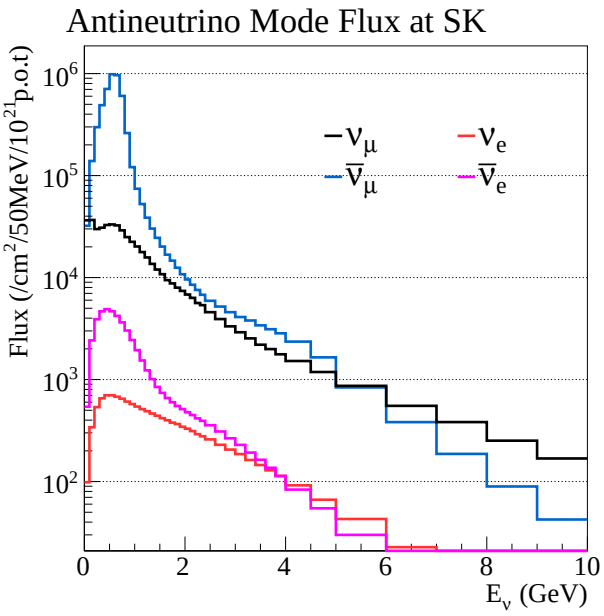

(d) RHC at Super-Kamiokande

Figure 7.1: Predicted neutrino fluxes of the FHC and RHC mode at ND280 and Super-Kamiokande

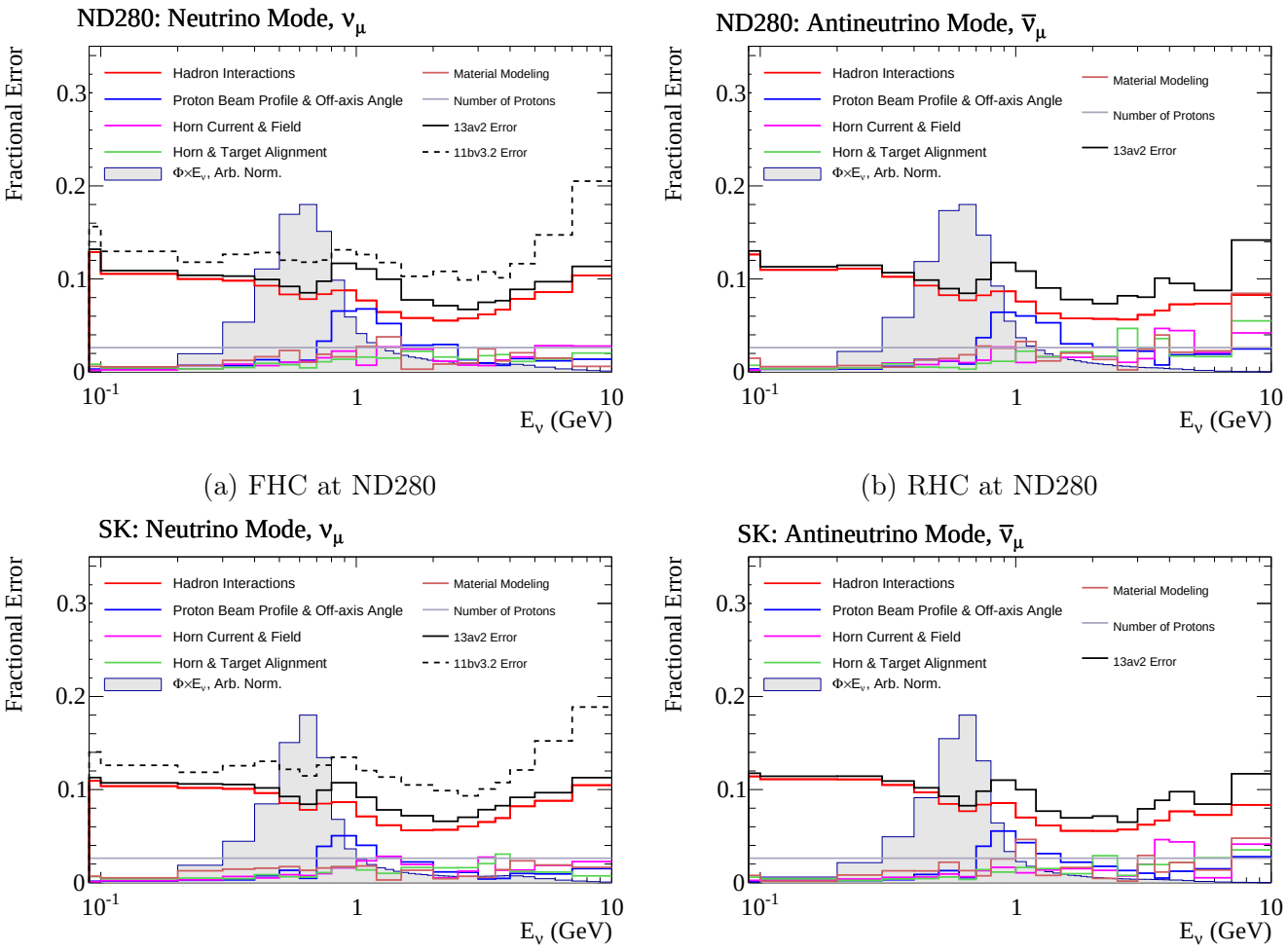

(a) FHC at ND280

(b) RHC at ND280

(c) FHC at Super-Kamiokande

(d) RHC at Super-Kamiokande

Figure 7.2: Fractional error of the neutrino flux at ND280 and Super-Kamiokande

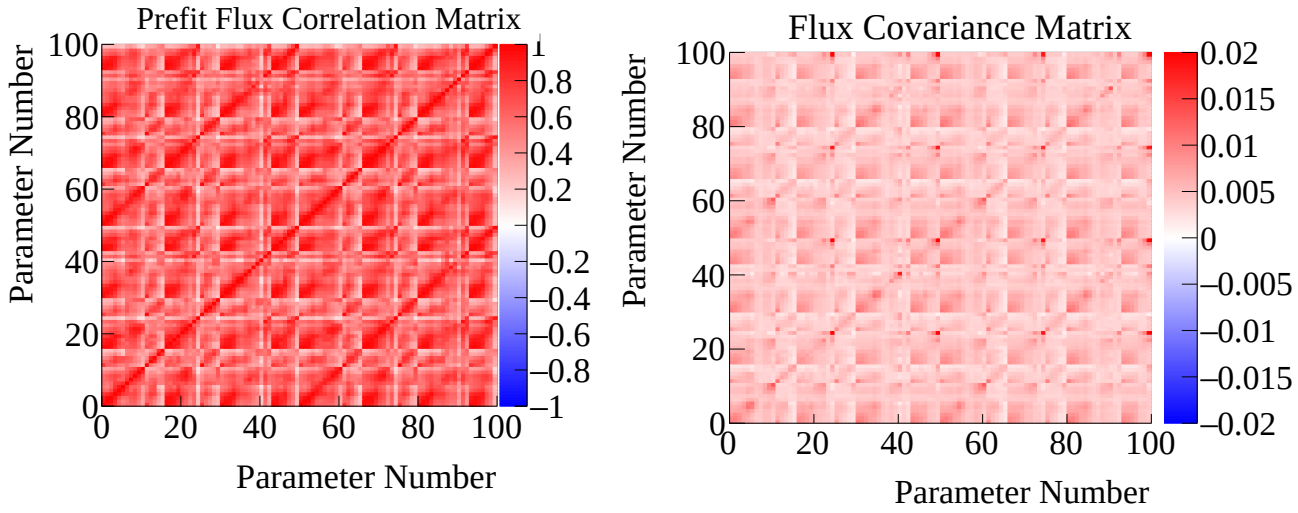

Figure 7.3: ND280 and Super-Kamiokande flux correlation matrix (Left) and covariance matrix(right)

- $\bar{\nu}_\mu$ in FHC/ν_μ in RHC : 0.0, 0.7, 1.0, 1.5, 2.5, 30.0 (GeV)
- ν_e in FHC/$\bar{\nu}_e$ in RHC : 0.0, 0.5, 0.7, 0.8, 1.5, 2.5, 4.0, 30.0 (GeV)
- $\bar{\nu}_e$ in FHC/ν_e in RHC : 0.0, 2.5, 30.0 (GeV)

Chapter 8

Neutrino-Nucleus Interaction

In this chapter, we describe neutrino-nucleus interaction modeling used in the Monte Carlo simulation and their parameterizations for the near detector fit.

8.1 Introduction

8.1.1 Overview of NEUT Generator

It is necessary to use neutrino-nucleus interaction models to predict the event rates and energy spectrum at Super-Kamiokande and ND280. In T2K, NEUT [157] is used to simulate the neutrino-nucleus interaction. NEUT covers a wide energy range of the neutrino interaction from several tens of MeV to hundreds of TeV.

In this chapter, we first briefly introduce the neutrino-nucleus interaction models used in the NEUT simulation. In spite of many efforts to understand the neutrino-nucleus interaction, there are still discrepancies between data and simulations as shown in Chapter 1. Therefore, many alternative interaction models are being proposed in many years. Each model predicts different cross-section, and the event rates are also different if the different model is used in the simulation. Second, we discuss the alternative interaction models and the difference from the NEUT models, which are studied with the simulated data in Chapter 12. As described in Chapter 6, we fit the data to the simulation at ND280 to reduce the uncertainties of the flux and cross-section. We parameterize the cross-section models based on the NEUT simulation. Finally, we show the parameterization of the interaction models which is used in the near detector fit.

8.1.2 General Description of Neutrino-Nucleus Interaction

Effective Lagrangian

Before going into detail about NEUT interaction models, we explain the general description of the interaction model.

The neutrino-nucleus interaction in NEUT is based on "Impulse Approximation", which means that the cross-section is calculated as the incoherent sum of the interaction probability on each single nucleon (or pair of nucleons) in the nucleus.

The effective Lagrangian density of neutrino-nucleus interaction in Fig. 8.1 is written as follows:

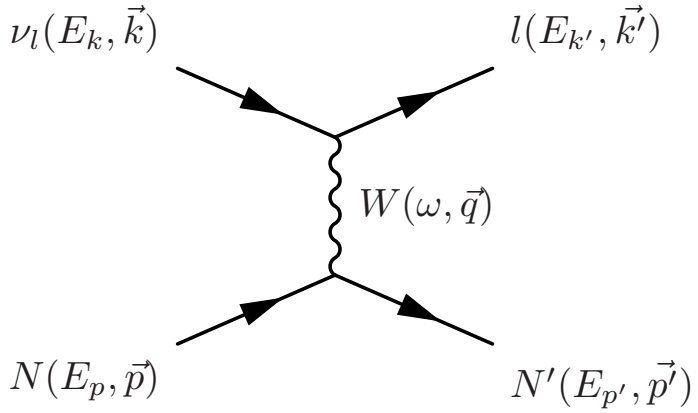

Figure 8.1: Feynman diagrams of Charged current interaction

$$\mathcal{L}_{eff} = \frac{G_F}{\sqrt{2}}(j^{\dagger}_{\lambda}(k,k')J^{\lambda}(p,p') + h.c) \tag{8.1}$$

where j_λ and J_λ are leptonic and hadronic current respectively. The differential cross section is proportional to the product of leptonic and hadronic tensors which are calculated from the leptonic and hadronic current respectively [1].

$$\frac{d\sigma}{dq^2} = \frac{1}{32\pi}\frac{1}{M^2E_\nu^2}G_F^2 c_{EW}^2 L_{\mu\nu}H^{\mu\nu} \tag{8.2}$$

where E_ν is the (anti)neutrino energy in the laboratory frame, M is the nucleon mass, G_F is the Fermi constant and c_{EW} is a constant which is $\cos\theta_c$ in terms of the Cabibbo angle for CC, and $1/4$ for NC.

The leptonic tensor is easy to calculate:

$$L_{\mu\nu} = k_\mu k'_\nu + k'_\mu k_\nu - g_{\mu\nu}(k\cdot k') \pm i\epsilon_{\mu\nu\rho\sigma}k'^{\rho}k^{\sigma} \tag{8.3}$$

where $g_{\mu\nu}$ is Lorentz metric tensor and $\epsilon_{\mu\nu\rho\sigma}$ is Levi-Civita symbol. On the other hand, the hadronic tensor $H^{\mu\nu}$ normally has a complicated form. Thus, the treatment of the hadronic tensor depends on the models, and the cross-section becomes different in each model.

W Boson Self Energy

It is convenient to describe the hadronic tensor as the W-boson self energy as shown in Fig. 8.2a. Figure 8.2b is an example for the W-boson self energy representation. If we cut the diagram at the blue line (dashed line in 8.2a), this diagram is equivalent to the hadronic tensor of the CCQE interaction[2]. The many-body effects are easier to implement to the models by considering the shaded circle in Fig. 8.2a. We will show nuclear effects are described this manner in the latter part.

[1]The cross section is calculated with momentum transfer $q(\omega, \vec{q})$. The momentum transfer is sometimes referred to as $Q^2 = -q^2$.

[2]The CCQE calculated by this framework is referred to as one-particle-one-hole (1p1h)

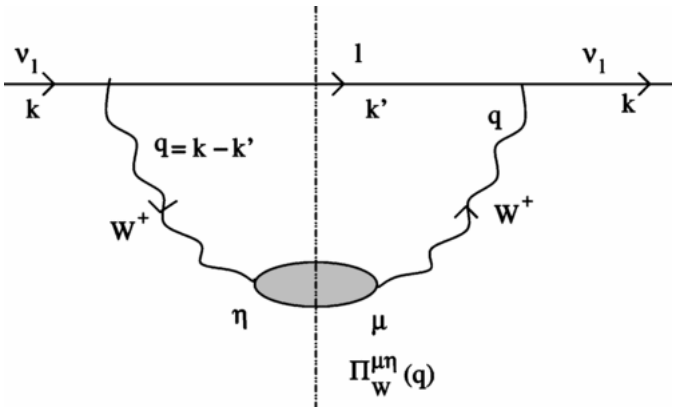

(a) Diagrammatic representation of the neutrino self-energy in nuclear matter. The figure is taken from [167]

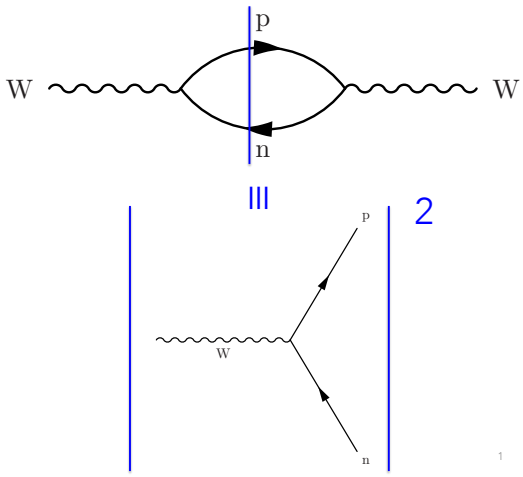

(b) Self energy representation of CCQE.

Figure 8.2: The Feynman diagram of the neutrino nucleus interaction using W-boson self energy

8.2 Neutrino-Nucleus Interaction Models in NEUT

8.2.1 Neutrino-Nucleon Interactions

The Charged Current (CC) neutrino-nucleon interactions are categorized mainly three types: CC quasi-elastic interaction, pion production, where a pion is produced in the final state via resonance, and deep inelastic scattering, where the nucleon is broken into another nucleon and hadrons.

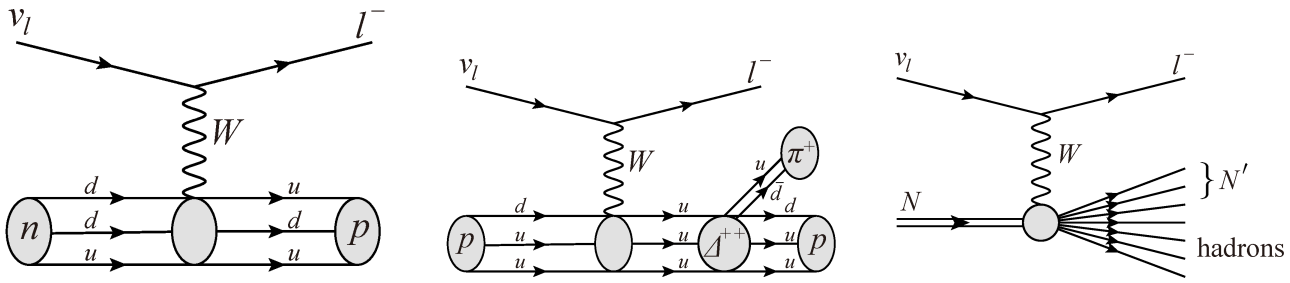

(a) Charged Current Quasi-Elastic Scattering

(b) Charged Current single pion production

(c) Charged Current Deep Inelastic Scattering

Figure 8.3: Feynmann diagrams of Charged Current neutrino-nucleon interaction

Charged Current Quasi-Elastic (CCQE) Scattering Interaction

Llewellyn-Smith formalization [168] is commonly used to describe CCQE interaction.

In this formalization, hadronic current is split into vector and axial vector parts:

$$J^{\lambda}(p,p') = \bar{u}(p')\Gamma^{\lambda}u(p) = V^{\lambda} - A^{\lambda} \tag{8.4}$$

where Γ is a general description of Lorentz invariant current with the combination of p and q. The vector and axial vector parts are given as follows:

$$V^{\lambda} = \bar{u}(p') \left[\gamma^{\lambda} F_V^1(q^2) + \frac{i}{2M} \sigma^{\lambda\mu} q_{\mu} F_V^2(q^2) \right] u(p) \tag{8.5}$$

$$A^{\lambda} = \bar{u}(p') \left[\gamma^{\lambda} \gamma_5 F_A(q^2) + \gamma_5 \frac{q^{\lambda}}{M} F_P(q^2) \right] u(p). \tag{8.6}$$

where $F(q^2)$s are the form factors that include nucleon structure information. These factors are also written by different form factors G_E^p, G_M^p, G_E^n, G_M^n (E and M denote electric and magnetic dipole form factors, n and p denote neutron and proton respectively):

$$F_V^1(q^2) = \left(1 - \frac{q^2}{4M^2}\right)^{-1} \left[(G_E^p(q^2) - G_E^n(q^2)) - \frac{q^2}{4M^2} (G_M^p(q^2) - G_M^n(q^2)) \right] \tag{8.7}$$

$$\xi F_V^2(q^2) = \left(1 - \frac{q^2}{4M^2}\right)^{-1} \left[(G_M^p(q^2) - G_M^n(q^2)) - (G_E^p(q^2) - G_E^n(q^2)) \right] \tag{8.8}$$

where $\xi = 3.71$ is the difference of anomalous dipole moments between a proton and neutron. The form factor $G(q^2)$s can be determined by the electron-nucleus scattering experiment. For the axial vector part, F_P is merged into F_A, according to the Partially Conserved Axial Current (PCAC) hypothesis [169].

$$F_P = \frac{2M^2}{m_{\pi}^2 - q^2} F_A(q^2) \tag{8.9}$$

Using Eq. (8.5) and Eq. (8.6), one gets differential cross section of CCQE interaction:

$$\frac{d\sigma}{dq^2} = \frac{M^2 G_F^2 \cos^2\theta_c}{8\pi E_{\nu}^2} \left[A(q^2) - B(q^2) \frac{s-u}{M^2} + C(q^2) \frac{(s-u)^2}{M^4} \right] \tag{8.10}$$

where, s and u are Mandelstam variables, M is the target nucleon mass, and E_{ν} is the neutrino energy. $A(q^2)$, $B(q^2)$ and $C(q^2)$ are:

$$\begin{aligned} A(q^2) &= \frac{m^2 - q^2}{4M^2} \left[(4 - \frac{q^2}{M^2}) |F_A|^2 - (4 + \frac{q^2}{M^2}) |F_V^1|^2 - \frac{q^2}{M^2} |\xi F_V^2|^2 \left(1 + \frac{q^2}{4M^2}\right) \right. && (8.11) \\ &- \left. \frac{4q^2 F_V^1 \xi F_V^2}{M^2} - \frac{m^2}{M^2} ((F_V^1 + \xi F_V^2)^2 + |F_A|^2) \right] && (8.12) \end{aligned}$$

$$B(q^2) = \frac{q^2}{M^2} ((F_V^1 + \xi F_V^2) F_A) \tag{8.13}$$

$$C(q^2) = \frac{1}{4} \left(|F_A|^2 + |F_V^1|^2 - \frac{q^2}{4M^2} |\xi F_V^2|^2 \right) \tag{8.14}$$

where m is the outgoing lepton mass.

$G(q^2)$s are set as dipole functions with vector mass free parameter $M_V = 0.84$ (GeV/c^2) and determined by electron-nucleon scattering experiments [170].

$$G_E^V(q^2) = \left(1 - \frac{q^2}{M_V^2}\right)^{-2} \tag{8.15}$$

$$G_M^V(q^2) = (1 - \xi) \left(1 - \frac{q^2}{M_V^2}\right)^{-2} \tag{8.16}$$

F_A is assumed to be the same form as F_Vs:

$$F_A(q^2) = F_A(0)\left(1 - \frac{q^2}{M_A^2}\right)^{-2} \tag{8.17}$$

$F_A(0) = 1.267$ is determined by beta decay experiments [171]. The axial vector mass $M_A = 1.06 \pm 0.021$ [172] is determined by neutrino scattering data only.

In NEUT, $M_A = 1.2 \pm 0.03$ is used as a nominal value [3]. It is known from the electron-scattering data that the electromagnetic form factors deviate significantly from the dipole form factor in the $Q^2 > 1$ GeV region. In NEUT, BBBA07 form factor [179] are also implemented.

Charged Current Single Pion Production

Rein-Sehgal model [180] with some modifications is used in the NEUT simulation to predict the single pion production. This model describes the single pion production mediated by a resonance state and the interference with the other nearby resonances with relativistic quark model [181].

In the Rein-Sehgal model, there are three charged current channels as shown in Fig. 8.4:

$$\begin{aligned}
\nu_l + p &\to l^- + p + \pi^+ \\
\nu_l + n &\to l^- + n + \pi^+ \\
\nu_l + n &\to l^- + p + \pi^0
\end{aligned}$$

and four neutral-current channels:

$$\begin{aligned}
\nu_l + p &\to \nu_l + n + \pi^+ \\
\nu_l + p &\to \nu_l + p + \pi^0 \\
\nu_l + n &\to \nu_l + n + \pi^0 \\
\nu_l + n &\to \nu_l + p + \pi^-
\end{aligned}$$

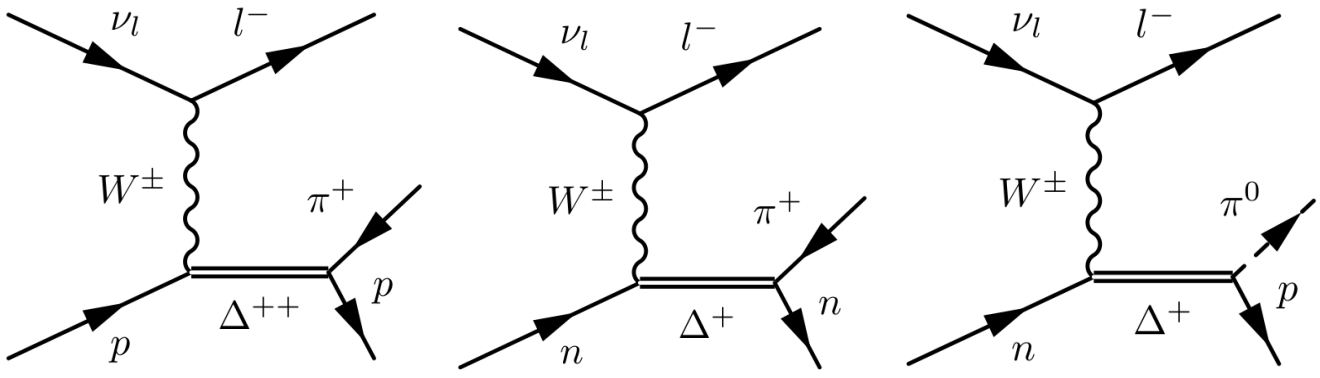

(a) $\nu_l + p \to l^- + p + \pi^+$ (b) $\nu_l + n \to l^- + n + \pi^+$ (c) $\nu_l + n \to l^- + p + \pi^0$

Figure 8.4: Feynman diagrams of Single Pion Production mediated by Δ resonance

The differential cross section for a single resonance with the finite decay width is given:

[3] Recent experiment such as K2K [173, 174], MiniBooNE [175, 176] and MINOS [177] reported large M_A value in the 2010s, which has the discrepancy between NOMAD data [178]. After the improvement of the model (such as 2p2h modeling describes later) the theoretical models agree with the data without enhancing the M_A value.

$$\frac{d\sigma}{dq^2 dW} = \frac{1}{32\pi m_N E_\nu^2}\frac{1}{2}\sum_{spin}|T(\nu N \to lN^*)|^2 \frac{1}{2\pi}\frac{\Gamma}{(W-M)^2+\Gamma/4} \tag{8.18}$$

The calculation of amplitude $|T(\nu N \to lN^*)|^2$ is similar to CCQE one, except its baryon mass and spin state. The double differential cross section of the single meson production in a certain channel is given by the amplitude sum of the production and its decay of all possible resonances. In Rein-Sehgal model, 18 resonances with $W < 2$ GeV are taken into account. The amplitude of each resonance is given by the isospin Clebsch-Gordan rules.

Several modifications were made to improve its modeling. In the Rein-Sehgal model, lepton mass is neglected. The lepton mass effect is corrected based on [182]. The single pion production also depends on the structure of the nucleon similar to the CCQE interaction. In the T2K energy region, $\Delta^{++}(1232)$ is the most dominant state. Therefore, the form factor of $\Delta^{++}(1232)$ resonance is adopted based on a paper of Graczyk-Sobczyk [183] in the NEUT simulation to describe the form factors more accurately. The Graczyk-Sobczyk form factor is given based on Rarita-Schwinger field:

$$F^V(W,q^2) = \frac{1}{2}\left(1-\frac{q^2}{(M+W)^2}\right)^{\frac{1}{2}}\left(1-\frac{q^2}{4M^2}\right)^{-\frac{N}{2}}\sqrt{3(G_V^{f_3}(W,q^2))^2+(G_V^{f_1}(W,q^2))^2} \tag{8.19}$$

with

$$G_V^{f_3}(W,q^2) = \frac{1}{2\sqrt{3}}\left[C_4^V\frac{W^2+q^2-M^2}{2M^2}+C_5^V\frac{W^2-q^2-M^2}{2M^2}+\frac{C_3^V}{M}(W+M)\right] \tag{8.20}$$

$$G_V^{f_1}(W,q^2) = \frac{1}{2\sqrt{3}}\left[C_4^V\frac{W^2+q^2-M^2}{2M^2}+C_5^V\frac{W^2-q^2-M^2}{2M^2}+C_3^V\frac{MW}{(W+M)M-q^2}\right]. \tag{8.21}$$

where M is the mass of the resonant state and W is the hadronic invariant mass. C_3^V, C_4^V and C_5^V are assumed to be dipole form and determined by the electro-pion production [184].

$$C_3^V = 2.13\left(1-\frac{q^2}{4M_V^2}\right)^{-1}\left(1-\frac{q^2}{M_V^2}\right)^{-2} \tag{8.22}$$

$$C_4^V = -1.51\left(1-\frac{q^2}{4M_V^2}\right)^{-1}\left(1-\frac{q^2}{M_V^2}\right)^{-2} \tag{8.23}$$

$$C_5^V = 0.48\left(1-\frac{q^2}{4M_V^2}\right)^{-1}\left(1-\frac{q^2}{0.776M_V^2}\right)^{-2} \tag{8.24}$$

For the axial vector part, it is given:

$$F^A(W,q^2) = \frac{\sqrt{3}}{2}\left(1-\frac{q^2}{(M+W)^2}\right)^{\frac{1}{2}}\left(1-\frac{q^2}{4M^2}\right)^{-\frac{N}{2}}\left[1-\frac{W^2+q^2-M^2}{8M^2}\right]C_5^A(q^2) \tag{8.25}$$

$C_5^A(q^2)$ is assumed to be the dipole form.

$$C_5^A(q^2) = \frac{C_5^A(0)}{\left(1-\frac{q^2}{M_A^2}\right)^2} \tag{8.26}$$

There are also several pion production processes which don't make resonance states as shown in Fig. 8.5. In the Rein-Sehgal model, I=1/2 non resonant part is added incoherently. $P_{11}(1451)$

resonance is taken as non resonant part with Breit-Wigner factor replaced by an adjustable constant[4]. The nominal value of the parameters, $C_5^A(0) = 1.01 \pm 0.12$, $M_A = 0.95 \pm 0.15$ and $I_{1/2} = 1.30 \pm 0.20$ are determined by MiniBooNE [185–187] and K2K [188].

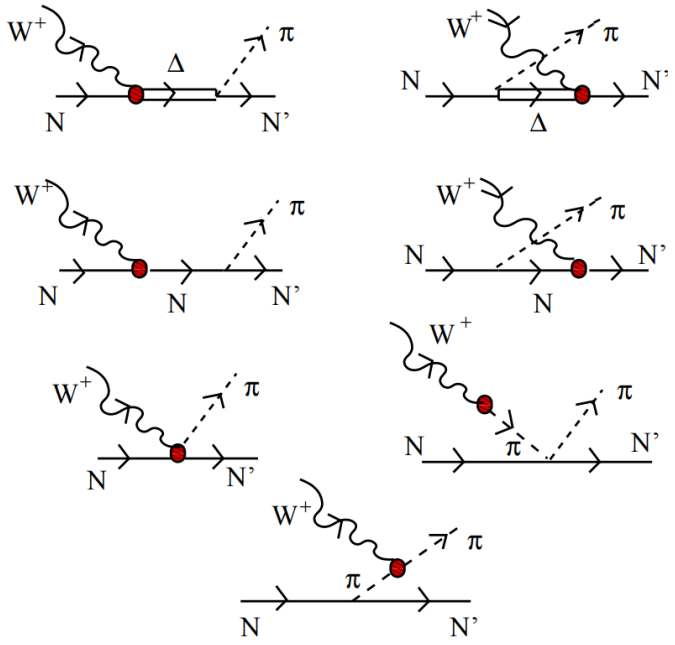

Figure 8.5: Diagrams of the non-resonant contribution for the single pion production. The two plots on the top are the diagrams of resonant pion productions. The figure is taken from [189].

Deep Inelastic Scattering

The double differential cross section for Deep Inelastic Scattering (DIS) is calculated as [190]:

$$\frac{d^2\sigma}{dxdy} = \frac{G_F^2 m_N E_\nu}{\pi}\left[\left(1 - y + \frac{1}{2}y^2 + C_1\right)F_2(x) \pm y\left(1 - \frac{1}{2}y + C_2\right)xF_3(x)\right] \tag{8.27}$$

$$C_1 = \frac{m_l^2(y-2)}{4m_N E_\nu x} - \frac{m_N xy}{2E_\nu} - \frac{m_l^2}{4E_\nu^2} \tag{8.28}$$

$$C_2 = -\frac{m_l^2}{4m_N E_\nu x} \tag{8.29}$$

where $x \equiv -q^2/(2m_N(E_\nu - E_l)) + m_N^2$ and $y \equiv (E_\nu - E_l/E_\nu)$ are the Bjorken scaling parameters. The Parton Distribution Function (PDF) $F_2(x)$ and $xF_3(x)$ are determined by GRV98 PDF [191] modified by Bodek and Yang [192]. The events where the number of pions is equal to one with $W < 2$ GeV are subtracted to avoid double counting by using multiplicity function. Above 2 GeV NEUT uses PYTHIA generators [193]. Multiplicity is determined based on the experimental result [194].

Coherent Pion Production

Coherent pion production interaction is a process in which a neutrino scatters off a nucleus, producing a pion without exciting the nucleus (Fig. 8.6). NEUT uses the Rein-Sehgal model [195], which is

[4]We refer to this non-resonant contribution as "background"

known to overestimate the cross section as shown in Fig. 8.7. We also implemented the Barger-Sehgal model in NEUT [196] which has a better agreement with the MINERνA experiment [197]. We apply the weighting factor to the NEUT Rein-Sehgal model so that the lepton kinematics get close to the Barger-Sehgal model.

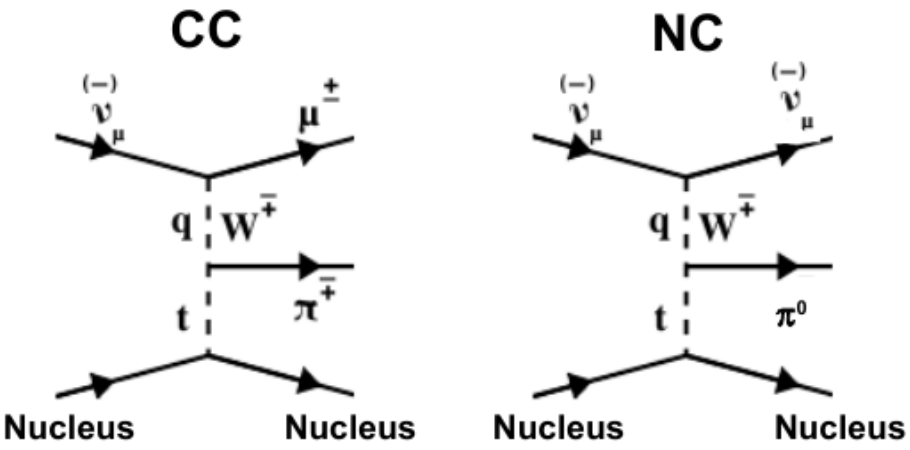

Figure 8.6: Feynman diagrams of Coherent Pion Production

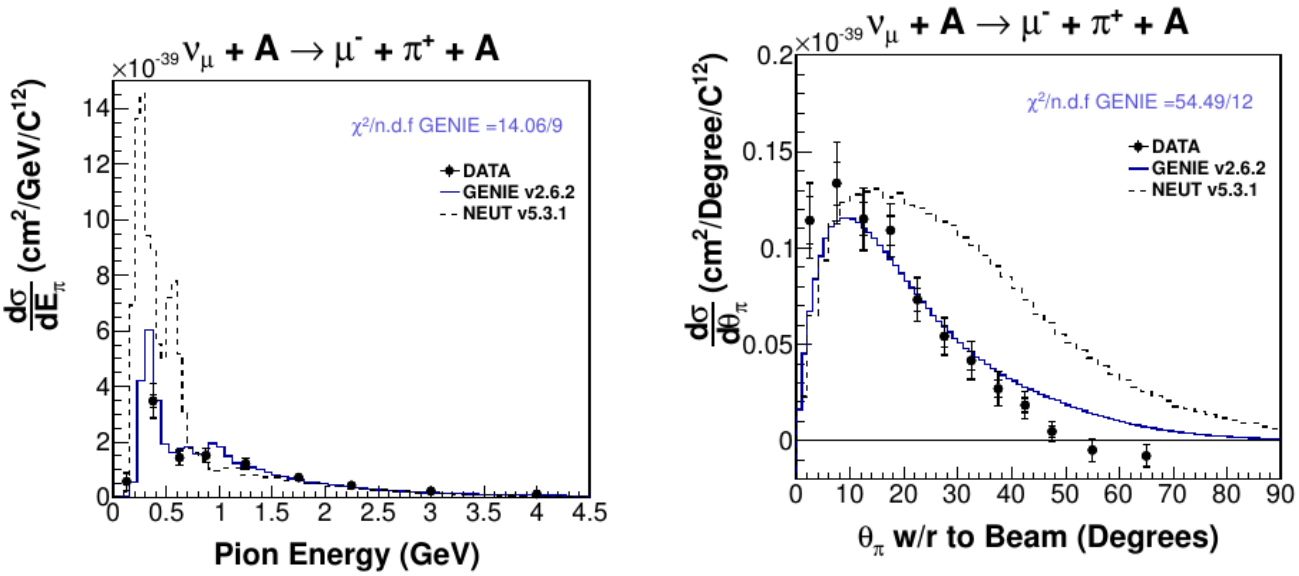

(a) pion momentum

(b) pion angle with respect to the beam

Figure 8.7: Pion momentum and angle distributions of the Coherent pion production measured by MINERνA [197]

Neutral Current Interaction

NC interactions are described by the same framework as charged current one except its coefficient. It is difficult to measure NC interaction in ND280 since the observed particles are only scattered

nucleon and pion or de-excitation γ [5]. On the other hand, NC interactions are one of the main backgrounds for Super-Kamiokande. For ν_e selection, NC π^0 production events where pion decays into 2γ can be mis-reconstructed as one electron-like ring, if the one ring is missing or merged into the other ring. For ν_μ selection, π^+ produced by NC single pion production is misidentified as μ like track.

8.2.2 Nuclear Effects

We mainly describe the neutrino-nucleon interaction so far. However, various target nuclei such as Argon, Carbon, Oxygen are used in neutrino experiments. The interaction model should be modified to describe the nuclear effects.

Relativistic Fermi Gas Model (Smith-Moniz model)

In NEUT, Smith-Moniz [198] model is adopted to apply the effects of the Fermi momentum, the Pauli blocking and the binding energy. In this model, they assume the hadronic current is obtained by the sum of the individual nucleon current:

$$J^\mu(p,p') = \sum_{\mathbf{p},\mathbf{p}',\lambda,\lambda'} a^\dagger_{\mathbf{p}'\lambda'} < \mathbf{p}'\lambda'|J^\mu_{nucleon}|\mathbf{p}\lambda > a_{\mathbf{p},\lambda} \tag{8.30}$$

We describe the target state as a superposition of non-interacting neutron and proton Fermi gases with momentum distributions $n_n(k)$ and $n_p(k)$ respectively. Hadronic tensor is given:

$$(W_{\mu\nu})_{lab} = \int d\mathbf{p} f(\mathbf{p},\mathbf{q},\omega) T_{\mu\nu} \tag{8.31}$$

$T_{\mu\nu}$ is the hadronic tensor of single nucleon. The scaling factor $f(\mathbf{p},\mathbf{q},\omega)$ describes the effects of Fermi momentum and Pauli-blocking.

$$f(\mathbf{p},\mathbf{q},\omega) = \frac{m_T}{(2\pi)^3} \frac{\delta(E_p - E_{p-q} + \omega) n_i(p)(1 - n_f(|\mathbf{p}-\mathbf{q}|))}{E_p E_{k-q}} \tag{8.32}$$

$(1 - n_f(|\mathbf{p}-\mathbf{q}|))$ term corresponds to the Pauli-Blocking effects. E_p is given:

$$E_p = \sqrt{\mathbf{p}^2 + M_N} - E_B \tag{8.33}$$

where E_B is referred to as the binding energy.

In the Relativistic Fermi Gas (RFG) model, the Fermi momentum is given assuming constant nuclear density:

$$p_F = \left(\frac{9\pi Z}{4A}\right)^{1/3} \frac{\hbar}{r_0}. \tag{8.34}$$

In this case, $n_i(p)$ takes a simple form

$$n_i(p) = \theta(p_F - |p|) \tag{8.35}$$

where the θ is a step function.

The RFG modifies the lepton kinematics at low momentum region.

[5] P0D detector is motivated to measure NC interaction. However, the P0D analysis is not used in the oscillation analysis yet.

Random Phase Approximation

From β decay experiments in early 1970s, the large quenching of axial vector part contribution was well established. This effect is implemented as Random Phase Approximation (RPA) of long range nucleus-nucleus correlation diagrammatically described in Fig. 8.8. RPA is adapted in recent models [167, 199] of the neutrino-nucleus interaction to describe the collective effects due to the interactions and correlations of the nucleons inside the nucleus.

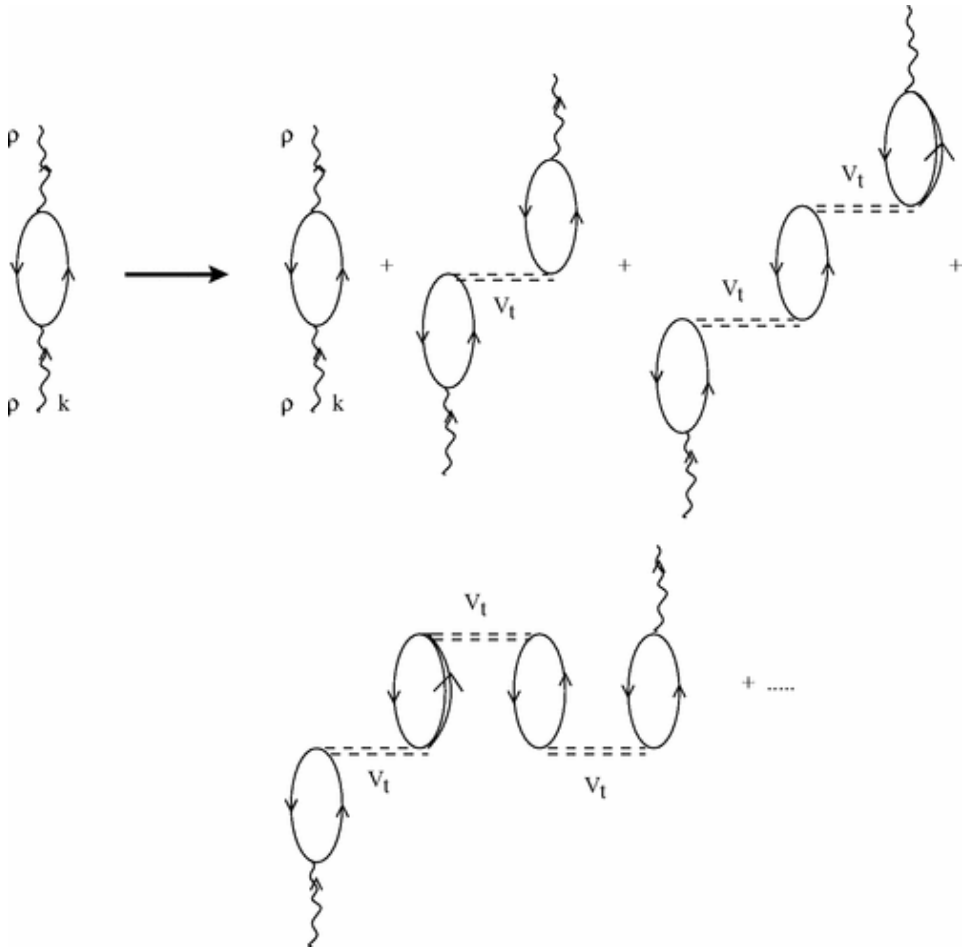

Figure 8.8: Feynman Diagrams of RPA series. Taken from [189].

In NEUT, calculations by Nieves et al. [167] is used. RPA effects are implemented as the weighting factor to the bare CCQE interaction as a function of q^2 (Eq. (8.36)) as shown in Fig. 8.9. RPA suppresses the cross-section at low Q^2.

$$f_{RPA}(q^2) = \frac{\sigma_{RPA,CCQE}(q^2)}{\sigma_{noRPA,CCQE}(q^2)} \tag{8.36}$$

Multi-Nucleon Correlation

It is pointed out that the "CCQE-like" such as two-particle-two-hole (2p2h) state contributes to the CCQE cross section measurement when the associated protons are not observed [199]. The 2p2h is an interaction where correlated two nucleons participate the interaction via pion exchange and nucleon-nucleon correlation as shown in Fig. 8.10. The 2p2h is estimated about 10% contribution to the CCQE interaction. In NEUT, the 2p2h calculation by Nieves et al. [189] is implemented. Considering all contribution 1p1h + RPA + 2p2h, the model has a good agreement with the experimental results [200].

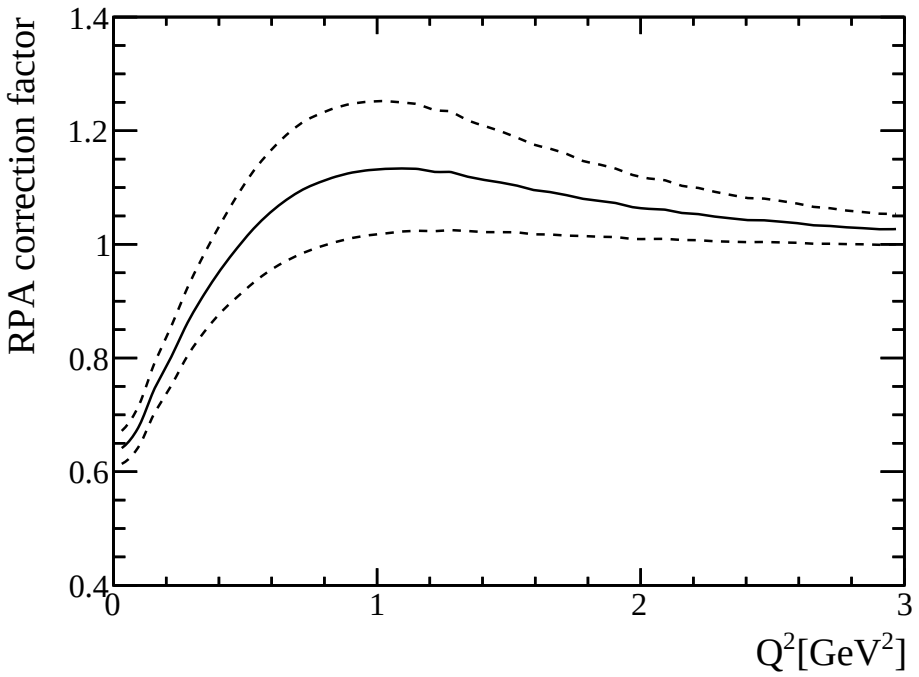

Figure 8.9: RPA factors calculated by the models by Nieves et al. Solid line corresponds to nominal value and dashed lines show the 1σ error

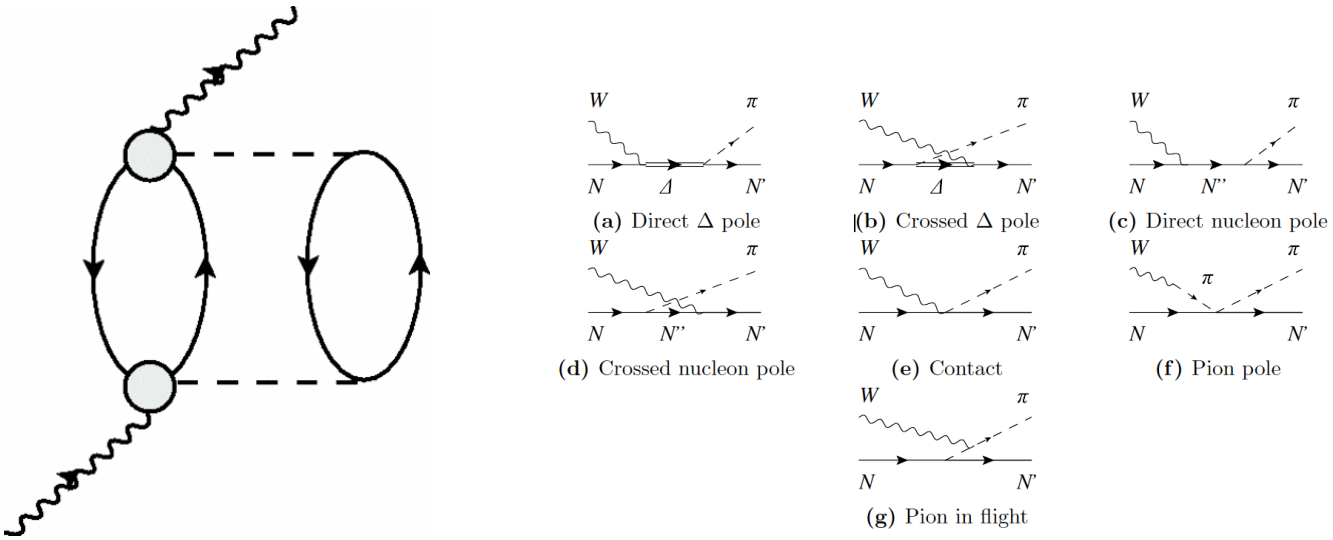

Figure 8.10: Left: W self energy of 2p2h. Wave lines correspond to W, solid lines correspond to nucleons and dashed lines correspond to pions. Right: Contributions in the circle in the left plot. Taken from [189].

Final State Interaction and Secondary Interaction

The leptons and hadrons from neutrino interaction with nuclear targets must propagate through the nuclear medium before they are observed. The final state hadrons are therefore affected largely by these nuclear effects. These effects are called Final State Interaction (FSI). Furthermore, the outgoing particles after FSI also interact with the detector materials before they are observed. This is referred to as Secondary Interaction (SI).

The most striking effects for T2K are absorption, scattering and charge exchange of pion in the nucleus. If the pion produced by the single pion production is absorbed, the event is misidentified as the CCQE interaction. The kinematics of the outgoing pion is affected by the pion scattering, changing the efficiency of the pion identification. Finally, pion charge exchange processes affect the rate of π^0 production, which is an important background for the ν_e appearance.

In NEUT simulation, the cascade model [201] is adopted to describe both FSI and SI interactions. The particles are treated as classical objects moving inside the nucleus (detector). Pions travel in the nucleus (detector) with random impact parameter, and the interaction probability is calculated step by step until the pions are absorbed or its position exceeds the effective radius of nucleus (detector). For pion momentum less than 500 MeV/c, momentum and density dependence of the mean free path (MFP) is calculated based on the Delta-hole model by Oset et al. [201]. For higher momentum, MFP is calculated from free π-p scattering data from PDG [202].

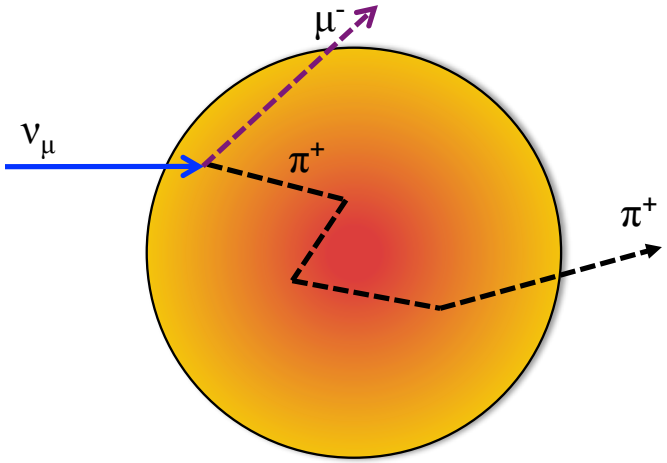

Figure 8.11: Graphical representation of the Intra-Nuclear cascade model

8.3 Alternative Interaction Models

8.3.1 Local Fermi Gas Model and Spectral Function

Local Fermi Gas Model

Local Fermi gas model (LFG) is an extension of the relativistic Fermi gas model to describe the Fermi-gas picture based on local density approximation. The global Fermi gas model assumes the constant nuclear density while LFG uses the nuclear density $\rho(r)$ measured by electron scattering data.

$$p_F(r) = \hbar \left(3\pi^2 \rho(r) \frac{Z}{A} \right)^{1/3} \tag{8.37}$$

This model modifies the initial nucleon momentum in the nucleus as shown in Fig. 8.12a

Spectral Function

The spectral function (SF) describes a distribution of momenta and removal energies of nucleons inside nucleus. Eq. (8.32) is the spectral function for RFG case. Benhar et al. calculated the spectral function for more realistic case [203]. Figure 8.12b shows the energy and momentum distribution of the nucleons in the nucleus. In NEUT, the spectral function calculated by Benhar et al. are implemented.

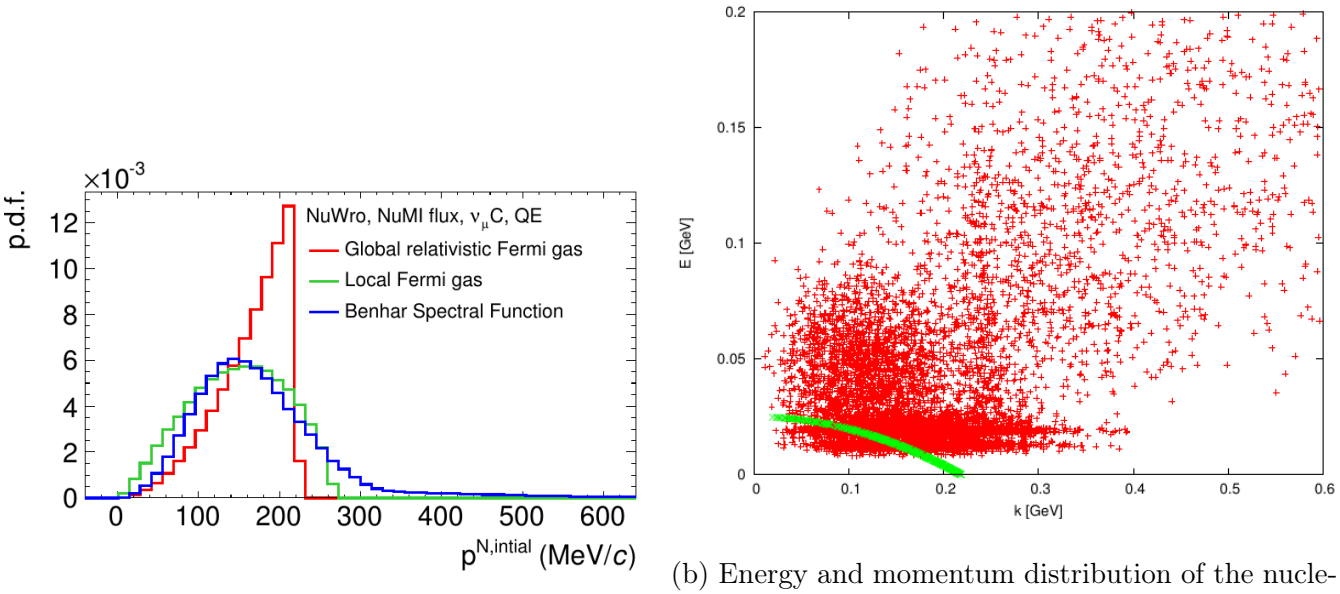

(a) Initial momentum distribution of the nucleon in a carbon nucleus taken from [204]

(b) Energy and momentum distribution of the nucleons inside the nucleus for SF (red) and LFG (green) taken from [205]

Figure 8.12: Alternative Fermi gas model

The LFG model includes correlations between the initial nucleons which account for about 10% of the total cross-section, increasing the tail of the neutrino interaction cross-section at high transferred energy. SF in turn suppresses the cross-section for small transferred energy, suppressing the total integrated cross-section by 5-10% with respect to the Fermi gas model.

8.3.2 Alternative Form Factors

NEUT uses the dipole form factors for the CCQE interaction as described Eq. (8.17). The parameters of the axial form factor are determined by bubble chamber experiments ANL [206, 207], BNL [208], FNAL [209] and BEBC [210]. With these data, a tight constraint is obtained on the form factor at low-Q^2, however this tight constraint is propagated to the high-Q^2 region where the data is sparse due to the limited shape freedom in the model [211, 212]. To describe the uncertainties at high Q^2 correctly, alternative models for the axial form factors are implemented and tuned to the bubble chamber data.

3-Component Form Factor

The 2-component model has been introduced in [213] to describe the pion electro-production.

$$F_A(Q^2) = \left[(1+\gamma Q^2)^{-2} \times \left(1-\alpha+\alpha\frac{m_a^2}{m_a^2+Q^2}\right)\right] \tag{8.38}$$

where γ is a free parameter which represents the contribution from quark core of the nucleon, free parameter α represents the contribution from the axial meson quark-antiquark cloud, and m_a is the mass of the lightest axial meson (m_a = 1.230 GeV). This 2-component form factor cannot cover the high-Q^2 region of the bubble chamber data, the 3-component model was therefore created to provide additional shape freedom by extending the 2-component model with an additional exponential term:

$$F_A(Q^2) = \left[(1+\gamma Q^2)^{-2} \times \left(1-\alpha+\alpha\frac{m_a^2}{m_a^2+Q^2}\right)\right] + \left[\theta' Q^2 e^{-\beta Q^2}\right] \tag{8.39}$$

$$\theta' = sign(\theta)\sqrt{|\theta|\beta}. \tag{8.40}$$

where θ β are the free parameters.

z-Expansion Form Factor

The z-expansion is a model-independent parameterization based on QCD sum rules introduced in [214]. The form factor is given as a power of series of z:

$$F_A(z) = \sum_{k=0}^{N} a_k z^k \tag{8.41}$$

The z is defined as:

$$z = \frac{\sqrt{t_c+Q^2}-\sqrt{t_c-t_0}}{\sqrt{t_c+Q^2}+\sqrt{t_c-t_0}} \tag{8.42}$$

where $t_c = 9\ m_\pi^2$, t_0 = -0.280 GeV^2 and a_k are free parameters to be determined from fits to neutrino scattering data. We consider the series up to N = 8 and a_5, a_6, a_7, a_8 are set as functions of a_1, a_2, a_3, a_4. Thus, only four free parameters are considered in the fit.

The parameters in the model are determined by the fit to the bubble chamber data. Figure 8.13 shows the comparisons between the dipole form factor and alternative form factors. In both models, the uncertainties at high Q^2 are well modeled compare with the dipole form factor.

8.3.3 Improved Single Pion Production Model

In the Rein-Sehgal model, the I = 1/2 non-resonant background is not correctly calculated. Furthermore, the interference between resonance and non-resonance was not taken into account.

Monireh Kabirnezhad treated the non-resonant background more precisely [215] based on [216]. The modifications such as lepton mass correction [182] and Graczyk-Sobczyk form factor [183] in the NEUT simulation are also considered in her model. Her calculation enables us to describe more correct pion kinematics than the Rein-Sehgal model as shown in Fig. 8.14.

8.3.4 Alternative Multi-Nucleon Interaction Model : Martini Model

Martini et al. [199] also calculated "CCQE-like" interaction with 1p1h + RPA + 2p2h framework. The CCQE cross section is almost same as Nieves et al, while, the model by Martini et al. has about two times larger 2p2h contribution than the model by Nieves et al as shown in Fig. 8.15.

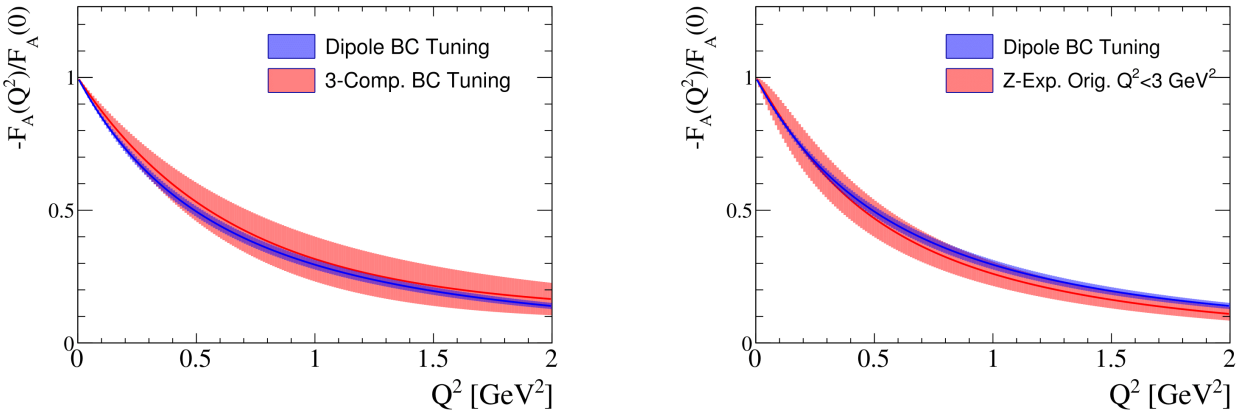

(a) 3-compoment model

(b) z-expansion model

Figure 8.13: Comparison between the dipole form factor and the alternative form factors. "BC" means that the parameters are tuned with bubble chamber data. The red band corresponds to the 1σ error.

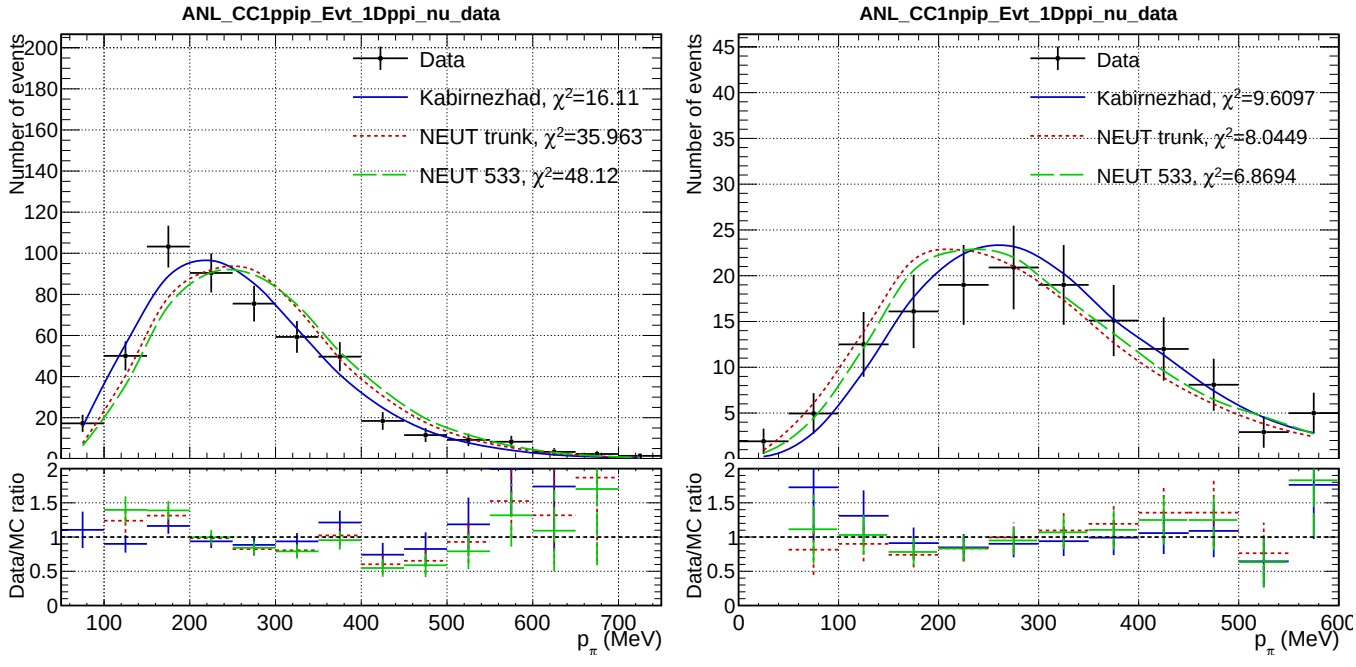

(a) $\nu + p \to \mu + \pi^+ + p$

(b) $\nu + n \to \mu + \pi^0 + p$

Figure 8.14: Pion momentum distributions of the ANL experiment and predictions by the NEUT Rein-Sehgal model and the Kabirnezhad model [217].

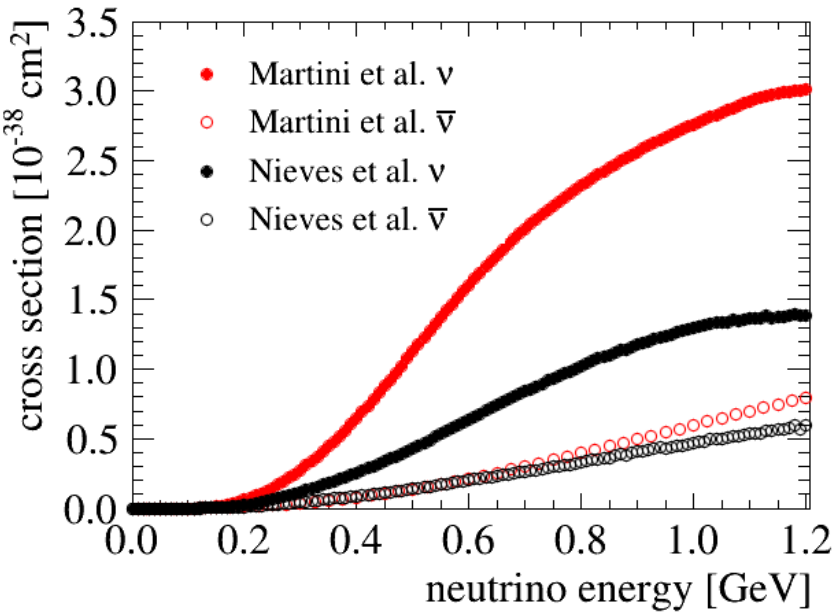

Figure 8.15: 2p2h cross-section Comparisons between the model by Nieves et al and by Martini et al

However, neither the ND280 data, nor the external data are sensitive enough to constrain the 2p2h contribution separately from the CCQE-1p1h contribution, and there are still large theoretical uncertainties on the 2p2h modeling.

8.3.5 Nieves 1p1h and NEUT CCQE Difference

Nieves et al. calculation of 1p1h cross-section uses different parameter values and different calculation framework from that of NEUT [218]. Therefore, the model by Nieves and NEUT predict different cross section. Nieves et al. evaluates the binding energy from the different excitation level (ΔE) of the nucleus before and after the nucleon ejection, thus giving a very different value with respect our reference model in NEUT. The difference is summarized in Table 8.1. This difference is taken into account as an additional systematic uncertainty in the near detector fit described in Chapter 9.

Table 8.1: The Parameter differences between NEUT CCQE and Nieves 1p1h calculation

Model	Fermi gas model	Binding energy of C ($\nu/\bar{\nu}$)	Binding energy of O ($\nu/\bar{\nu}$)
NEUT	RFG	25/25 MeV	27/27 MeV
Nieves	LFG	$\Delta E \sim$ 16.5/14 MeV	$\Delta E \sim$ 15.5/12.5 MeV

8.4 Parameterization of the Neutrino-Nucleus Cross-Section

8.4.1 Parameterization

We set 32 interaction parameters in the near detector fit. The prior values of these parameters are summarized in Table 8.2. We generated the response function for each parameter with the NEUT

simulation.

CCQE Interaction

We parameterized the three parameters for the CCQE interaction and five parameters for the RPA correction. To account for the nuclear effects in the different target nucleus, we set different parameters for Carbon and Oxygen, which are the main target nucleus in ND280 and Super-Kamiokande, respectively. We set:

- M_{QE}^{A} : Parameter for the axial vector form factor.
- $p_F C$,$p_F O$: Fermi momentum parameters for the Smith-Moniz model (C:Carbon, O:Oxygen).

In the Smith-Moniz model, the binding energy parameters are also required in addition to the Fermi momentum. However, we found the response of the binding energy parameter was not correctly implemented. Figure 8.16 shows the CCQE muon angle with respect to the beam direction $\cos\theta$ ratio generated by NEUT to that reweighted by response function used in the near detector fit corresponding to each binding energy. At the high angle region, there are large discrepancies, which indicates that the binding energy makes a bias on the near detector fit. Therefore, we decided not to use the binding energy parameters in the near detector fit in this analysis.

Instead of this, we investigated the effects on the oscillation fit for these parameters with simulated data study as discussed in Chapter 12.

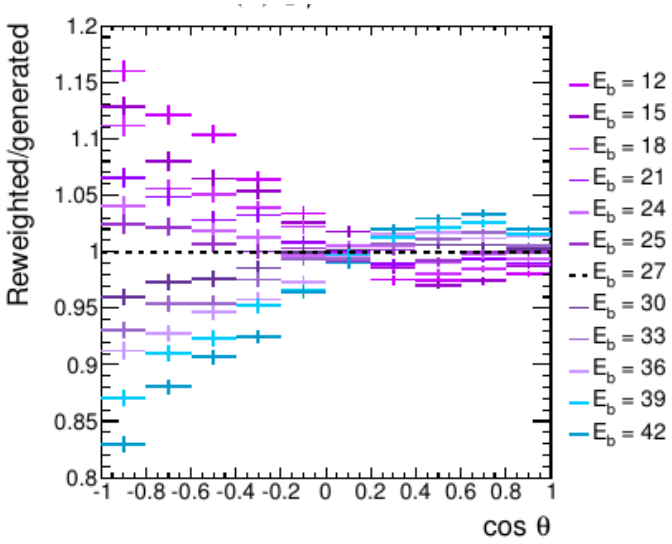

Figure 8.16: The ratio of the nominal to reweighted distributions with various energy parameters

For the RPA correction, we implemented the correction as the weighting factor for the CCQE interaction. We set an arbitrary function and parameters which covers the Nieves RPA calculation [167]. We defined the RPA parameterization based on the Bernstein function as follows (named "BeRPA") [219]:

$$f(Q^2) = \begin{cases} A(1-x')^3 + B(1-x)^2x' + p_1(1-x')x'^2 + Cx'^3 & x < U \\ 1 + p_2\exp(-D(x-U)) & x > U \end{cases} \tag{8.43}$$

where $x = Q^2/U$. p_1 and p_2 are set to keep the continuity condition at U.

Table 8.2: Parameters and relevant values of the near detector fit. Parameter 13 (BeRPA U) is fixed in fits.

Index	Parameter	Prior Mean	Error	Lower Bound	Upper Bound	norm/shape
1	M_A^{QE}	1.20	0.03	0.00	9999.00	norm. & shape
2	p_F C	217.00	13.00	0.92 (200)	1.27 (275)	norm. & shape
3	p_F O	225.00	13.00	0.89 (200)	1.22 (275)	norm. & shape
4	2p-2h norm ν	1.00	1.00	0.00	9999.00	norm.
5	2p-2h norm $\bar{\nu}$	1.00	1.00	0.00	9999.00	norm.
6	2p-2h norm C to O	1.00	0.20	0.00	9999.00	norm.
7	2p-2h shape C	0.00	3.00	-1.00	1.00	shape
8	2p-2h shape O	0.00	3.00	-1.00	1.00	shape
9	BeRPA A	0.59	0.12	0.00	9999.00	norm. & shape
10	BeRPA B	1.05	0.21	0.00	9999.00	norm. & shape
11	BeRPA D	1.13	0.17	0.00	9999.00	norm. & shape
12	BeRPA E	0.88	0.35	0.00	9999.00	norm. & shape
13	BeRPA U	1.20	0.10	0.00	9999.00	norm. & shape
14	CA5	0.96	0.15	0.00	9999.00	norm. & shape
15	M_A^{RES}	1.07	0.15	0.00	9999.00	norm. & shape
16	ISO BKG	0.96	0.40	0.00	9999.00	norm.
17	ν_e/ν_μ	1.00	0.03	0.00	9999.00	norm.
18	$\bar{\nu_e}/\bar{\nu_\mu}$	1.00	0.03	0.00	9999.00	norm.
19	CC DIS	0.00	0.40	-9999.00	9999.00	norm.
20	CC Coherent C	1.00	0.30	0.00	9999.00	norm.
21	CC Coherent O	1.00	0.30	0.00	9999.00	norm.
22	NC Coh	1.00	0.30	0.00	9999.00	norm.
23	NC 1γ	1.00	1.00	0.00	9999.00	norm.
24	NC other near	1.00	0.30	0.00	9999.00	norm.
25	NC other far	1.00	0.30	0.00	9999.00	norm.
26	FSI Inelastic LO	0.00	0.41	-9999.00	9999.00	norm.
27	FSI Inelastic HI	0.00	0.34	-9999.00	9999.00	norm.
28	FSI PI PROD	0.00	0.50	-9999.00	9999.00	norm.
29	FSI PI ABS	0.00	0.41	-9999.00	9999.00	norm.
30	FSI Charge Exchange LO	0.00	0.57	-9999.00	9999.00	norm.
31	FSI Charge Exchange HI	0.00	0.28	-9999.00	9999.00	norm.

$$p_1 = C + \frac{UD(C-1)}{3} \tag{8.44}$$

$$p_2 = C - 1 \tag{8.45}$$

We used A,B,D,E as free parameters in the near detector fit. U is fixed to avoid unnecessary correlation. The initial values and errors of these parameters are determined by the fit to the Nieves RPA calculation. The fit results and their uncertainties are shown in Fig. 8.17. The error of each parameter is shown in Appendix C.

- BeRPA A
- BeRPA B
- BeRPA D
- BeRPA E

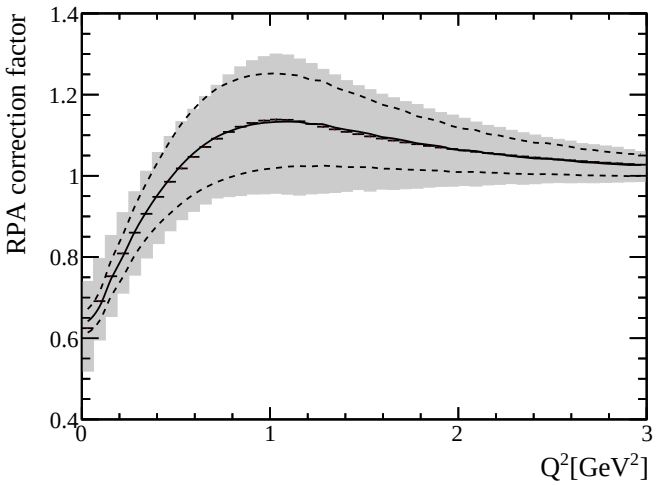

Figure 8.17: RPA factors calculated by Nieves and their uncertainties. Solid black line corresponds to the Nieves RPA, and dotted lines are the 1σ uncertainties. The horizontal lines are the center value of BeRPA, and shaded region is the 1σ uncertainties of BeRPA

2p2h Interaction

We parameterized the 2p2h interactions with five parameters. The 2p2h interaction is kinematically separated into two parts. Figure 8.18 shows the $\omega - |\vec{q}|$ distribution for the CCQE and the single pion production, and 2p2h [220]. The ω is the 0th component of the momentum transfer, and $|\vec{q}|$ is the norm of the three momentum transfer. When the 2p2h interaction is Pion-less Delta Decay-like (PDD-like) (MEC in the figure), the reconstruction energy difference is largely shifted toward lower value as shown in Fig. 8.19a since the momentum transfer is similar to the single pion production. On the other hand, the energy deviation is small in the non PDD-like (NN region in the figure) case, since the momentum transfer is similar to CCQE. Therefore, the energy reconstruction of 2p2h changes depending on the amount of PDD-like 2p2h.

As described in Section 8.3, there are several 2p2h models by Martini and Nieves. They calculated the same physics process, however, the 2p2h cross-section is different by factor two. To cover the

Martini and Nieves model difference, we split the 2p2h parameters into a normalization parameter which changes the number of events and a shape parameter which changes the energy dependency. Figure 8.19b shows the reconstructed energy - true energy dependence of the 2p2h shape parameter. For the normalization parameters, we set five parameters considering the target nucleus, neutrino-antineutrino difference.

- 2p2h norm ν, 2p2h norm $\bar{\nu}$, 2p2h norm C to O : normalization parameters for ν and $\bar{\nu}$ and ratio Carbon to Oxygen.
- 2p2h shape C, 2p2h shape O : 2p2h shape parameters for C and O.

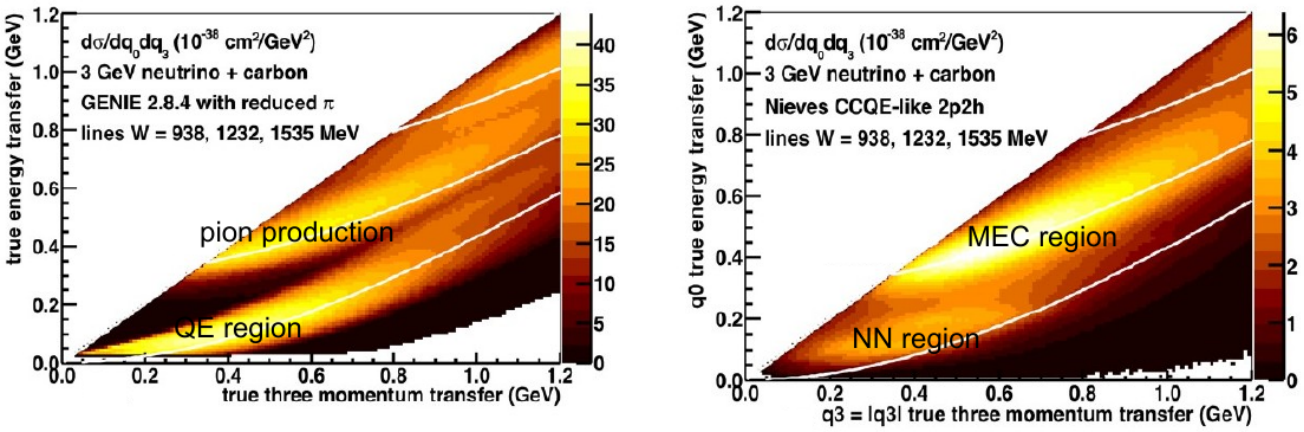

Figure 8.18: $\omega - |\vec{q}|$ distribution for Left: CCQE and single pion production, Right: 2p2h interaction [221].

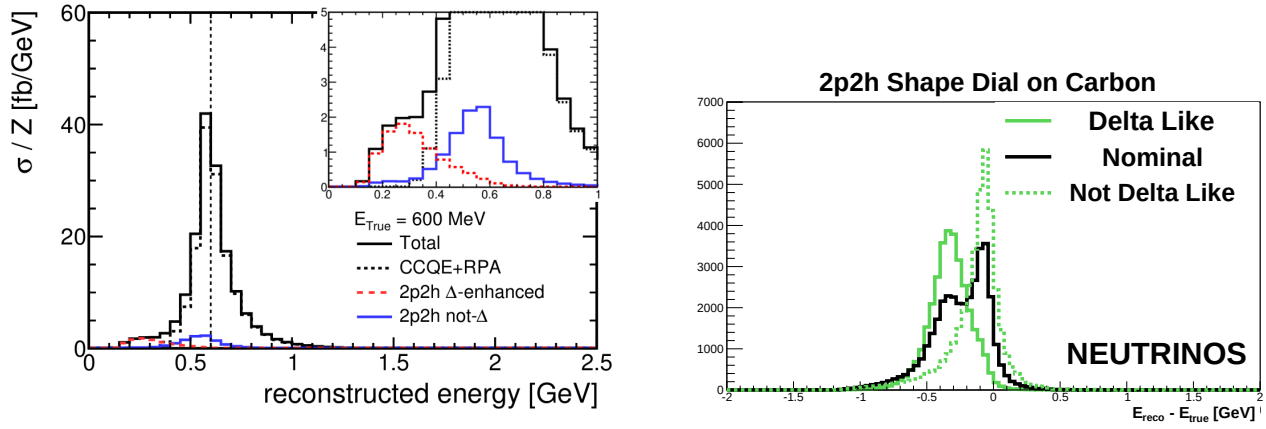

(a) Reconstructed energy dependence of 2p2h

(b) Response of the 2p2h shape parameter

Figure 8.19: Effects of the 2p2h on the energy reconstruction.

CC Single Pion Interaction

We parameterized CC single pion production with three parameters. Two of them (M_A^{res}, $C_5^A(0)$) are related to the form factor as described in Eq. (8.25), and the rest is the normalization parameter for the non-resonant background.

- M_A^{res}: Axial vector mass for the single pion production
- $C_5^A(0)$: Form factor parameter for the single pion production
- ISO BKG : Normalization of the non-resonant background

The prior values are slightly different from NEUT nominal values. The nominal NEUT values are determined by the cross-section measurement with respect to the neutrino energy. To obtain the parameter values determined by the lepton kinematics, we tuned the parameters with ANL [222,223], BNL [224–226] and MiniBooNE [185].

Difference Between ν_μ and ν_e

Difference between neutrino species is not precisely known. Since the outgoing lepton mass is different, it may affect the available phase space for the interaction, and the cross-section may change. Furthermore, mass difference effects get convoluted with the nucleon form factors and with the nuclear response functions which in turn have large and not well known uncertainties, therefore, the nucleon and nuclear effect may also have different effects on ν_e and ν_μ in principle. Therefore, we introduced two normalization parameters to cover the difference.

- ν_e/ν_μ: normalization ratio between ν_e and ν_μ
- $\bar{\nu}_e/\bar{\nu}_\mu$: normalization ratio between $\bar{\nu}_e$ and $\bar{\nu}_\mu$.

DIS and the Other Interaction

We set one normalization parameter for DIS. For CC-Coherent interaction, we also set normalization parameters for Carbon and Oxygen. For NC interactions, we set four normalization parameters, which are not used in the near detector fit but used for the oscillation analysis in Super-Kamiokande.

- DIS : DIS normalization
- CC Coherent C, CC Coherent O : Normalization of CC Coherent pion production.
- NC Coh : normalization of NC Coherent pion production
- NC 1γ : normalization of NC 1γ
- NC other near, NC other far: normalization of the other NC processes

FSI

The FSI is parameterized by six scale factors. Each parameter scales the corresponding microscopic probability of π interaction at each step, except for charge exchange interaction, which scales the charge exchange fraction of the low momentum CCQE scattering. We consider following parameters for FSI.

- FSI Inelastic LO : QE scattering (Low energy)
- FSI Inelastic HI : QE scattering (High energy)
- FSI PI PROD : Pion production
- FSI PI ABS : Pion Absorption

- FSI Charge Exchange LO : Single charge exchange (Low energy)
- FSI Charge Exchange HI : Single charge exchange (High energy)

We set different parameters for the QE scattering and the charge exchange. We have developed the response function for ND280 but not for Super-Kamiokande. Therefore, we treated FSI effects differently for ND280 and Super-Kamiokande. We used the FSI parameters in the fit in ND280, while we generated a covariance matrix relating the number of events in each bin and added in the Super-Kamiokande covariance matrix for the detector uncertainties. The detail is described in Chapter 10.

8.4.2 Covariance Matrix for the Neutrino-Nucleus Interaction Parameters

The covariance matrix for the interaction parameters is shown Fig. 8.20. The correlation between parameters are estimated by the external data. We will use this matrix in the near detector fit.

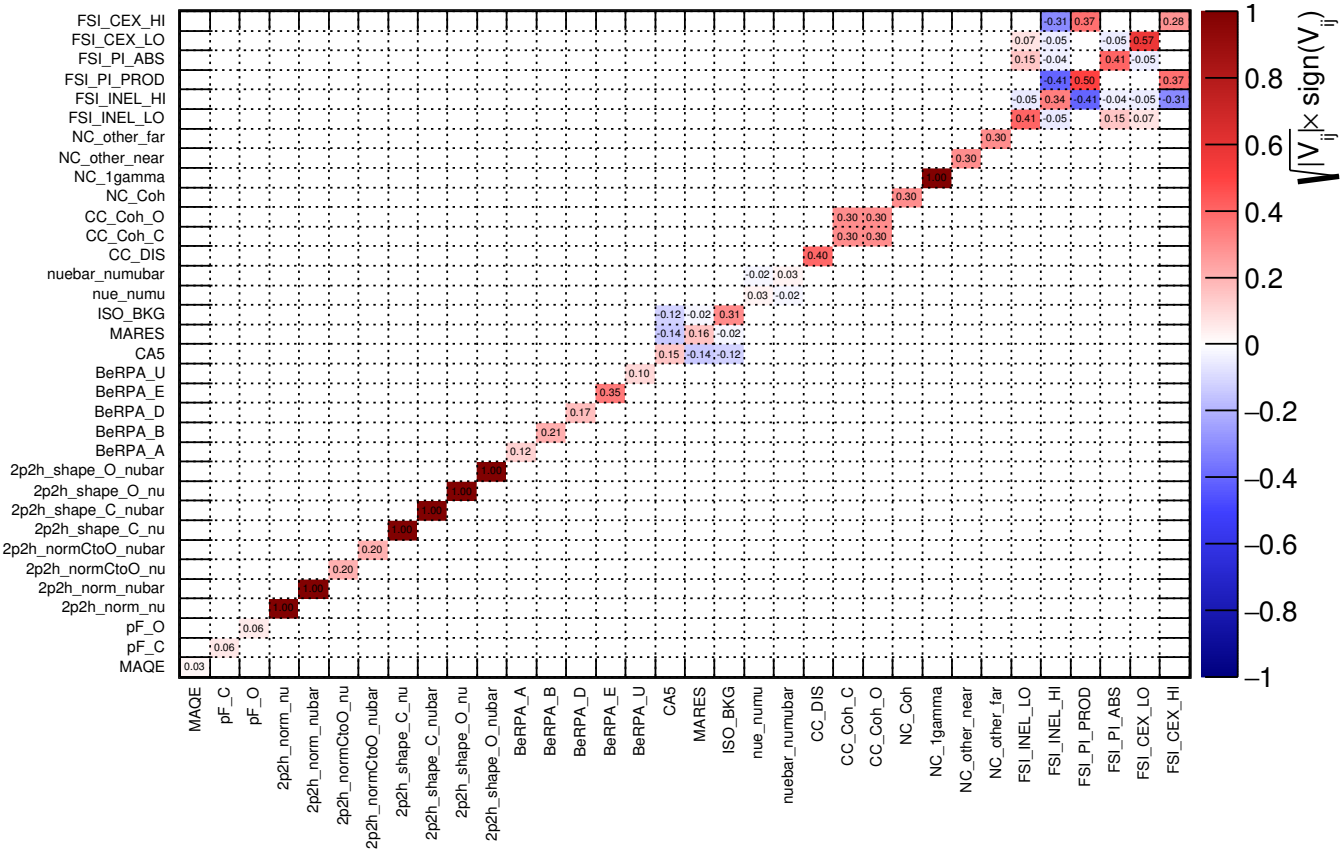

Figure 8.20: Covariance matrix of the interaction parameters

Chapter 9

Near Detector Fit

As mentioned in Chapter 6, the flux and cross-section parameters are constrained by the simulation fit to the data in ND280. The constrained parameters are then propagated to Super-Kamiokande to predict energy spectrum. In this chapter, we summarize the near detector analysis for the oscillation analysis.

9.1 Overview of the Near Detector Fit

The near detector log-likelihood Eq. (6.5) is again written here:

$$\ln \mathcal{L}(\vec{b},\vec{x}|M_{ND}) = \ln P(M_{ND}|\vec{b},\vec{x}) - \frac{1}{2}\Delta\vec{b}(V_b^{-1})\Delta\vec{b}^T - \frac{1}{2}\Delta\vec{x}(V_x^{-1})\Delta\vec{x}^T - \frac{1}{2}\Delta\vec{d}(V_d^{-1}(\vec{b},\vec{x}))\Delta\vec{d}^T \quad (9.1)$$

The probability of observing N_i^{obs} events in ith bin given a predicted event rate N_i^{pred} is given by the Poisson distribution.

$$P(N_i^{obs}|N_i^{pred}) = \frac{(N_i^{pred})^{N_i^{obs}} e^{-N_i^{pred}}}{N_i^{obs}!} \quad (9.2)$$

We maximize the likelihood ratio, where the denominator is evaluated $N^{obs} = N^{pred}$.
Taking the negative log of L_{ND}^r and dropping the constant term, we get:

$$\begin{aligned} -2\ln L_{ND}^r &= 2\sum_i^{N_{bin}} \left[N_i^{pred}(\vec{b},\vec{x},\vec{d}) - N^{obs} + N_i^{obs}\ln(N_i^{obs}/N_i^{pred}(\vec{b},\vec{x},\vec{d})) \right] \\ &+ \sum_{i,j}^{N_b} \Delta\vec{b}_i (V_b)_{ij}^{-1} \Delta\vec{b}_j + \sum_{i,j}^{N_x} \Delta\vec{x}_i (V_x)_{ij}^{-1} \Delta\vec{x}_j + \sum_{i,j}^{N_d} \Delta\vec{d}_i (V_d)_{ij}^{-1} \Delta\vec{d}_j \end{aligned} \quad (9.3)$$

We minimize this quantity with respect to flux and cross-section parameters instead of maximizing the likelihood Eq. (9.1).

For the observable N^{obs}, we would fit all ND280 data that has power to constrain the parameters ideally. But in practice, we chose muon momentum p and cosine of the angle with respects to the beam direction $\cos\theta$. We made 2D histograms of these observables and used them in the fit.

9.2 Event Reconstruction and Event Selection

We measured the CC interaction events by reconstructing muon tracks and associated tracks. In ND280, there are two target trackers (FGD1, FGD2). FGD1 is made of fully plastic scintillator, while FGD2 contains water layers to measure the neutrino-interaction with water, which is the same target nucleus as Super-Kamiokande. We used both FGD1 and FGD2 events to get better constraints on cross-section parameters for water target.

9.2.1 Data Used in the Near Detector Fit

We used the data set shown in Table 9.1 for the near detector analysis. The amount of POT accumulated in ND280 is less than that delivered from the neutrino beam line or that of recorded in Super-Kamiokande due to the ND280 detector trouble.

Table 9.1: The numbers of accumulated POT accumulated in ND280

T2K Run	Beam Mode	POT ($\times 10^{19}$)
Run 2	FHC	4.286
Run 2	FHC	3.551
Run 3b	FHC	2.146
Run 3c	FHC	13.482
Run 4	FHC	16.282
Run 4	FHC	18.443
Run 5c	RHC	4.298
Run 6	RHC	24.156
Total	FHC	58.190
Total	RHC	28.454

9.2.2 Event Reconstruction

The ND280 reconstruction uses an external reconstruction toolkit, RecPack, for various fitting, propagation and matching routines [227]. The neutrino events interacted with FGDs are used for the oscillation analysis. In the FGD reconstruction, there are two separate parts: the tracks contained only in FGD, and tracks both in FGD and TPC. Charged leptons (mostly muons) from interaction have high enough momentum to leave the target volume and enter other detectors. Therefore, the TPC track is reconstructed first, then the FGD reconstruction is run to find the FGD-TPC matched track.

TPC Reconstruction

For the TPC track reconstruction, clusters of hit waveforms is made first, then the TPC track is reconstructed using a pattern recognition algorithm based on a cellular automaton [228]. Once

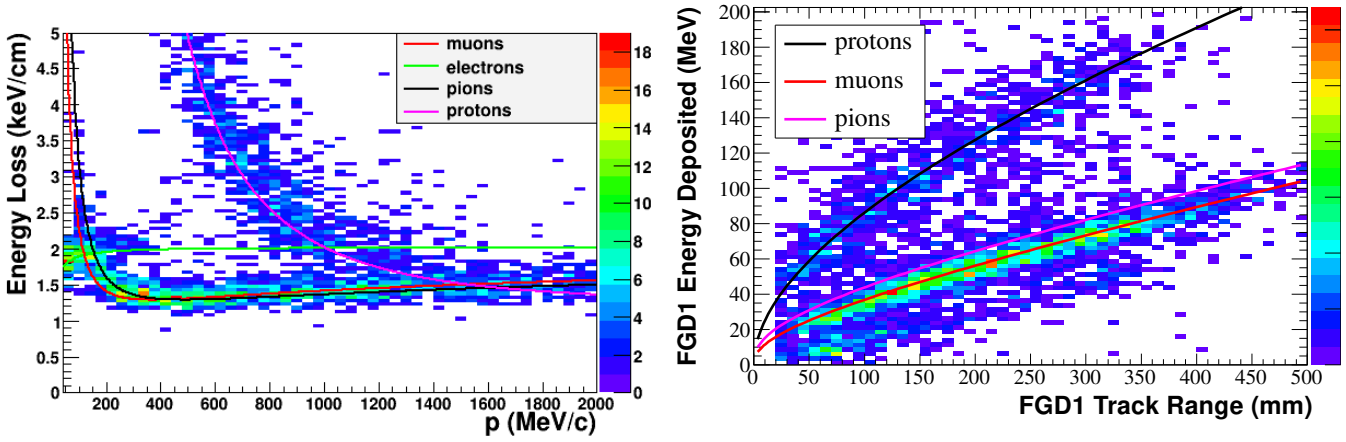

(a) TPC dE/dx distribution

(b) FGD energy deposit vs length distribution

Figure 9.1: Energy loss distribution as a function of the reconstructed momentum or track length for positively charged particles.

tracks are reconstructed, the tracks are refitted with the likelihood algorithm to determine charge, interaction vertex and momentum of the track.

TPC also provides the particle identification (PID) for the track [111]. Particle identification in TPC uses the energy deposit along the track and calculate "pull" to provide the probability of the particle type. Figure 9.1 shows the energy loss vs. momentum of the particle tracks in TPC.

The pull for particle type α is defined as:

$$Pull_\alpha = \frac{\left(\frac{dE}{dx}\right)_{meas} - \left(\frac{dE}{dx}\right)_{MC,\alpha}}{\sigma} \tag{9.4}$$

where $(dE/dx)_{meas}$ is the measured energy loss, $(dE/dx)_{MC,\alpha}$ is the expected energy loss as a function of momentum for given particle α, σ is the total width including the variance and the uncertainty in the measurement. The likelihood is defined as follows:

$$L_\alpha = \frac{e^{-pull_\alpha^2}}{\sum_i e^{-pull_i^2}} \tag{9.5}$$

where the denominator is sum of the pulls of the particle hypothesis to consider.

FGD Reconstruction

First, the initial time for the TPC track is within the time window of the FGD time bin is checked. The TPC track is then extrapolated back to the closest layer of hits in the FGD using Kalman Filter. The remaining tracks in FGD are treated as FGD-only tracks. The FGD reconstruction also uses the same cellular automaton algorithm as that of TPC. Once tracks are reconstructed, a fitting is done assuming a straight line to calculate the length and direction of the track. FGD PID is done with similar way to the TPC one except dE/dx is defined as a function of the particle range (track length) not the momentum [112].

Finally, to check the direction of TPC-FGD matched track, the time difference between FGD1 and FGD2 is calculated. If the $t_{FGD1} - t_{FGD2} > 3$ns, the track is considered to be backward-going track.

9.2.3 Event Selection

CC Inclusive Event Selection

We selected CC inclusive [1] sample as follows:

- Data quality flag
  We require all sub-detectors in ND280 are working properly.
- Time bunching
  The tracks are grouped together in bunches according to their times to avoid the accidental pile-up events.
- Total Multiplicity cut
  At least one TPC track is reconstructed.
- Quality and Fiducial cut
  We require at least one track exists in the FGD1 or FGD2 fiducial volume associated with TPC track. The TPC track must contain at least 18 clusters to ensure the reliability of the momentum reconstruction and the particle identification. We require that the highest momentum track has negative charge for FHC and RHC wrong-sign, and positive charge for RHC.
- Backwards-going tracks veto
  Our reconstruction algorithm sometimes fails to properly link the tracks, instead it reconstructed as the two separate tracks. The tracks from P0D passing through FGD1, for example, is difficult to identify to the backward track from FGD1. Therefore, the events are removed if there exist upstream lepton tracks for both FGD1 and FGD2. The FGD2 selection also cuts events which have tracks starting in the FGD1 fiducial volume.
- Broken Track Cut
  The algorithm also fails to properly reconstruct the candidate track which starts from FGD but two separate tracks of FGD-only track and FGD-TPC track. We remove any events where the muon candidate starts in the last two layers of the FGDs.
- Muon Particle Identification Cut
  Particle identification is done with dE/dx measurements at TPC. We require two cuts to remove electrons, protons, and pions from muon tracks for FHC (Fig. 9.2).

$$\begin{aligned} (L_\mu + L_\pi)/(1 - l_p) &> 0.8 \\ L_\mu &> 0.05 \end{aligned} \tag{9.6}$$

  The first cut is applied to the tracks with the momentum p $<$ 500 MeV/c to remove electrons. The Second cut is applied to the other muon candidates.

  For RHC, we require (Fig. 9.3):

$$\begin{aligned} (L_\mu + L_\pi)/(1 - l_p) &> 0.9 \\ 0.1 < L_\mu &< 0.7 \end{aligned} \tag{9.7}$$

[1] Here we refer to the events where the muon from neutrino interaction exists as CC inclusive sample.

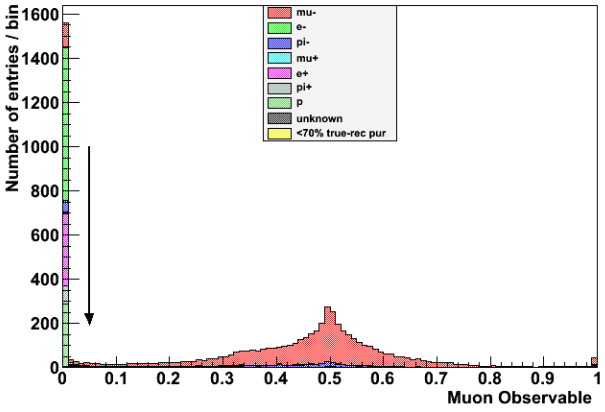

(a) MIP like track

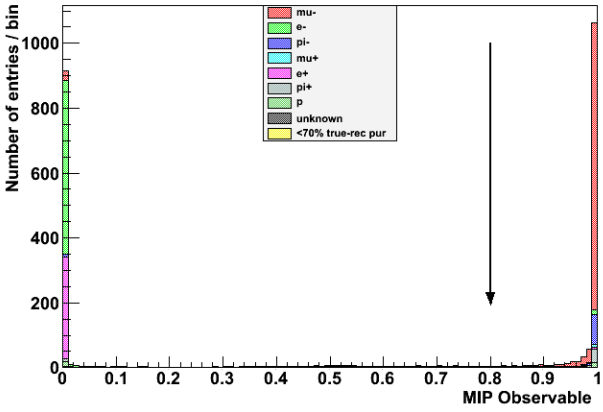

(b) p $<$ 500 MeV/c track

Figure 9.2: PID selection for FHC mode. Red lines show the selection criteria.

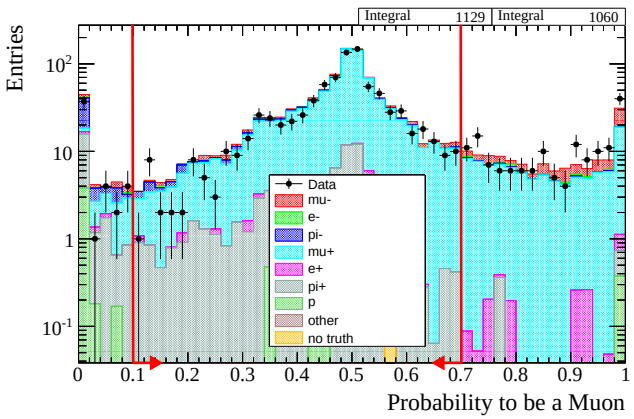

(a) MIP like track

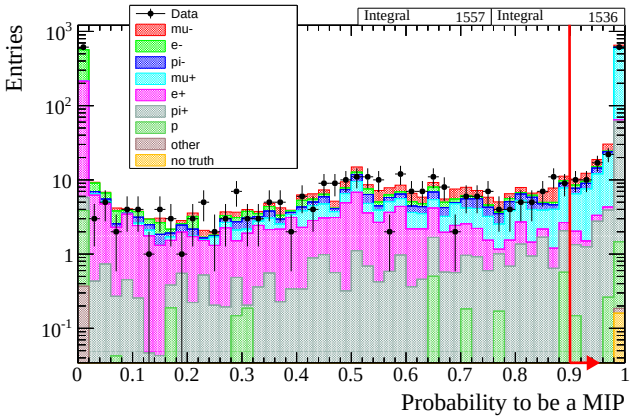

(b) p $<$ 500 MeV/c track

Figure 9.3: PID selection for RHC mode. Red lines show the selection criteria.

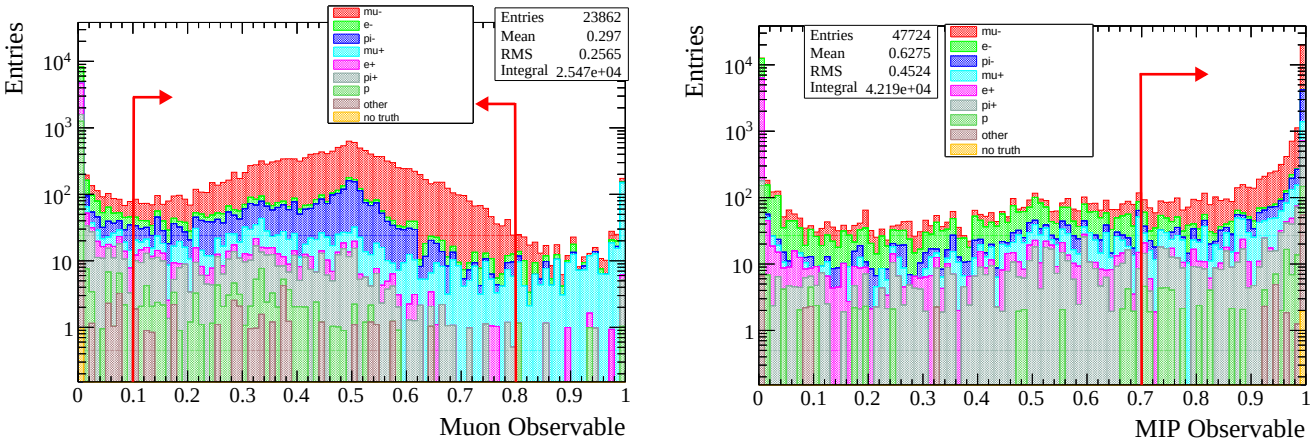

(a) MIP like track

(b) p $<$ 500 MeV/c track

Figure 9.4: PID selection for wrong-sign RHC mode. Red lines show the selection criteria.

These cuts are applied to the highest momentum track with positive charge. The upper limit of the second cut is set to remove the wrong-sign component.

For RHC wrong-sign ν_μ sample, we require the following cuts (Fig. 9.4):

$$\begin{aligned} (L_\mu + L_\pi)/(1 - l_p) &> 0.7 \\ 0.1 < L_\mu &< 0.8 \end{aligned} \tag{9.8}$$

Pion Selection

After the CC inclusive events are selected, the events are categorized by the number of charged pions. The pions associated with the CC interaction are selected as follows:

- TPC Pion Track Cuts
  We apply the pion PID cut to the secondary tracks that start from the same fiducial volume as the muon candidate. The secondary tracks also must be in the same FGD fiducial volume as the selected muon candidate. The application of the cut is similar to the muon PID cuts:

$$\begin{aligned} (L_\mu + L_\pi)/(1 - l_p) &> 0.8 \\ L_\pi &> 0.3. \end{aligned} \tag{9.9}$$

  The first cut is applied to the events below $p < 500$ MeV/c and the second cut is applied to all other cases. The pion, positron and proton hypothesis are used for the positive track cut. For negative tracks, the pion and electron hypotheses are considered instead.

- FGD Isolated Reconstruction Track Cut
  The FGD isolated reconstruction cut is applied to the tracks originating in the same FGD fiducial volume as the muon candidate, but do not leave FGDs. First, we require FGD-only tracks must contain both start and end of the track within the fiducial volume. We then calculate a PID pull using the energy deposit as a function of the track length like the TPC PID pulls.

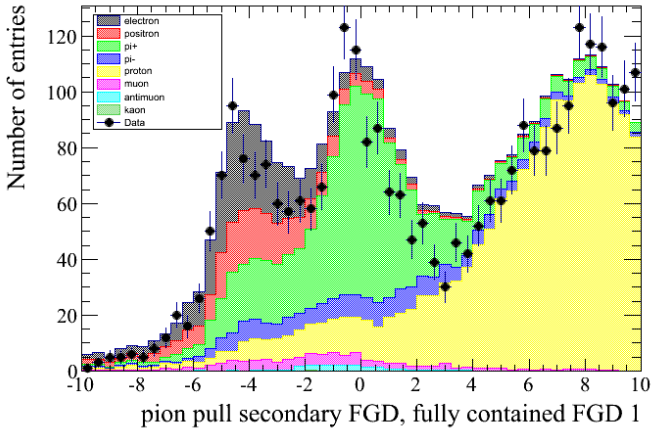

Figure 9.5: PID selection for FGD pion track

To be considered a contained positive pion track, the FGD-only track must have $\cos\theta > 0.3$ where θ is angle with respect to the beam direction due to the reconstruction efficiencies. A pion pull greater than -2 and less than 2.5 is also required.

- Determining the Michel cut
  The pions produced by neutrino interactions sometimes do not deposit enough energy to be reconstructed as an FGD-only track as described in the previous cut. In order to avoid miss identification of such an event, we select out events that have a delayed Michel electron originating from the decay pion.

  To identify these Michel electrons, we look for the delayed activity in the FGD containing the muon track. The delayed activity is defined as the activity as a group of at least two hits occurring at least 100 ns after the initial neutrino interaction for that event.

The number of positive pions are calculated as the sum of the TPC positive pions, the number of Michel electron events and the number of FGD-only pion tracks.

Event Categorization

We divide the FHC mode events into three categories: CC0π, CC1π, CCOther, which are dominated by CCQE, CC single pion production, and DIS, respectively. For RHC, the wrong-sign contamination is estimated to be $\sim$30 %. Therefore, anti-ν CC interaction and wrong-sign CC interaction are categorized as different samples. We divide the RHC mode events into four categories : ACC (Anti-ν CC) 1 track, ACC N track, CC 1 track and CC N track, which are dominated by $\bar{\nu}$CCQE, $\bar{\nu}$ CC non-QE, νCCQE, ν CC non-QE, respectively. For RHC, The CC candidates events are not categorized according to the number of pions due to the low statistics.

The bin edges of the event category for each sample are summarized as follows.

- FHC CC0π : one negative muon and no pions are observed in FHC.
  p(MeV/c) : 0, 300, 400, 500, 600, 700, 800, 900, 1000, 1250, 1500, 2000, 3000, 5000, 30000
  $cos\theta$:-1, 0.6, 0.7, 0.8, 0.85, 0.9, 0.92, 0.94, 0.96, 0.98, 0.99, 1

- FHC CC1π : one negative muon, one positive pions and no negative pions are observed in FHC.
  p(MeV/c) : 0, 300, 400, 500, 600, 700, 800, 900, 1000, 1250, 1500, 2000, 5000, 30000

$cos\theta$:-1, 0.6, 0.7, 0.8, 0.85, 0.9, 0.92, 0.94, 0.96, 0.98, 0.99, 1

- FHC CCOther : one negative muon and multiple/negative pions are observed in FHC.
  p(MeV/c) : 0, 300, 400, 500, 600, 700, 800, 900, 1000, 1250, 1500, 2000, 3000, 5000, 30000
  $cos\theta$:-1, 0.6, 0.7, 0.8, 0.85, 0.9, 0.92, 0.94, 0.96, 0.98, 0.99, 1

- RHC ACC1track : one positive muon and no pions are observed in RHC.
  p(MeV/c) : 0, 400, 500, 600, 700, 800, 900, 1100, 1400, 2000, 10000
  $cos\theta$: -1., 0.6, 0.7, 0.8, 0.85, 0.88, 0.91, 0.93, 0.95, 0.96, 0.97, 0.98, 0.99, 1.00

- RHC ACCNtrack : one positive muon and associated pions are observed in RHC.
  p(MeV/c) : 0, 700, 950, 1200, 1500, 2000, 3000, 10000.
  $cos\theta$:-1., 0.75, 0.85, 0.88, 0.91, 0.93, 0.95, 0.96, 0.97, 0.98, 0.99, 1.00

- RHC CC1track : one negative muon and no pions are observed in RHC.
  p(MeV/c) : 0, 400, 600, 800, 1100, 2000, 10000.
  $cos\theta$:-1., 0.7, 0.8, 0.85, 0.90, 0.93, 0.95, 0.96, 0.97, 0.98, 0.99, 1.00

- RHC CCNtrack : one negative muon and associated pions are observed in RHC.
  p(MeV/c) : 0, 500, 700, 1000, 1250, 1500, 2000, 3000, 10000
  $cos\theta$:-1., 0.7, 0.8, 0.85, 0.90, 0.93, 0.95, 0.96, 0.97, 0.98, 0.99, 1.00

Figure 9.6 shows the momentum and $\cos\theta$ distribution of FGD1 $CC0\pi$, $CC1\pi$, $CCOther$ samples. The other distributions are shown in Appendix D. The predicted number of events and observed events are shown in Table 9.3

9.3 Systematic Uncertainties

In ND280, the detector systematic uncertainties are implemented as two different types: variation systematics and weight systematics. The variation systematics modifies the reconstructed quantities such as particle ID, while the weight systematics only has an effect on the overall event weight and does not modify any of the reconstructed values. The variation systematics is applied to smear the relevant reconstructed observables and the weight systematics is implemented as a weight applied to relevant events. We considered six variation systematics and eleven weight systematics listed in Table 9.2. The error size for the CC inclusive selection are also shown in the table.

To include these systematic uncertainties into the near detector fit, we introduced a set of observable normalization parameters describing the effect of the systematic variations on the event rates for each sample. The uncertainties of the normalization parameters and their covariance are calculated from 2000 variations of the detector systematic parameters. In addition, in order to alleviate possible biases on the estimation of the oscillation parameters, the uncertainty on the model difference (NEUT vs Nieves 1p1h), which covers the lepton kinematics difference between the models is also added to the near detector covariance matrix as an additional uncertainty.

Figure 9.7 shows the covariance matrix of the near detector. The binning and bin number of the matrix are as follows:

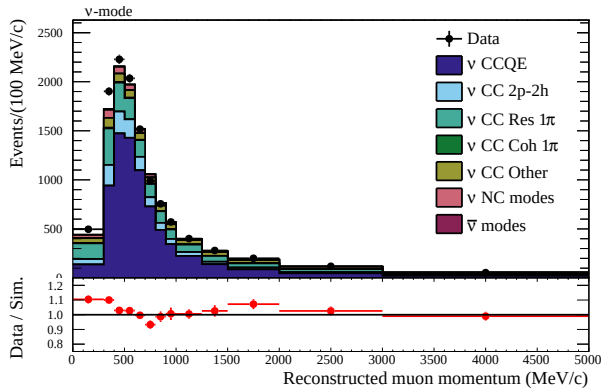

PRELIMINARY

(a) FHC CC0pi momentum distribution

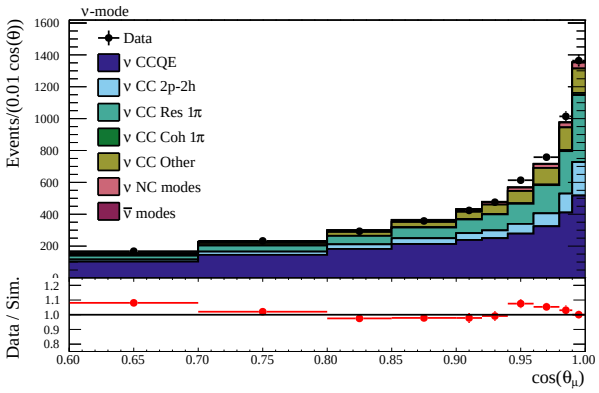

PRELIMINARY

(b) FHC CC0pi $\cos\theta$ distribution

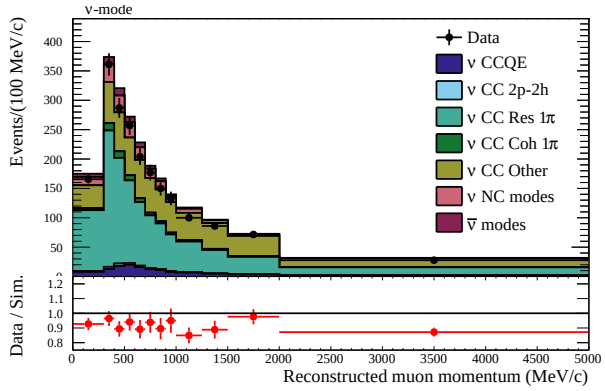

PRELIMINARY

(c) FHC CC1pi momentum distribution

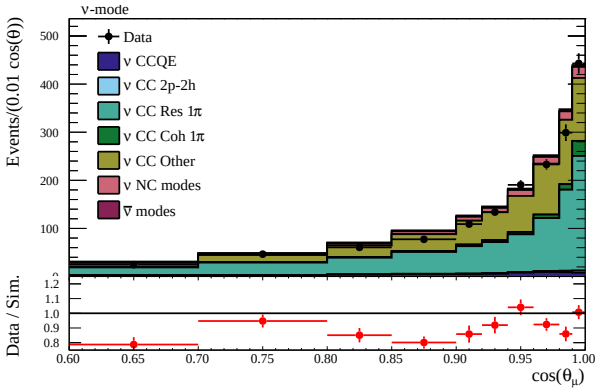

PRELIMINARY

(d) FHC CC1pi $\cos\theta$ distribution

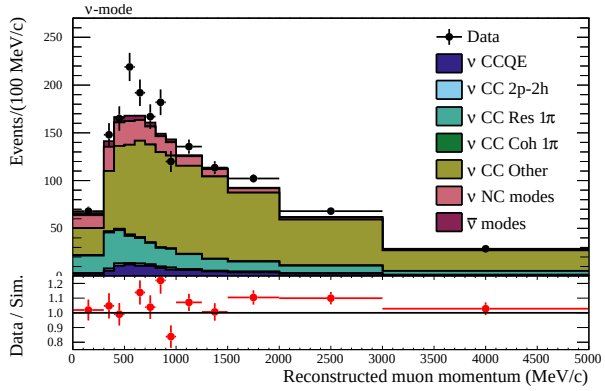

PRELIMINARY

(e) FHC CCOther momentum distribution

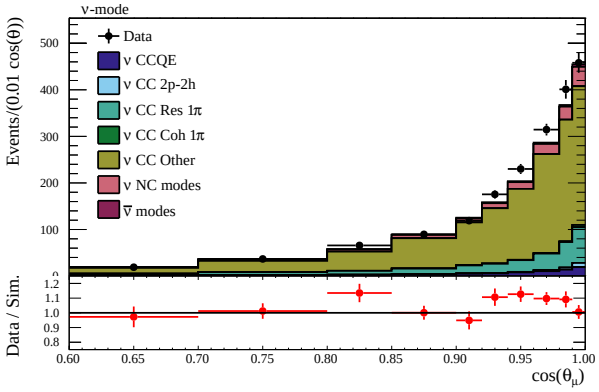

PRELIMINARY

(f) FHC CCOther $\cos\theta$ distribution

Figure 9.6: ND280 muon momentum and $\cos\theta$ distribution for each event selection before the near detector fit

Table 9.2: List of detector systematic sources and types for the ND280 and error of the CC inclusive selection.

Systematic source	Type	error (in %)
TPC Systematics		
Magnetic Field Distortion	Variation	0.0393
Momentum Resolution	Variation	0.0823
Momentum Scaling	Variation	0.0877
TPC PID	Variation	0.3428
Cluster Efficiency	Weight	0.0006
Track reconstruction	Weight	0.4221
Charge ID	Weight	0.1276
FGD systematics		
TPC - FGD matching	Weight	0.2298
FGD PID	Variation	0.0002
Time of Flight	Variation	0.0381
FGD reconstruction	Weight	0.0385
Michel Electron Detection	Weight	0.0011
Background		
Out of Fiducial Volume Events	Weight	0.3975
Sand Muon Events	Weight	0.0671
Event Pile-up	Weight	0.1117
Monte Carlo Modeling		
Pion Secondary Interactions	Weight	2.1245
FGD mass	Weight	0.5926
Total		
		2.2937

- FHC CC0π (FGD1: 0-41, FGD2: 278-319):
  p(MeV/c) : 0, 1000, 1250, 2000, 3000, 5000, 30000
  $cos\theta$: -1, 0.6, 0.7, 0.8, 0.85, 0.94, 0.96, 1

- FHC CC1π (FGD1: 42-81, FGD2: 320-359):
  p(MeV/c) : 0, 300, 1250, 1500, 5000, 30000
  $cos\theta$: -1, 0.7, 0.85, 0.9, 0.92, 0.96, 0.98, 0.99, 1

- FHC CCOther (FGD1: 82-121, FGD2: 360-399):
  p(MeV/c) : 0, 1500, 2000, 3000, 5000, 30000
  $cos\theta$: -1, 0.8, 0.85, 0.9, 0.92, 0.96, 0.98, 0.99, 1

- RHC ACC 1 track (FGD1: 122-161, FGD2: 400-439):
  p(MeV/c) : 0, 400, 900, 1100, 2000, 10000
  $cos\theta$: -1., 0.6, 0.7, 0.88, 0.95, 0.97, 0.98, 0.99, 1.00

- RHC ACC N track (FGD1: 162-197, FGD2: 440-475):
  p(MeV/c) : 0, 700, 1200, 1500, 2000, 3000, 10000
  $cos\theta$: -1, 0.85, 0.88, 0.93, 0.98, 0.99, 1.00

- RHC CC 1 track (FGD1: 198-237, FGD2: 476-515):
  p(MeV/c) : 0, 400, 800, 1100, 2000, 10000
  $cos\theta$: -1, 0.7, 0.85, 0.90, 0.93, 0.96, 0.98, 0.99, 1.00

- RHC CC N track (FGD1: 238-277, FGD2: 516-555):
  p(MeV/c) : 0, 1000, 1500, 2000, 3000, 10000
  $cos\theta$:-1., 0.8, 0.90, 0.93, 0.95, 0.96, 0.97, 0.99, 1.00

9.4 Fit Results

The fit is performed by using the MINUIT program [229]. The ND280 detector systematic uncertainties are treated as nuisance parameters. For the CCQE interaction parameters, they are constrained solely by the ND280 data while external constraints are applied for parameters for the other interactions.

Figure 9.9 shows the normalization parameter values of neutrino flux at ND280 and Super-Kamiokande, and Fig. 9.10 shows the cross section parameters before and after the fit as a ratio to the nominal values, along with their prior constraints. These fitted parameter values are listed in Appendix E, showing the best-fit point and its uncertainty. The flux parameters are well constrained within the prior errors. For the CC0π parameters, M_A and the Fermi momentum are mostly unchanged, while the 2p2h parameters are shifted largely. The 2p2h is fully PDD-like [2], and the event

[2]The 2p2h shape parameters are implemented to move from -1 to 1. If the parameter is 1, 2p2h becomes fully 2p2h PDD-like. If the parameter is -1, 2p2h becomes fully non PDD-like.

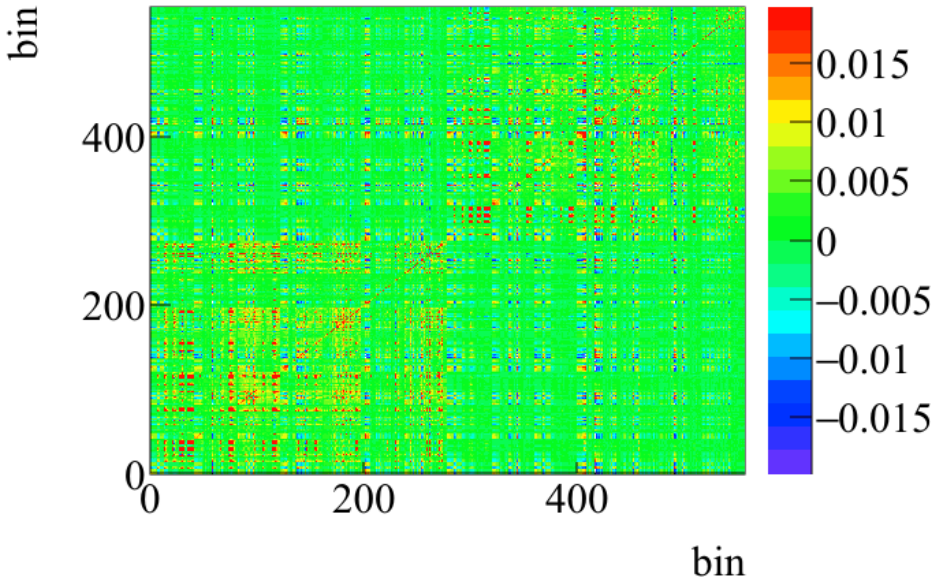

Figure 9.7: Covariance matrix of ND280 detector systematic uncertainties

rates are enhanced $\sim 50\%$ for ν and decreased $\sim 40\%$ for $\bar{\nu}$. For the RPA parameters, parameters for $Q^2 < 1$ GeV are shifted largely. Figure 9.8 shows the RPA correction factor calculated with the best fit values. The postfit error bands are away from the prefit constraint. We re-parameterized the RPA collection with simple polynomials as described in Section 8.4.1, therefore, the parameter shifts are difficult to interpret physically.

We investigated these features of the fit, and we found that the simulation slightly underestimated the CC0π events to data, at low momentum region as shown in Fig. 9.6 and the fit successfully compensated the deficit by increasing the event at that region by changing cross-section parameters. The flux and cross-section become highly correlated to each other as shown in Fig. 9.11, which reduces systematic uncertainties of the number of neutrino events. Therefore, it is difficult to interpret these results simply with the shifts of the interaction parameters. Hence, we investigated the potential effects of this data-prediction difference on the oscillation parameters with simulated data in Chapter 12. Figure 9.12 shows the muon momentum and $\cos\theta$ distribution using best-fit value and Table 9.3 shows the event rates after the fit. Both distributions and event rates show better agreements with the data with a p-value of 0.47, demonstrating that the fitted parameter values propagated to the oscillation analysis are reasonable. The other distributions are shown in Appendix F.

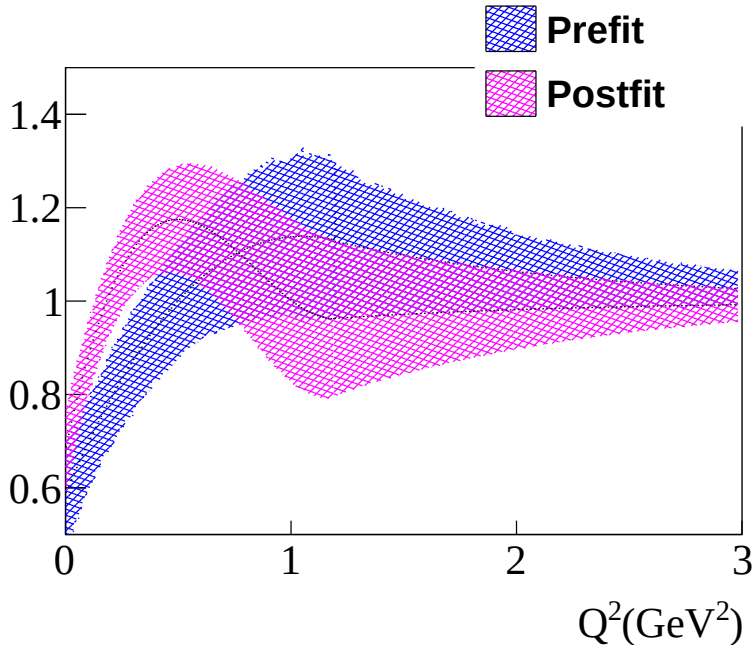

Figure 9.8: RPA factor before and after the near detector fit

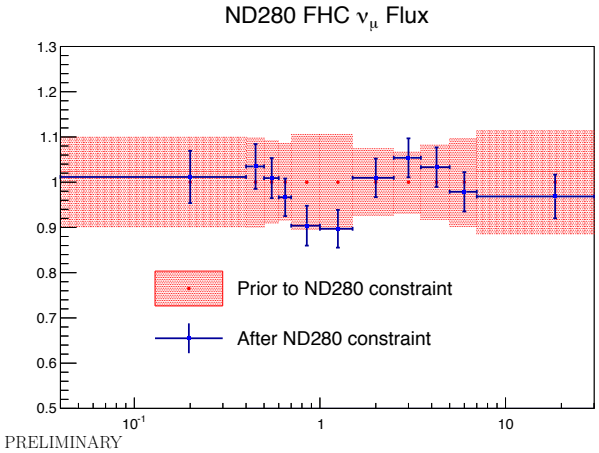

(a) ND280 FHC ν_μ Flux

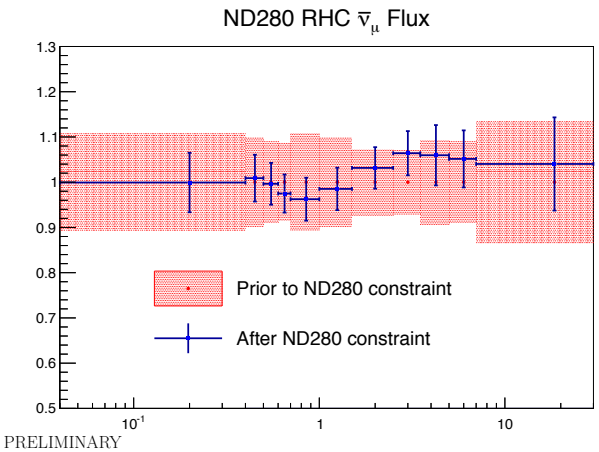

(b) ND280 RHC $\bar{\nu}_\mu$ Flux

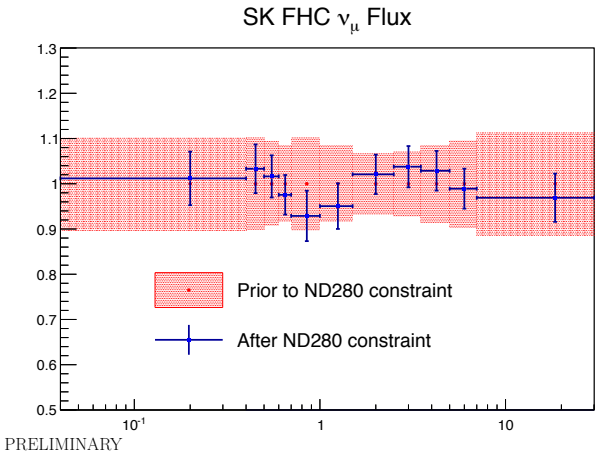

(c) Super-Kamiokande FHC ν_μ Flux

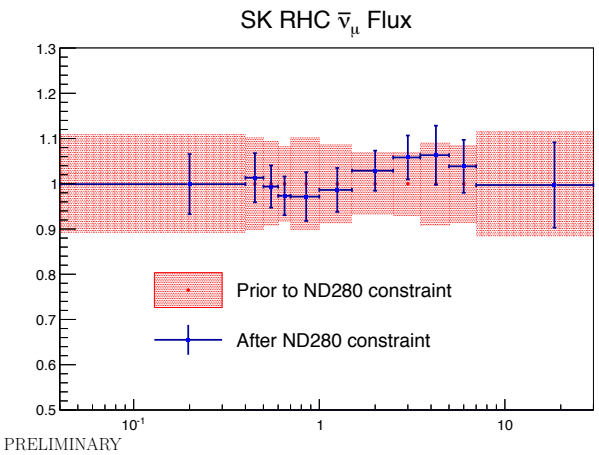

(d) Super-Kamiokande RHC $\bar{\nu}_\mu$ Flux

Figure 9.9: Flux parameters before and after the near detector fit

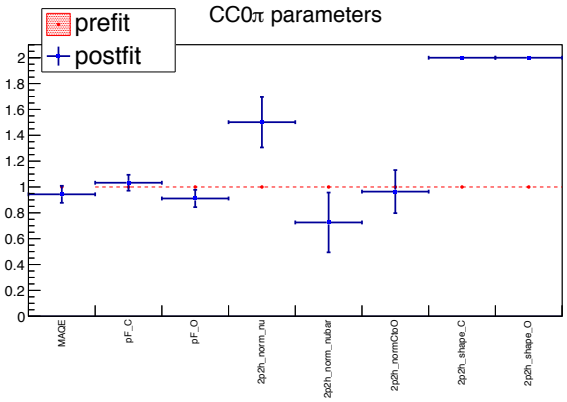

PRELIMINARY

(a) CC 0π parameters

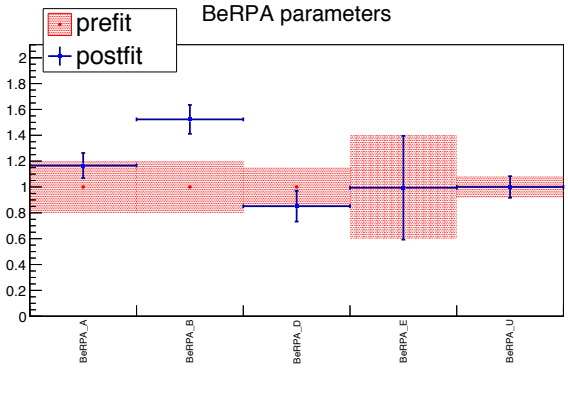

PRELIMINARY

(b) RPA parameters

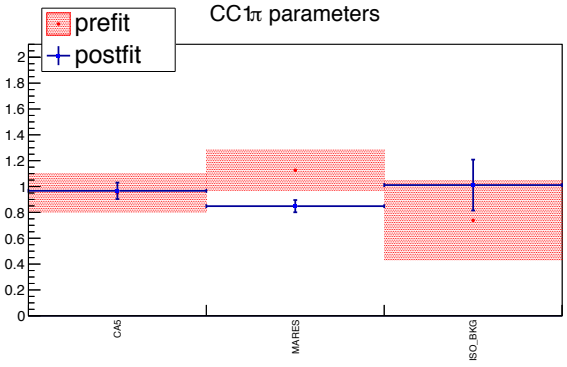

PRELIMINARY

(c) CC 1π parameters

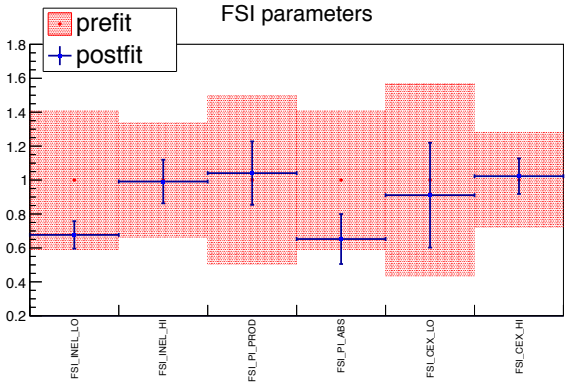

PRELIMINARY

(d) FSI parameters

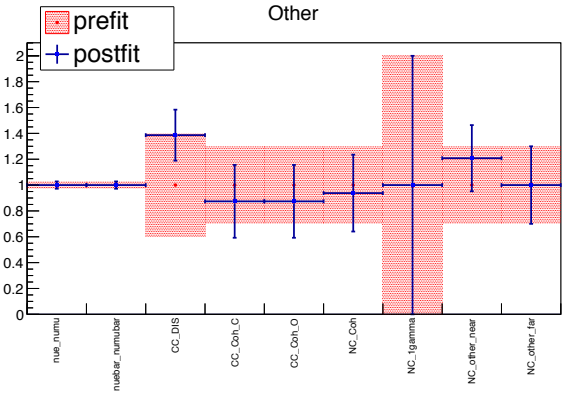

PRELIMINARY

(e) Other interaction parameters

Figure 9.10: Interaction parameters before and after the near detector fit

Table 9.3: Predicted and observed number of events of each event selection before and after the near detector fit

Sample	Data	Prefit simulation	Postfit simulation
FHC FGD1 ν_μ CC0π	17136	16723.80	17122.22
FHC FGD1 ν_μ CC1π	3954	4381.47	4061.65
FHC FGD1 ν_μ CCOther	4149	3943.95	4095.58
RHC FGD1 $\bar{\nu}_\mu$ CC 1 Track	3527	3587.77	3503.79
RHC FGD1 $\bar{\nu}_\mu$ CC N Track	1054	1066.91	1052.79
RHC FGD1 ν_μ CC 1 Track	1363	1272.17	1353.44
RHC FGD1 ν_μ CC N Track	1370	1357.45	1354.02
FHC FGD2 ν_μ CC0π	17443	16959.30	17494.56
FHC FGD2 ν_μ CC1π	3386	3564.23	3416.28
FHC FGD2 ν_μ CCOther	4075	3570.94	3915.36
RHC FGD2 $\bar{\nu}_\mu$ CC 1 Track	3732	3618.29	3685.46
RHC FGD2 $\bar{\nu}_\mu$ CC N Track	1026	1077.24	1097.38
RHC FGD2 ν_μ CC 1 Track	1320	1262.63	1330.40
RHC FGD2 ν_μ CC N Track	1253	1246.71	1263.12
Total	64768	63632.90	64746.02

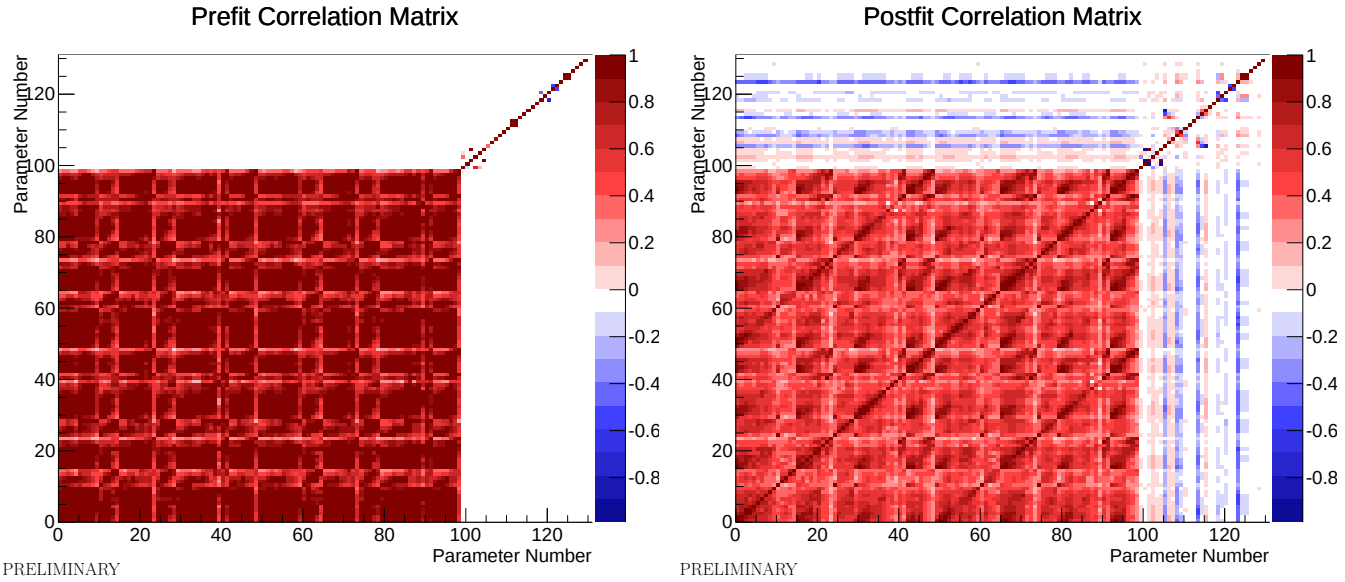

(a) before near detector fit

(b) After near detector fit

Figure 9.11: Correlation matrix for the cross-section and flux parameters before and after the near detector fit. The 0-99 bin corresponds to flux parameters, 100-131 bin corresponds to cross-section parameters.

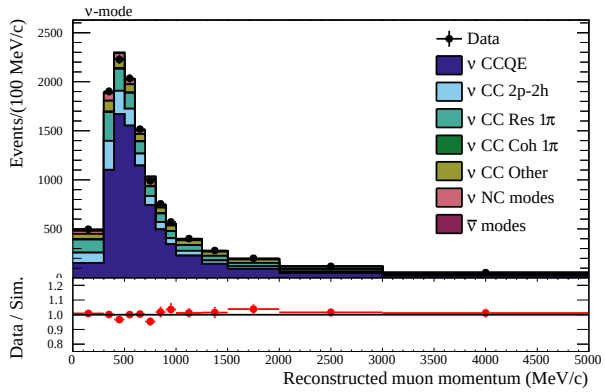

PRELIMINARY

(a) CC0pi momentum distribution

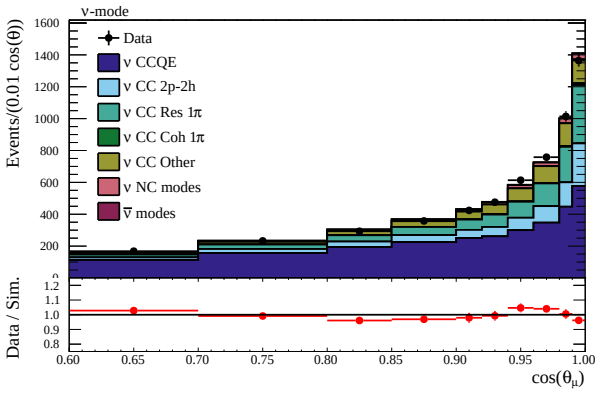

PRELIMINARY

(b) CC0pi $\cos\theta$ distribution

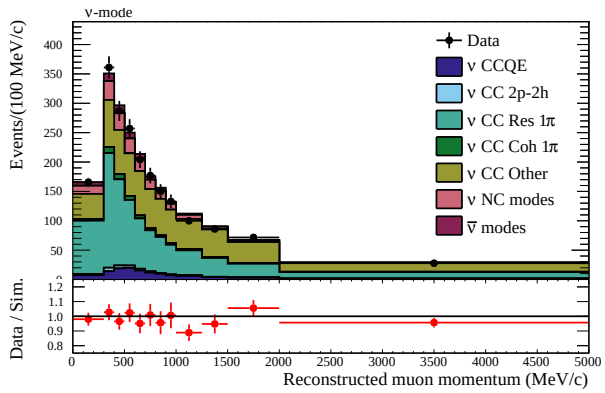

PRELIMINARY

(c) CC1pi momentum distribution

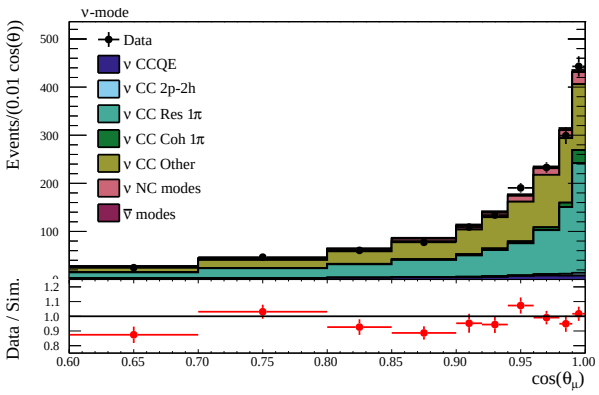

PRELIMINARY

(d) CC1pi $\cos\theta$ distribution

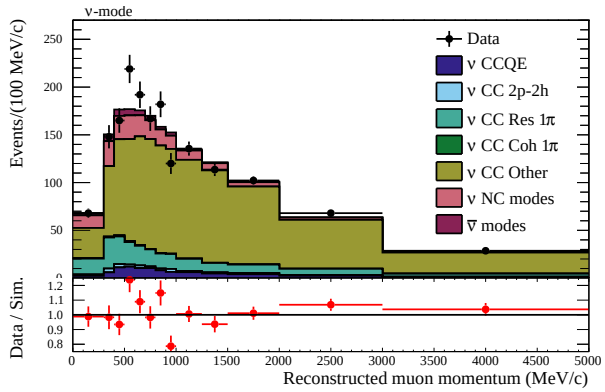

PRELIMINARY

(e) CCOther momentum distribution

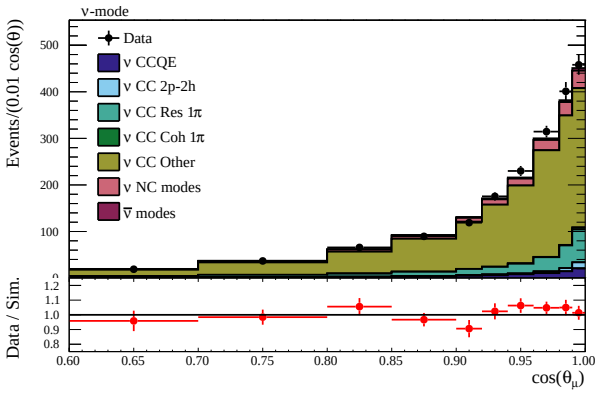

PRELIMINARY

(f) CCOther $\cos\theta$ distribution

Figure 9.12: ND280 momentum and $\cos\theta$ distribution for each event selection after the near detector fit

Chapter 10

Super-Kamiokande Analysis

In this chapter, we describe the event selection at Super-Kamiokande. We also introduce a reconstruction algorithm called "fiTQun" to improve the detection efficiency.

10.1 Event Reconstruction

10.1.1 FitQun Reconstruction Algorithm

In Super-Kamiokande, momentum, interaction vertex, and angle with respect to the beam direction are reconstructed by using PMT hits and timing of Cherenkov light emitted by charged particles. Super-Kamiokande also can identify electrons and muons with the shape of Cherenkov ring. Electron makes a fuzzy ring because of multiple scattering or electromagnetic shower, while muon makes a clear ring.

To reconstruct the Cherenkov ring more precisely, we developed a new reconstruction algorithm called "fiTQun" [230]. "fiTQun" is a reconstruction software based on maximum likelihood fit originally developed for the MiniBooNE experiment. The fiTQun treats timing, charge of PMTs and "unhit" PMT information simultaneously to get precise reconstruction. We have been using the fiTQun algorithm to reject π^0 in electron like sample since 2013 analysis, and extended to use all charged particles in 2017 analysis. FiTQun enables us to reconstruct the vertex near the wall without reducing of the detection efficiency or significantly increasing systematic errors. Therefore, fitQun also enables us to extend the fiducial volume by optimizing the event selection. The details of the event selection are shown in the latter section.

10.1.2 Energy Reconstruction

In Super-Kamiokande, we measure "CCQE-like" interaction by identifying single electron or muon events. For the CCQE interaction, the neutrino energy is reconstructed assuming the target nucleon is at rest:

$$E_\nu^{rec} = \frac{M_p^2 - (M_n - E_b)^2 - M_l^2 + 2(M_n - E_b)E_l}{2(M_n - E_b - E_l + p_l \cos\theta_l)} \tag{10.1}$$

where M_p, M_n and M_l represent the proton, neutron and outgoing lepton mass respectively, $E_b = 27\ MeV$ is the binding energy of the target nucleus, E_l, p_l and $\cos\theta_l$ represent the energy, the momentum and the emission angle relative to the beam direction of the outgoing lepton, respectively.

To increase the statistics, we introduced CC 1π samples partially to the oscillation analysis. We loosened the number of decay electron cut from 2016 analysis which is described in the latter section. These samples are dominated by the CC single pion production where the pion momentum is below Cherenkov threshold (160 MeV/c). The pions below the threshold don't produce Cherenkov rings, while decay electron signals are detected via following decay:

$$\begin{aligned} \pi^+ \rightarrow \quad & \mu^+ \quad + \nu_\mu \\ & \downarrow \\ & \mu^+ \quad \rightarrow \nu_\mu + e^+ + \nu_e \end{aligned} \tag{10.2}$$

These interactions are mostly mediated by $\Delta^{++}(1232)$ resonance state, therefore, we reconstruct the neutrino energy from the lepton kinematics assuming two-body interaction $\nu + N \rightarrow \mu + N^*$:

$$E_\nu^{rec} = \frac{2M_p E_e + M_\Delta^2 - M_p^2 - M_e^2}{2(M_p - E_e + p_e \cos\theta_e)} \tag{10.3}$$

where M_p,M_e and M_Δ are the mass of proton, electron and Δ^{++} respectively, E_e, p_e and $\cos\theta_e$ are the electron energy, momentum and the angle between the beam direction.

10.1.3 Data Set

We select Fully-Contained (FC) events, where the neutrino interacts inside the detector of Super-Kamiokande and all tracks are in it. We require the number of PMT hits in the largest cluster in the outer detector is less than 16 to remove the cosmic ray background.

To identify whether a neutrino event comes from J-PARC, the timing information from GPS system is used. Figure 10.1 shows the timing distributions of low energy, outer detector and FC events. ΔT_0 is defined as the difference between the observed and expected arrival time of the leading edge of each spill. A clear peak is observed around $\Delta T_0 = 0$ in the large amount of background from the low energy (LE) and outer detector (OD) events. On-timing events where ΔT_0 is from -2 μs to 10 μs are selected for T2K oscillation analysis. There are several off-timing FC events. These events are thought to be atmospheric neutrino events and the event rate agrees with the expected value.

We used the data set shown in Table 10.1.

10.2 Event Selection

We optimized the selection at Super-Kamiokande to get "CCQE-like" enriched samples, where only single lepton is detected. The samples are categorized by the event selection:

- one electron-like ring samples for FHC (FHC 1Re)
- one muon-like ring samples for FHC (FHC 1Rμ)
- one electron-like ring samples for RHC (RHC 1Re)
- one muon-like ring samples for RHC (RHC 1Rμ)
- one electron-like ring with one decay electron samples for (FHC 1Re+1d.e)

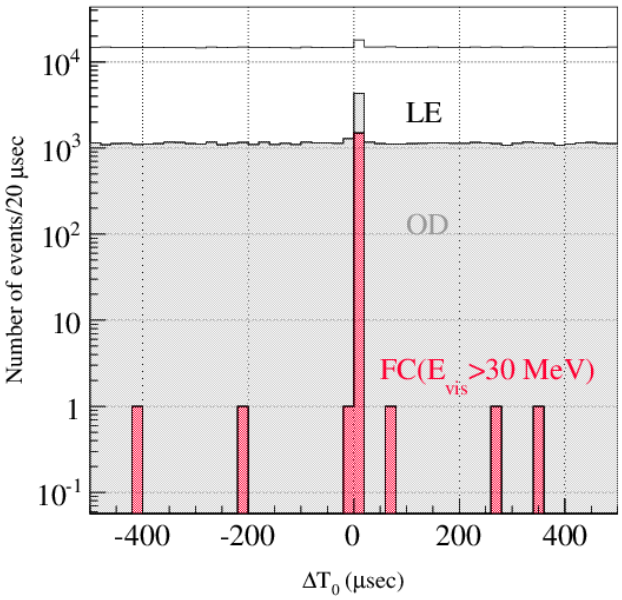

Figure 10.1: Event timing of the FC events

Table 10.1: The collected POT and beam mode for each T2K run number.

T2K Run	Beam Mode	POT ($\times 10^{20}$)	Period
Run 1	FHC	0.326	23/Jan. 2010 ∼ 26/Jun. 2010
Run 2	FHC	1.122	18/Nov. 2010 ∼ 11/Mar. 2011
Run 3b	FHC	0.217	08/Mar. 2012 ∼ 21/Mar. 2012
Run 3c	FHC	1.382	08/Apr. 2012 ∼ 09/Jun. 2012
Run 4	FHC	3.597	19/Oct. 2012 ∼ 08/May 2013
Run 5a	FHC	0.066	21/May 2014 ∼ 29/May 2014
Run 5b	FHC	0.178	29/May 2014 ∼ 26/Jun. 2014
Run 5c	RHC	0.512	04/Jun. 2014 ∼ 24/Jun. 2014
Run 6	FHC	0.192	30/Oct. 2014 ∼ 03/Jun. 2015
	RHC	3.546	04/Nov. 2014 ∼ 31/May 2015
Run 7	FHC	0.088	01/Feb. 2016 ∼ 03/Feb. 2016
	RHC	3.498	03/Feb. 2016 ∼ 18/May. 2016
	FHC	0.396	19/May. 2016 ∼ 27/May. 2016
Run 8	FHC	7.169	27/Oct. 2016 ∼ 12/Apr. 2017
Total		22.279	

The selection for RHC and FHC is the same since Super-Kamiokande cannot measure the sign of a particle's charge. First, we select the FC events. Second, we require the vertexes are within the fiducial volume (FV), to ensure the reconstruction quality. The FV cut selection was optimized for each event selection. Thereafter, we apply the selection depending on each sample and rejection of NC events.

10.2.1 Fiducial Volume Optimization

Figure 10.2 shows the illustration of the fiducial volume parameters. Here *wall* refers to the minimum distance between the particle vertex and the inner detector wall, and *towall* refers to the distance along the reconstructed particle track to the inner detector wall. Previously, the events where *wall* $>$ 200 cm are selected. Ideally, smaller *wall* is preferred to obtain larger statistics. However, the background event rate is relatively high and the reconstruction purity is worse at the small *wall* region. Therefore, fiducial volume cut should be optimized from the point of view of the statistics improvement and the effect of systematic uncertainties. We then introduce *towall* parameter to optimize the fiducial volume cut. The number of events depends on the fiducial volume and the detection efficiency depends on how clear the Cherenkov ring is observed in the detector. The event where *wall* is small, while *towall* is larger, generally has well-imaged Cherenkov ring. On the other hand, the event where both *wall* and *towall* are small, the number of PMT hits are also small. As a result, the events have poor-imaged Cherenkov ring, and should be cut from the selection. We optimized these two parameters by maximizing the Figure of Merit defined as Eq. (10.4) with respect to the oscillation parameters.

$$Figure\ of\ Merit = \frac{\left(\frac{\partial N}{\partial \theta}\right)^2}{N^2 + \sigma^2_{syst.}} \tag{10.4}$$

where N is the predicted number of events, $\sigma_{syst.}$ is the systematic uncertainties and θ is the oscillation parameters (θ_{23} for 1Rμ samples and δ_{CP} for 1Re samples). Figure 10.3 shows the distribution of figure of merits for each selection. The selection criteria are given in the next section.

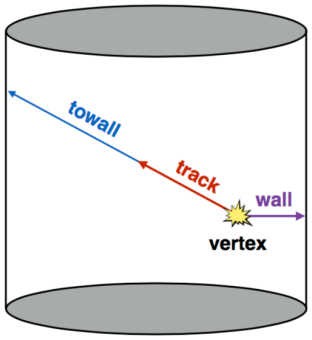

Figure 10.2: Illustration of the definitions of the wall and towall variables

10.2.2 ν_e Selection

We select 1Re sample as follows:

1. Fully Contained events in the fiducial volume (FCFV): wall $>$ 80cm, towall $>$ 170cm

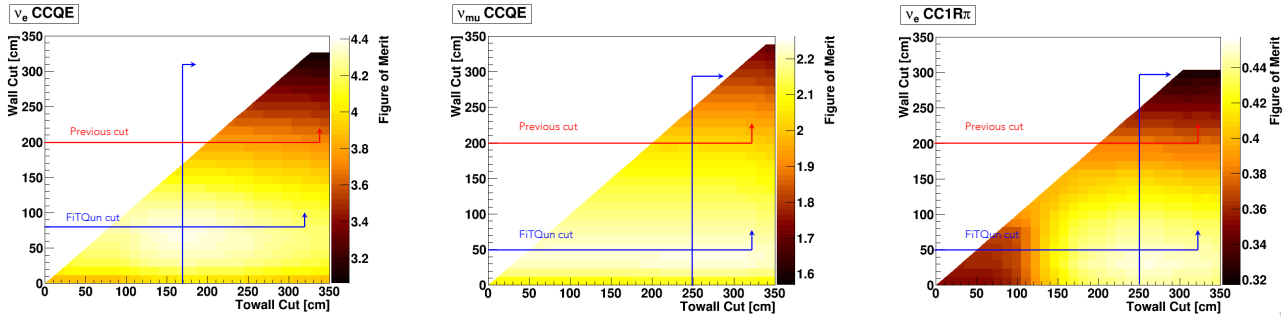

(a) ν_e (b) ν_μ (c) ν_e 1 decay electron

Figure 10.3: Figure of Merit for each event sample. Red line shows the previous FV selection, and blue lines show the fiTQun FV selection.

2. The number of rings found by fiTQun is one.
3. The ring is identified as electron-like by the single-ring fitter: $\ln(L_e/L_\mu) > 0.2p_e$, where L_e is the fiTQun single-ring e-like likelihood, L_μ is the single-ring μ-like likelihood, and p_e is the reconstructed electron momentum of the single-ring e-like hypothesis.
4. Visible energy (E_{vis}) is greater than 100 MeV
5. The number of decay electrons is zero
6. The reconstructed neutrino energy E_{rec} is less than 1250 MeV.
7. fiTQun π^0 rejection cut:$\ln(L_{\pi^0}/L_e) < 175 - 0.875m_{\pi^0}$, where L_{π^0} is the likelihood from fiTQun dedicated π^0 fit, and m_{π^0} the reconstructed π^0 mass.

We select single e-like rings in the first, second and third selections. The forth selection rejects low energy background events, which are difficult to reconstruct the neutrino energy. The fifth selection rejects the NC interaction and invisible $\mu^\pm$ events. The sixth selection cuts the high energy tails, which contains mostly beam intrinsic ν_e background. The last selection rejects the NCπ^0 production background. The selection criteria are shown in Fig. 10.4 for the FHC mode.

10.2.3 ν_e with One Decay Electron Selection

We select FHC 1Re+1d.e sample as follows. The criteria are almost the same as FHC 1Re samples except the fiducial volume and decay electron cut. The selection criteria are shown in Fig. 10.5.

1. Fully Contained events in fiducial volume (FCFV): wall $>$ 50cm, towall $>$ 250cm
2. The number of rings found by fiTQun is one.
3. The ring is identified as electron-like by the single-ring fitter: $\ln(L_e/L_\mu) > 0.2p_e$.
4. Visible energy (E_{vis}) is greater than 100 MeV
5. The number of decay electrons is one
6. The reconstructed neutrino energy E_{rec} is less than 1250 MeV.
7. fiTQun π^0 rejection cut:$\ln(L_{\pi^0}/L_e) < 175 - 0.875m_{\pi^0}$.

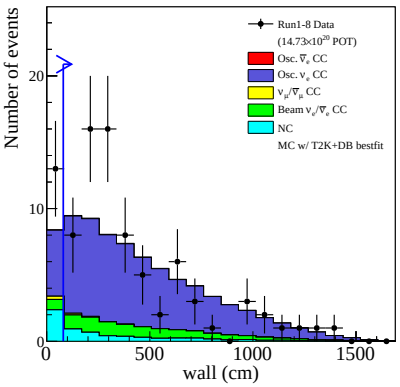

(a) wall cut

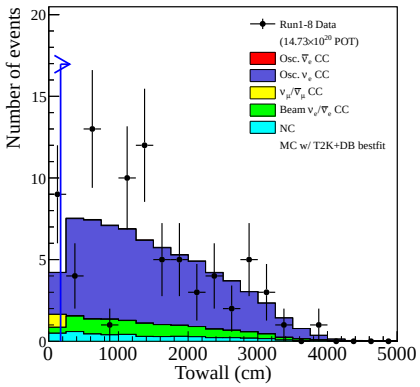

(b) Towall cut

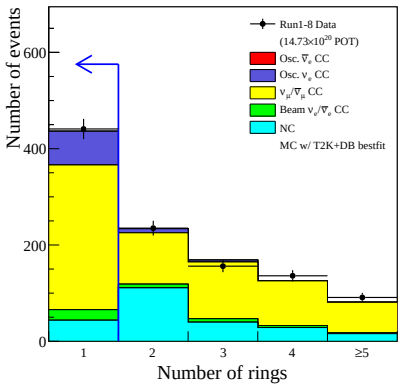

(c) Number of rings

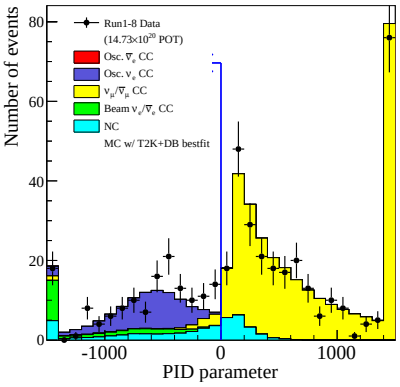

(d) PID cut

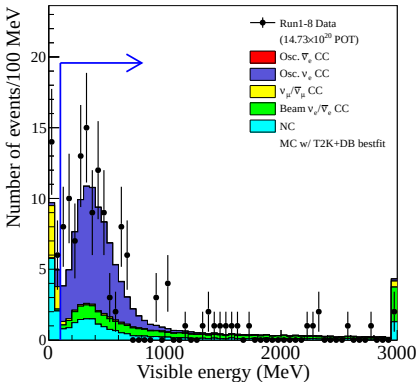

(e) Visible energy cut

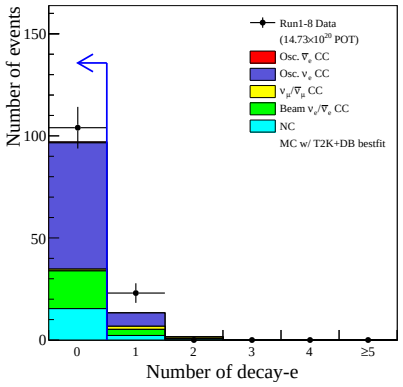

(f) number of decay electron cut

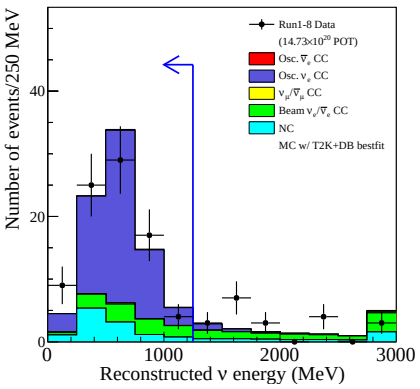

(g) Reconstructed Energy cut

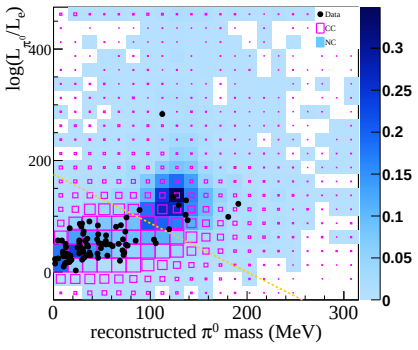

(h) π^0 cut

Figure 10.4: Cut criteria for ν_e samples

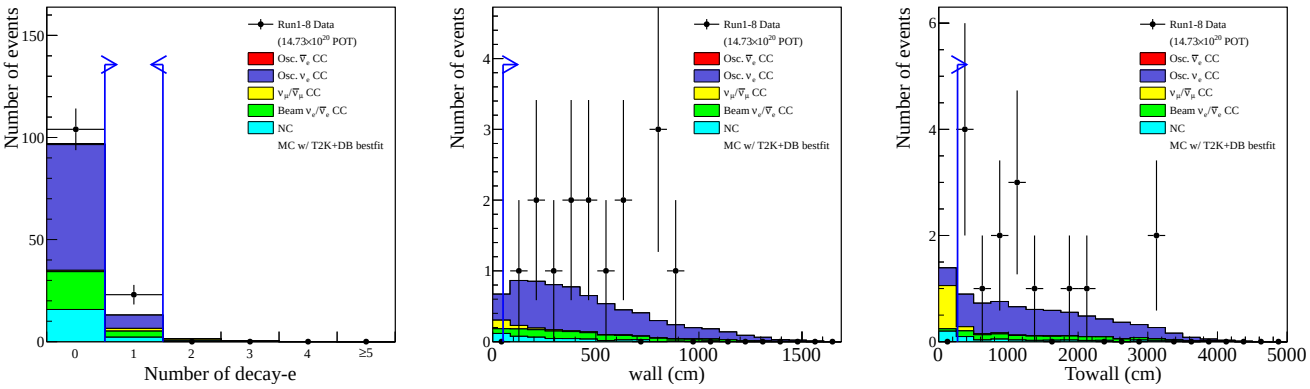

(a) number of decay electron cut (b) wall cut (c) Towall cut

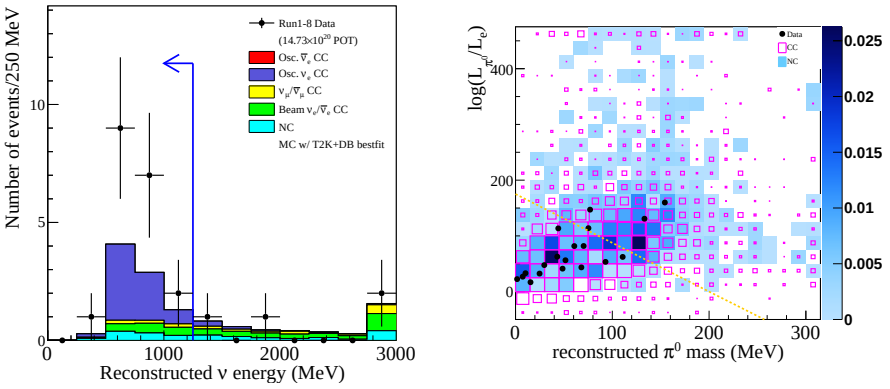

(d) Reconstructed Energy cut (e) π^0 cut

Figure 10.5: Cut criteria for ν_e 1 decay electron samples

10.2.4 ν_μ Selection

We select 1Rμ samples as follows.

1. Fully Contained events in fiducial volume (FCFV) classified by OD activity and total PMT hits as fully contained events; wall $>$ 50cm, towall $>$ 250cm.
2. The number of rings found by the fiTQun multi-ring fitter is one
3. The ring is identified as muon-like by the single-ring fitter: $\ln(L_e/L_\mu) < 0.2p_e$.
4. Reconstructed muon momentum is greater than 200 MeV.
5. The number of decay electrons is zero or one.
6. fiTQun π^+ rejection cut : $\ln(L_{\pi^+}/L_\mu) < 0.15p_\mu$, where L_{π^+} is the likelihood of fiTQun single-ring π^+ hypothesis.

We select single μ-likes ring in the first, second and third selections. The forth selection rejects low energy background events, which are difficult to reconstruct the neutrino energy. The fifth selection rejects the non-CCQE interaction. The last selection rejects NCπ^+ production background. The selection criteria are shown in Fig. 10.6 for the FHC mode.

10.3 Systematic Uncertainties

The detector errors describe the mis-characterization of the observable event topologies based on the measured cut parameters values. The detector uncertainties are calculated using control samples, atmospheric neutrino samples and hybrid-π^0 samples by Monte Carlo simulation. To estimate a set of systematic error parameters related to the fiTQun reconstruction performance, we first take the data-simulation difference in the atmospheric neutrino samples as "detector uncertainties" in Super-Kamiokande. Using these uncertainties, we generated toy data sets varying the systematic uncertainties randomly and the systematic variations on the event rates for each sample is implemented as a covariance matrix. For the cross-section and flux uncertainties, we adopted the near detector fit results. An oscillation weight is also applied derived from the oscillation parameter set A in Table 11.1.

To evaluate the systematic uncertainty in modeling π^0 in Super-Kamiokande for the ν_e sample, we construct a set of "hybrid-π^0" sample. These events are built by overlaying one electron-like ring from the SK atmospheric neutrino samples or decay electron ring from a stopping cosmic ray muon with one simulated photon ring. Figure 10.7 shows the correlation matrix and the covariance matrix of the detector systematic uncertainties for the detector systematic uncertainties. The binning of the matrix is summarized in Table 10.2.

As described in Chapter 8, FSI+SI uncertainties are independently evaluated. The SK detector simulation contains a model of the photo-nuclear (PN) effect in which a photon from a π^0 is absorbed by the nucleus. The PN effect may change the emitted yield of the Cherenkov light, therefore photon would not be reconstructed and efficiency may change. In addition to the detector systematic uncertainties, the covariance matrix for the FSI, SI and PN effects are added to the detector systematic covariance matrix in order to take these effects into account.

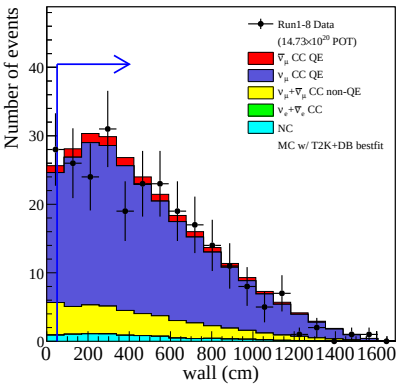

(a) wall cut

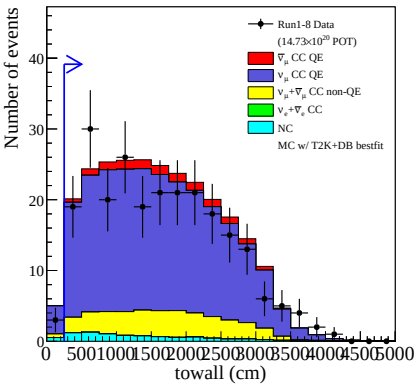

(b) Towall cut

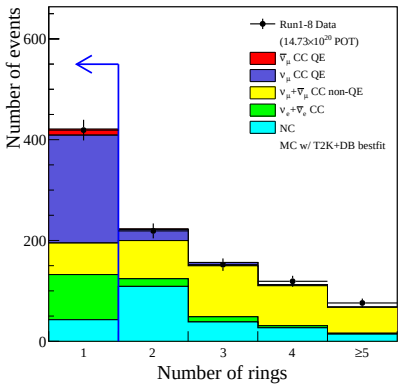

(c) Number of Rings

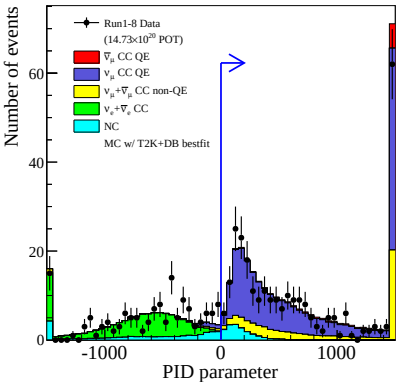

(d) PID cut

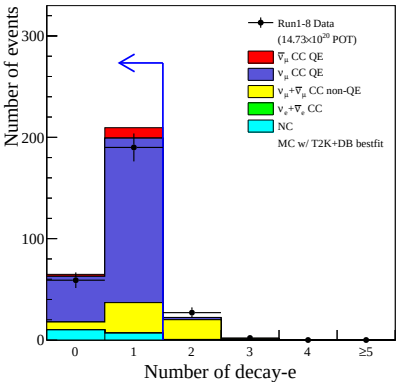

(e) number of decay electron cut

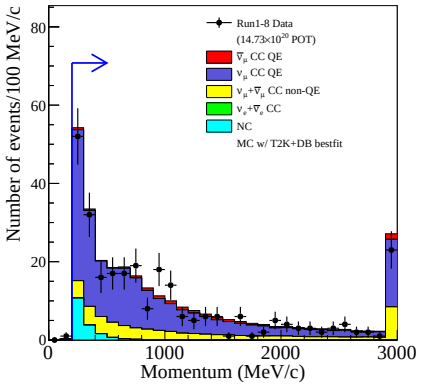

(f) Reconstructed Energy cut

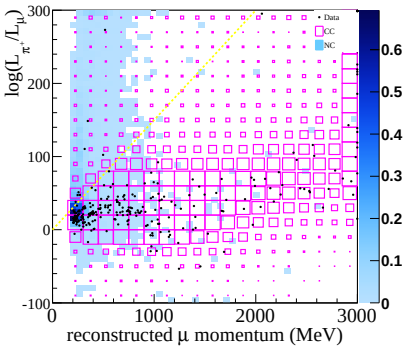

(g) π^+ cut

Figure 10.6: Cut criteria for ν_μ samples

Table 10.2: Binning of the covariance matrix

Sample		Component	E_{rec} or P Range (MeV)	Bin Number
CCQE	ν_e	Osc. ν_e	0-300	1
			300-700	2
			700-	3
		ν_μ	0-300	4
			300-700	5
			700-	6
		Beam ν_e	0-300	7
			300-700	8
			700-	9
		NC	0-300	10
			300-700	11
			700-	12
	ν_μ	ν_μ CCQE	0-400	13
			400-1100	14
			1100-30000	15
		ν_μ CC non-QE	0-30000	16
		ν_e CC	0-30000	17
		NC	0-30000	18
	$\bar{\nu}_e$	Osc. ν_e	0-300	19
			300-700	20
			700-	21
		ν_μ	0-300	22
			300-700	23
			700-	24
		Beam ν_e	0-300	25
			300-700	26
			700-	27
		NC	0-300	28
			300-700	29
			700-	30
	$\bar{\nu}_\mu$	ν_μ CCQE	0-400	31
			400-1100	32
			1100-30000	33
		ν_μ CC non-QE	0-30000	34
		ν_e CC	0-30000	35
		NC	0-30000	36
CC1π	ν_e	Osc. ν_e	0-300	37
			300-700	38
			700-	39
		ν_μ	0-300	40
			300-700	41
			700-	42
		Beam ν_e	0-300	43
			300-700	44
			700-	45
		NC	0-300	46
			300-700	47
			700-	48

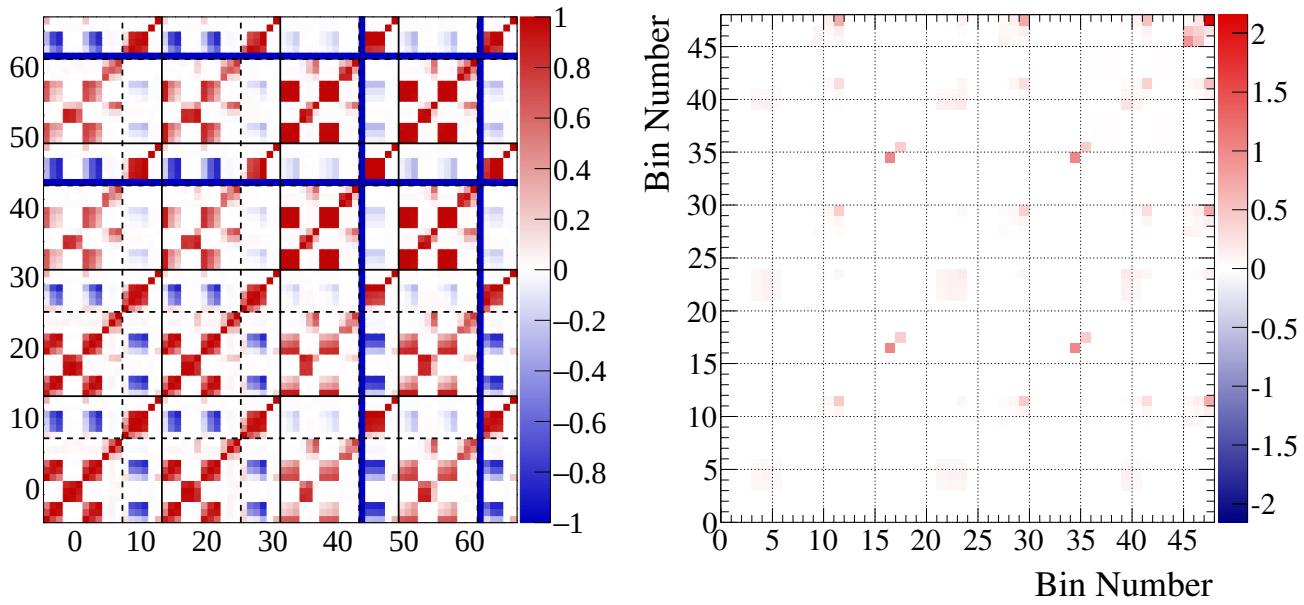

(a) Correlation Matrix

(b) Covariance Matrix

Figure 10.7: Detector systematic uncertainties of Super-Kamiokande

Chapter 11

Derivation of the Neutrino Oscillation Parameters

In this chapter, we describe the details of the oscillation fit, which derives the oscillation parameters from the observed events.

11.1 Neutrino Oscillation Parameter Sets

11.1.1 Oscillation Parameter Set

We define two sets of reference oscillation parameters which are derived from the 2016 analysis to evaluate the expected number of events. Set A represents parameter values close to the T2K best fit for Run 1-7 [71], while Set B modifies these parameters such that CP is conserved and $\sin^2\theta_{23}$ is changed to the non-maximal mixing value preferred by NOνA [100].

Table 11.1: Reference values of the neutrino oscillation parameters for Sets A and B

Parameters	Set A	Set B
Δm^2_{21}	7.53×10^{-5} eV^2	7.53×10^{-5} eV^2
Δm^2_{32}	2.509×10^{-3} eV^2	2.509×10^{-3} eV^2
$\sin^2\theta_{23}$	0.528	0.45
$\sin^2\theta_{12}$	0.304	0.304
$\sin^2\theta_{13}$	0.0219	0.0219
δ_{CP}	-1.601	0
Earth Matter density	2.6 g/cm^3	2.6 g/cm^3
Baseline Length	295 km	295 km
Mass hierarchy	Normal	Normal

11.1.2 Reactor Constraint

Reactor experiments such as Daya Bay [67], RENO [68], Double Chooz [69] give a better constraint on θ_{13} than accelerator experiments. Therefore, using this reactor constraint in the T2K oscillation analysis resolves the $\delta_{CP} - \theta_{13}$ degeneracy. We take the value and the error from PDG 2016 summary table [231]:

$$\sin^2(2\theta_{13}) = 0.0857 \pm 0.0046 \tag{11.1}$$

and so a Gaussian constraint is applied.

11.2 Fit Procedure

11.2.1 Definition of Likelihood

We fit the data to prediction at Super-Kamiokande for all of five samples (FHC 1Re, FHC 1Rμ, RHC 1Re, RHC 1Rμ, FHC 1Re+1d.e) simultaneously.

Negative Log-Likelihood

The likelihood at Super-Kamiokande after the near detector constraint Eq. (6.6) is re-written as follows:

$$\mathcal{L}(\vec{N}_e^{obs}, \vec{N}_\mu^{obs}, \vec{x}_e, \vec{x}_\mu, \vec{o}, \vec{f}) = \mathcal{L}_e(\vec{N}_e^{obs}, \vec{x}_e, \vec{o}, \vec{f}) \times \mathcal{L}_\mu(\vec{N}_\mu^{obs}, \vec{x}_\mu, \vec{o}, \vec{f}) \times \mathcal{L}_{syst.}(\vec{f}) \tag{11.2}$$

where $N_{e,\mu}^{obs}$ is the number of events of 1Re or 1Rμ candidate in Super-Kamiokande, $\vec{x}_{e,\mu}$ is the measurement variables (electron momentum and angle for 1Re events, reconstructed neutrino energy for 1Rμ events), $\vec{o}$ is the oscillation parameters and $\vec{f}$ is the systematic uncertainties.

$\mathcal{L}_e$ and $\mathcal{L}_\mu$ are the likelihood ratios defined as:

$$\mathcal{L}_{e,\mu}(N_{e,\mu}^{obs}, \vec{x}_{e,\mu}, \vec{o}, \vec{f}_i) = \frac{\prod_i^N P(N_{e,\mu}^{obs}, N_{e,\mu}^{pred}(\vec{o}, \vec{f}))}{\prod_i^N P(N_{e,\mu}^{pred}(\vec{o}, \vec{f}), N_{e,\mu}^{pred}(\vec{o}, \vec{f}))} \tag{11.3}$$

where $P(N^{obs}, N_{e,\mu}^{pred}(\vec{o}, \vec{f}))$s are the Poisson distribution and the negative log-likelihood (-2ln $\mathcal{L}$) of Eq. (11.2) is given as the sum of the likelihood for each sample.

$$\begin{aligned} -2\ln\mathcal{L}(N_{e,\mu}^{obs}, \vec{x}_e, \vec{x}_\mu, \vec{o}, \vec{f}) = 2 \sum^{N_{samples}} \sum_i^{N_{bin}} (N_i^{pred} - N_{i\ e,\mu}^{obs}) + N_{i\ e,\mu}^{obs} \ln\left(\frac{N_{i\ e,\mu}^{obs}}{N_i^{pred}}\right) \\ - \sum_{i,j}^{N_f} \Delta\vec{f}_i V_{ij}^{-1} \Delta\vec{f}_j \end{aligned} \tag{11.4}$$

The prior of systematic uncertainty is defined as a multi dimensional Gaussian distribution with covariance matrix V_{ij}.

Marginal Likelihood

We minimize Eq. (11.4) with respect to the oscillation parameters $\vec{o}$ and the systematic parameters $\vec{f}$.

$$(\vec{o},\vec{f})_{best} = argmin_{\vec{o},\vec{f}}(frm{-}e\ln\mathcal{L}_{e,\mu}(N^{obs}_{e,\mu},\vec{x}_{e,\mu},\vec{o},\vec{f})) \tag{11.5}$$

To calculate the confidence interval and the credible interval, we need to construct a likelihood function that depends only on $\vec{o}$ while taking into account the effect of the systematic uncertainties. We use a Bayesian marginalization method, in which we compute the marginal likelihood by integrating the full likelihood over the nuisance parameters $\vec{f}$ to handle the systematic uncertainties $\mathcal{L}_{syst.}(\vec{f})$.

We marginalize over the nuisance parameters using numerical integration. We throw systematic uncertainties parameters $\vec{f}$ N_{throws}=10000 times according to their prior distributions and calculate:

$$\mathcal{L}_{marg.}(N^{obs}_e,N^{obs}_\mu,\vec{x}_e,\vec{x}_\mu,\vec{o}) = \frac{1}{N_{throws}}\sum_i^{N_{throws}}\mathcal{L}_e(N^{obs}_e,\vec{x}_e,\vec{o},\vec{f}_i)\times\mathcal{L}_\mu(N^{obs}_\mu,\vec{x}_\mu,\vec{o},\vec{f}_i) \tag{11.6}$$

We then find the best fit point and calculate the confidence level and credible intervals based on the distribution of this marginal likelihood.

11.2.2 Fit Sensitivity

Confidence Level Interval

The Frequentist confidence level intervals are built using the fixed $\Delta\chi^2$ method. The $\Delta\chi^2$ function is given as:

$$\Delta\chi^2(\vec{o}) = -2\ln\frac{\mathcal{L}_{marg}(\vec{o})}{\mathcal{L}^{best}_{marg.}} \tag{11.7}$$

where $\mathcal{L}^{best}_{marg.}$ is the maximum of the marginal likelihood. We define the interval as the region of the parameter space for which the $\Delta\chi^2$ is inferior to a certain fixed value $\Delta\chi^2_{fix}$ which depends on the target coverage and number of parameters. We use the standard values presented in Table 11.2, which would give the desired coverage for the intervals assuming the likelihood is approximately Gaussian.

Table 11.2: Fixed $\Delta\chi^2$ values used for the interval calculation.

Target Coverage	1 parameter	2 parameters
68.3%(1σ)	1	2.3
90%	2.71	4.61

We maximize the marginal likelihood to the four dimensional oscillation parameters. However, it's difficult to display and calculate the sensitivity. In practice, we look at the results for only one or two parameters at a time. The remaining oscillation parameters become effectively nuisance parameters, which are marginalized over.

Credible Level Intervals

It is also possible to use the marginalized likelihoods to produce Bayesian credible intervals. The posterior probability $p(\mathbf{o}|N^{obs}_e,N^{obs}_\mu,\mathbf{x}_e,\mathbf{x}_\mu)$ for the oscillation parameters $\mathbf{o}$ after the measurement ($N^{obs.}_e$,$N^{obs.}_\mu$) is given:

$$p(\mathbf{o} \mid N_e^{obs.}, N_\mu^{obs.}, \mathbf{x}_e, \mathbf{x}_\mu) = \frac{\mathcal{L}_{marg}(N_e^{obs.}, N_\mu^{obs.}, \mathbf{x}_e, \mathbf{x}_\mu, \mathbf{o}) \cdot p(\mathbf{o})}{\int \mathcal{L}_{marg}(N_e^{obs.}, N_\mu^{obs.}, \mathbf{x}_e, \mathbf{x}_\mu, \mathbf{o}') \cdot p(\mathbf{o}')\, d\mathbf{o}'} \tag{11.8}$$

where $p(\mathbf{o})$ is the prior probability for $\mathbf{o}$. The credible interval is calculated as the region where the fraction of the likelihood lies within the target interval (Eq. (11.9)).

$$\int_{interval} p(\mathbf{o} \mid N_e^{obs.}, N_\mu^{obs.}, \mathbf{x}_e, \mathbf{x}_\mu) = \alpha\%. \tag{11.9}$$

11.3 Prediction of Observables at Super-Kamiokande

We generate the predicted number of events histograms in $p - \theta$ for 1Re sample and in E_{rec} for 1Rμ sample for each flavor, interaction category, and true neutrino energy. The number of events in each bin can be can be written as:

$$N_{pred}(b) = \sum_{C,I,e} M(C, e, I, b) P_{osc}(C, e, I) R(C, e, I, b) \tag{11.10}$$

- $M(C, e, I, b)$ represents the prediction to observe a neutrino in the (C, e, I, b) bin.
- $P_{osc}(C, e, I)$ represents the oscillation probability.
- $R(C, e, I, b)$ is the reweighting factor from the near detector constraint.

For the interaction mode and flavor category, we consider the following categories:

Interaction mode

- CCQE
- 2p2h
- CC single pion production
- CC coherent
- CC other
- NC single pion production
- NC coherent
- NC 1γ
- NC other

Flavor Category

- oscillated ν_e : $\nu_\mu \to \nu_e$
- un-oscillated ν_μ : $\nu_\mu \to \nu_\mu$
- oscillated $\bar{\nu}_e$: $\bar{\nu}_\mu \to \bar{\nu}_e$
- un-oscillated ν_μ : $\bar{\nu}_\mu \to \bar{\nu}_\mu$
- intrinsic ν_e : $\nu_e \to \nu_e$
- intrinsic $\bar{\nu}_e$: $\bar{\nu}_e \to \bar{\nu}_e$

The predicted number of events are shown in Table 11.3 for each δ_{CP} value, and the $p - \cos\theta$ distribution for 1Re sample and the reconstructed energy spectrum for 1Rμ are shown in Fig. 11.1. The oscillation parameter set A is used in these plots.

Table 11.3: Predicted number of events table using oscillation parameter set A while varying δ_{CP}

	$\delta_{CP} = -\pi/2$	$\delta_{CP} = 0$	$\delta_{CP} = \pi/2$	$\delta_{CP} = \pi$
FHC 1Rμ	267.755	267.409	267.725	268.163
FHC 1Re	73.512	61.463	49.931	61.980
RHC 1Rμ	63.054	62.910	63.055	63.211
RHC 1Re	7.921	9.035	10.044	8.930
FHC 1Re+1d.e	6.923	6.010	4.868	5.781

11.4 Systematic Uncertainties

The uncertainties on the predicted number of events are estimated by making 10,000 throws of the systematic and oscillation parameters and evaluating the standard deviation of the predicted number of events among the throws. Table 11.4 shows the summary of the errors. We consider the systematic errors of the cross-section and flux parameters from the near detector fit, and the detector systematic uncertainties including FSI+SI+PN. However, there may exist additional systematic uncertainties which are not constrained from the near detector fit which will be discussed in the next chapter. Figure 11.2 shows comparisons between with and without the near detector fit constraint. The near detector fit significantly reduces the uncertainties on the prediction at Super-Kamiokande by approximately 60%.

11.5 Sensitivity

In order to estimate the T2K ability to measure oscillation parameters, the analysis is first performed with the simulated data using actual result of the near detector fit. The sensitivity obtained as a

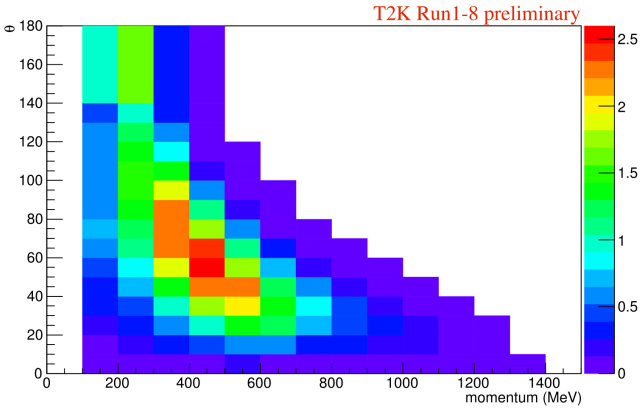

(a) FHC 1Re

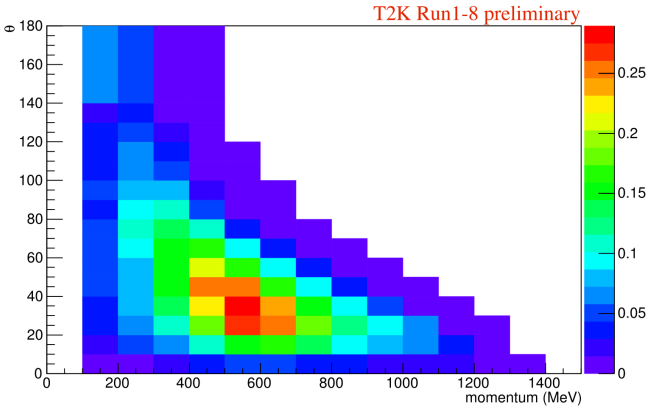

(b) RHC 1Re

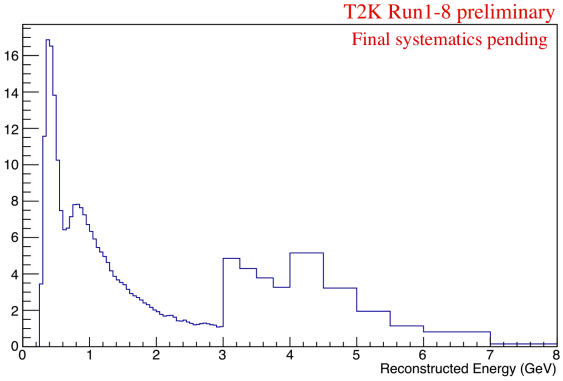

(c) FHC 1Rμ

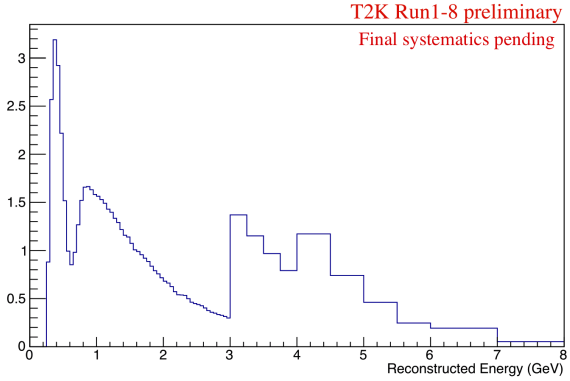

(d) RHC 1Rμ

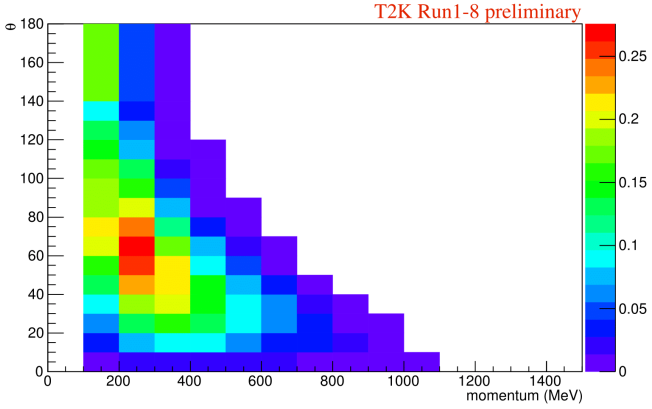

(e) FHC 1Re+1d.e

Figure 11.1: Predicted number of events and spectrum in $p - \cos\theta$ and E_{rec} of each sample.

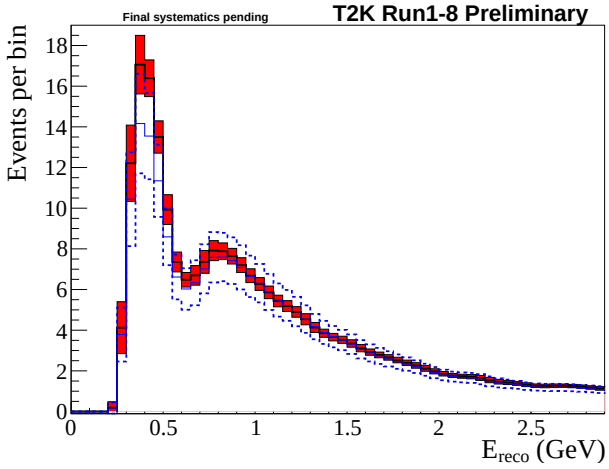

(a) FHC 1Rμ sample

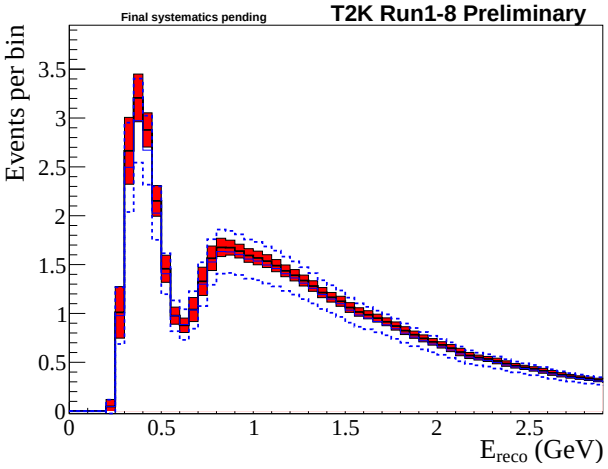

(b) RHC 1Rμ sample

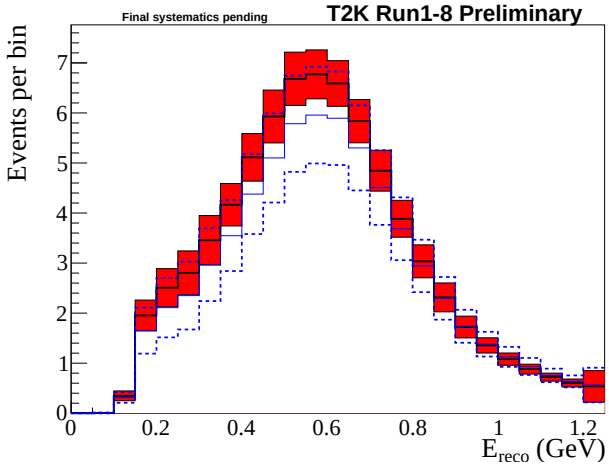

(c) FHC 1Re sample

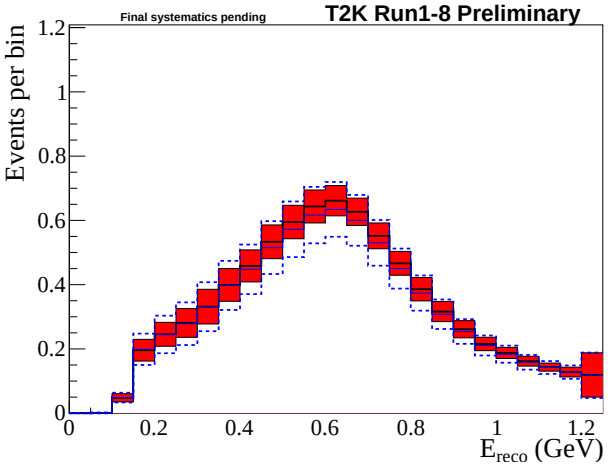

(d) RHC 1Re sample

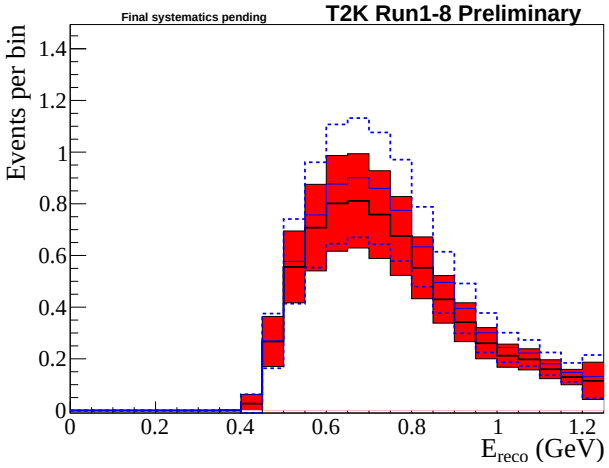

(e) FHC 1Re+1d.e sample

Figure 11.2: Energy spectrum Comparison at Super-Kamiokande with and without the near detector fit. Blue solid line shows the predicted spectrum before the fit, blue dashed line shows the 1σ error band without the near detector fit. Black line and red bands show the predicted spectrum and error with the near detector fit.

Table 11.4: Percent errors on the predicted number of events in each sample. The last column is the error on the ratio of the predicted number of events in the FHC and RHC mode 1Re samples.

	1Rμ		1Re			
Error Source	FHC	RHC	FHC	RHC	FHC+1d.e.	FHC/RHC
SK Detector	1.9	1.6	3.0	4.2	16.5	1.6
SK FSI+SI+PN	2.2	2.0	2.9	2.5	11.3	1.6
SK Detector+FSI+SI+PN	2.9	2.5	4.2	4.8	19.2	2.1
w/o ND280 const. flux & xsec	14.5	12.0	15.2	12.3	11.7	
w/ ND280 const. flux & xsec	3.3	2.7	3.2	2.9	4.1	2.5
$\sigma(\nu_e)/\sigma(\nu_\mu)$, $\sigma(\bar{\nu}_e)/\sigma(\bar{\nu}_\mu)$	0.0	0.0	2.6	1.5	2.6	3.1
NC1γ	0.0	0.0	1.1	2.6	0.3	1.5
NC Other	0.3	0.3	0.1	0.3	1.0	0.2
Syst. Total	4.4	3.8	6.3	6.4	19.6	4.7

confidence interval of the simulated data [1] for the parameter set A are shown in Fig. 11.3. The sensitivity study for parameter Set B is shown in Appendix G. The CP violation sensitivity where $\delta_{CP} \neq 0, \pi$ reaches to the 1σ with the reactor constraint and the normal hierarchy is slightly preferred. For $\sin^2\theta_{23}$, lower octant ($\sin^2\theta_{23} < 0.5$) is slightly preferred without the reactor constraint case, while higher octant (($\sin^2\theta_{23} > 0.5$) is preferred with the reactor constraint.

[1] In this thesis, the frequentist confidence level interval is referred to as "Sensitivity", and we take Bayesian credible intervals as fit results in the actual data fit.

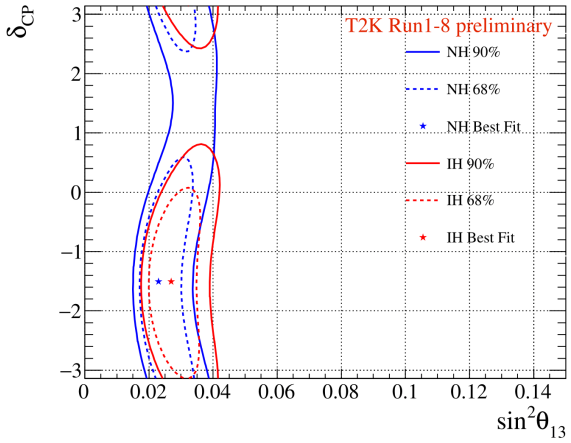

(a) $\sin^2\theta_{13} - \delta_{CP}$ without reactor constraint

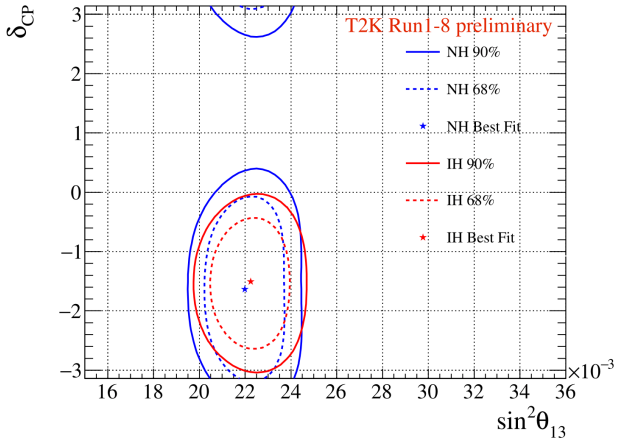

(b) $\sin^2\theta_{13} - \delta_{CP}$ with reactor constraint

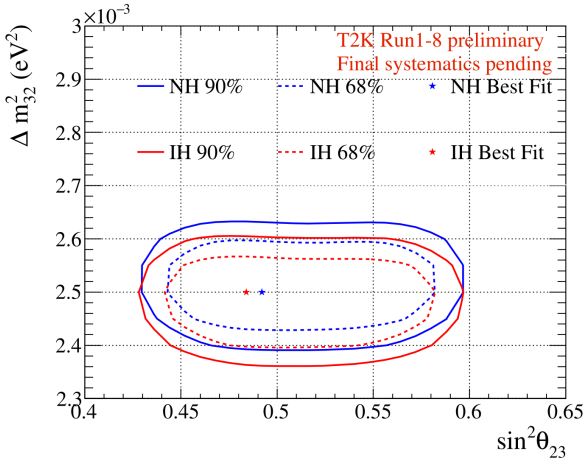

(c) $\sin^2\theta_{23} - \Delta m^2_{32}$ without reactor constraint

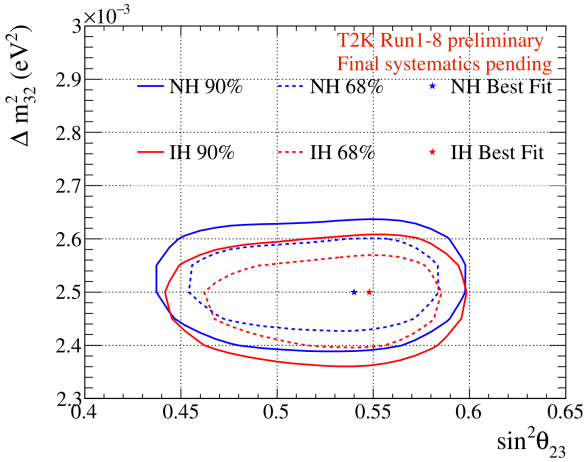

(d) $\sin^2\theta_{23} - \Delta m^2_{32}$ with reactor constraint

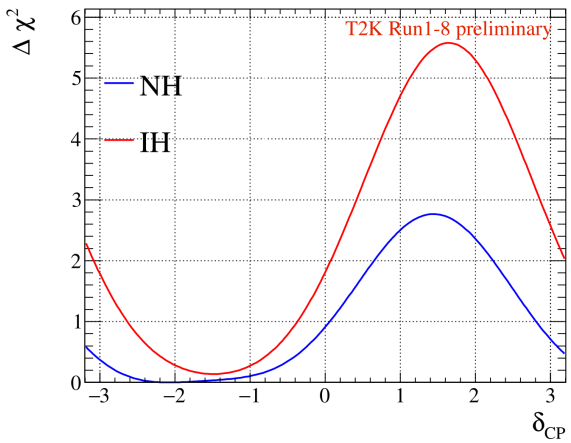

(e) 1D δ_{CP} without reactor constraint

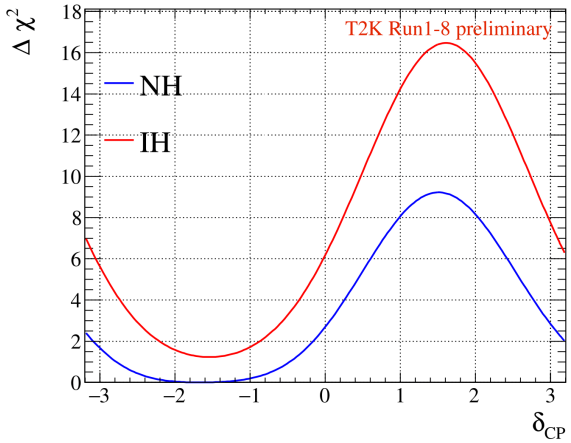

(f) 1D δ_{CP} with reactor constraint

Figure 11.3: Sensitivity curve for each oscillation parameter and 2D confidence level contours for $\sin^2\theta_{13} - \delta_{CP}$ and $\Delta m^2_{32} - \sin^2\theta_{23}$

Chapter 12

Neutrino Interaction Studies for the Oscillation Analysis

As shown in the Chapter 8, there exist various neutrino-nucleus interaction models. A different interaction model predicts different cross-section, and changes the expected event rates and energy spectra both at ND280 and Super-Kamiokande. This change would cause some effects on the oscillation analysis. In this chapter, we describe the investigation of the effects of the neutrino-nucleus interaction model on the oscillation analysis.

12.1 The Effects of the Neutrino-nucleus Interaction Models in the Oscillation Analysis

As explained in Chapter 9, we fitted our model to the observed data and tuned the cross-section and flux parameters to make the model close to the data at ND280. The near detector fit can compensate differences between the models and the ND280 data by optimizing the cross-section and flux parameters. However, the fit does not always predict the event rates correctly. The oscillation analysis with such a wrong prediction may cause systematic shifts on the measured oscillation parameters. In this chapter, this systematic shift is referred to as "bias". The illustration of how the bias emerges is shown in Fig. 12.1. Even though the near detector fit can compensate the differences, the prediction at Super-Kamiokande may change in a different way from the changes at ND280 since the flux shape and the event selection at ND280 are different from those at Super-Kamiokande. As shown in Chapter 11, the oscillation fit is done by comparing observed data with the predicted spectrum. Therefore, the wrong prediction directly affects the determination of the oscillation parameters. To avoid the oscillation parameters bias, it is important to check whether the near detector fit and our parameterization of the neutrino interaction model is robust against the possible variation of the model in the oscillation analysis.

In the T2K oscillation analysis, we use interaction models based on the NEUT simulation and on a certain interaction model by Nieves. [167, 189, 218]. In this chapter, we call this model "nominal". As described in Chapter 8, there exist several neutrino-nucleus interaction models which predict different cross sections and there are still large theoretical uncertainties. If a different interaction model from nominal one is used in the simulation, the predicted event rates at ND280 and Super-Kamiokande could be changed. As described in Section 8.4.1, the parameters and their systematic uncertainties of the neutrino interaction is estimated based on the nominal model, therefore, it is

also possible that the near detector fit cannot cover the difference if an interaction model that is not yet implemented in the simulation is used. As a result, the choice and the variation of interaction models are possible sources of the systematic bias. Hence, we performed simulated data studies with the following procedure to investigate the systematic bias due to the interaction modeling in the T2K oscillation analysis.

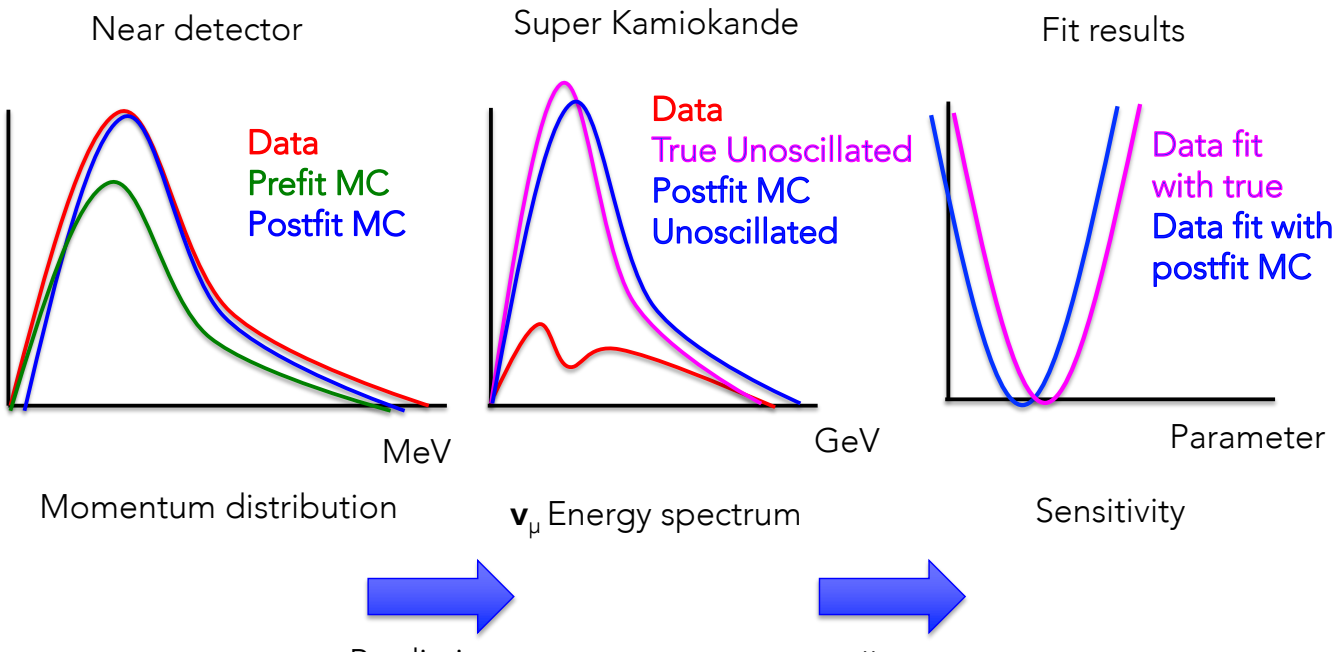

Figure 12.1: The schematic view of the fitting bias due to a wrong model

12.2 Procedure of the Simulated Data Study

Figure 12.2 shows an overview of the simulated data study. This study is done by generating "simulated" data sets at ND280 and Super-Kamiokande and fitting them instead of actual data with the current oscillation analysis framework. The left side in Fig. 12.2 shows the oscillation analysis with the simulated data of the nominal model. These fit results can be taken as the results when the prediction is perfect and "reference values" for this study. These results are referred to as "Asimov" in the latter sections [1]. Figure 12.3 shows the sensitivity for the nominal model simulated data with the reactor constraint assuming the normal hierarchy using parameter set A.

The right side of Fig. 12.2 shows the oscillation analysis with an alternative model. We replace the simulated data with the nominal model by those with an alternative model. To avoid a confusion, we refer to the simulated data of such an alternative model as simply simulated data, and we call specially the simulated data of the nominal model as "Asimov" data. The near detector fit compensates the difference between the nominal model and the alternative model by changing the parameters of the near detector fit. If the parameterization of the near detector fit can fully compensate the difference between the nominal model and the alternative model, the prediction at Super-Kamiokande from the near detector fit would match the expectation from the alternative model. The oscillation fit results then would match the Asimov fit results. If not, the prediction from the near detector fit and the

[1] This Asimov fit result is different from that in Chapter 11. The Asimov sensitivity shown in Chapter 11 use actual data fit results at near detector. On the other hand, the Asimov sensitivity in this chapter uses the simulated data of the nominal model in the near detector fit.

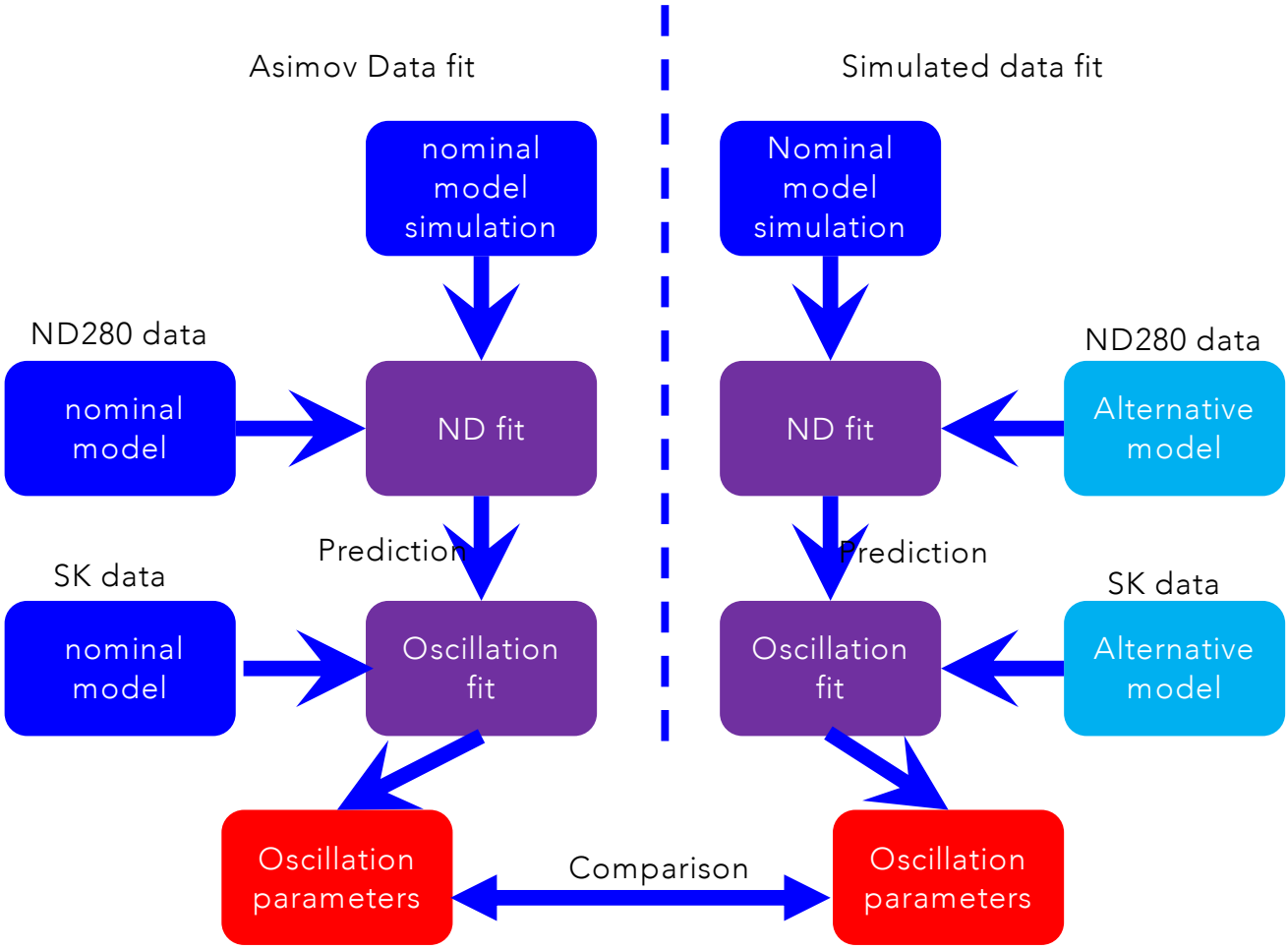

Figure 12.2: Procedure of simulated data study

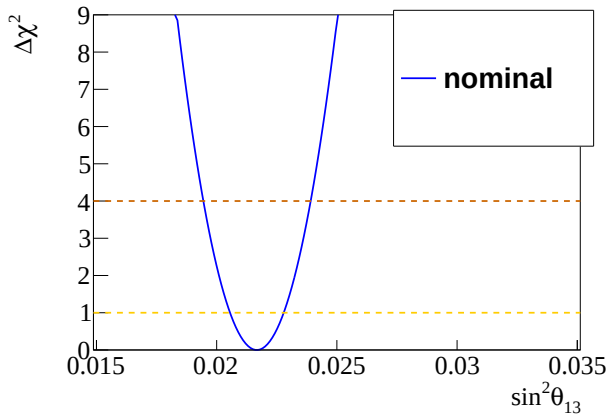

(a) $\sin\theta_{13}$

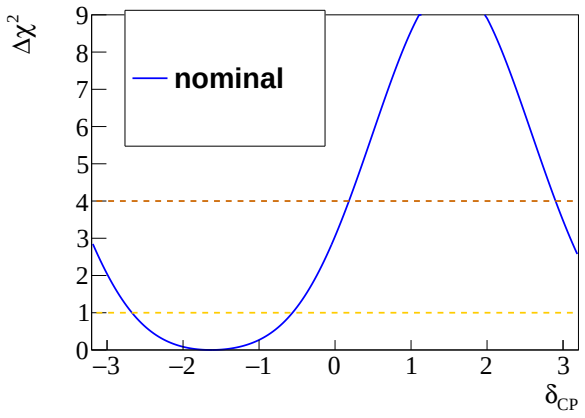

(b) δ_{CP}

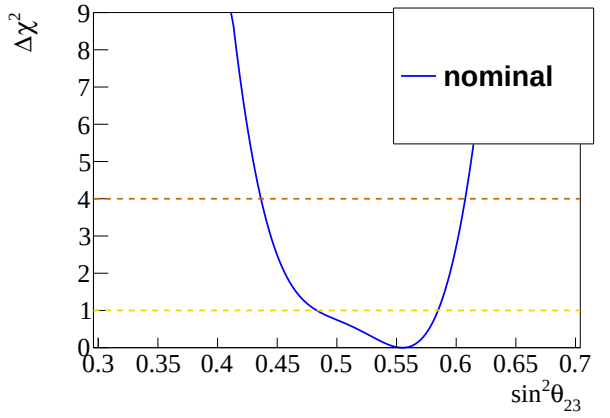

(c) $\sin\theta_{23}$

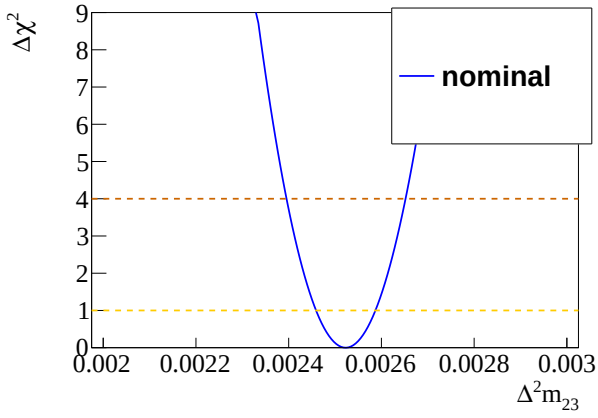

(d) Δm^2_{32}

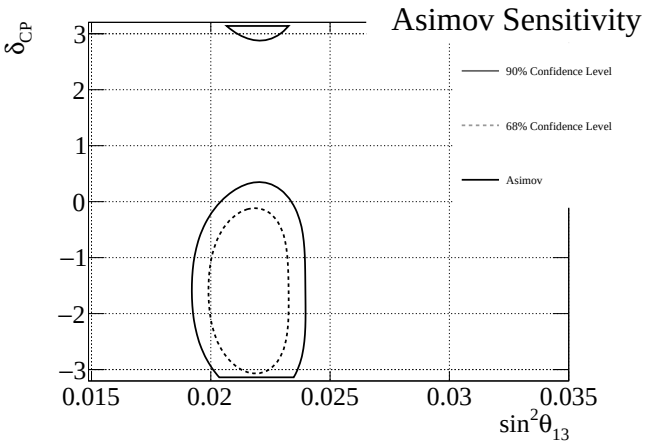

(e) $\delta_{CP} - \sin^2\theta_{13}$

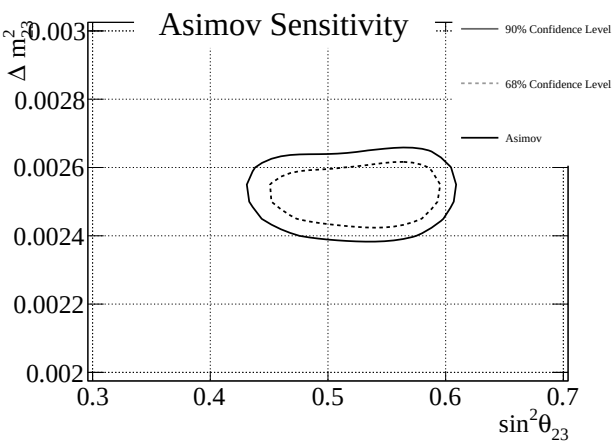

(f) $\Delta m^2_{32} - \sin^2\theta_{23}$

Figure 12.3: The one dimensional sensitivity curves and the 2D 68% and 90% contours for nominal simulated data fits including the reactor constraint on $\sin^2\theta_{13}$, assuming the normal hierarchy. Parameter set A is used.

expectation from the alternative model would have a discrepancy. In this case, oscillation fit results may have a systematic bias. We therefore compared the Asimov fit results with the simulated data fit results to verify the systematic bias.

We generated three types of simulated data as possible variations of the models in the oscillation analysis: the alternative cross-section model which is described in Section 8.3, binding energy variation described in Section 8.4, and the simulated data for data-simulation difference (data-driven simulated data) described in Chapter 9[2]. In all three cases, we generated 2D histograms in reconstructed muon momentum versus cosine of the muon angle, corresponding to the 14 samples used in the near detector fit by applying weighting factors in each bin corresponding the model difference (see Chapter 9 for more details). The simulated data at Super-Kamiokande was generated in a similar way as ND280.

Bias Definition

We calculated the bias from the mean points of the 1σ and 2σ intervals instead of the best fit points considering non-Gaussianity of some parameters. The 1σ and 2σ intervals are calculated as the width of the allowed region at each confidence level (yellow line for 1σ and brown line for 2σ in the sensitivity curves in Fig. 12.3). We also considered the several definitions of σ. We calculated the statistic only σ with toy simulation throwing without the systematics (referred as $\sigma_{stat.}$) and systematic only σ as $\sigma_{syst.} = \sqrt{\sigma^2 - \sigma^2_{stat.}}$ [3]. Table 12.1 shows the mean of the 1σ and 2σ intervals of the fit results of Asimov data [4].

Table 12.1: Mean of the 1σ and 2σ intervals of the fit results of Asimov data for each parameter

		$\sin^2\theta_{23}$	Δm^2_{32} (eV^2)	δ_{CP}
Asimov A	Mean of the 1σ interval	0.5279	2.526e-3	-1.457
	1σ interval size	0.05592	6.2e-5	1.313
	$1\sigma_{Stat}$ interval size	0.04943	5.6e-5	1.289
	$1\sigma_{Syst} = \sqrt{\sigma^2_{Syst+Stat} - \sigma^2_{Stat}}$	0.02614	2.6e-5	0.2499
	Mean of the 2σ interval	0.5214	2.524e-3	-1.357
	2σ interval size	0.08983	1.39e-4	2.312
	$2\sigma_{Stat}$ interval size	0.08399	1.315e-4	1.935
	$2\sigma_{Syst} = \sqrt{(2\sigma_{Syst+Stat})^2 - (2\sigma_{Stat})^2}$	0.03186	4.5e-5	1.265
Asimov B	Mean of the 1σ interval	0.4630 and 0.5701	2.533e-3	1.629
	1σ interval size	0.03237 and 0.02543	6.35e-5	1.901
	$1\sigma_{Stat}$ interval size	0.03477 and 0.0283	6.2e-5	1.775
	$1\sigma_{Syst} = \sqrt{\sigma^2_{Syst+Stat} - \sigma^2_{Stat}}$	Not calculated	1.37e-5	0.6805
	Mean of the 2σ interval	0.5159	2.533e-3	Not calculated
	2σ interval size	0.1103	1.45e-4	Not calculated
	$2\sigma_{Stat}$ interval size	0.10445	1.395e-5	Not calculated
	$2\sigma_{Syst} = \sqrt{(2\sigma_{Syst+Stat})^2 - (2\sigma_{Stat})^2}$	0.03544	4.0e-5	Not calculated

We did the same thing for each simulated data and computed the bias as:

[2] We refer to all of three types of variations simply as "alternative model".

[3] σ without subscript is $\sigma_{stat.+syst.}$, which is the normal definition of σ

[4] We cannot define the 2σ of δ_{CP} for parameter set B since the sensitivity doesn't reach to 2σ. We also cannot define $1\sigma_{syst}$ of $\sin\theta_{23}$ since it also doesn't reach to 1σ

$$\text{bias} = \frac{|\text{mean}_{Asimov} - \text{mean}_{simulated}|}{\sigma_{Asimov}}. \quad (12.1)$$

This value simply shows how much the mean point is shifted relative to the nominal uncertainty of the oscillation parameter. We fitted the simulated data both for oscillation parameter sets A and B. The results for parameter set B are shown in Appendix J since the tendency is similar to that for parameter set A. We also tested the fit without the reactor constraint and the inverted hierarchy conditions. However, we focus on the fit with the reactor constraint and the normal hierarchy here since they give the tightest constraint on the oscillation parameters, therefore the bias affects largely.

12.3 Alternative Interaction Models

We investigated the following alternative interaction models. We generated weighting factor corresponding to each interaction mode and variables (reconstructed neutrino energy, true neutrino energy, $\cos\theta$ and so on) depending on each model. The detail of each model was already described in Section 8.3.

- Alternative form factor (z-expansion, 3-component)
- Martini 2p2h model
- Spectral function (SF)
- Nieves 1p1h - NEUT CCQE difference
- Kabirnezhad single pion production model

We show the fit results of the Kabirnezhad model simulated data, which show the large bias in this study. For the other simulated data, the bias is relatively small, and we just show the summary in Section 12.3.2.

12.3.1 Fit Results of Kabirnezhad model Simulated Data

We generated the simulated data for the Kabirnezhad model at ND280 and Super-Kamiokande with $E_{true} - \cos\theta$ weight. The ND280 CC0π and CC1π $p - \cos\theta$ distribution for the simulated data of the Kabirnezhad model and the ratios to the nominal model are shown in Fig. 12.4.

The Kabirnezhad model changes not only the CC1π distribution but also the CC0π distribution at low momentum muon via FSI. The fit results of the simulated data and comparison to the Asimov data are shown in Fig. 12.5[5]. The fit result changes the CC1π parameters ($M_A^{res}, C_A^5(0), ISO\_BKG$) as expected. It also changes the CC0π parameters especially 2p2h. The event decrease in CC0π sample should be compensated by CC1π related parameters, however the fit reduces the event by changing 2p2h parameters to non PDD-like. This indicates that the near detector fit misidentifies the CC1π events as the 2p2h events.

A comparison of the Kabirnezhad model simulated data, the prediction from the near detector fit and Asimov data at Super-Kamiokande is shown in Fig. 12.6. It shows that the simulated data spectrum at Super-Kamiokande decreases relative to the Asimov data at the low energy region in 1Re samples and dip region in 1Rμ samples, and increases at high energy region. It also shows that the prediction from the near detector fit to the Kabirnezhad model simulated data tends to

[5]The order of the flux parameters are described in Chapter 7.

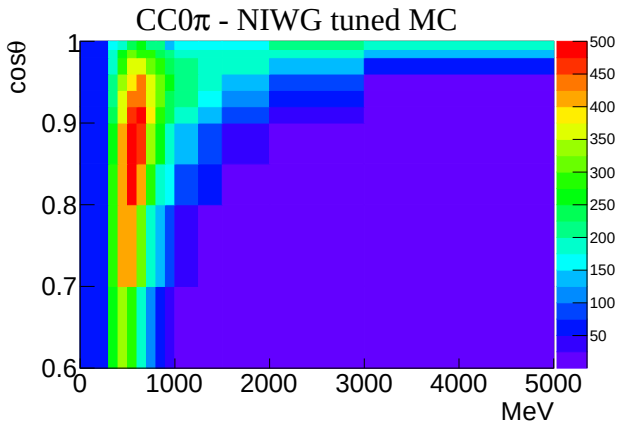

(a) CC0π

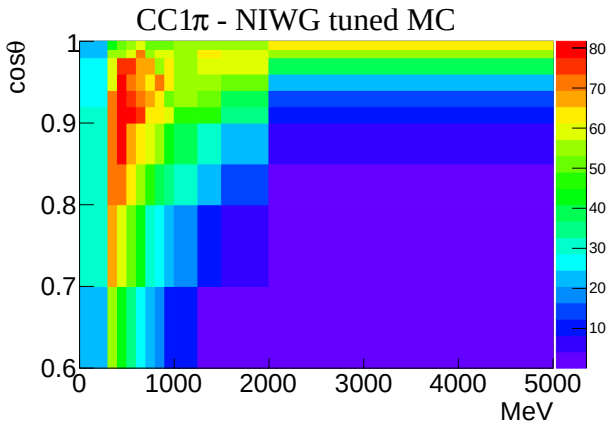

(b) CC1π

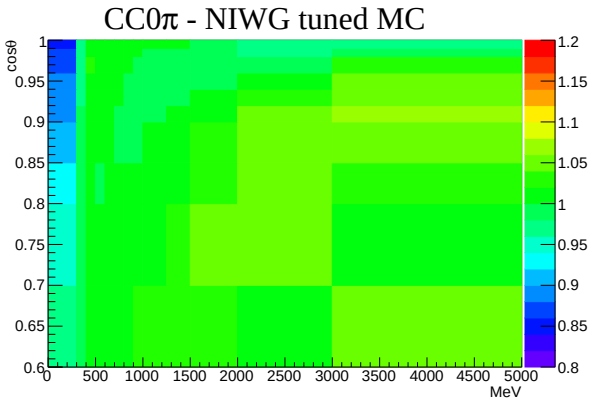

(c) CC0π ratio to the Asimov data

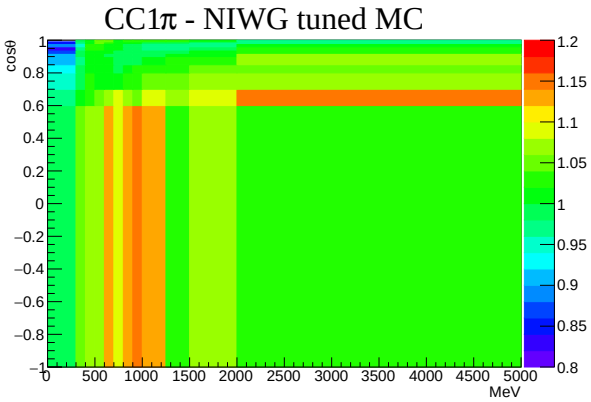

(d) CC1π ratio to the Asimov data

Figure 12.4: CC0π and CC1π $p - \cos\theta$ distributions for the Kabirnezhad model simulated data at ND280 and the ratio of Kabirnezhad model to the Asimov data at ND280.

overpredict the events compared to the simulated data in the 1Re and 1Rμ samples. For FHC 1Re+1d.e sample, the spectrum changes largely. The simulated data is within the error of the near detector fit prediction. However, the center values of the prediction are deviated largely from the Kabirnezhad model simulated data. This indicates that the nominal model doesn't have enough degree of freedom for the CC1π parameters to fully cover the Kabirnezhad model.

The 1D sensitivity curves for $\sin^2\theta_{23}$ and Δm^2_{32} are shown in Fig. 12.7. The fit result has a tighter constraint on the $\sin^2\theta_{23}$ sensitivity and the best fit point of Δm^2_{32} is slightly shifted to the lower value. The fit results for $\sin^2\theta_{13} - \delta_{CP}$ contours are almost the same as the Asimov sensitivity.

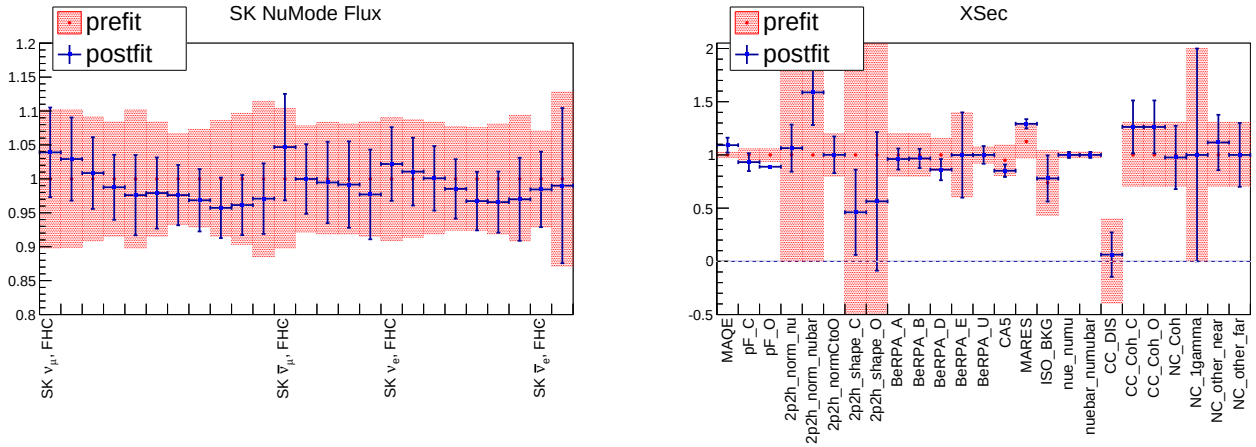

(a) SK flux

(b) Cross-section

Figure 12.5: Best-fit parameters from the near detector fit to the Kabirnezhad model simulated data and prefit parameters.

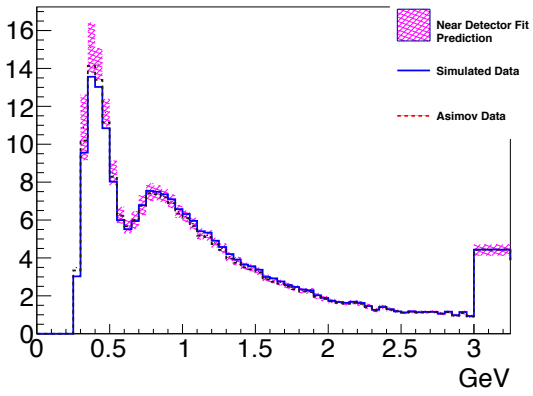

(a) FHC 1Rμ sample

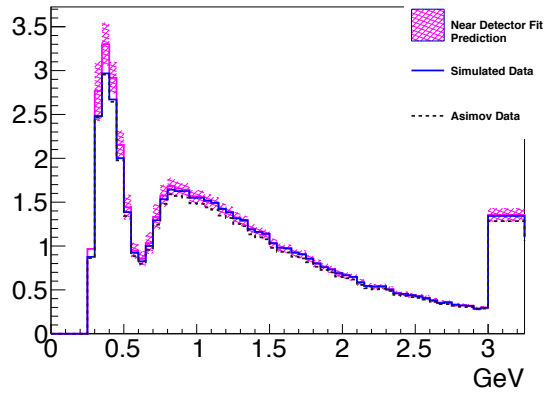

(b) RHC 1Rμ sample

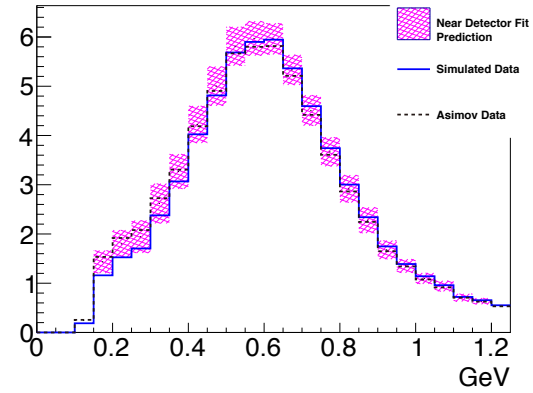

(c) FHC 1Re sample

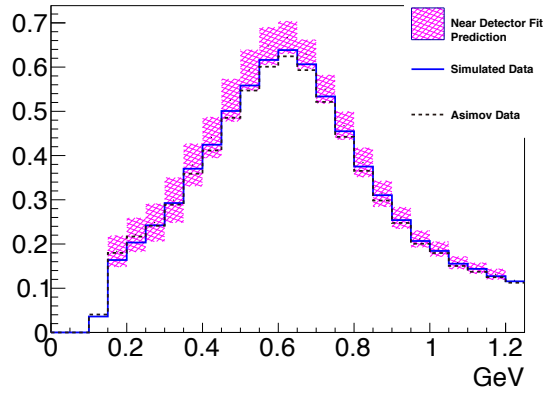

(d) RHC 1Re sample

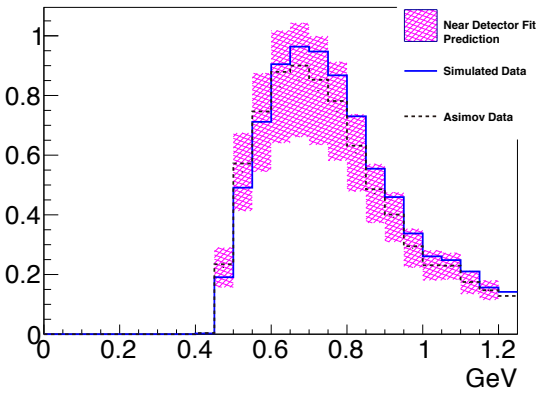

(e) FHC 1Re+1d.e. sample

Figure 12.6: Comparison between the Asimov data (Black), the Kabirnezhad model simulated data expectation (Blue), and the prediction from the near detector fit to the simulated data (Magenta).

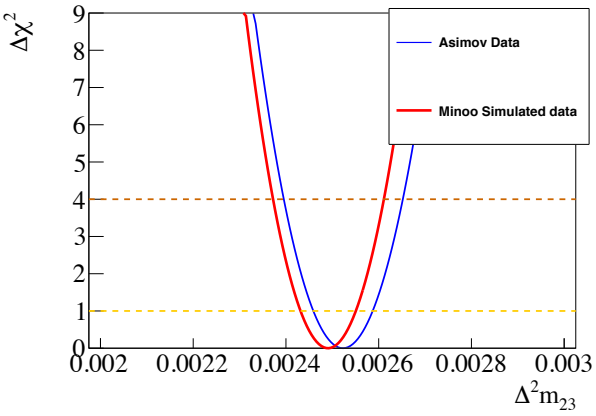

(a) Δm^2_{32}

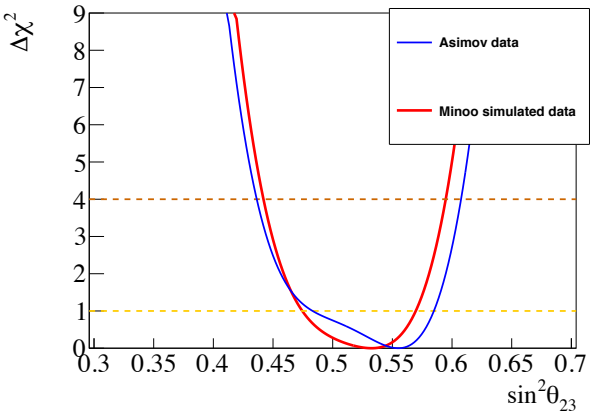

(b) $\sin^2\theta_{23}$

Figure 12.7: The 1D sensitivity curves of $\sin^2\theta_{23}$ and Δm^2_{32} for the Kabirnezhad (Minoo) model simulated data fit and the Asimov data fit

Table 12.2: Bias study of the Kabirnezhad model simulated data

		$\sin^2\theta_{23}$	Δm^2_{32} (eV^2)	δ_{CP}
Asimov A	Mean of the 1σ interval	0.521	2.549e-3	-1.521
	1σ interval size	0.046	5.775e-5	1.217
	Bias computed with the 1σ mean and interval	**12%**	**55%**	**4.9%**
	Bias relative to σ_{Syst} computed with the 1σ mean and interval	**25%**	**130%**	**26%**
	Mean of the 2σ interval	0.517	2.492e-3	-1.540
	2σ interval size	0.0745	1.155e-5	2.00
	Bias computed with the 2σ mean and interval	**4.5%**	**23%**	**7.9%**
	Bias relative to σ_{Syst} computed with the 2σ mean and interval	**13%**	**71%**	**15%**

Bias Study

Table 12.2 shows the result of the calculated biases for the Kabirnezhad model simulated data. The biases for θ_{23} and δ_{CP} are 12% and 4.9% of the total uncertainty, and 25% and 26% of the systematic uncertainty, respectively. The most biased parameter is Δm^2_{32}. The bias is 55% of the total uncertainty and 130% of the systematic uncertainty. We took into account the effect of this bias in the oscillation analysis by the smearing method which is described in Section 12.6.

12.3.2 Summary of the Other Simulated Data Study

Here is the brief summary of the results of the other simulated data studies. Computed biases are shown as the reference values in Table 12.8.

Alternative Form Factor

The near detector fits of the alternative form factors simulated data show large change in M_A^{QE} and small change for the 2p2h and BeRPA parameters in all cases. The large change in M_A^{QE} is expected since this parameter is related to the axial form factor. The flux parameters are almost unchanged. In all cases, the near detector fit is able to predict the Super-Kamiokande simulated data well and no big change is observed in the oscillation fit results. This indicates that the model difference of the form factor is well absorbed mostly by the parameter M_A. Since the form factor mis-modeling has no impact on the oscillation analysis, no action was taken to include these uncertainties in the oscillation analysis.

Martini 2p2h

Martini simulated data changes the amount of the 2p2h events. The near detector fit results show the difference is well covered by the 2p2h parameters. The near detector fit prediction agrees the simulated data at Super-Kamiokande and the oscillation fit results don't show significant changes in all parameters.

Spectral Function

In the near detector fit, most of the cross-section parameters move only slightly. The 2p2h normalization goes up and 2p2h becomes more PDD-like. In both 1Re and 1Rμ samples, the prediction from the near detector fit tends to slightly overestimate the Super-Kamiokande simulated data, but the simulated data is within the error of the prediction of the near detector fit. The oscillation fit result is not affected by this difference.

Nieves 1p1h – NEUT CCQE Difference

For the near detector fit of the Nieves model simulated data, the flux parameters fitted to the simulated data are slightly decreased, mostly in low energy bins. Most of the cross-section parameters move only slightly, except for the decrease of the BeRPA A for low Q^2 events, and 2p2h shape parameters going towards more non-PDD like values. This simulated data partially changes CCQE (1p1h) events, thus the fit results indicate that the fit mis-identified some of the 1p1h events as the 2p2h events. For the spectrum at Super-Kamiokande, the prediction from the near detector fit tends to underestimate the simulated data of Super-Kamiokande in both 1Rμ and 1Re samples. The oscillation fit results for $\sin^2\theta_{13} - \delta_{CP}$ contours show no big difference. However, the best fit point of the Δm^2_{32} is shifted to the lower value and the $\sin^2\theta_{23}$ sensitivity is slightly tighter than the nominal model. We took into account the effect of this bias in the oscillation analysis by the smearing method which is described in Section 12.6.

12.4 Binding Energy Variation

As described in Chapter 9, the binding energy parameters were not used in the T2K oscillation analysis because of limitations of the reweighting procedure. Therefore, a simulated data study was performed to understand the biases from the lack of the binding energy parameters. The 2D templates, $E_\nu - \theta_\mu$, were produced for each neutrino species, both targets (carbon and oxygen) and the different binding energy values. The binding energy values were set at: 16MeV, 34 MeV (nominal) and 43 MeV on carbon, 18 MeV, 36 MeV (nominal) and 45 MeV on oxygen.

12.4.1 Fit Results of Biding Energy Simulated Data

For the binding energy variation, we tested the variation for the maximum value (43 MeV for carbon and 45 MeV for oxygen) and a minimum value (16 MeV for carbon and 18 MeV for oxygen). Here we show the results for the maximum value variation. In this chapter, we call this simulated data as binding energy simulated data. The CC0π $p - \cos\theta$ distribution of the binding energy simulated data and its ratio to the nominal model are shown in Fig. 12.8.

The binding energy variation migrates events in the 1000 MeV region to the lower momentum region by 10% in the CC0π sample. The fit results of the simulated data and the comparison to the Asimov data fit are shown in Fig. 12.9. The lower energy flux parameters are shifted to enhance the events at the low momentum regions of the CC0π muon distribution. The 2p2h events became more PDD-like and increased by 20%, which indicates the CCQE events enhanced by the binding energy are mis-identified as the 2p2h events. A comparison of the binding energy simulated data, Asimov data and the prediction from the near detector fit at Super-Kamiokande is shown in Fig. 12.10. It shows that the change of the binding energy shifts the peak of the ν_e samples and the dip in the ν_μ samples. It also shows the prediction from the near detector fit cannot cover the shifts of the peak and dip points, and the simulated data below 0.7 GeV are out of the prediction from the near

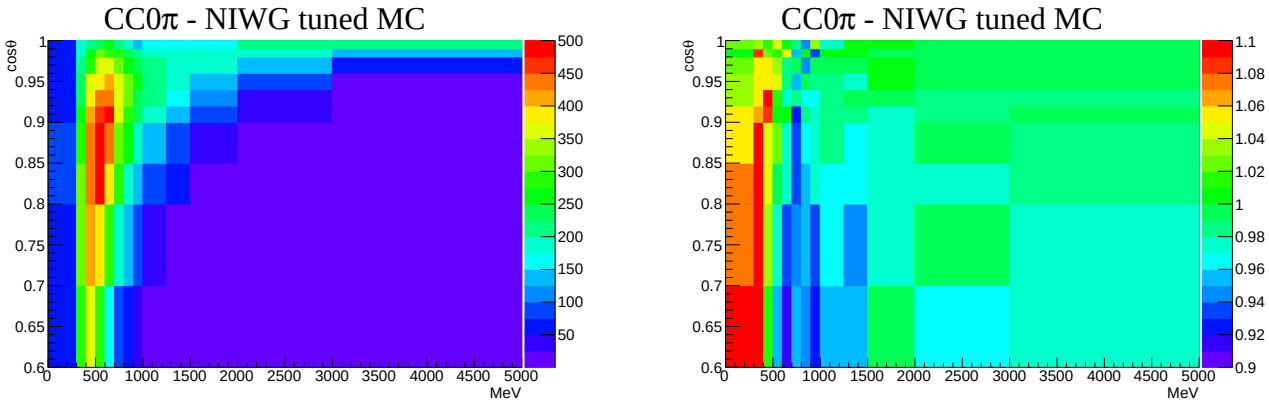

(a) CC0π (b) ratio to the nominal model

Figure 12.8: CC0π $p-\cos\theta$ distribution of the binding energy simulated data and ratio of the binding energy simulated data to the Asimov data at ND280.

detector fit for the 1Rμ samples. This shows that our model doesn't have enough degree of freedom to fully cover the binding energy variations.

The 1D sensitivity curves for $\sin^2\theta_{23}$ and Δm^2_{32} are shown in Fig. 12.11. The fit result of the binding energy simulated data has a tighter constraint on the $\sin^2\theta_{23}$ sensitivity. The best fit point of Δm^2_{32} is largely shifted to the lower value. The fit results for $\sin^2\theta_{13} - \delta_{CP}$ contour is almost the same as the Asimov sensitivity.

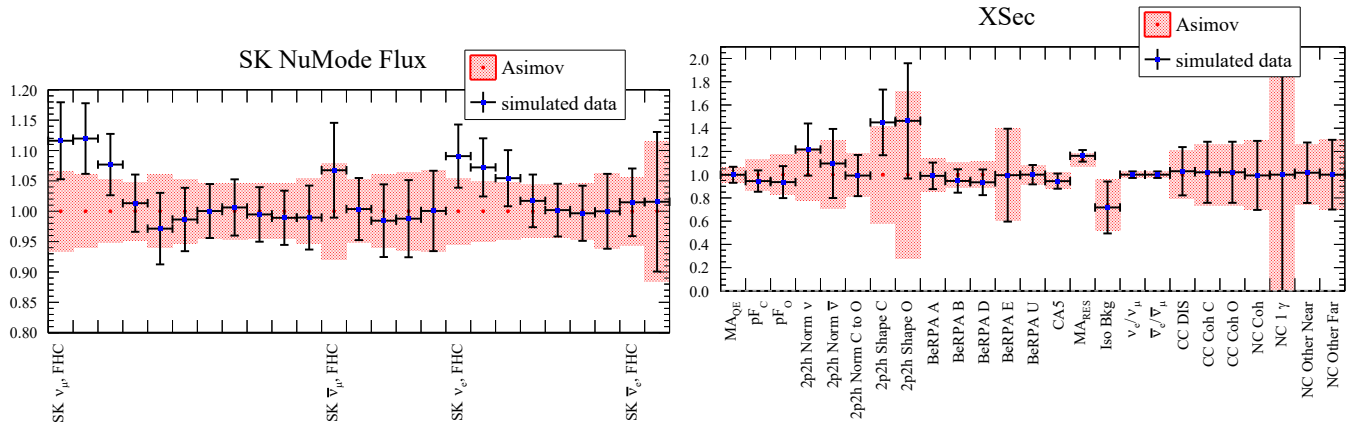

(a) SK flux (b) Cross-section

Figure 12.9: Best-fit parameters from the near detector fit to the binding energy simulated data.

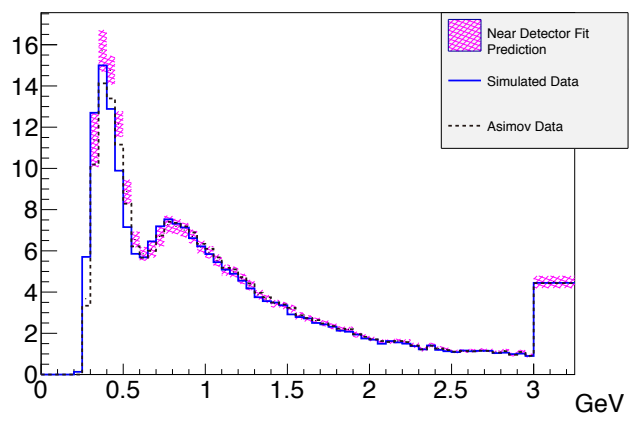

(a) FHC 1Rμ sample

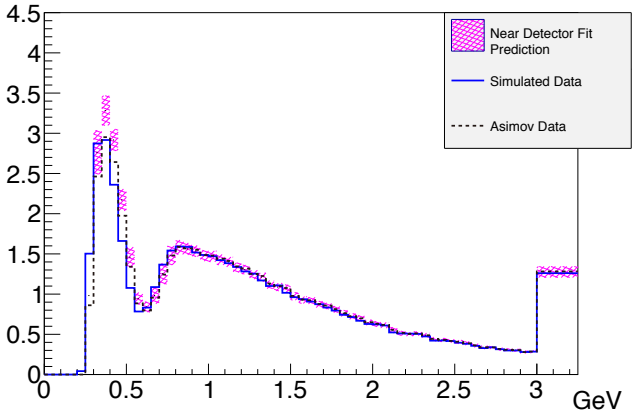

(b) RHC 1Rμ sample

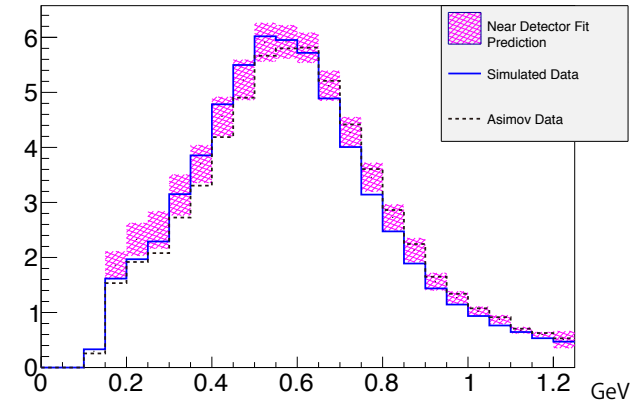

(c) FHC 1Re sample

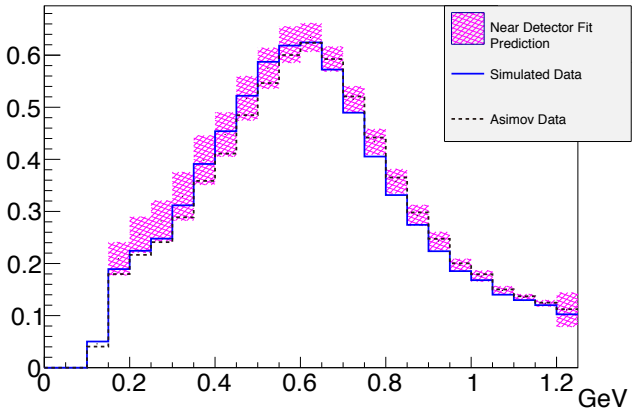

(d) RHC 1Re sample

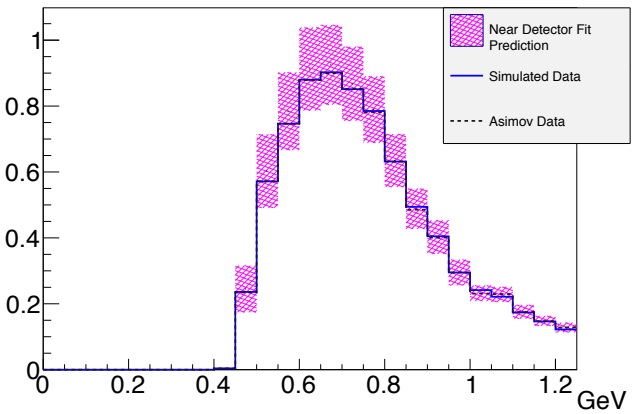

(e) FHC 1Re+1d.e. sample

Figure 12.10: Comparison between the Asimov data (dotted Black), the simulated data expectation (Blue), and the prediction from the near detector fit to the simulated data (Magenta).

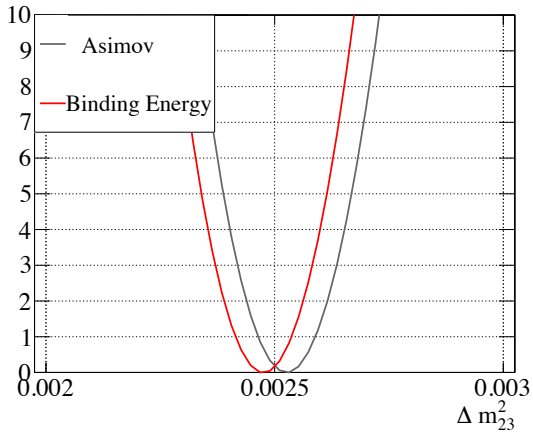

(a) Δm^2_{32}

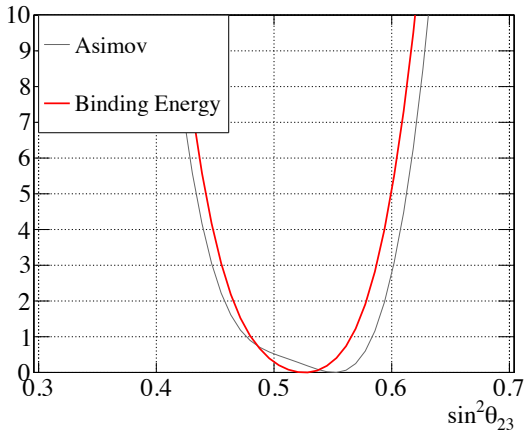

(b) $\sin^2\theta_{23}$

Figure 12.11: The 1D sensitivity curves of the $\sin\theta^2_{23}$ and Δm^2_{32} for the binding energy simulated data fits and the Asimov fits.

Bias Study

Table 12.3 shows the result of this bias study for the binding energy variation. The biases for θ_{23} and δ_{CP} are 14% and 2.2% of the total uncertainty, and 38% and 9.7% of the systematic uncertainty, respectively. The most biased parameter is Δm^2_{32}. It shows 89% of the total uncertainty, and 206% of the systematic uncertainty. We took into account the effect in this bias in the oscillation analysis by the smearing method which is described in Section 12.6. The tight constraint (overconstraint) seen in the binding energy simulated data is also treated in a specific way. The detail is also described in Section 12.6.

Table 12.3: Binding energy simulated data bias study

		$\sin^2\theta_{23}$	Δm^2_{32} (eV^2)	δ_{CP}
Asimov A	Middle of the 1σ interval	0.5231	2.474e-3	-1.580
	1σ interval size	0.04301	6e-05	1.337
	1σ interval ratio to Asimov	0.76	0.97	1.08
	Change in the 1σ interval ratio to syst interval	-51%	-7.5%	37%
	Bias computed with the 1σ middle and interval	**14%**	**89%**	**2.2%**
	Bias relative to σ_{Syst} computed with the 1σ middle and interval	**38%**	**206%**	**9.7%**
	Middle of the 2σ interval	0.5208	2.479e-3	-1.511
	2σ interval size	0.07933	1.365e-04	2.277
	2σ interval ratio to Asimov	0.88	0.97	1.04
	Bias computed with the 2σ middle and interval	**3.6%**	**69%**	**1.8%**
	Bias relative to σ_{Syst} computed with the 2σ middle and interval	**11%**	**188%**	**6.2%**

12.5 ND280 Data-Driven Simulated Data

We observed the data-simulation difference at ND280 as shown in Chapter 9. In the CC0π selections at ND280, which is the most relevant to the oscillation analysis, the prediction underestimates the data by approximately 5%. As previously shown in Chapter 9, the fit gives a good agreement with the data with a p-value of 48%. However, the 2p2h events became fully pion-less delta-decay-like (PDD-like), and RPA parameters at low Q^2 are enhanced in the near detector fit. The RPA shift is hard to understand as described in Section 8.4.1, and the fit results means there are no nucleon-nucleon correlation in the 2p2h interaction, which seems unrealistic.

This indicates that the observed difference is difficult to cover with the nominal model in spite of its goodness of the fit. Therefore, we constructed the simulated data based on the actual data to investigate the effects of the observed difference.

There are two main components in the CC0π samples: 1p1h and 2p2h. To produce simulated data, we need to assume interaction types otherwise the relation between $p-\cos\theta$ and E_ν is unknown. We generated simulated data sets driven by the data-simulation difference, where the difference between data and simulation is ascribed totally to a specific interaction type; 1p1h, 2p2h PDD-like or 2p2h non-PDD-like.

Each simulated data set was created as follows:

1. Two dimensional distributions in muon $p-\cos\theta$ are prepared for the CC0π FHC selection for data and simulation. The events of FGD1 and FGD2 are combined to reduce statistical fluctuations.

2. The difference in each bin of $p - \cos\theta$ between data and simulation is calculated.

3. The difference in step 2 is added to the specific interaction mode in the simulation (1p1h, 2p2h PDD-like or non-PDD-like).

4. The ratio of the adjusted interaction mode in step 3 to the nominal model, per bin, is calculated. If this ratio is below zero, it is set to zero. Additionally, if the number of data events is less than 20, the ratio is set to 1 to reduce statistical fluctuations.

5. The $p - \cos\theta$ weights are converted to $E_\nu - Q^2$ space to propagate the weights to Super-Kamiokande since $p - \cos\theta$ difference at ND280 cannot be added directly to the events at Super-Kamiokande.

6. The simulated data is generated at ND280 and Super-Kamiokande using the $E_\nu - Q^2$ weights.

Fig. 12.12 shows steps 1–4 of the above procedure.

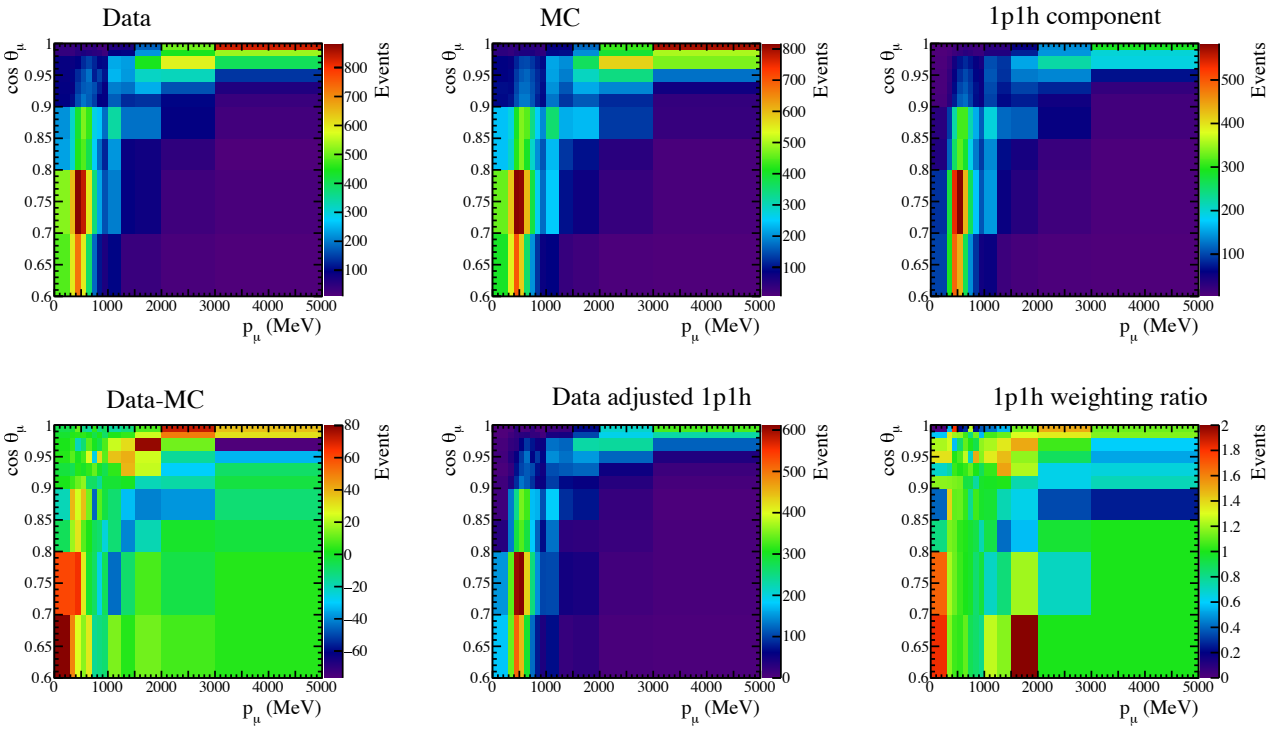

Figure 12.12: Example of how the data-driven simulated data sets are generated using 1p1h. The top row shows the data, nominal simulation, and 1p1h simulation. The bottom row shows the difference between data and simulation, the adjusted 1p1h mode, and the ratio of the adjusted mode to the nominal 1p1h one.

12.5.1 Fit Results of ND280 Data-driven Simulated Data

It is expected that the ND280 data-driven simulated data as a whole should produce the same or similar biases to the actual data when correctly propagated from near to far detector. Figure 12.13

shows the residuals of $p - \cos\theta$ distribution of data-driven 1p1h, 2p2h PDD-like and 2p2h non PDD-like simulated data for the CC0π sample at FGD1. The residuals are calculated as :

$$residual = \frac{N_{data} - N_{simulated}}{\sqrt{N_{data}}} \tag{12.2}$$

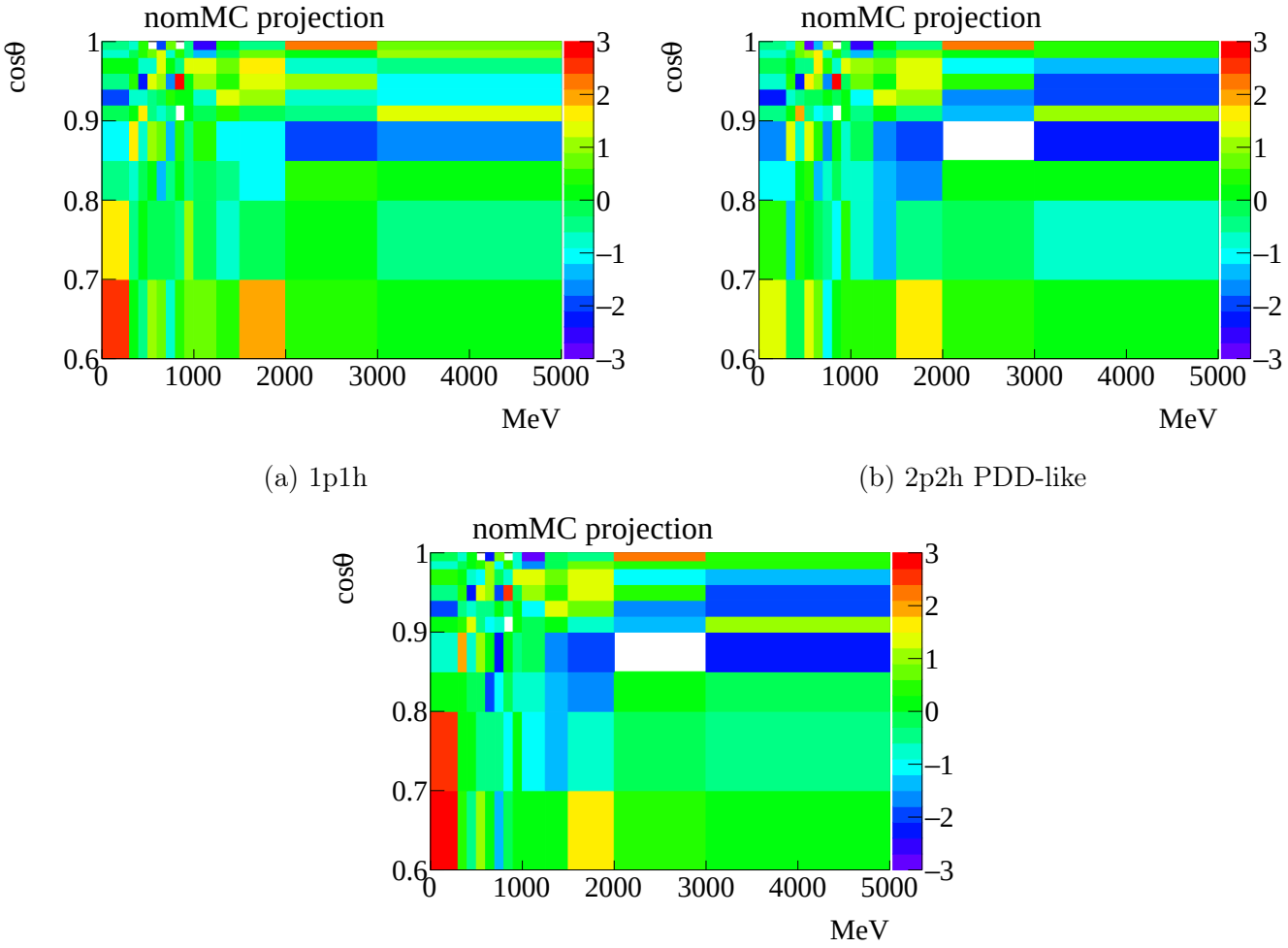

(a) 1p1h

(b) 2p2h PDD-like

(c) 2p2h non PDD-like

Figure 12.13: The residuals of data-driven simulated data to actual data

The 2p2h PDD-like simulated data reproduces the actual data most similarly at ND280 among three cases, especially at low momentum and high energy bin. As described before, we generated the simulated data at Super-Kamiokande with $E_\nu - Q^2$ weights, therefore, the weight which at least reproduces the similar prediction to the data at ND280 may correctly propagates the data-simulation difference to Super-Kamiokande [6]. Therefore, we decided to use 2p2h PDD-like simulated data as the data-driven simulated data results. Here we show the 2p2h PDD-like simulated data fit results

[6] We apply the same data-simulation difference to each interaction mode, therefore each simulated data should be similar each other. However, the residual distributions are different each other. To investigate the reason, we also tested with the simulated data with $p - \cos\theta$ weights at ND280 and we found the simulated data with $p - \cos\theta$ reproduce the actual data well in all three cases. However, we saw large bias in $\Delta m^2_{32} - \sin^2\theta_{23}$ contours in all three cases. We take $E_\nu - Q^2$ weights as data-driven simulated data because the same weight should be applied both ND280 and Super-Kamiokande. The discussion is described in Appendix I in more detail.

and we just show the summary for the other data-driven simulated data to avoid a repetition. The details of the other results are shown in Appendix H.

12.5.2 Fit Results of Data-driven 2p2h PDD-like Simulated Data

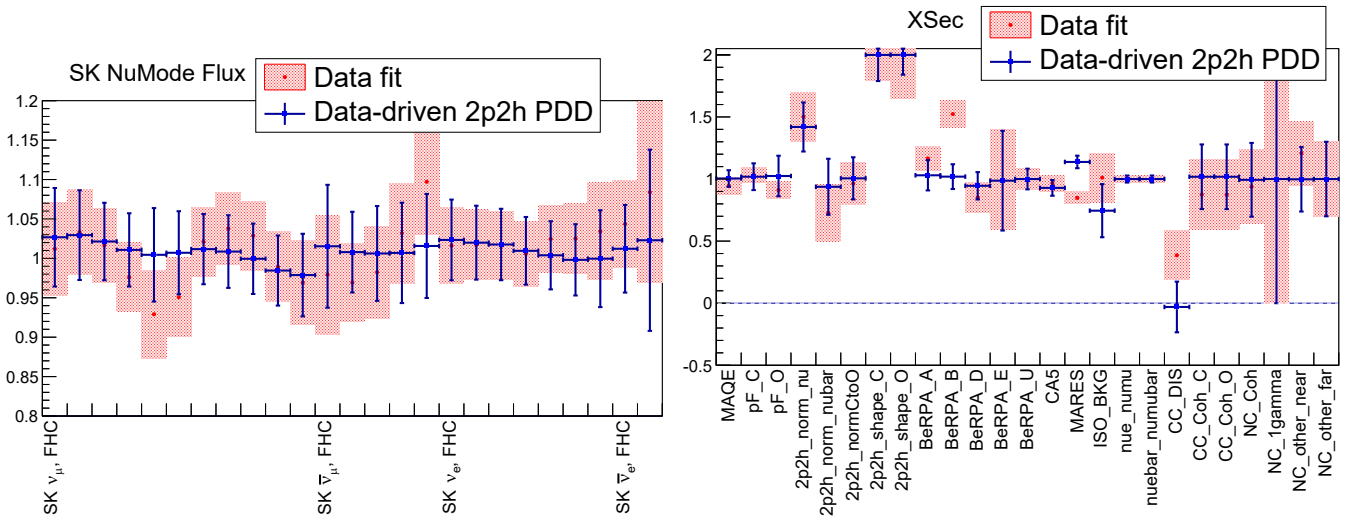

(a) SK flux

(b) Cross-section

Figure 12.14: Best-fit parameters from the near detector fit to the ND280 data-driven 2p2h PDD-like simulated data.

The best-fit parameter values with the 2p2h PDD-like simulated data, compared to those from the actual data fit are shown in Fig. 12.14. The fit results should be close to the actual data fit since this simulated data is motivated to mimic the actual data. However, we found there are some differences between the simulated data fit and actual data fit results especially in the BeRPA parameters and flux parameters [7]. The flux decrease at high energy region is slightly loosened, and BeRPA_A and BeRPA_B are almost one in data-driven simulated data fit. On the other hand, 2p2h parameters agree with the actual data fit.

A comparison of the ND280 data-driven 2p2h PDD-like simulated data and the prediction from the near detector fit at Super-Kamiokande is shown in Fig. 12.15. It shows that the simulated data spectrum at Super-Kamiokande increases relative to the Asimov data at the low energy region in ν_e samples and dip region in ν_μ samples. It also shows that the prediction from the near detector fit is consistent with the simulated data well within the error.

The 2D 68% and 90% confidence level contours for the simulated data fit results and that for the Asimov data fit are shown in Fig. 12.16. The $\sin^2\theta_{13} - \delta_{CP}$ contours of the simulated data fit were almost the same as the Asimov data fit. For the $\Delta m^2_{32} - \sin^2\theta_{23}$ contours, they are slightly shifted to the lower value in the Δm^2_{32} direction. To see this more clearly, the 1D sensitivity curves for $\sin^2\theta_{23}$ and Δm^2_{32} are shown in Fig. 12.17.

[7] The difference of CC1π and DIS parameter is expected since we considered $CC0\pi$ difference but not $CC1\pi$ difference at ND280. Therefore, $CC1\pi$ samples is almost the same as the Asimov data and the fit results should be different from the actual data fit.

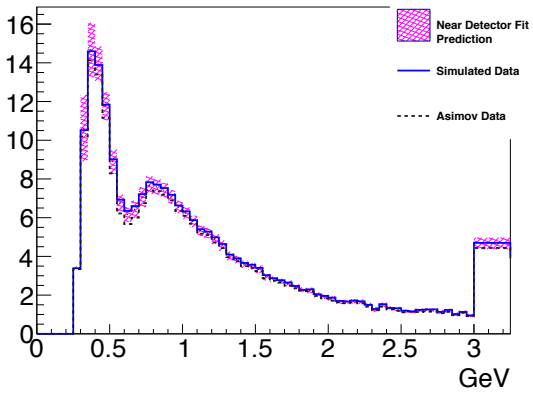

(a) FHC 1Rμ sample

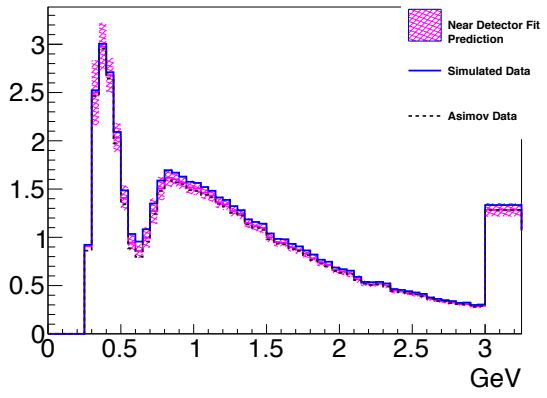

(b) RHC 1Rμ sample

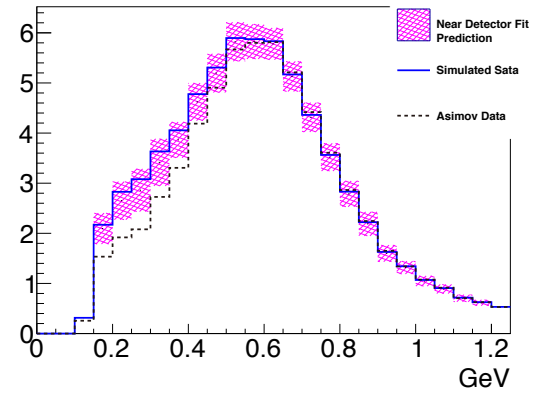

(c) FHC 1Re sample

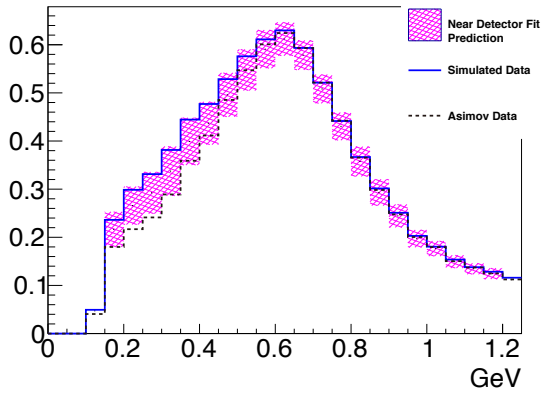

(d) RHC 1Re sample

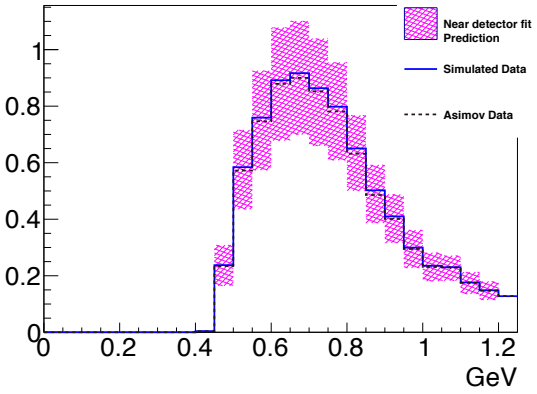

(e) FHC 1Re+1d.e. sample

Figure 12.15: Comparison between the Asimov data (dotted black), the simulated data expectation (Blue), and the prediction from the near detector fit to the simulated data (Magenta) for the data-driven 2p2h PDD-like simulated data.

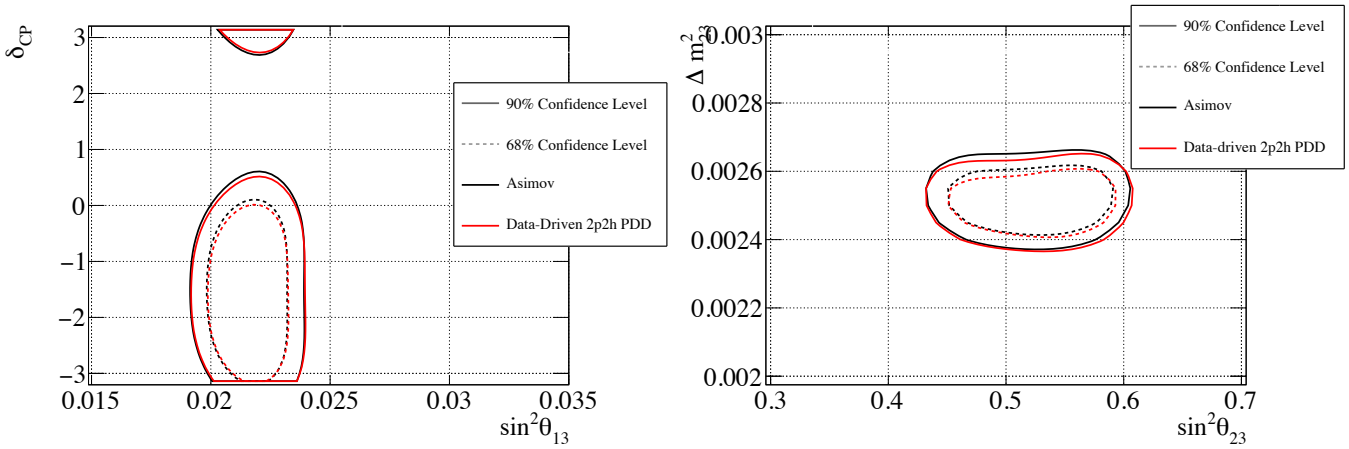

(a) $\delta_{CP} - \sin^2\theta_{13}$ (b) $\Delta m^2_{32} - \sin^2\theta_{23}$

Figure 12.16: The 2D contours of 68% and 90% confidence level for the data-driven 2p2h PDD-like simulated data fit and Asimov data fit.

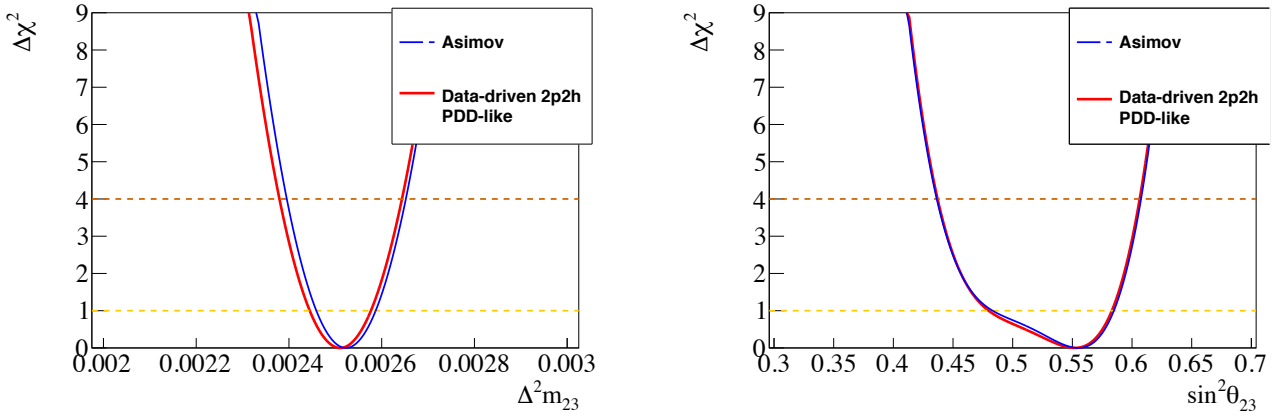

(a) Δm^2_{32} (b) $\sin^2\theta_{23}$

Figure 12.17: The 1D sensitivity curves of the $\sin^2\theta_{23}$ and Δm^2_{32} for the data-driven 2p2h PDD-like simulated data fit and Asimov data fit.

Table 12.4: Bias study of the ND280 Data-driven 2p2h PDD-like simulated data

		$\sin^2\theta_{23}$	Δm^2_{32} (eV^2)	δ_{CP}
Asimov A	Mean of the 1σ interval	0.532	2.508e-3	-1.649
	1σ interval size	0.051	6.563e-5	1.169
	Bias computed with the 1σ mean and interval	**6.7%**	**29%**	**16%**
	Bias relative to σ_{Syst} computed with the 1σ mean and interval	**14%**	**70%**	**77%**
	Mean of the 2σ interval	0.5255	2.508e-3	-1.588
	2σ interval size	0.084	1.286e-5	1.925
	Bias computed with the 2σ mean and interval	**4.6%**	**12%**	**10%**
	Bias relative to σ_{Syst} computed with the 2σ mean and interval	**13%**	**36%**	**18%**

Bias Study

Table 12.4 shows the result of this bias study with the data-driven 2p2h PDD-like simulated data. The bias to θ_{23} is 6.7% of the total uncertainty, and 15% of the systematic uncertainty. For δ_{CP}, the bias is 16%, while it's 77% of the systematic uncertainty. However, δ_{CP} has large statistical uncertainties, and the sensitivity easily changes due to the flat curve at the minimum in Fig. 12.3. We checked the effects on the δ_{CP} measurement and found the bias of data-driven simulated data with $p-\cos\theta$ weights changes the allowed region by only 2%. Therefore, we concluded that the bias on δ_{CP} was negligible. (See Appendix I more details).

The most biased parameter is Δm^2_{32}, where the bias is 29% of the total uncertainty and 70% of the systematic uncertainty. We took into account the effect of this bias in the oscillation analysis by the smearing method which is described in Section 12.6.

Fit Results of the Other Data-driven Simulated Data

The fit results of 1p1h and 2p2h non PDD-like simulated data are shown in Table 12.5 and Table 12.6. In all cases, Δm^2_{32} has the largest bias. The bias for θ_{23} and δ_{CP} is smaller than 15% in all cases.

Table 12.5: Bias study of ND280 Data-driven 1p1h simulated data

		$\sin^2\theta_{23}$	Δm^2_{32} (eV^2)	δ_{CP}
Asimov A	Mean of the 1σ interval	0.527	2.539e-3	-1.617
	1σ interval size	0.051	5.775e-5	1.121
	Bias computed with the 1σ mean and interval	**0.6%**	**22%**	**12%**
	Bias relative to σ_{Syst} computed with the 1σ mean and interval	**1.4%**	**51%**	**64%**
	Mean of the 2σ interval	0.521	2.539e-3	-1.588
	2σ interval size	0.082	1.208e-5	1.860
	Bias computed with the 2σ mean and interval	**0.0%**	**11%**	**10%**
	Bias relative to σ_{Syst} computed with the 2σ mean and interval	**0.0%**	**34%**	**18%**

Table 12.6: Bias study of ND280 Data-driven 2p2h non-PDD-like simulated data

		$\sin^2\theta_{23}$	Δm^2_{32} (eV^2)	δ_{CP}
Asimov A	Mean of the 1σ interval	0.526	2.529e-3	-1.617
	1σ interval size	0.0490	5.775e-5	1.201
	Bias computed with the 1σ mean and interval	**4.2%**	**4.6%**	**12%**
	Bias relative to σ_{Syst} computed with the 1σ mean and interval	**9.2%**	**11%**	**64%**
	Mean of the 2σ interval	0.519	2.529e-3	-1.588
	2σ interval size	0.079	1.208e-5	1.957
	Bias computed with the 2σ mean and interval	**2.3%**	**3.5%**	**10%**
	Bias relative to σ_{Syst} computed with the 2σ mean and interval	**6.3%**	**11%**	**18%**

12.5.3 ND280 Data-driven Pion Simulated Data

The ν_e sample with one decay electron at Super-Kamiokande (FHC 1Re+1d.e sample) has been included in the oscillation analysis since 2016. This sample mostly contains CC1π interaction where the momentum of the pion is below Cherenkov threshold (160 MeV/c), as shown in Fig. 12.18. We also observed a difference between data and simulation in the pion momentum distribution in ND280 TPC even after the near detector fit as shown in Fig. 12.19 [8]. The pion detection efficiency is not flat as a function of the pion momentum and the number of observed events at Super-Kamiokande is affected by a systematic uncertainty on the pion momentum prediction.

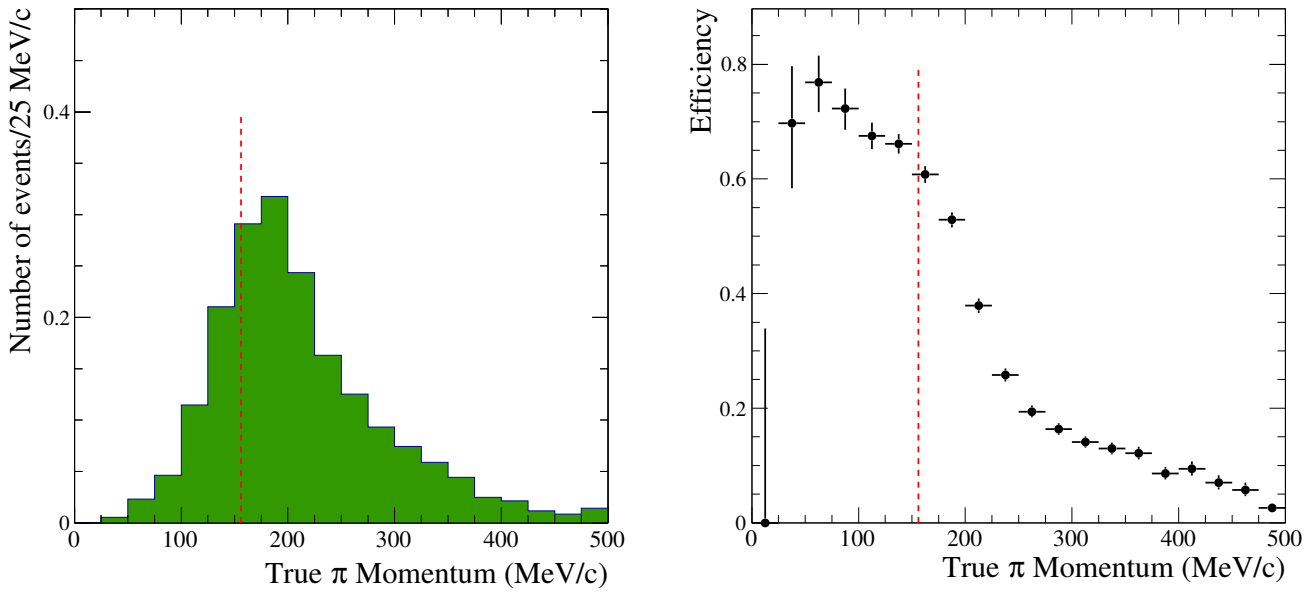

Figure 12.18: (Left)True pion momentum distribution, (Right) detection efficiency for pion at Super-Kamiokande. Red lines show the Cherenkov threshold.

The near detector fit does not yet exploit the pion kinematics to constrain the model and no dedicated systematic uncertainties have been developed to cover possible mismodeling of the pion

[8] We also observed data-simulation difference in the number of pions in ND280 FGD. However, we cannot convert the number of FGD pions to pion momentum information right now.

kinematics. Therefore, the full difference was applied to Super-Kamiokande events to estimate the impact on the oscillation analysis. We made the reweighting factor for the pion momentum in Fig. 12.19 and applied the weights to the events at Super-Kamiokande.

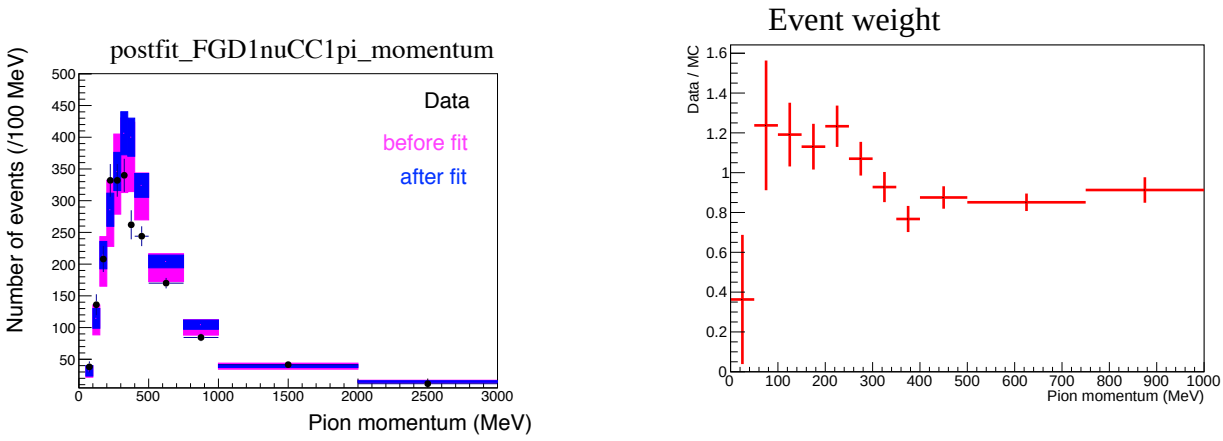

Figure 12.19: Left: Observed pion momentum distribution (black dots), prefit(Magenta) and postfit(blue) simulated distributions at ND280. Right: The pion momentum ratio between data and the postfit simulation.

The weight shown in Section 12.5.3 is applied as a function of true pion momentum at Super-Kamiokande since the difference between the true and reconstructed pion momentum at ND280 is small. Ideally, the weights should be applied to both ND280 and Super-Kamiokande. However, as discussed in Chapter 9, there are three pion selections and only TPC difference was calculated in this simulated data. Therefore, applying the weight at ND280 is complicated. Tentatively, the weight is applied only to Super-Kamiokande simulation for this simulated data study. The results of the near detector fit for the actual data are used as the input to the oscillation fitter. Figure 12.20 shows the true momentum distribution of the highest momentum pion for the FHC 1Re+1d.e sample before and after the weights are applied.

A comparison of the 1Re+1d.e simulated data and the prediction from the actual data fit at Super-Kamiokande is also shown in Fig. 12.20. The energy spectrum of the FHC 1Re+1d.e sample slightly changes as expected. This sample has a ~ 10 % increase compared to the Asimov data, well within the error on that sample. We found the pion momentum uncertainties don't affect the other samples, therefore, the $\Delta m^2_{32} - \sin^2\theta_{23}$ contours are unchanged. The sensitivity for δ_{CP} decreases compared to the Asimov data fit when fitting the simulated data, but no significant effect. We found the systematic uncertainty of pion momentum is small enough for the current oscillation analysis. No action was taken to include this uncertainty to the oscillation analysis.

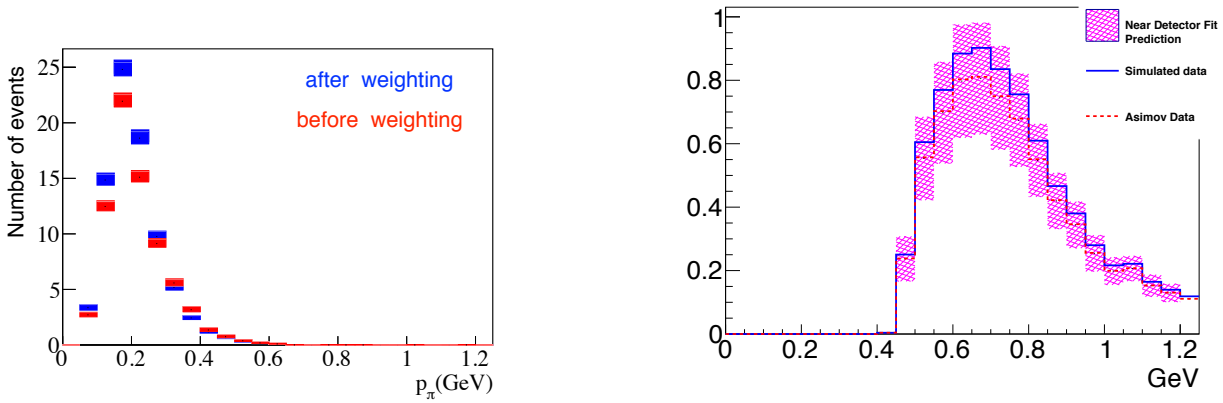

Figure 12.20: Left: The FHC 1Re+1d.e sample true pion momentum distribution before reweighting (Red) and after reweighting (Blue). Right:Energy spectrum comparison between the Asimov data, the simulated data expectation, and the prediction from the near detector fit for the FHC 1Re+1d.e sample.

12.6 Inclusion of the Effects of the Simulated Data into the Oscillation Analysis

As shown in Sections 12.3, 12.4.1 and 12.5, the non-negligible biases were seen especially in Δm^2_{32}. In addition to Δm^2_{32} bias, over constraint was observed in $\sin^2\theta_{23}$ for the binding energy and Kabirnezhad model simulated data [9]. The fit sensitivity depends on the size of the systematic and statistical uncertainties. Considering the statistical uncertainty on the FHC 1Rμ sample, the size of systematic uncertainty is already comparable. Therefore, the bias occurs due to neutrino interaction modeling, and it is important to estimate the systematic uncertainty due to the interaction modeling more correctly. Thus, we included the simulated data-prediction difference as an additional uncertainty in the oscillation fit.

12.6.1 Addition of New Parameters to Cover the Binding Energy Simulated Data

The binding energy simulated data produced the largest bias in oscillation parameters other than Δm^2_{32}. This indicates that the model doesn't allow the predicted Super-Kamiokande spectrum to vary sufficiently due to the lack of the binding energy parameters in the near detector fit. The inclusion of the binding energy effects on the energy spectrum at Super-Kamiokande mitigates the observed bias and overconstraint. Thus, we generated a response function of each energy bin at Super-Kamiokande to account for the difference by taking the ratio between the simulated data and the near detector fit prediction. We produced simulated data sets for +1 σ (45 MeV) and –0.5 σ (18 MeV) variations of the binding energy parameters and constructed the response function by interpolating these data sets. We then introduced one parameter to describe the binding energy difference, and the parameter was thrown with the other systematic uncertainties. Figure 12.21 shows an example of the response function of the binding energy and Fig. 12.22 shows the energy spectrum of 1Rμ samples when the binding energy parameter varies -1 σ to +1 σ.

To check the effects of the newly introduced parameter, the binding energy simulated data was fitted again and Fig. 12.23 shows the fit result of the simulated data with and without the new parameter, and Asimov fit result. The over constraint seen in $\sin^2\theta_{23}$ recovered, and the bias on Δm^2_{32} was decreased. The bias of Δm^2_{23} are reduced to be 30% of the total uncertainty, as shown in Table 12.7. This method was successful in relaxing the observed bias in Δm^2_{23} and loosen the over constraint seen in $\sin^2\theta_{23}$.

12.6.2 Smearing of Δm^2_{32}

Although the binding energy parameter was added, it is not sufficient to absorb the bias observed on Δm^2_{32}. Even with the binding energy parameter, there are still ∼50% biases on Δm^2_{32} for some Asimov B simulated data. The 1D Δm^2_{32} likelihood shows that this parameter is quite close to a Gaussian parameter. Therefore, we performed a smearing of the likelihood surface assuming the Gaussianity of the parameter to include the bias observed in Δm^2_{32} as an additional uncertainty. This method was applied to include any residual bias in Δm^2_{32} remaining after the response function was included in the fit.

[9] The data-driven simulated data with $p - \cos\theta$ reweight also showed the large over constraint. See Appendix I for more details

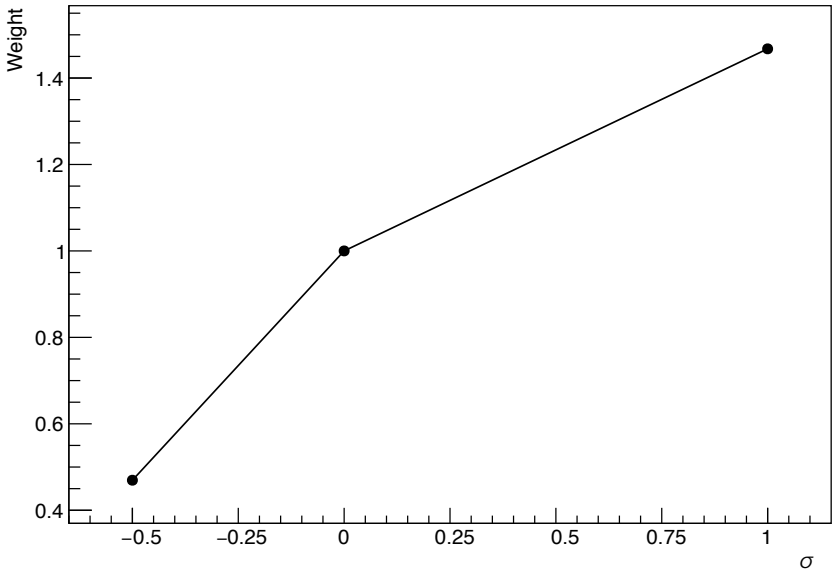

Figure 12.21: Example of response function for the binding energy.

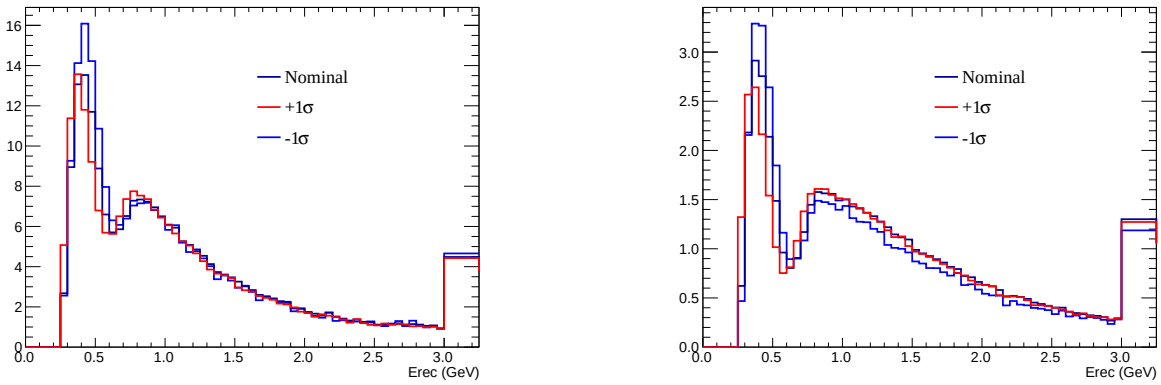

(a) FHC 1Rμ sample

(b) RHC 1Rμ sample

Figure 12.22: Energy spectrum of the FHC 1Rμ and RHC 1Rμ samples when the binding energy parameter varies $\pm 1\sigma$.

Table 12.7: Bias table of the binding energy simulated data with the binding energy parameter. The values in parentheses are fit results without the parameter as reference.

		$\sin^2\theta_{23}$	Δm^2_{32} (eV^2)	δ_{CP}
Asimov A	Middle of the 1σ interval	0.522	2.504e-3	1.60
	1σ interval size	0.049	6.5e-05	1.24
	1σ interval ratio to Asimov	0.92	0.95	1.04
	Bias with 1σ	**9%**(13%)	**28%**(82%)	**2%**(2%)
	Bias with σ_{Syst}	**23%**(38%)	**47%**(216%)	**6%**(11%)

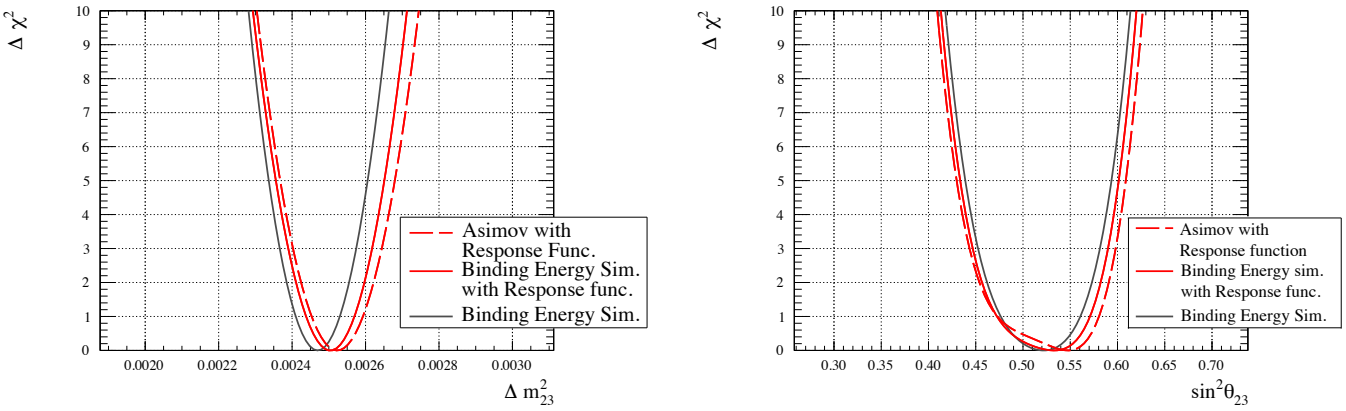

(a) Δm^2_{32} (b) $\sin^2_{\theta_{23}}$

Figure 12.23: The 1D sensitivity curves of Δm^2_{23}, $\sin^2\theta_{23}$ for Asimov (dashed red) and the binding energy simulated data with (solid red) and without (Solid black) the binding energy parameter.

Procedure

The smearing is done by convoluting the bias to the fit likelihood:

1. Define the overall bias on Δm^2_{32}, Δ_{bias}, by quadratically summing all the biases observed in the different simulated data sets. We used the ND280 data driven 2p2h PDD-like, SF, Nieves 1p1h - NEUT CCQE difference, Martini 2p2h, Kabirnezhad model and the binding energy simulated data sets. We used the biases in Asimov A only for the fits with the binding energy response function. The quadrature sum gives $\Delta_{bias} = 3.5 \times 10^{-5}$ eV^2.

2. Divide the 2D $\Delta m^2_{32} - \sin^2\theta_{23}$ space in a grid with bin size smaller than the error from step 1 on the Δm^2_{32} axis. In the following procedure, a bin size of 5×10^{-6} eV^2 is used.

3. Compute the Likelihood $L' = e^{-0.5(-2\log(L))}$ where $-2\log(L)$ is the fit's output in each grid point.

4. Draw a Gaussian distribution with deviation Δ_{bias} and normalized by the likelihood L' in each bin:
$$L' \frac{1}{\sqrt{2\pi\Delta^2_{bias}}} \exp\left[\frac{(\Delta m^2_{32} - \Delta m^2_{32,\,i})^2}{2\Delta^2_{bias}}\right]. \tag{12.3}$$
where $\Delta m^2_{32,\,i}$ is the Δm^2_{32} value at i bin.

5. Integrate the bias effect from the other grid points. Since the smearing is applied only on Δm^2_{32}, we should be running over the bins that are at the same $\sin^2\theta_{23}$ value point.

6. Convert the likelihood back to $-2\log(L)$.

Results

In order to show the results of this smearing procedure, the binding energy simulated data fit with the binding energy parameter was used.

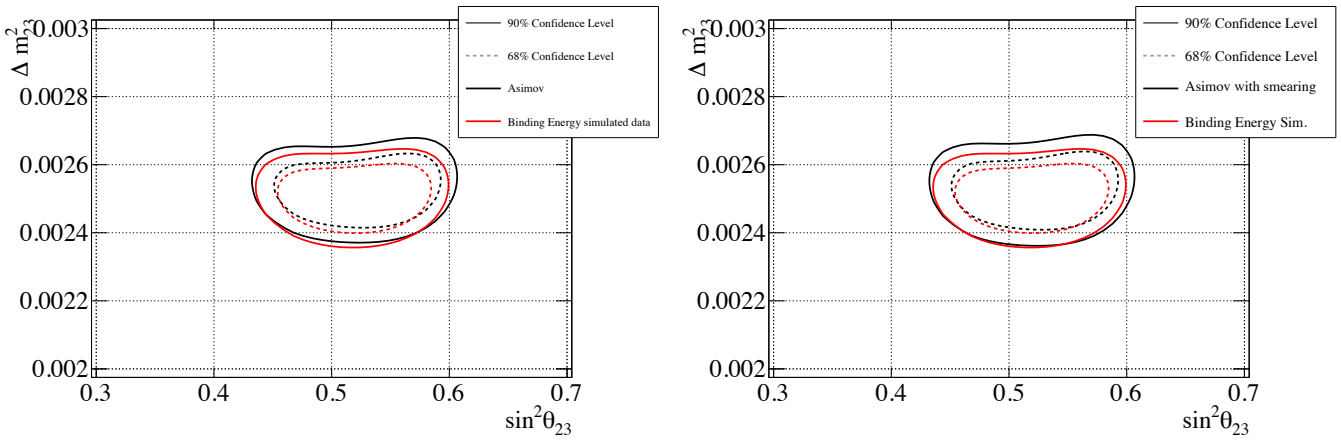

Figure 12.24: The 2D Δm^2_{32}–$\sin^2\theta_{23}$ contours without (left) and with (right) smearing to the Asimov data fit.

Figure 12.24 shows $\Delta m^2_{32} - \sin^2\theta_{23}$ contours with and without the smearing applied to the Asimov data sensitivity. The comparison shows that this smearing procedure allows us to inflate the error size of the Asimov data fit, therefore, the size of the bias was reduced.

Table 12.8 shows the summary of the bias calculated after the binding energy parameter inclusion and the Δm^2_{32} smearing method are applied. All of the biases were reduced to below 50% relative to the total uncertainty.

We compared with and without the effects of the binding energy parameter and the smearing in the actual data fit. The plots are shown in Appendix K. The sensitivity for δ_{CP} is almost unchanged, while the $\sin^2\theta_{23}$ and Δm^2_{32} sensitivities are loosened slightly compare to the sensitivity without the binding energy parameter and the Δm^2_{32} smearing.

12.7 Discussion

12.7.1 Impact on the T2K Oscillation Analysis

The bias due to the choice of neutrino-interaction model has been discussed in a theoretical context [232] and a similar study has been done in 2016 T2K oscillation analysis [71]. In the previous study, no significant difference was observed and no action was taken. However, this study showed that the current parameterization of the near detector fit cannot cover the possible variation of alternative interaction models, and it causes the bias on the oscillation parameters given higher statistics than that of the previous study. This study indicates that cross-section modeling is now one of the main issues for the determination of the oscillation parameters especially θ_{23} and Δm^2_{32}. The impact is currently small for δ_{CP} since the statistical error is still large. However, it may also be a big issue in the future. For example, the difference between neutrino and anti-neutrino, or electron neutrino and muon neutrino would have large effect on δ_{CP}. Therefore, understanding of the neutrino cross-section will be more essential for the future neutrino oscillation analysis.

We developed the bias smearing method and it successfully relaxed the bias due to the interaction modeling. The smearing method can be also applied to the other sources of the bias such as the detector or flux systematic bias. However, this method is a tentative way to smear the bias.

Table 12.8: Bias table of the simulated data with the binding energy parameter and the smearing applied to Δm^2_{32}. The values in parentheses are fit results without the binding energy parameter nor the smearing as reference. The smearing procedure is applied to Asimov, and therefore, included in the systematic only error.

Asimov A		θ_{23}	Δm^2_{32}	δ_{CP}
Martini 2p2h	Bias computed with 1σ	**11%**(14%)	**12%**(12%)	**0%**(0.3%)
	Bias computed with σ_{Syst}	**28%**(40%)	**18%**(33%)	**0%**(1%)
SF	Bias computed with 1σ	**5%**(3%)	**17%**(24%)	**1%**(0%)
	Bias computed with σ_{Syst}	**11%**(10%)	**24%**(65%)	**2%**(0%)
Nieves 1p1h	Bias computed with 1σ	**6%**(9%)	**22%**(36%)	**6%**(7%)
	Bias computed with σ_{Syst}	**16%**(26%)	**31%**(98%)	**25%**(30%)
Kabirnezhad	Bias computed with 1σ	**6%**(6%)	**26%**(38%)	**1%**(1%)
	Bias computed with σ_{Syst}	**15%**(18%)	**37%**(102%)	**3%**(4%)
data-driven 1p1h	Bias computed with 1σ	**11%**(7%)	**31%**(31%)	**3%**(3%)
	Bias computed with σ_{Syst}	**30%**(19%)	**43%**(84%)	**12%**(12%)
Data-driven 2p2hD	Bias computed with 1σ	**11%**(13%)	**20%**(27%)	**2%**(5%)
	Bias computed with σ_{Syst}	**30%**(38%)	**28%**(72%)	**9%**(22%)
data-driven 2p2hnD	Bias computed with 1σ	**0%**(1%)	**23%**(22%)	**4%**(5%)
	Bias computed with σ_{Syst}	**0%**(2%)	**33%**(60%)	**17%**(22%)
binding energy	Bias computed with 1σ	**9%**(14%)	**23%**(89%)	**2%**(2%)
	Bias computed with σ_{Syst}	**21%**(38%)	**42%**(206%)	**6%**(11%)

The current version of NEUT uses outdated model (such as RFG) and the nuclear effect (such as binding energy, RPA correction) is not fully implemented. Therefore, the construction of the correct interaction modeling and simulation is desired.

12.7.2 Impact on the Neutrino-nucleus Interaction Modeling and Measurement

We have not changed the ND280 data set from the 2016 analysis but changed the cross-section parameterization. We added the 2p2h shape parameter and BeRPA parameters from the 2016 analysis and withdrew the binding energy parameters. Adding parameters enables the near detector fit to get more degrees of freedom, therefore a better p-value of 48% was obtained than the previous analysis of 8%. However, this study showed that our parameterization is still insufficient.

As shown in this chapter, the binding energy variation showed the largest effect, and the variation which showed relatively large bias made a difference especially at low muon momentum region. This tendency can be understood as follows. Due to the lack of the binding energy parameters, the 2p2h shape parameters were the only parameters which can change the muon kinematics at that region. Therefore, the difference of the events at the low momentum region is absorbed by the 2p2h shape parameters even though the difference is not actually from the 2p2h events. If the 2p2h becomes PDD-like, the energy reconstruction at Super-Kamiokande is biased. As a result, the oscillation parameters are also biased. Thus, the correct implementation of the binding energy parameter response is desired.

Comparing with the actual data, data - Asimov data difference is seen especially at low momen-

tum and high angle region. Modern neutrino cross-section measurements mostly focus on the high momentum and forward region due to the detector configuration. The data at low momentum and high angle region is relatively sparse. To obtain more precise neutrino interaction modeling and parameterization, it is important to measure the neutrino cross-section in low momentum and high angle region.

12.7.3 Future Improvement of the Simulated Data Study

In this study, we evaluated the bias from mean point of confidence level intervals. However, this evaluation is not enough to describe the bias correctly. This definition describes the "accuracy" of the oscillation fit framework rather than "precision". It is also important to know the bias on the "precision", otherwise we get unfairly tight or loose constraint on the oscillation parameters than that of actual one. For example, we obtained a tighter constraint on θ_{23} with the binding energy simulated data, however our bias definition Eq. (12.1) cannot evaluate this effect. We also calculated the percentage of the overlapped region of two contours, however it's difficult to interpret since this calculation gives us information entangled both over-prediction and the bias. Therefore, a better description of the bias using "variance" of the fit is required.

For the data-driven simulated data, the simulated data doesn't reproduce the actual data well as described in Section 12.5. NOνA [100] and MINERνA [233] also observed data-simulation difference similar to ND280 data and treated it in a more sophisticated way. They treated data-simulation difference in $q_0 - q_3$ space and assigned as "empirical MEC" [234]. q_0 is the first component of the momentum transfer and q_3 is the norm of the three-dimensional momentum transfer. Including this, the simulation agrees with actual data well. We are planning to make simulated data with similar approach to them. However, it is difficult to extract $q_0 - q_3$ information from ND280 measurement since ND280 reconstructs the neutrino energy from lepton kinematics not from hadronic energy measurement. For the pion momentum, we just applied the weight to the Super-Kamiokande simulation. If the pion momentum is shifted, the lepton kinematics and the number of the events are also affected since the pion detection efficiency changes as a function of the momentum. Therefore, the effect of the pion momentum may be larger than our expectation. Thus, more study is needed to improve the data-driven simulated data.

The construction of the data-driven simulated data may help us to understand not only the bias but also the 2p2h itself. As described in Section 8.3, there are still large uncertainties of the 2p2h modeling. NOνA implemented theoretical model by Nieves in 2017, however the "empirical MEC" is still the best match to the data, and it is still used in the oscillation analysis [97]. If we can confirm that the data-Asimov data difference observed in T2K has the same phase space or the same physics process as the one observed in the other experiments, this difference may make a big impact on the construction of the 2p2h model. Therefore, a simulated data motivated by the MINERνA data-simulation difference is planned in the future.

12.7.4 Conclusion

In this chapter, we investigated the systematic bias due to the neutrino interaction modeling in the oscillation analysis. We generated simulated data sets for the possible variations of the cross-section model and performed the oscillation fit with these simulated data to assess the possible systematic bias. This study showed that the current interaction modeling in the oscillation analysis makes a bias of more than 100% on Δm^2_{32} in several cases. We developed the methods to loosen the observed bias, and succeeded in reducing the bias below 50%. This study indicates that the parameterization of the cross-section in the oscillation analysis is still insufficient to cover all possible variation in

the cross-section modeling. A more precise understanding of neutrino interaction is necessary in the future.

Chapter 13

Measurement of the Neutrino Oscillation Parameters

We successfully reduced the bias on Δm^2_{32} with the binding energy parameter and the smearing method. In this chapter, we show the fit results of the oscillation analysis.

13.1 Systematic Uncertainties Including Binding Energy Uncertainties

We included the binding energy parameter in the oscillation analysis. Therefore, the systematic uncertainties and the sensitivity should be updated.

Table 13.1 shows the percentage error on the number of events for each sample broken down by the error source. The new binding energy parameter is considered as a non-constrained cross-section parameter by ND280. The new total error is larger than the previous value by 10% to 20% except in the FHC 1Re+1 d.e sample.

13.2 Updated Sensitivity

Figure 13.1 shows the updated sensitivity for parameter set A. The results for parameter set B are shown in Appendix G.

13.3 Oscillation Fit Results

13.3.1 Observed Spectrum

Figure 13.2 shows the observed spectrum at Super-Kamiokande. We observed 74 1Re, 240 1Rμ and 15 1Re+1d.e candidate events in the FHC mode, 7 1Re and 68 1Rμ in the RHC mode for 1.47×10^{21} POT in FHC and 0.76×10^{21} POT in RHC exposure.

Table 13.1: Uncertainty on the number of events in each Super-Kamiokande sample broken down by the error source. The new binding energy parameter is included in the non-constrained cross-section parameters by ND280.

	1-Ring μ		**1-Ring e**		
Error source	FHC	RHC	FHC	RHC	FHC 1d.e
Beam	4.1%	3.8%	4.2%	3.9%	4.3%
Cross-section (constr. by ND280)	4.7%	4.0%	4.8%	4.1%	4.1%
Cross-section (all)	5.5%	4.3%	8.5%	6.3%	5.7%
Beam + Cross-section (constr. by ND280)	3.2%	2.7%	3.2%	2.8%	4.1%
Beam + Cross-section (all)	4.4%	3.1%	7.9%	5.6%	5.7%
SK FSI+SI+PN	3.3%	2.8%	4.0%	4.3%	16.9%
Total	5.5%	4.2%	8.9%	7.1%	17.6%

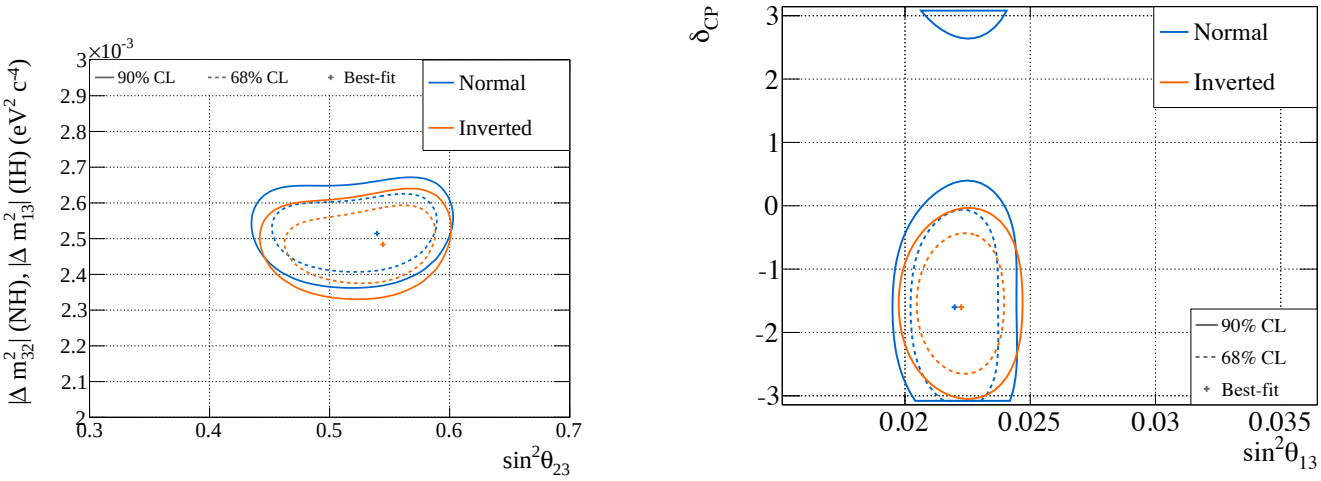

(a) $\sin^2\theta_{23} - \Delta m^2_{32}$

(b) $\sin^2\theta_{13} - \delta_{CP}$

Figure 13.1: Sensitivity for parameter set A with the reactor constraint. The binding energy parameter and the Δm^2_{32} smearing are applied

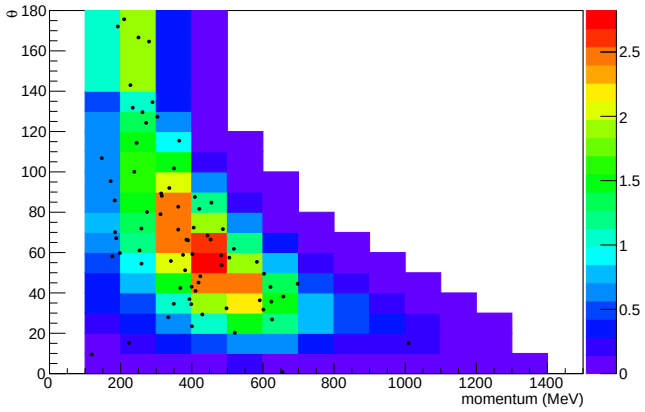

(a) FHC 1Re sample

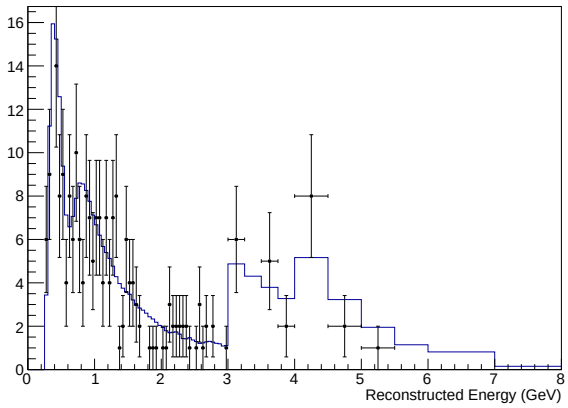

(b) FHC 1Rμ sample

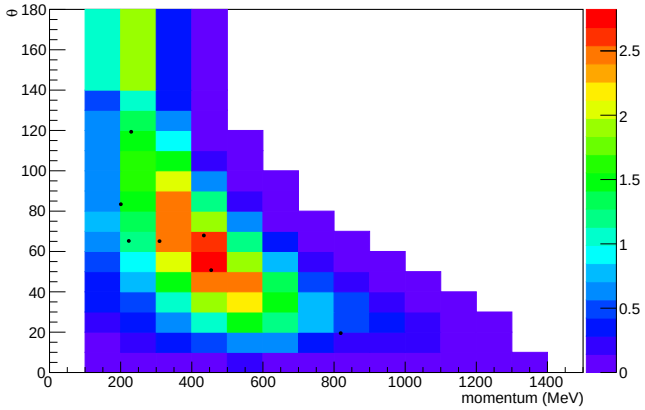

(c) RHC 1Re sample

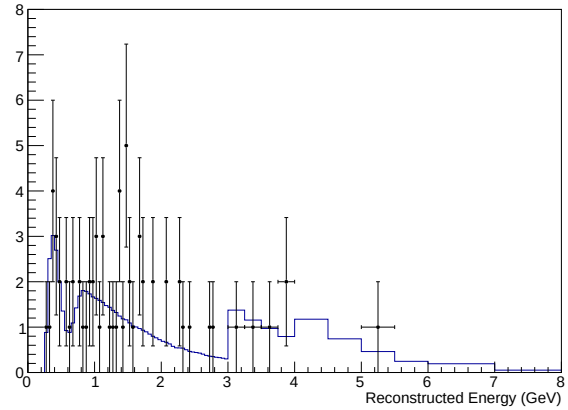

(d) RHC 1Rμ sample

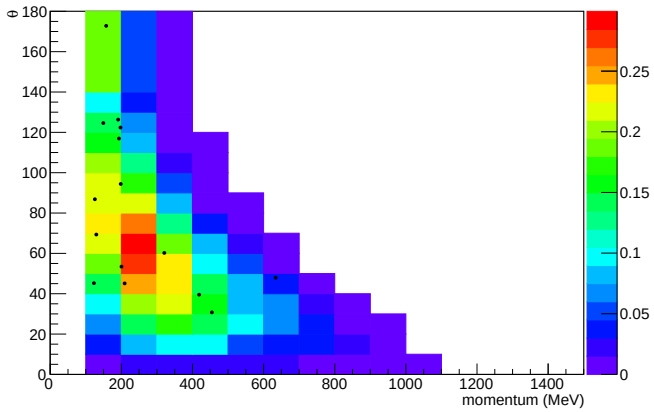

(e) FHC 1Re 1 d.e sample

Figure 13.2: Observed and predicted spectrum using parameter set A.

13.3.2 Fit Results with T2K Data Only

The oscillation fit results without the reactor constraint is shown in Fig. 13.3. We obtained the following best-fit values and 1σ credible interval for the oscillation parameters as shown in Table 13.2. "Both" is the fit results marginalized over the mass hierarchy. The fit result for δ_{CP} excludes the CP-conserving values $\delta_{CP} = 0, \pi$ with 1σ confidence level. $\delta_{CP} = \pi/2$ point is excluded more than 2σ. For $\sin^2\theta_{23}$, the best-fit point is close to the maximal mixing value $\sin^2\theta_{23} = 0.5$.

Table 13.2: Data fit results T2K only

parameter	Normal hierarchy	Inverted hierarchy	both
$\sin^2(\theta_{13})$	$0.02716^{+0.0058}_{-0.0043}$	$0.03114^{+0.0060}_{-0.0048}$	$0.02917^{+0.0063}_{-0.0049}$
$\sin^2(\theta_{23})$	$0.5136^{+0.03753}_{-0.03556}$	$0.5185^{+0.03407}_{-0.03605}$	$0.5165^{+0.03556}_{-0.03605}$
$\lvert\Delta m^2_{32}\rvert$ (eV^2)	$0.002473^{+6.419\times10^{-5}}_{-6.419\times10^{-5}}$	$0.002442^{+6.152\times10^{-5}}_{+6.133\times10^{-5}}$	$0.002457^{+6.514\times10^{-5}}_{-6.419\times10^{-5}}$
δ_{CP}	$-1.937^{+0.9659}_{-0.8315}$	$-1.343^{+0.6752}_{-0.7283}$	$-1.699^{+0.8721}_{-0.8815}$

13.3.3 Fit Results with Reactor Constraint on $\sin^2\theta_{13}$

The oscillation fit results with the reactor constraint are shown in Fig. 13.4. We obtained the following best-fit oscillation parameters as shown in Table 13.3.

Table 13.3: data fit results T2K+reactor

parameter	Normal hierarchy	Inverted hierarchy	Both
$\sin^2(\theta_{13})$	$0.02231^{+0.0011}_{-0.0011}$	$0.02257^{+0.0011}_{-0.0011}$	$0.02244^{+0.0011}_{-0.0011}$
$\sin^2(\theta_{23})$	$0.5358^{+0.02815}_{-0.03901}$	$0.5358^{+0.02716}_{-0.03556}$	$0.5358^{+0.02765}_{-0.03704}$
Δm^2_{32} (eV^2)	$0.002472^{+6.552\times10^{-5}}_{-6.419\times10^{-5}}$	$0.002439^{+6.381\times10^{-5}}_{-6.305\times10^{-5}}$	$0.002455^{+6.667\times10^{-5}}_{-6.571\times10^{-5}}$
δ_{CP}	$-1.746^{+0.6565}_{-0.6127}$	$-1.458^{+0.5819}_{-0.5314}$	$-1.699^{+0.6377}_{-0.6189}$

The fit result for δ_{CP} excludes the CP-conserving values $\delta_{CP} = 0, \pi$ with 2σ confidence level. $\delta_{CP} = \pi/2$ point is excluded more than 4σ.

13.3.4 Measurement of δ_{CP}

The critical $\Delta\chi^2$ value for δ_{CP} is calculated using the Feldman-Cousins approach [235] to get the significance more accurately. The $\Delta\chi^2$ values are calculated based on the difference between the χ^2 values calculated using the values of δ_{CP} and mass hierarchy of interest and the best fit values:

$$\Delta\chi^2(\delta_{CP}, MH) = \chi^2(\delta_{CP}, MH) - \chi^2(\delta_{CP}^{bestfit}, MH^{bestfit}) \tag{13.1}$$

with MH is mass hierarchy, δ_{CP} and MH are the values of δ_{CP} and mass hierarchy of interest, $\delta_{CP}^{bestfit}$ and $MH^{bestfit}$ are the best-fit values.

It gives the δ_{CP} values of [-2.894,-0.561] and [-1.504,-1.265] with 2σ confidence level for the normal and inverted hierarchy hypotheses respectively as shown Fig. 13.5.

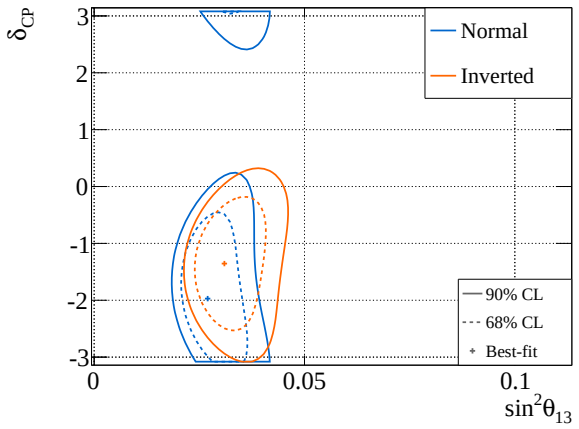

(a) $\sin^2\theta_{13} - \delta_{CP}$

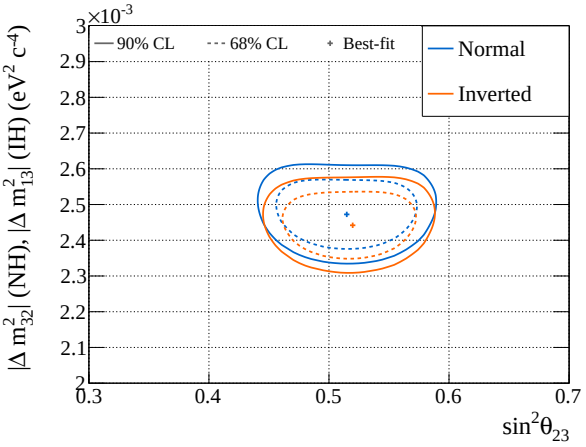

(b) $\sin^2\theta_{23} - \Delta m^2_{32}$

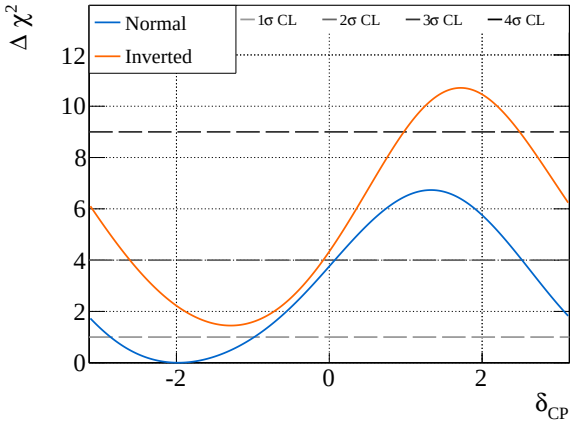

(c) δ_{CP}

Figure 13.3: The 2D contour for 68% and 90% confidence level and the 1D $\Delta\chi^2$ surfaces for δ_{CP} using T2K data only.

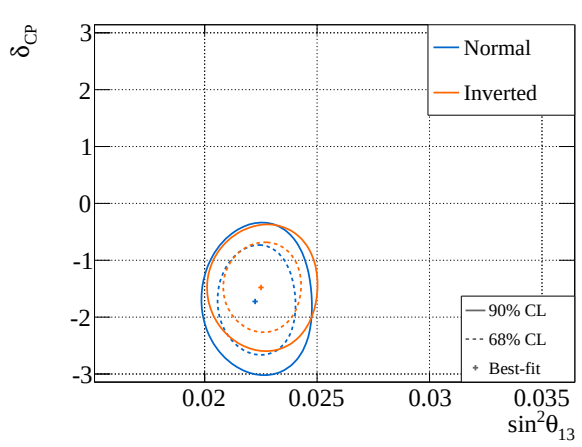

(a) $\sin^2\theta_{13} - \delta_{CP}$

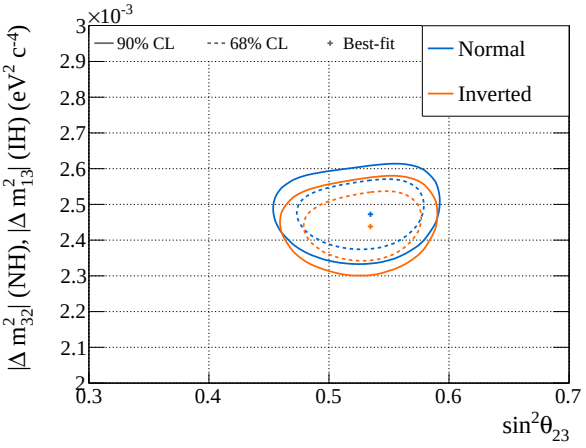

(b) $\sin^2\theta_{23} - \Delta m^2_{32}$

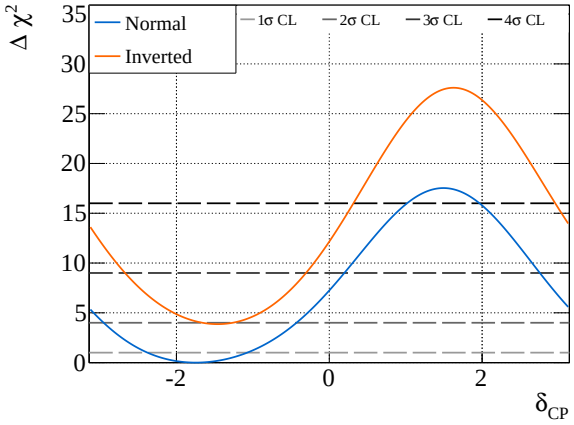

(c) δ_{CP}

Figure 13.4: The 2D contour for 68% and 90% confidence level and the 1D $\Delta\chi^2$ surfaces for δ_{CP} using T2K data and the reactor constraint.

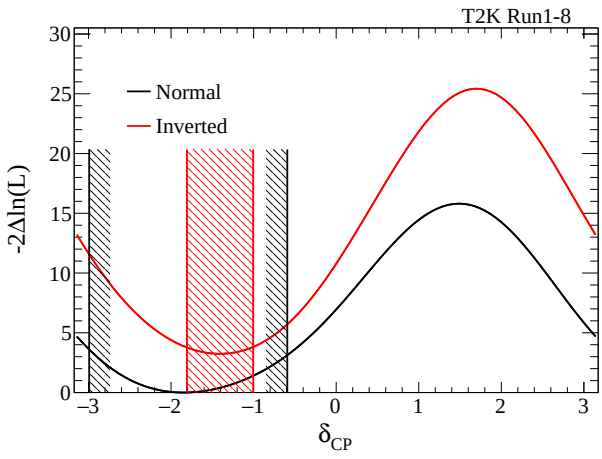

Figure 13.5: 1D $\Delta\chi^2$ distribution as a function of δ_{CP} of the data fit the with reactor constraint and 2σ interval calculated with the Feldman-Cousins method.

13.3.5 Mass Hierarchy and $\sin^2\theta_{23}$

The posterior probabilities for the various combinations of the mass hierarchies and $\sin^2\theta_{23}$ are summarized in Table 13.4 and Table 13.5. In both cases, the normal hierarchy and the higher octant ($\sin^2\theta_{23} > 0.5$) are slightly preferred while the contour includes the maximal mixing value $\sin^2\theta_{23} = 0.5$. The significance is still weak to conclude.

Table 13.4: Posterior probabilities for different hypotheses from T2K data only

	$\sin^2\theta_{23} < 0.5$	$\sin^2\theta_{23} > 0.5$	Line total
Inverted hierarchy	0.126	0.205	0.33
Normal hierarchy	0.244	0.425	0.67
Column total	0.37	0.63	1

Table 13.5: Posterior probabilities for different hypotheses from T2K with the reactor constraint

	$\sin^2\theta_{23} < 0.5$	$\sin^2\theta_{23} > 0.5$	Line total
Inverted hierarchy	0.024	0.104	0.128
Normal hierarchy	0.191	0.681	0.872
Column total	0.216	0.784	1

13.4 Discussion

13.4.1 Latest results of δ_{CP} measurements

Figure 13.6 shows the latest results of the δ_{CP} measurement from T2K and NOνA reported in NEUTRINO 2018 conference [96,97]. T2K obtained $\delta_{CP} = -1.822^{+0.653}_{-0.59}$ (assuming normal hierarchy) and $\delta_{CP} = 0,\ \pi$ are excluded with 2σ significance. NOνA excluded $\delta_{CP} = -\pi/2$ at more than 1σ in all cases, however, the best fit value is still uncertain.

T2K improved statistics: 1.0×10^{20} POT of RHC mode was accumulated in addition to 2017 analysis. The analysis framework was the same as the 2017 analysis described in this thesis. The uncertainty of the δ_{CP} is slightly reduced by $\sim 6\%$ thanks to the statistics improvement.

13.4.2 Future Improvement of the Oscillation Parameter Measurements

Future Statistics Improvement

As described in Section 1.5.1, the statistical uncertainties are still the dominant error source. As written in Section 6.1, the number of the events at Super-Kamiokande depends on the neutrino flux, the cross-section, the detection efficiency and the oscillation probability. The cross-section and the oscillation probability cannot be changed, therefore, it is important to improve the neutrino flux and

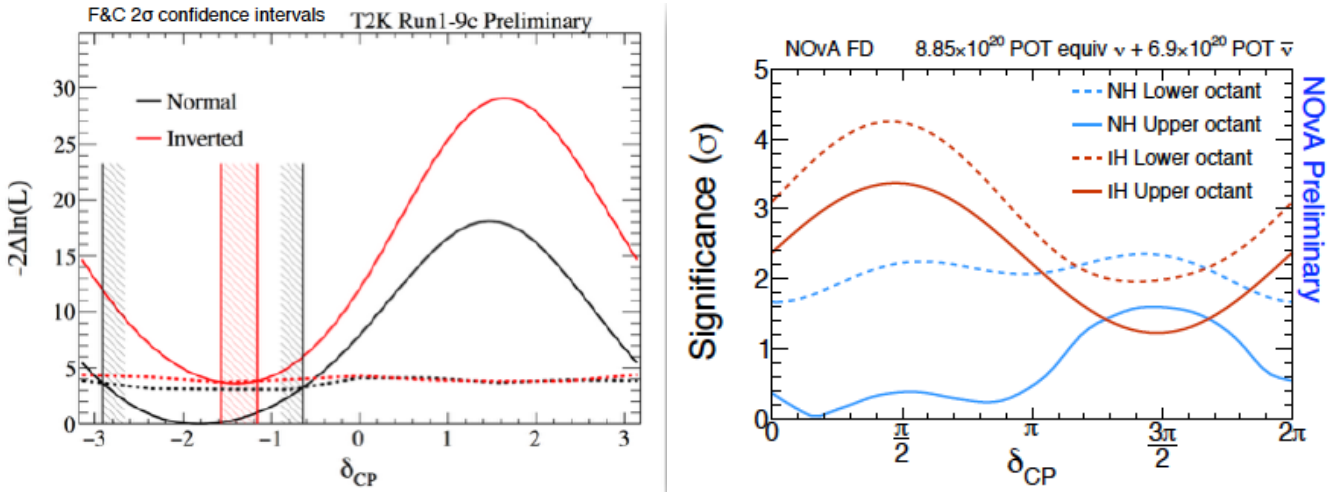

(a) T2K (b) NOνA

Figure 13.6: The results of δ_{CP} measurement from T2K and NOνA reported in NEUTRINO 2018 conference [96, 97].

the detection efficiency to reduce the statistical error. As described in Chapter 5, J-PARC Main Ring will increase the beam power up to 1.3 MW in the future. The neutrino flux is proportional to the proton beam intensity, a three times larger flux than the current one will be obtained in the future. To accumulate the pions from the target more effectively, T2K is planning to increase the horn current up to 320kA [236]. This upgrade to 320 kA is expected to increase the neutrino flux by 10% and reduce the wrong-sign neutrino by 5-10%. There are several beam monitor R&D to monitor such a high intensity the beam [237, 238] in the neutrino beamline.

For the detection efficiency at Super-Kamiokande, we have developed a new reconstruction algorithm fiTQun and achieved a better reconstruction efficiency across large fiducial volume. We also introduced new sample of one electron-like ring with a decay electron. Thanks to the better reconstruction efficiency, more complicated event selections are possible. We are planning to introduce CC single pion production of two or three ring samples. Introduction of CC single pion production will increase the event rate by $\sim 20\%$, while more precise understanding of the cross-section is necessary.

The T2K experiment is planning to extend the operation until 2×10^{22} POT are accumulated (T2K phase-II) [50]. With this POT, indication of CP violation in lepton sector can be obtained with 3σ significance if $\delta_{CP} = -\pi/2$ and normal hierarchy.

However, the statistics is still insufficient to discover CP violation in wide region of δ_{CP} even with 2×10^{22} POT. To get more data, Hyper-Kamiokande project is on going which has about ten times larger target mass than Super-Kamiokande [239]. Hyper-Kamiokande can observe CP-violation with more than 3σ significance for 57% of the possible values of δ_{CP} with ten years exposure of 1.3 MW J-PARC neutrino beam.

A complementary experiment DUNE (Deep Underground Neutrino Experiment) is also planned in the future. They plan to build 40 kiloton liquid Argon TPC's and to upgrade the accelerator up to ~ 2 MW with a new superconducting LINAC [240]. The sensitivity of the discovery of CP-violation is comparable to the Hyper-Kamiokande.

Future Systematic Uncertainties Improvement

As described in Section 12.7, understanding of the neutrino interaction modeling becomes more important for the oscillation analysis. For the construction of the precise neutrino-nucleus interaction

model, it should account for the all of the observed data. However, it is difficult to make a comparison of various experiments or to extract an information from single experiment. The detector acceptance and efficiency, the target material, and the neutrino flux and energy are different by experiments, moreover, each experiment uses different neutrino interaction generator including NEUT, GENIE [241], NuWro [242], GiBUU [243] and NUANCE. Therefore, a theoretical work is desired to extract some cross-section related information from various experiments including the electron-proton and pion-proton scattering experiments in addition to the neutrino-nucleus scattering experiments.

It is important not only to construct the neutrino interaction model, but also to measure the kinematic properties of the neutrino interaction precisely to constraint the model. Especially, large angle and low momentum data is sparse as discussed in Section 12.7. Several improvements and experiments are planned in near future. As described in Chapter 9, we selected only forward going leptons in the near detector fit. ND280 is also capable to measure backward going track and large angle FGD track with improved selections. Figure 13.7 shows the efficiency curve for the improved CC inclusive selection [244]. Red plots show the current selection efficiency and black plots show the total efficiency with the improved selections. The near detector fit with these improved selections may help to obtain a better constraint on the neutrino interaction parameters for the oscillation analysis.

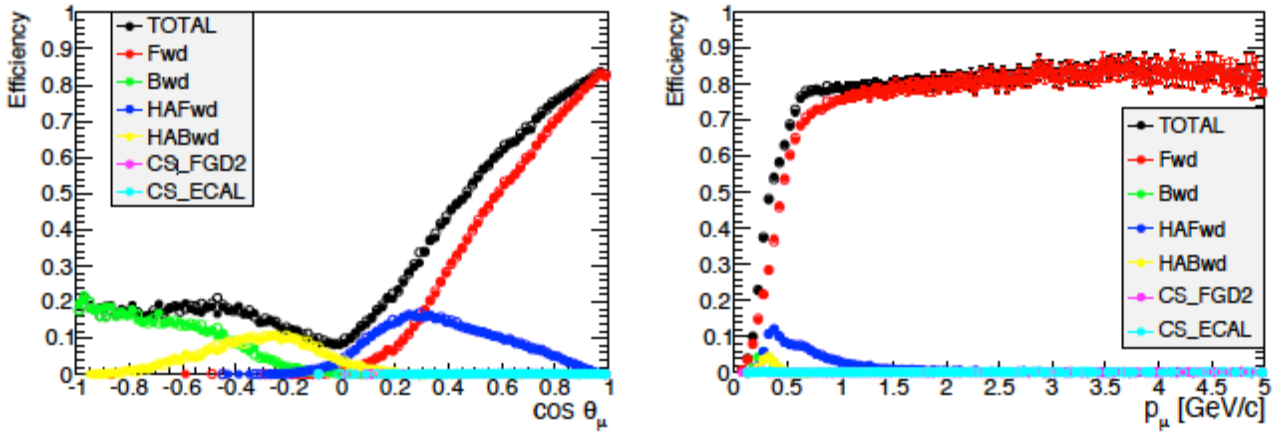

Figure 13.7: Efficiency of the angle and momentum for CC inclusive selection. Red points are for current selection, and yellow, blue and green points are for the improved selections.

T2K is also planning to upgrade ND280 so that it can measure high angle leptons [245]. The preliminary design of the ND280 upgrade and the estimated angle efficiency are shown in Fig. 13.8 [246]. The high efficiency measurement of high angle region will be obtained by using horizontal TPC (Horiz. TPC) and Super-FGD that has 4π acceptance [247]. There also exist WAGASCI (WAter Grid And SCIntillator) experiment which measures the high angle region with grid structure of the target [248].

To constrain the interaction model, it is also important to measure secondary particles such as protons and pions associated with the CC interaction since it is possible to characterize the nuclear effects by measuring muon and proton kinematics and their correlations [249]. T2K measured the muon and proton kinematics and compared with several models. They found all of the interaction models failed to describe at least part of the observed phase space [250]. Similar tendency was obtained by MicroBooNE [251] and ArgoNeuT [252] Liquid Argon TPC experiments. For CC single pion production, MiniBooNE [185] and MINERνA [253] observed a discrepancy in the pion momentum. To solve these discrepancies, more precise measurements of the secondary particles are necessary.

Comparing muons, protons make short tracks since the energy deposit is larger. ND280 upgrade

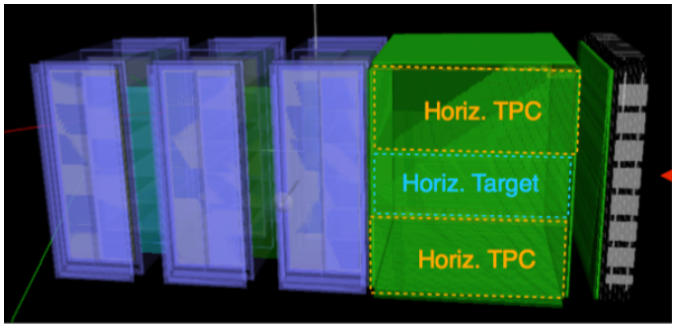

(a) Detector overview

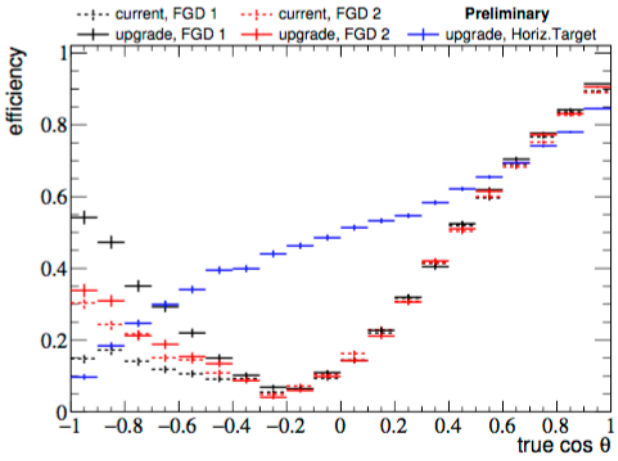

(b) Estimated angle efficiency of the ND280 upgrade detector (Black) comparing current FGD measurements.

Figure 13.8: ND280 upgrade detector

is also motivated to track such low momentum secondary particles with the fine grained cubic structure of Super-FGD. Another experiment called NINJA [254] is planned to measure low momentum particles with nuclear emulsions in J-PARC. There are also several experiments that use Liquid Argon TPC which have high capability of short track detection and 4π acceptance with large fiducial volume [255–257]. The goal for the future experiments are $\sim 4\%$ and $\sim 5\%$ for T2K phase2 and DUNE [50, 240] respectively.

13.5 Summary

We performed the oscillation fit simultaneously with five Super-Kamiokande samples (FHC/RHC 1Re, FHC/RHC 1Rμ and FHC 1Re+1d.e). We obtained following results with T2K only data:

$$\sin^2\theta_{13} = 0.0917^{+0.0063}_{-0.0049} \tag{13.2}$$

$$\sin^2\theta_{23} = 0.517^{+0.036}_{-0.035} \tag{13.3}$$

$$|\Delta m^2_{32}| = 2.457^{+0.065}_{-0.064} \times 10^{-3}(eV^2) \tag{13.4}$$

$$\delta_{CP} = -1.70^{+0.87}_{-0.88} \tag{13.5}$$

Including the reactor constraint on $\sin^2\theta_{13}$ we got:

$$\sin^2\theta_{13} = 0.02244 \pm 0.0011 \tag{13.6}$$

$$\sin^2\theta_{23} = 0.536^{+0.027}_{-0.037} \tag{13.7}$$

$$|\Delta m^2_{32}| = 2.455^{+0.067}_{-0.066} \times 10^{-3}(eV^2) \tag{13.8}$$

$$\delta_{CP} = -1.70^{+0.64}_{-0.62} \tag{13.9}$$

The results using the Feldman-Cousins method give the δ_{CP} values of [-2.84,-0.57] and [-1.57,-1.41] with 2σ confidence level for the normal and inverted hierarchy hypotheses respectively. T2K data weakly favors the normal hierarchy with a posterior probability of 87.2%, and prefer the higher octant ($\sin^2\theta_{23} > 0.5$) with a posterior probability of 78.1%. The CP-conserving values $\delta_{CP} = 0, \pi$ are excluded at more than 2σ significance.

Part IV

Conclusion

Chapter 14

Conclusion

Since the discovery of neutrino oscillation in 1998, various experiments have revealed the nature of neutrino oscillation. However, there still exists an unknown parameter δ_{CP} in the PMNS matrix which describes the size of CP violation in the lepton sector. The value of δ_{CP} is important to understand two fundamental questions in the high energy physics:

- Do neutrinos violate CP symmetry?
- Is there a new physics behind the mixing angle?

In this thesis, we reported the measurement of the neutrino oscillation parameters in the T2K experiment. The dominant uncertainty of the measurement is statistical uncertainty. The oscillation parameters are derived from a comparison between observed and predicted events at Super-Kamiokande. However, the statistical uncertainties for the event rates at Super-Kamiokande are estimated to be about 10% for the ν_e events and 6.5% for the ν_μ events assuming the Poisson distribution. To improve the statistical uncertainty, it is important to increase the beam intensity of J-PARC Main Ring since the neutrino beam intensity depends on the proton beam intensity.

The obstacle for the beam intensity improvement is the beam loss. Beam instabilities and miscontrol of the beam optics are the main sources of the beam loss. Therefore, the suppression of the beam instabilities and the precise control of the beam are keys for the reduction of the beam loss. We developed the intra-bunch feedback system and the new method of the beta function measurement during acceleration in order to reduce the beam loss. The intra-bunch feedback system suppressed the oscillation due to the beam instability better than the existing feedback system. The new beta function measurement method enabled us to optimize the beam optics at the beginning of the acceleration period where the beam loss was significant compared to the other periods. With these improvements, we achieved a 480kW continuous operation and a 520 kW single shot operation. We accumulated 1.51×10^{21} POT for FHC mode and 1.65×10^{21} POT for RHC mode from 2009 to 2018.

It is important to reduce not only the statistical uncertainties but also the systematic uncertainties for the precise measurement of the neutrino oscillation parameters. The neutrino-nucleus interaction modeling is the largest systematic uncertainty in the T2K experiment. If a different interaction model is used, the predicted neutrino event rate is changed, therefore, the interaction model affects the determination of the oscillation parameters. It is important to check whether our oscillation analysis is robust against the possible variation of the interaction models. We performed the robustness check of the oscillation analysis by using simulated data which describes the possible variation of the interaction model. We found the oscillation analysis made a bias especially on Δm^2_{32} by more than 100% relative to the total uncertainty on that parameter. To loosen the observed bias, we

developed smearing methods with the additional binding energy parameter and likelihood smearing. With these methods, the bias was reduced to below 50% relative to the total uncertainty. This study indicates that our understanding about the neutrino interaction model is still insufficient. Therefore, precise measurements of neutrino cross-section are important to constraint the interaction model. Several improvements and experiments are planned in near future including ND280 detector upgrade, WAGASCI and NINJA for the precise cross-section measurement.

We performed the oscillation analysis with these improvements and we obtained $\sin^2\theta_{13} = 0.0917^{+0.0063}_{-0.0049}$, $\sin^2\theta_{23} = 0.517^{+0.036}_{-0.035}$, $|\Delta m^2_{32}| = 2.457^{+0.065}_{-0.064} \times 10^{-3}$ eV^2, $\delta_{CP} = -1.70^{+0.87}_{-0.88}$ with the T2K data only. Using the constraint on $\sin^2\theta_{13}$ from reactor neutrino experiments, we got $\sin^2\theta_{13} = 0.02244 \pm 0.0011$, $\sin^2\theta_{23} = 0.536^{+0.027}_{-0.037}$, $|\Delta m^2_{32}| = 2.455^{+0.067}_{-0.066} \times 10^{-3}$ eV^2, $\delta_{CP} = -1.70^{+0.64}_{-0.62}$.

This measurement indicates that the CP symmetry is violated in the lepton sector at 2σ significance. The CP violation in the lepton sector may be another source of the CP violation in addition to that of baryon in the early universe. Therefore, the CP violation in the lepton sector may solve the Baryon Asymmetry in the Universe with the leptogenesis scenario. The CP violation from the PMNS matrix is not a direct confirmation of the leptogenesis, however, this result may be a clue to understand the Baryon Asymmetry in the Universe. However, the statistics is still insufficient to discover the CP violation or determine the value of δ_{CP} even with 3.16×10^{21} POT. To get more data, Hyper-Kamiokande project and J-PARC upgrade toward 1.3 MW beam power are on going. In near future, T2K or next generation experiments such as Hyper-Kamiokande and DUNE may determine the value of δ_{CP}.

Appendix A

The Theory of Circular Accelerators

A.1 Coordinates of Accelerators

In accelerators, Frenet-Serret coordinates is commonly used.

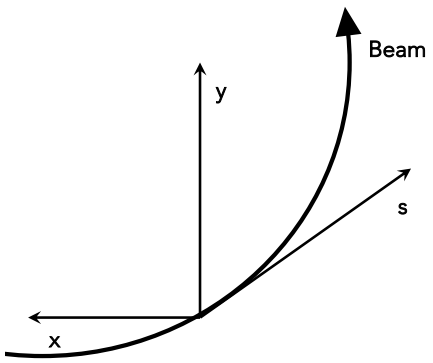

Figure A.1: Frenet-Serret coodination

"Transverse" corresponds to x and y plane in Fig. A.1 and "longitudinal" corresponds to s direction. "horizontal" denotes x direction and "vertical" denotes y direction in this thesis.

A.2 Theory of Accelerators

Synchrotron is an accelerator which accelerates particles with fixed closed-loop path. In this section, the theory of synchrotron is briefly summarized based on [258].

A.2.1 Longitudinal Dynamics

Principle of Synchrotron

A synchrotron accelerates a beam with a RF system. The RF field changes as $V = V_0 \sin \omega_s h t + \phi_s$ where ω_s denotes RF frequency, h denotes integer called "harmonic number" and ϕ_s denotes RF phase at the acceleration point. The equation of motion of the particle which has momentum p_s is written:

$$\frac{dp_s}{dt} = \frac{eV}{2\pi R} \sin \phi_s \tag{A.1}$$

The equation of motion of the particle which has momentum $p_s + \Delta p$ also follows Eq. (A.1). Thus the equation of the momentum deviation Δp is written as:

$$\frac{\Delta p}{dt} = \frac{eV}{2\pi R} (\sin \phi - \sin \phi_s) \tag{A.2}$$

where $\phi = h\omega_s t - h\theta + \phi_s$. Converting Eq. (A.2) with $\Delta E = v_s \Delta p$

$$\frac{d(\Delta E/\omega s)}{dt} = \frac{eV}{2\pi} (\sin \phi - \sin \phi_s) \tag{A.3}$$

Using Eq. (A.12) which will be discussed later and the relationship between $\Delta\omega = (\omega - \omega_s)$ and Δp becomes

$$\frac{\Delta \omega}{\omega_s} = \eta \frac{\Delta p}{p_s} \tag{A.4}$$

Considering the relationship

$$\frac{\Delta p}{p_s} = \frac{1}{\beta_s^2} \frac{\Delta E}{E_s} \tag{A.5}$$

and

$$\frac{d(\Delta\phi)}{dt} = h\omega_s - h\dot{\theta} = -h(\omega - \omega_s) = -h\Delta\omega \tag{A.6}$$

Eq. (A.7) can be derived:

$$\frac{d\Delta\phi}{dt} = h\eta \frac{\omega_s}{\beta_s} \frac{\Delta E}{E_s} \tag{A.7}$$

From Eq. (A.7) and Eq. (A.2), equation of motion of longitudinal direction can be written:

$$\frac{d}{dt} \left(\frac{\beta_s^2 E_s}{\eta \omega_s^2} \frac{d(\Delta\phi)}{dt} \right) = \frac{heV}{2\pi} (\sin \phi - \sin \phi_s) \tag{A.8}$$

If we consider the shift in the short period, the coefficient of $d(\Delta\phi)/dt$ is unchanged. We also consider the phase difference $\Delta\phi$ is small, Eq. (A.8) can be described as a harmonic oscillation equation:

$$\frac{d^2\Delta\phi}{dt^2} - \frac{heV\eta\omega_s^2 \cos\phi_s}{2\pi E_s} \Delta\phi = 0 \tag{A.9}$$

This equation indicates that the off-synchronized particle oscillates stably around the ϕ_s as long as the approximation used in Eq. (A.9) is valid. This is called the principle of phase stability. The frequency of this oscillation is called synchrotron frequency.

$$\Omega_s = \omega_s \sqrt{-\frac{heV\eta\cos\phi_s}{2\pi E_s}} \tag{A.10}$$

When the $\Delta\phi$ becomes large, synchrotron oscillation will be unstable. The particles within the stable region can be accelerated. This region is called RF bucket.

Transition Energy

Particle with momentum of$p$ circulates around the closed orbit C in an accelerator. The relationship between momentum and closed orbit can be described as follows:

$$\frac{\Delta C}{C} = \alpha \frac{\Delta p}{p} \tag{A.11}$$

This α is "momentum compaction factor" and it is determined by the lattice of the accelerator. The relationship between reputation cycle T and momentum is written using α:

$$\frac{\Delta T}{T} = (\alpha - \frac{1}{\gamma^2})\frac{\Delta p}{p} \equiv \eta \frac{\Delta p}{p} \tag{A.12}$$

This η is called slippage factor. The energy where $\alpha - \frac{1}{\gamma^2} = 0$ is called transition energy.

$$\gamma = \sqrt{\frac{1}{\alpha}} \tag{A.13}$$

If the energy of the beam is below the transition energy, the particle which has higher (lower) momentum than the nominal one, it circulates slower (faster) than nominal one. And if the energy of the beam is over the transition energy, it goes opposite. At the transition energy, the synchrotron oscillation frequency becomes zero and there is no phase focusing. Thus, beam becomes unstable and beam loss is occurred when the beam crosses the transition energy.

A.2.2 Transverse Dynamics

Betatron Tune

Tune in an accelerator is the number of betatron oscillation in a turn. The tune is related to the β function described in Eq. (4.2).

$$\nu = \frac{1}{2\pi} \oint \frac{ds}{\beta(s)} \tag{A.14}$$

As described in Chapter 3, the resonance will occur with the integer or factional values with small denominators such as $\frac{1}{2}$ tune. The resonance condition is given by Eq. (A.15).

$$n\nu_x + m\nu_y = N_s l \;\; where \;\; n, m, \in \mathcal{Z} \tag{A.15}$$

N_s is a number of super periods in an accelerator. (N_s=3 in J-PARC case).

Dispersion function

In real situation, the momentum of the particles are distributed around the mean of them. The orbits of the particle also change by the momentum deviation. The equation of motion of the particle which has the momentum of $p + \Delta p/p = (1 + \delta)p$ can be written ignoring second order of δ:

$$x'' + (\frac{1}{\rho^2} + k(s))x = \frac{\delta}{\rho}, \quad ks = \frac{1}{B\rho}\frac{\partial B_y}{\partial x} \tag{A.16}$$

The solution of Eq. (A.16) is defined as the linear combination of Eq. (A.18).

$$x(s) = x_\beta(s) + D(s)\delta \tag{A.17}$$

$$\begin{array}{c} x''_\beta + (\frac{1}{\rho} + k(s))x_\beta = 0 \\ D'' + (\frac{1}{\rho^2} + k(s))D = \frac{1}{\rho} \end{array} \tag{A.18}$$

This D(s) is called dispersion function where characterize the relationship between deviation of the orbit and that of momentum.

Chromaticity

The strength of quadrupole magnets depends on the momentum of the particle, thus the off-momentum particles feels different strength of focusing and pass through the different orbit. This is called chromatic aberration. The effects can be described by the tune spread. The tune spread of the momentum difference of δ can be written:

$$\frac{d(\Delta\nu)}{d\delta} = -\frac{1}{4\pi}\oint \beta(s)\Delta k(s)ds \tag{A.19}$$

where the $\Delta k(s)$ denotes the quadrupole field difference due to the momentum difference. Sextupole magnets are used to correct the chromaticity in accelerators. As discussed in Chapter 3, chromaticity is one of the sources of tune spread. Although the chromaticity spreads the tune and cause the possible beam loss, non-zero chromaticity is often set to stabilize the coherent oscillation discussed later.

Space Charge Effect

In high intensity accelerators, the Coulomb force between the particles of the beam will affect the beam dynamics. Since the particle in the beam has the same charge, the repulsive force is canceled out the magnetic field from the quadrupole magnet. Therefore, the space charge effects shift down the tune from the original point. The tune spread due to the space charge effect with the beam of emittance ϵ_x, ϵ_y can be written as:

$$\Delta\nu_y = -\frac{Nr_pF}{\pi\epsilon_y\left(1 + \sqrt{\frac{\epsilon_x}{\epsilon_y}}\right)\beta^2\gamma^3}\frac{1}{B_f} \tag{A.20}$$

where r_p is the classical proton radius, N is the number of protons, β and γ are velocity and Lorentz factor. F is a form factor which depends on the shape of the beam duct. B_f is a bunching factor which is the ratio of the mean and peak of the beam current. The tune spread becomes larger when the N becomes large.

Appendix B

Fractional Error of Neutrino Fluxes

B.1 FHC mode at ND280

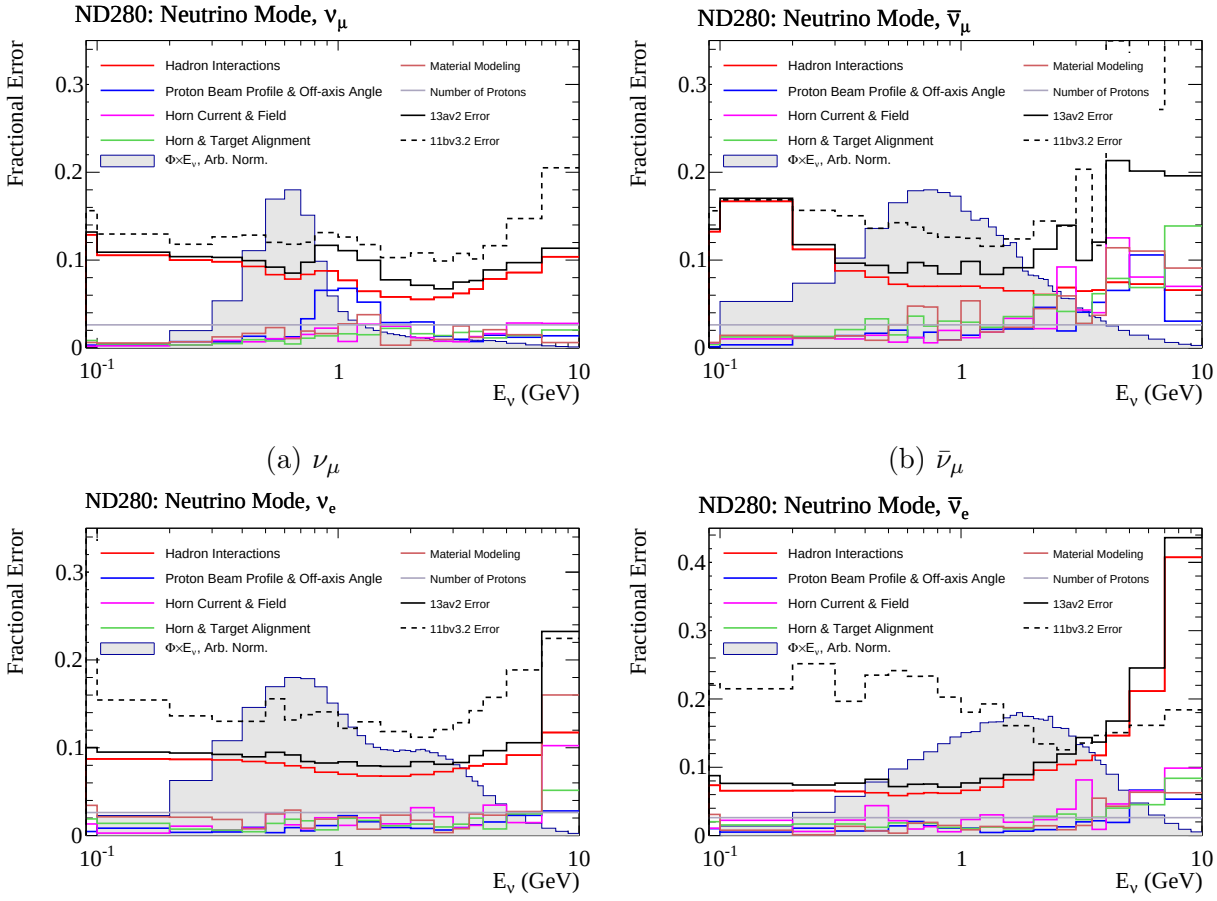

(a) ν_μ (b) $\bar{\nu}_\mu$

(c) ν_e (d) $\bar{\nu}_e$

Figure B.1: Fractional error of the neutrino flux at ND280 for FHC mode

B.2 RHC Mode at ND280

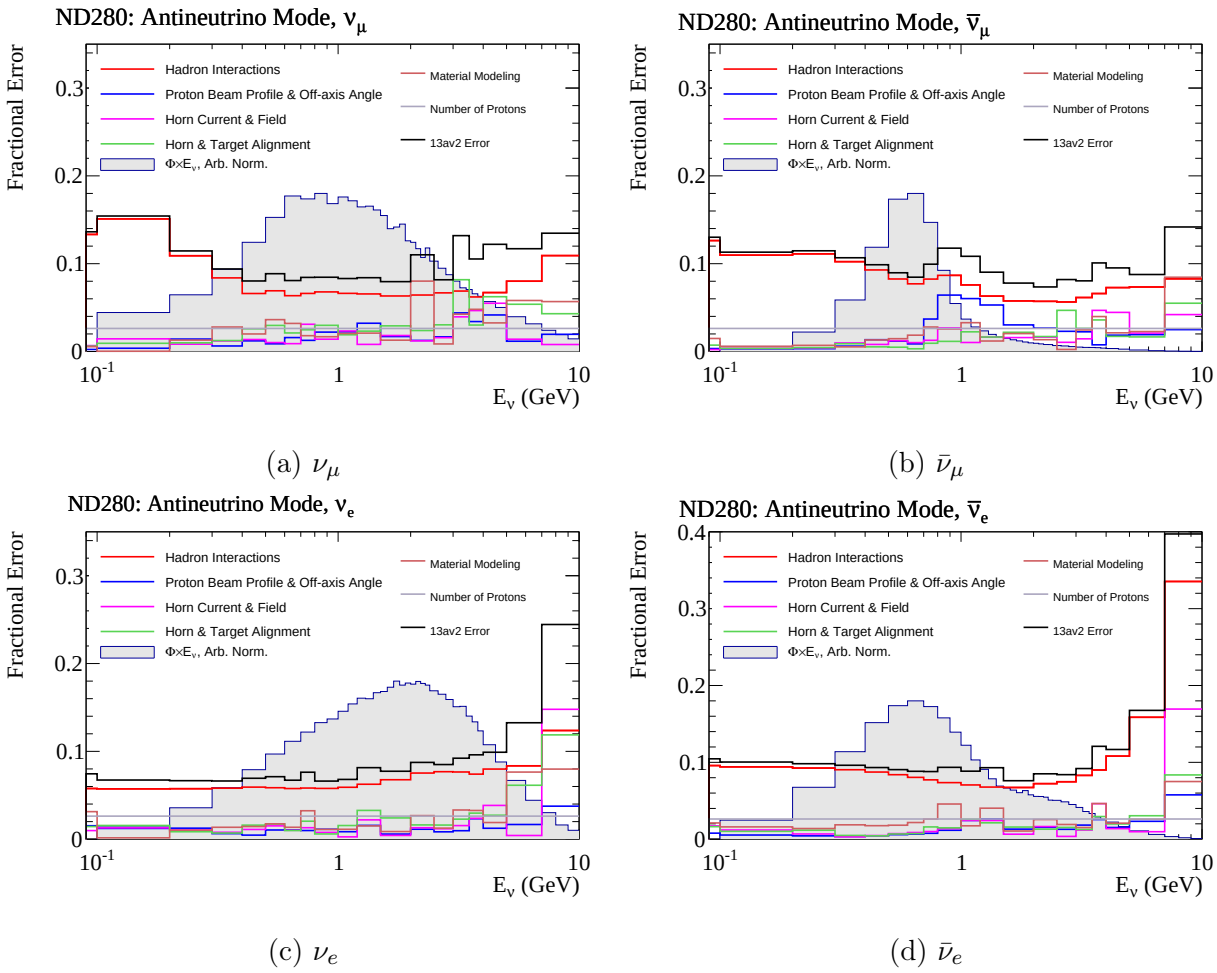

(a) ν_μ (b) $\bar{\nu}_\mu$

(c) ν_e (d) $\bar{\nu}_e$

Figure B.2: Fractional error of the neutrino flux at ND280 for RHC mode

B.3 FHC Mode at Super-Kamiokande

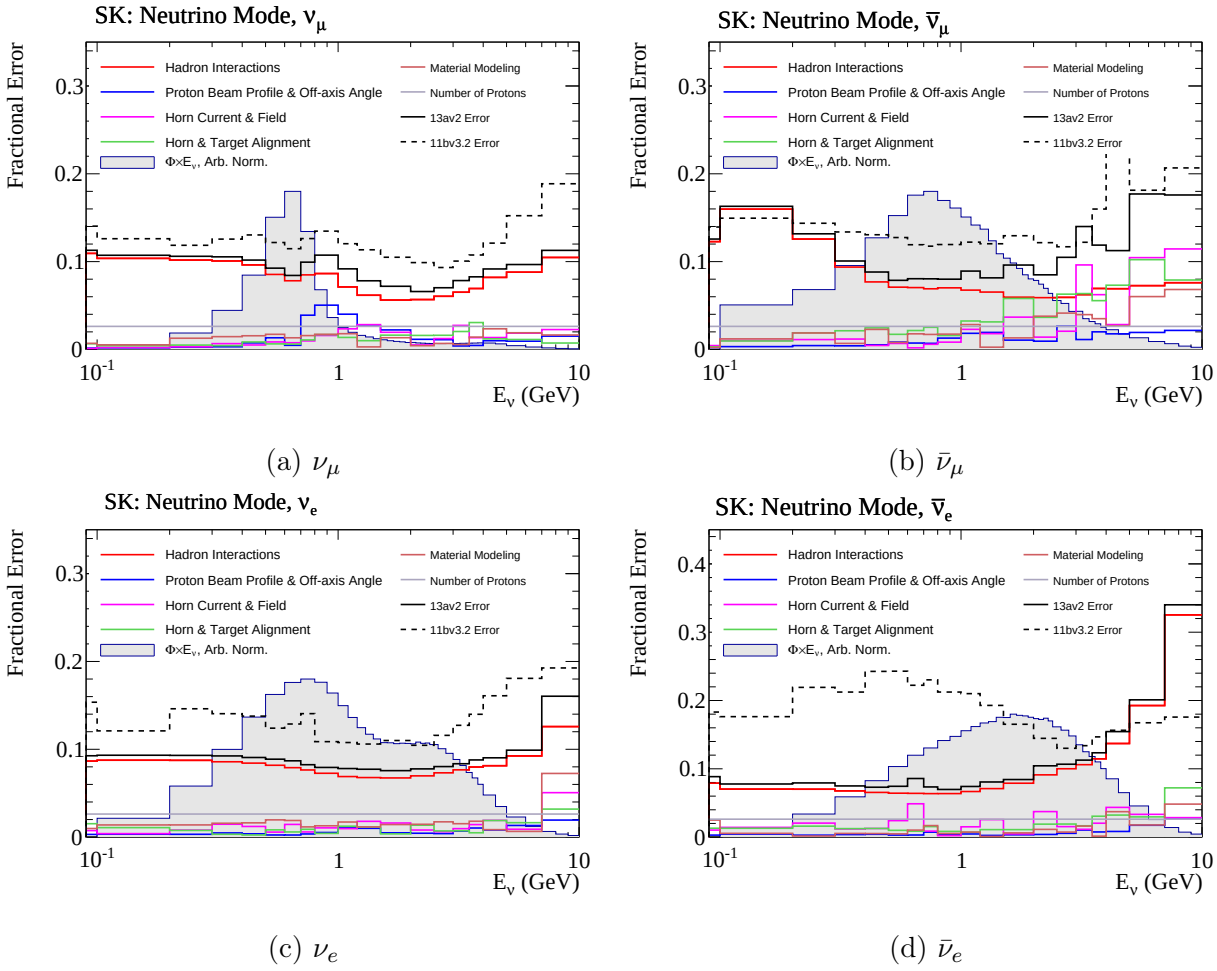

(a) ν_μ (b) $\bar{\nu}_\mu$

(c) ν_e (d) $\bar{\nu}_e$

Figure B.3: Fractional error of the neutrino flux at Super-Kamiokande for FHC mode

B.4 RHC Mode at Super-Kamiokande

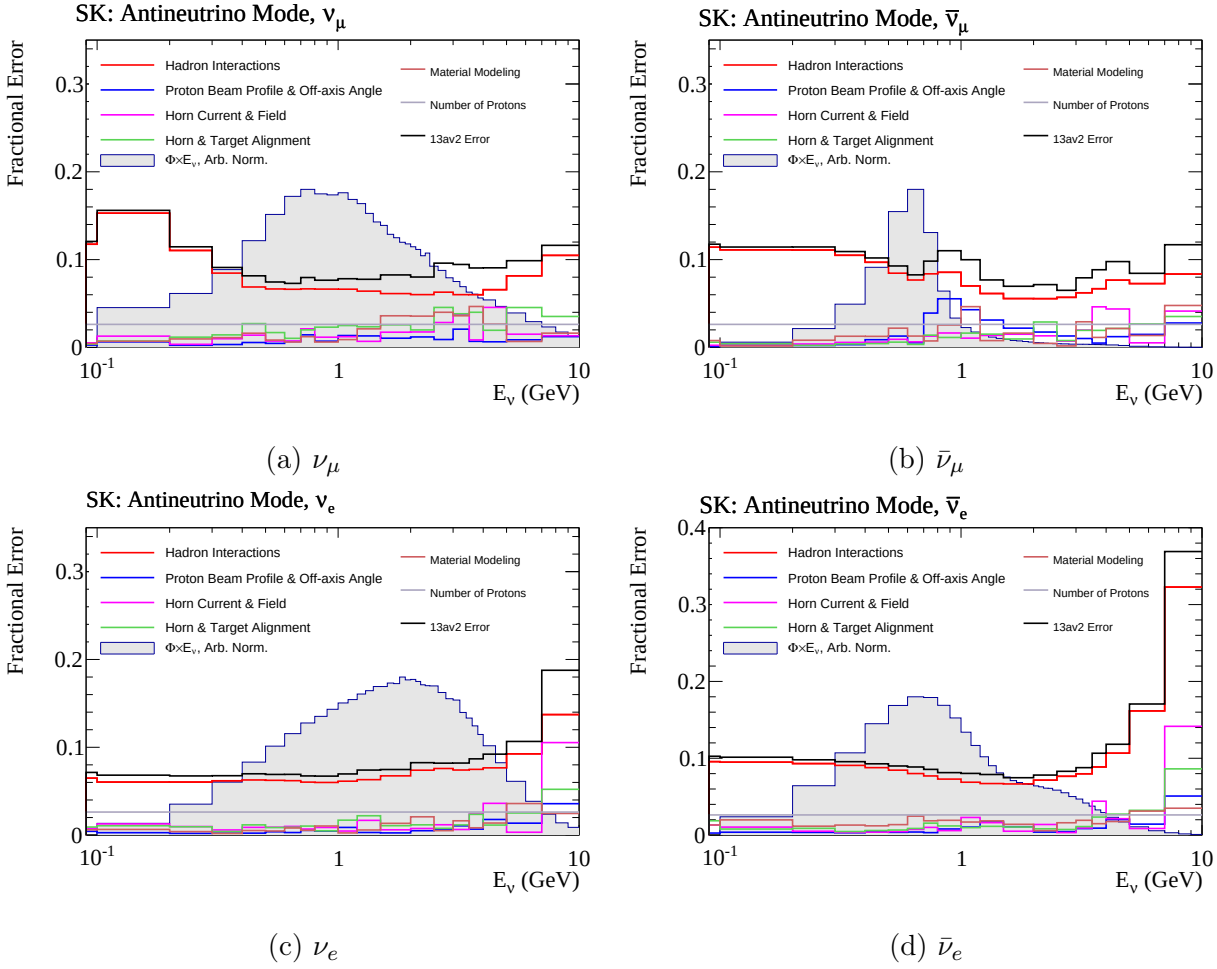

(a) ν_μ (b) $\bar{\nu}_\mu$

(c) ν_e (d) $\bar{\nu}_e$

Figure B.4: Fractional error of the neutrino flux at Super-Kamiokande for RHC mode

Appendix C

BeRPA Parameters

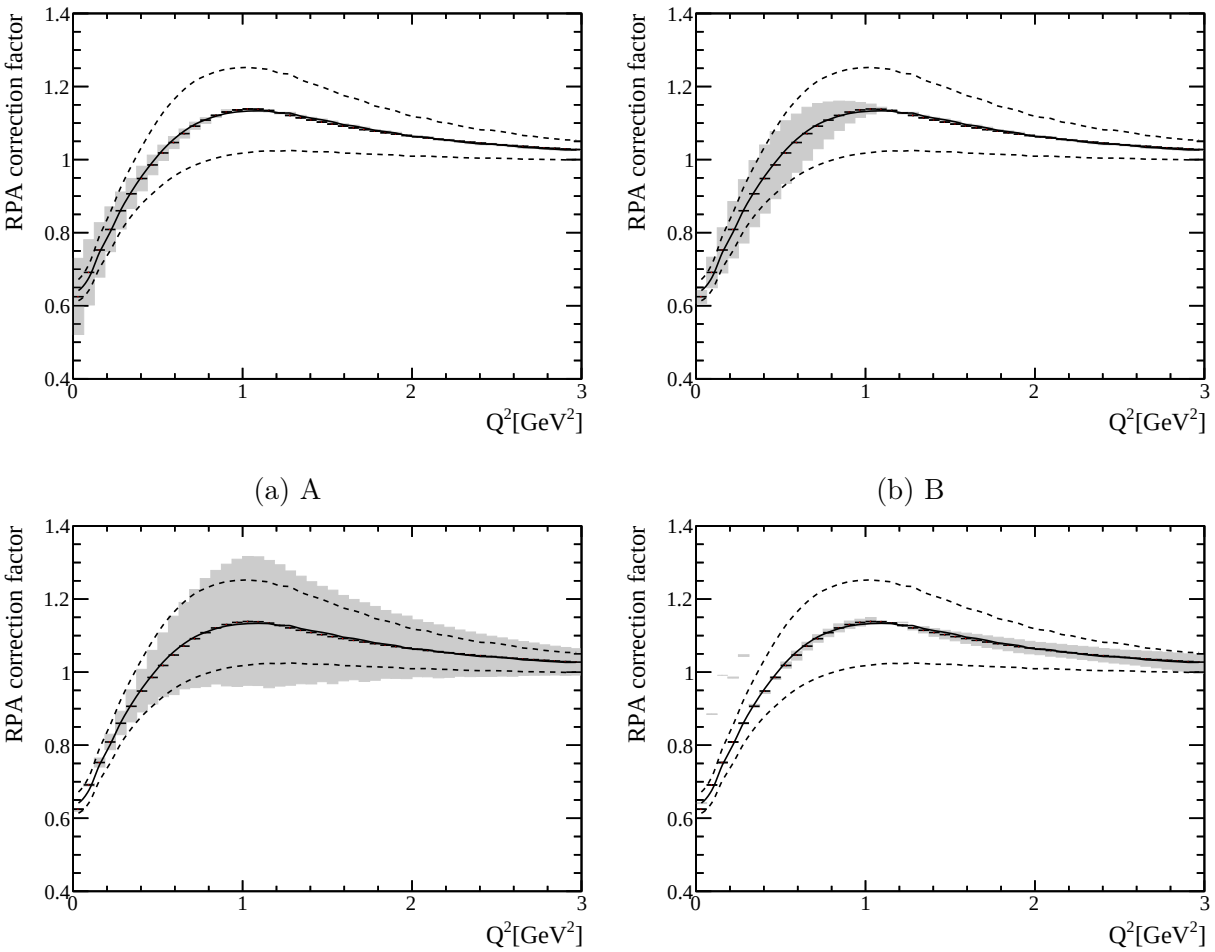

(a) A

(b) B

(c) C

(d) D

Figure C.1: The 1σ shift of each BeRPA parameter

Appendix D

Near Detector Distribution Before Near Detector Fit

D.1 FGD1 distribution

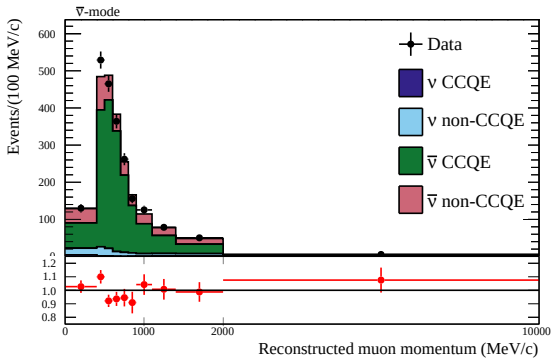

(a) RHC ACC1track momentum distribution

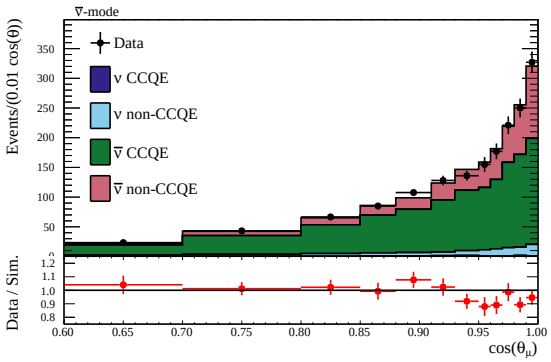

(b) RHC ACC1track $\cos\theta$ distribution

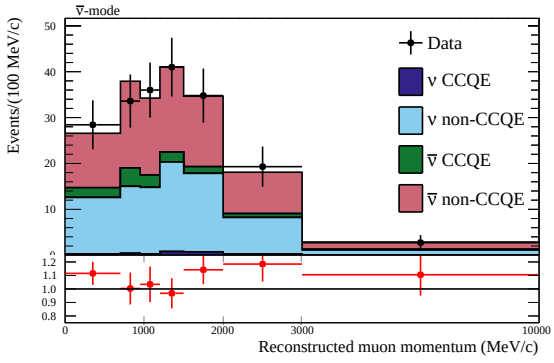

(c) RHC ACCNtrack momentum distribution

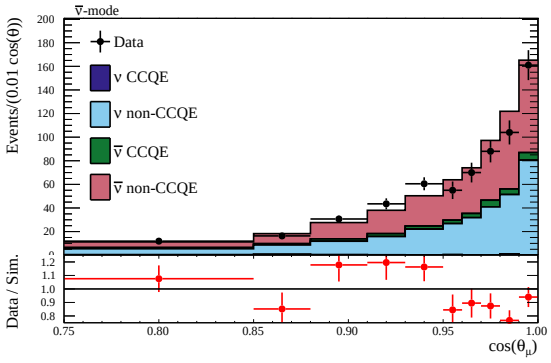

(d) RHC ACCNtrack $\cos\theta$ distribution

Figure D.1: FGD1 momentum and $\cos\theta$ distribution for each sample (ACC1track, ACCNtrack)

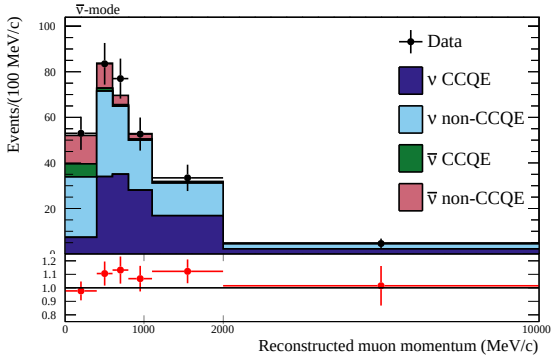

PRELIMINARY

(a) RHC CC1track momentum distribution

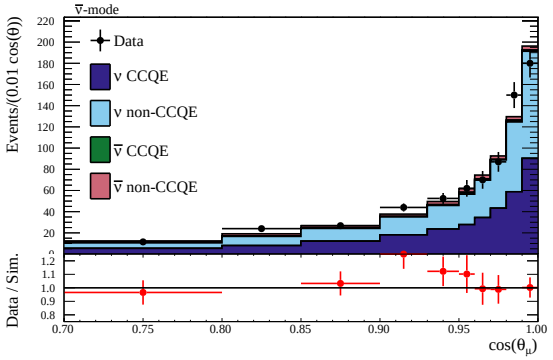

PRELIMINARY

(b) RHC CC1track $\cos\theta$ distribution

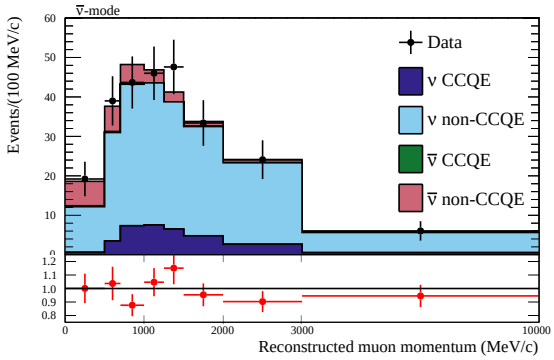

PRELIMINARY

(c) RHC CCNtrack momentum distribution

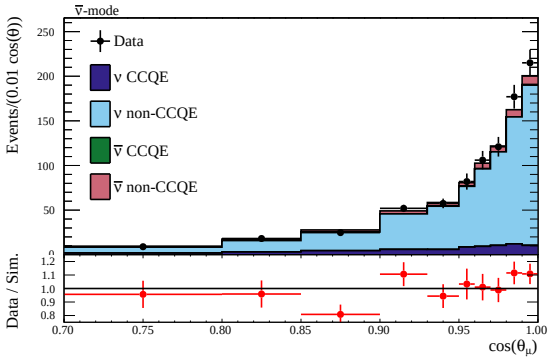

PRELIMINARY

(d) RHC CCNtrack $\cos\theta$ distribution

Figure D.2: FGD1 momentum and $\cos\theta$ distribution for each sample (CC1track, CCNTrack)

D.2 FGD2 distribution

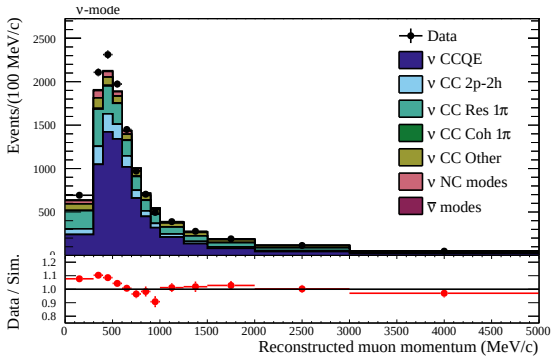

PRELIMINARY

(a) FHC CC0pi momentum distribution

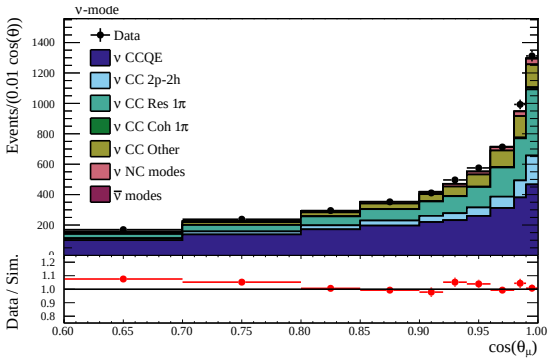

PRELIMINARY

(b) FHC CC0pi $\cos\theta$ distribution

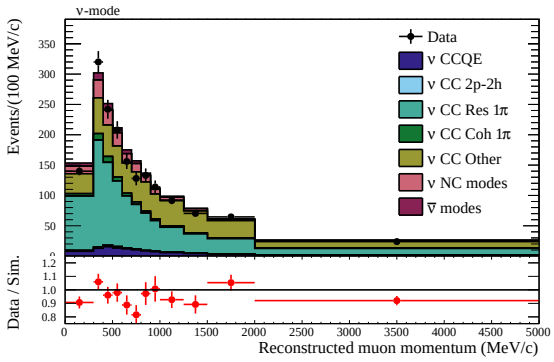

PRELIMINARY

(c) FHC CC1pi momentum distribution

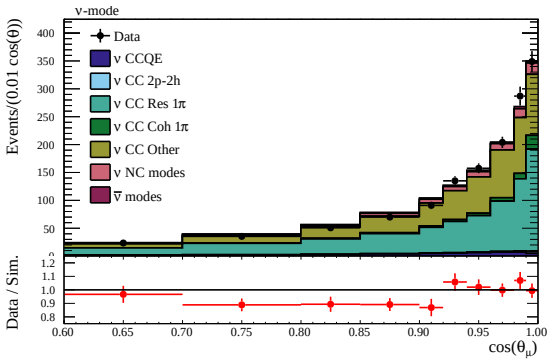

PRELIMINARY

(d) FHC CC1pi $\cos\theta$ distribution

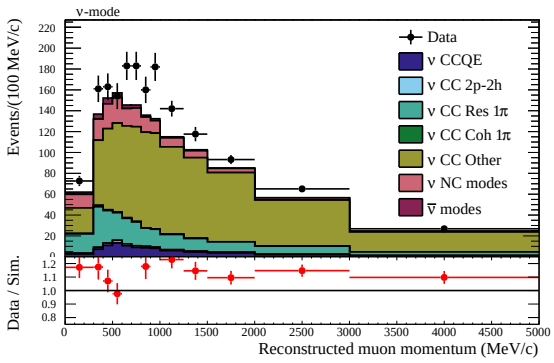

PRELIMINARY

(e) FHC CCOther momentum distribution

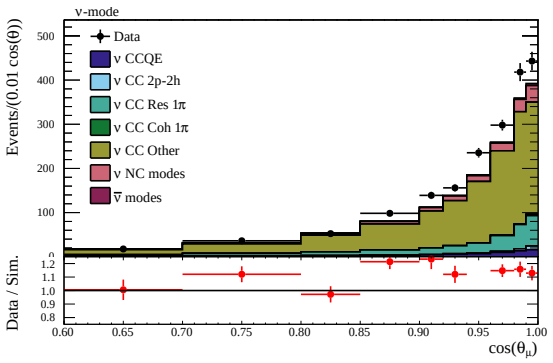

PRELIMINARY

(f) FHC CCOther $\cos\theta$ distribution

Figure D.3: FGD2 momentum and $\cos\theta$ distribution for each sample (CC0π, CC1π, CCOther)

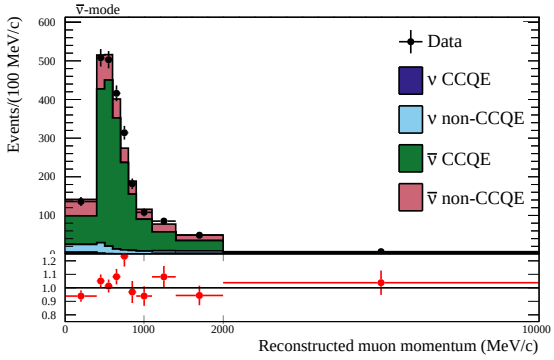

PRELIMINARY

(a) RHC ACC1track momentum distribution

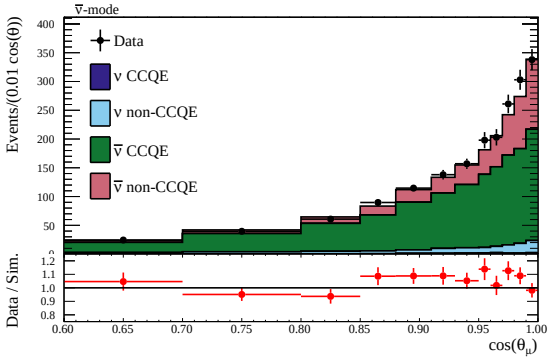

PRELIMINARY

(b) RHC ACC1track $\cos\theta$ distribution

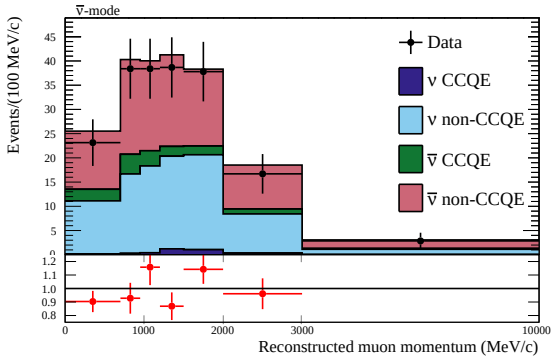

PRELIMINARY

(c) RHC ACCNtrack momentum distribution

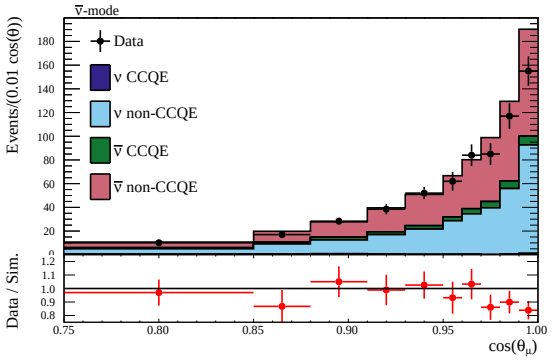

PRELIMINARY

(d) RHC ACCNtrack $\cos\theta$ distribution

Figure D.4: FGD2 momentum and $\cos\theta$ distribution for each sample (ACC1track, ACCNtrack)

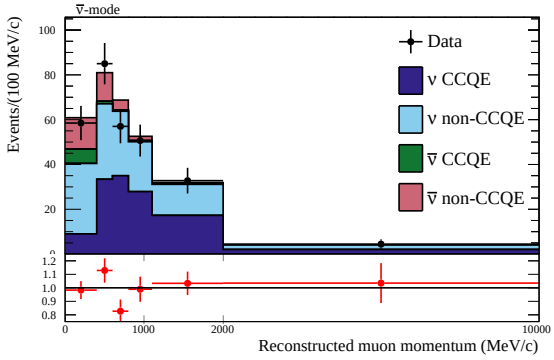

PRELIMINARY

(a) RHC CC1track momentum distribution

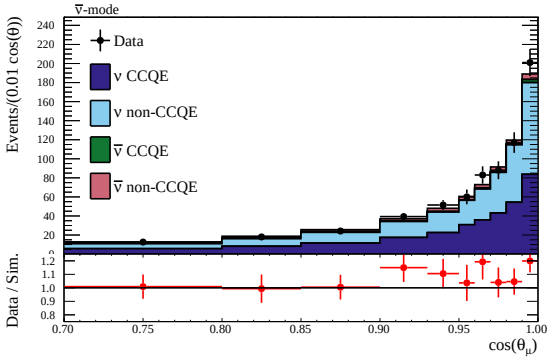

PRELIMINARY

(b) RHC CC1track $\cos\theta$ distribution

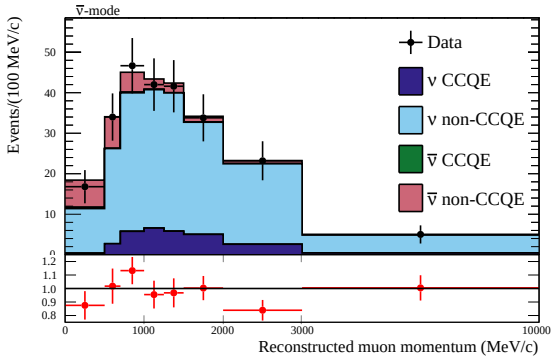

PRELIMINARY

(c) RHC CCNtrack momentum distribution

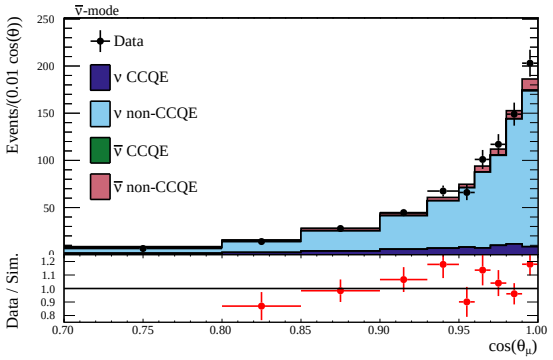

PRELIMINARY

(d) RHC CCNtrack $\cos\theta$ distribution

Figure D.5: FGD2 momentum and $\cos\theta$ distribution for each sample (CC1track, CCNtrack)

Appendix E

Near Detector Fit Results

E.1 Parameter shift

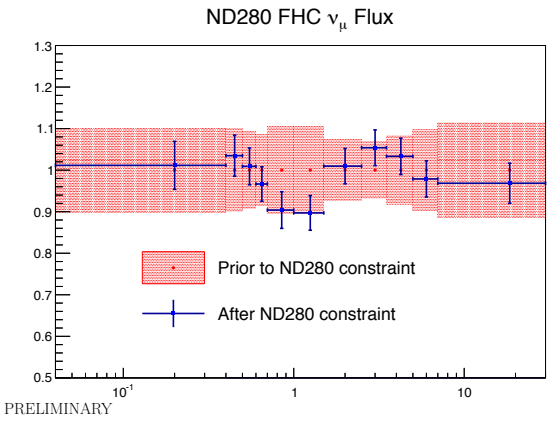

(a) ND280 FHC ν_μ flux

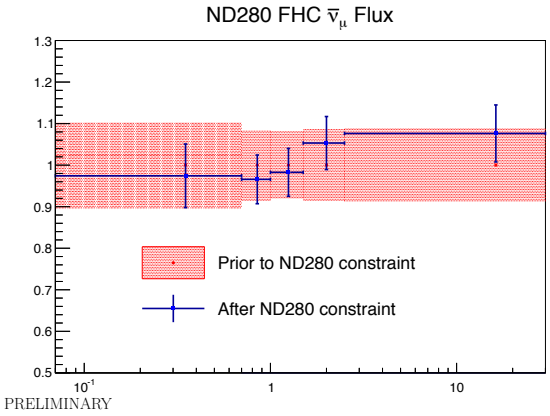

(b) ND280 FHC $\bar{\nu}_\mu$ flux

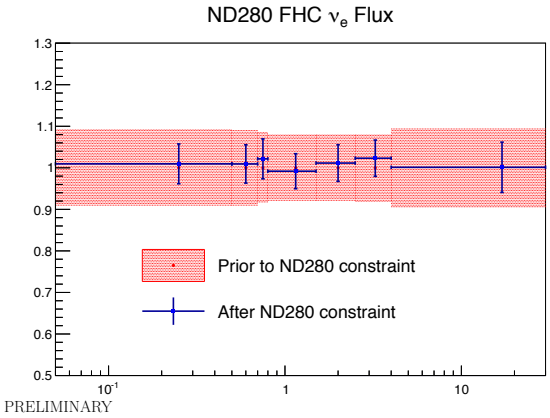

(c) ND280 FHC ν_e flux

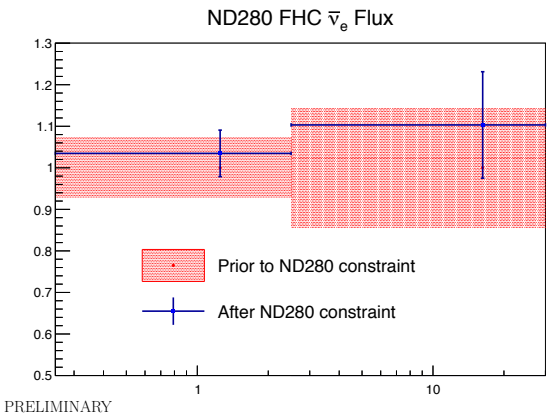

(d) ND280 FHC $\bar{\nu}_e$ flux

Figure E.1: Fit results for ND280 flux parameters

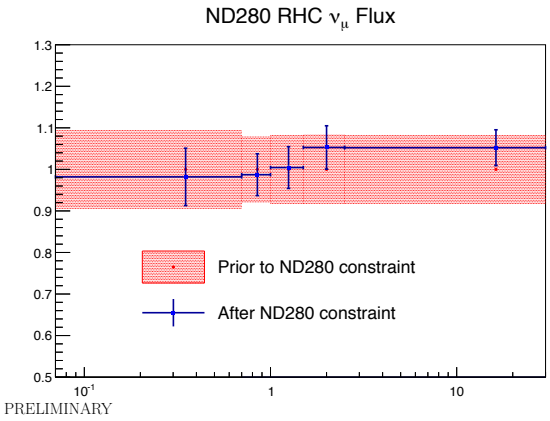

(a) ND280 RHC ν_μ flux

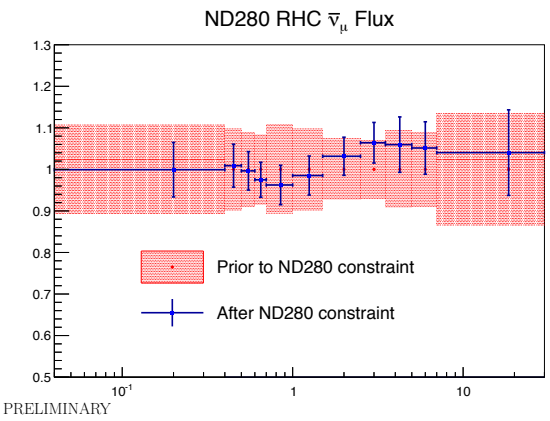

(b) ND280 RHC $\bar{\nu}_\mu$ flux

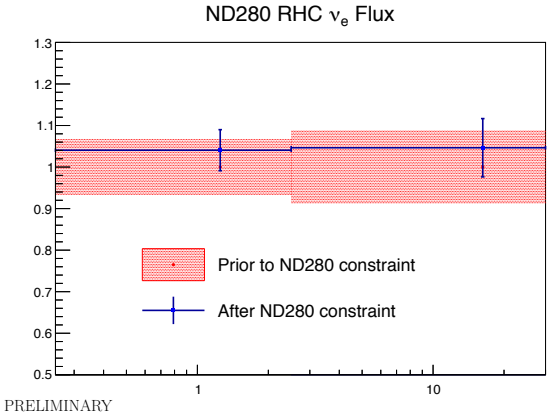

(c) ND280 RHC ν_e flux

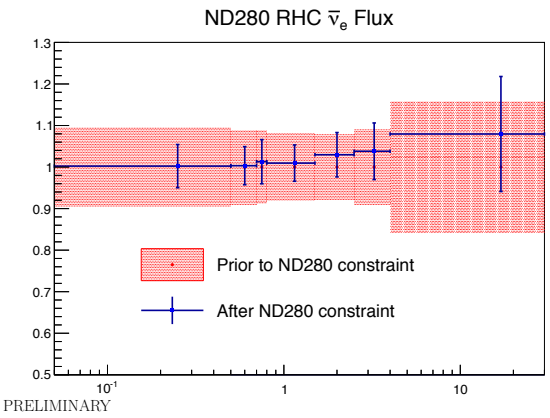

(d) ND280 RHC $\bar{\nu}_e$ flux

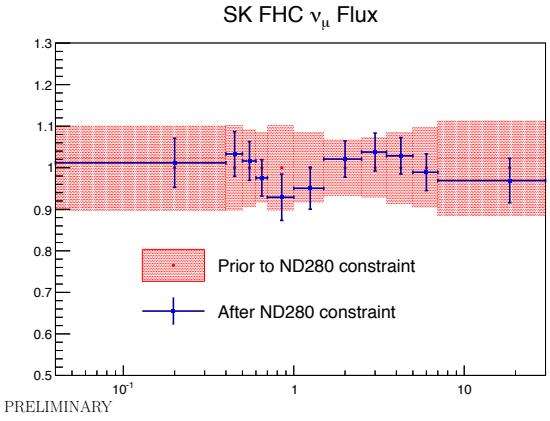

(e) Super-Kamiokande FHC ν_μ flux

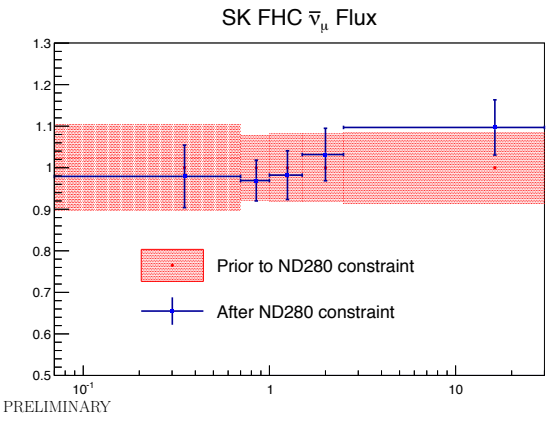

(f) Super-Kamiokande FHC $\bar{\nu}_\mu$ flux

Figure E.2: Fit results for ND280 and Super-Kamiokande flux parameters

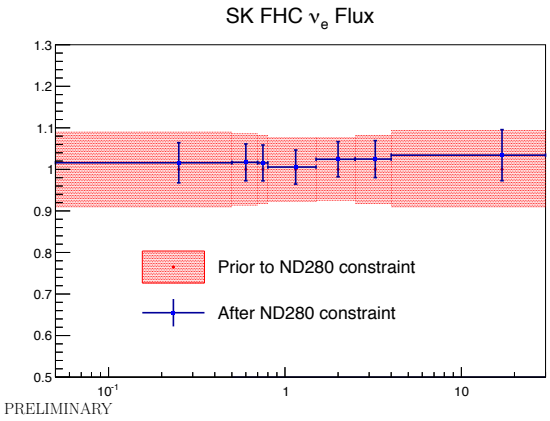

(a) Super-Kamiokande FHC ν_e flux

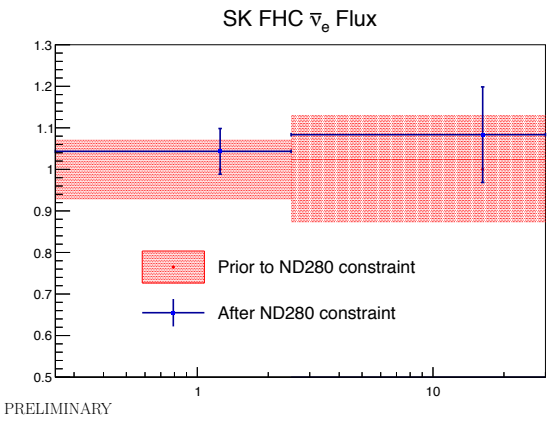

(b) Super-Kamiokande FHC $\bar{\nu}_e$ flux

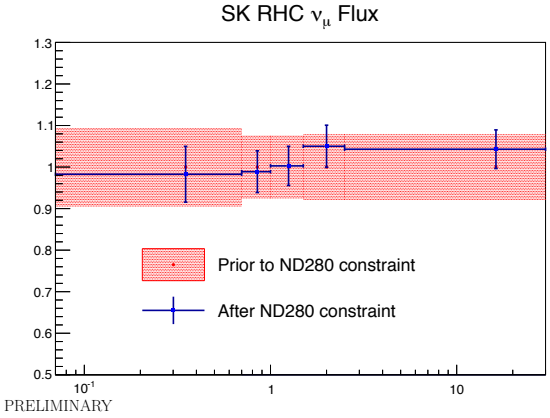

(c) Super-Kamiokande RHC ν_μ flux

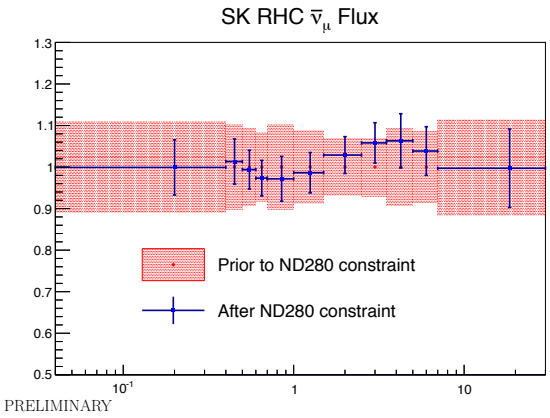

(d) Super-Kamiokande RHC $\bar{\nu}_\mu$ flux

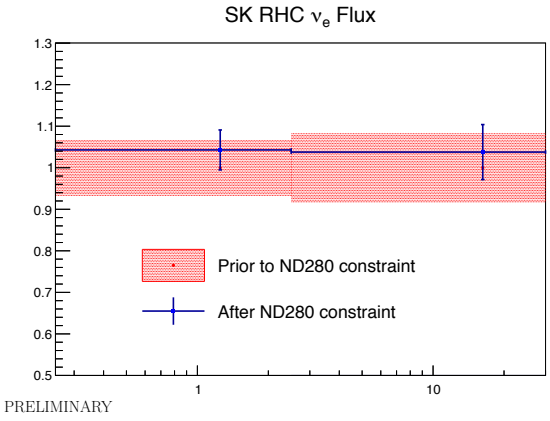

(e) Super-Kamiokande RHC ν_e flux

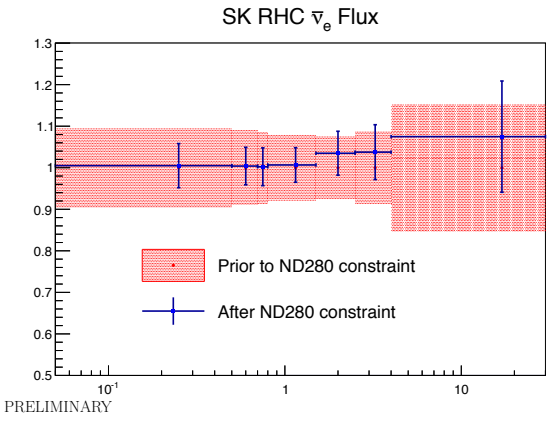

(f) Super-Kamiokande RHC $\bar{\nu}_e$ flux

Figure E.3: Fit results for Super-Kamiokande flux parameters

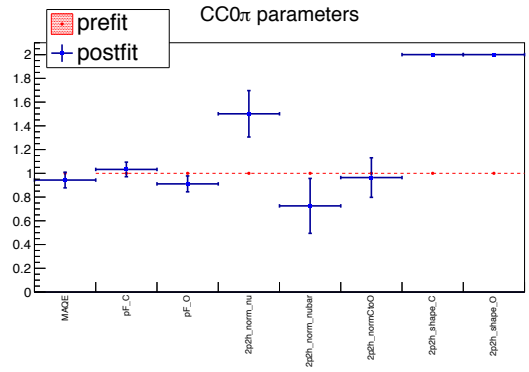

PRELIMINARY

(a) CC0π parameters

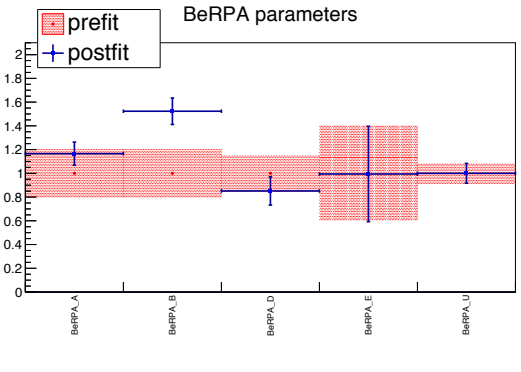

PRELIMINARY

(b) RPA parameters

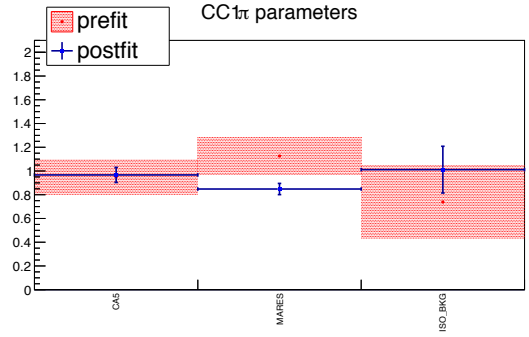

PRELIMINARY

(c) CC1π parameters

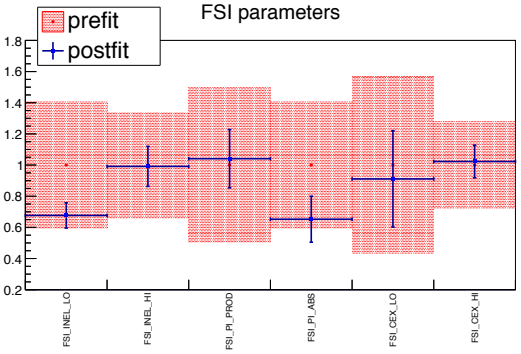

PRELIMINARY

(d) FSI parameters

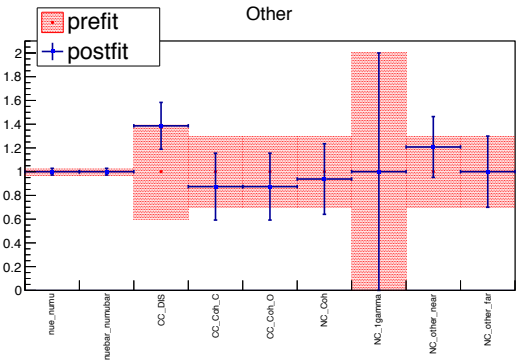

PRELIMINARY

(e) CCOther and NC parameters

Figure E.4: Fit results for cross-section parameters

E.2 Summary Table

Table E.1: Prefit and postfit parameter values and uncertainties.

Parameter	***PreFit***	***PostFit***
NDNuModeNumu0	1.0 ± 0.10091	1.0117 ± 0.057777
NDNuModeNumu1	1.0 ± 0.099431	1.035 ± 0.049528
NDNuModeNumu2	1.0 ± 0.092025	1.0092 ± 0.044345
NDNuModeNumu3	1.0 ± 0.085239	0.96679 ± 0.041487
NDNuModeNumu4	1.0 ± 0.10536	0.90408 ± 0.044063
NDNuModeNumu5	1.0 ± 0.10437	0.89722 ± 0.041704
NDNuModeNumu6	1.0 ± 0.073612	1.0098 ± 0.042558
NDNuModeNumu7	1.0 ± 0.068993	1.054 ± 0.043046
NDNuModeNumu8	1.0 ± 0.082334	1.0333 ± 0.043747
NDNuModeNumu9	1.0 ± 0.097308	0.97897 ± 0.043514
NDNuModeNumu10	1.0 ± 0.11471	0.96861 ± 0.048294
NDNuModeNumub0	1.0 ± 0.1038	0.97437 ± 0.076593
NDNuModeNumub1	1.0 ± 0.084158	0.96595 ± 0.058652
NDNuModeNumub2	1.0 ± 0.081349	0.98283 ± 0.057718
NDNuModeNumub3	1.0 ± 0.085208	1.0534 ± 0.063807
NDNuModeNumub4	1.0 ± 0.087735	1.0764 ± 0.068656
NDNuModeNue0	1.0 ± 0.091336	1.0097 ± 0.047882
NDNuModeNue1	1.0 ± 0.089699	1.0095 ± 0.046125
NDNuModeNue2	1.0 ± 0.084648	1.0217 ± 0.048056
NDNuModeNue3	1.0 ± 0.079722	0.99199 ± 0.042129
NDNuModeNue4	1.0 ± 0.079766	1.0116 ± 0.044172
NDNuModeNue5	1.0 ± 0.081399	1.0233 ± 0.043646
NDNuModeNue6	1.0 ± 0.095795	1.0014 ± 0.060518
NDNuModeNueb0	1.0 ± 0.072069	1.0349 ± 0.055968
NDNuModeNueb1	1.0 ± 0.14292	1.1034 ± 0.12812

Table E.2: Prefit and postfit parameter values and uncertainties.

Parameter	***PreFit***	***PostFit***
NDANuModeNumu0	1.0 ± 0.094066	0.98204 ± 0.069027
NDANuModeNumu1	1.0 ± 0.079866	0.9874 ± 0.050365
NDANuModeNumu2	1.0 ± 0.080948	1.0046 ± 0.050184
NDANuModeNumu3	1.0 ± 0.083251	1.0529 ± 0.052244
NDANuModeNumu4	1.0 ± 0.082653	1.0523 ± 0.043089
NDANuModeNumub0	1.0 ± 0.10728	0.99939 ± 0.065696
NDANuModeNumub1	1.0 ± 0.098851	1.0091 ± 0.051682
NDANuModeNumub2	1.0 ± 0.08971	0.99662 ± 0.046238
NDANuModeNumub3	1.0 ± 0.084692	0.97517 ± 0.042092
NDANuModeNumub4	1.0 ± 0.10687	0.96265 ± 0.047431
NDANuModeNumub5	1.0 ± 0.098711	0.98538 ± 0.046917
NDANuModeNumub6	1.0 ± 0.07335	1.0318 ± 0.045852
NDANuModeNumub7	1.0 ± 0.07052	1.0643 ± 0.048869
NDANuModeNumub8	1.0 ± 0.092905	1.0598 ± 0.066707
NDANuModeNumub9	1.0 ± 0.089083	1.0517 ± 0.063055
NDANuModeNumub10	1.0 ± 0.13491	1.0406 ± 0.10298
NDANuModeNue0	1.0 ± 0.066214	1.0407 ± 0.04941
NDANuModeNue1	1.0 ± 0.086977	1.0466 ± 0.070201
NDANuModeNueb0	1.0 ± 0.095575	1.0024 ± 0.051996
NDANuModeNueb1	1.0 ± 0.089033	1.0034 ± 0.045829
NDANuModeNueb2	1.0 ± 0.088406	1.0131 ± 0.053103
NDANuModeNueb3	1.0 ± 0.081472	1.0097 ± 0.043701
NDANuModeNueb4	1.0 ± 0.078353	1.0298 ± 0.053413
NDANuModeNueb5	1.0 ± 0.089427	1.0382 ± 0.068116
NDANuModeNueb6	1.0 ± 0.15697	1.0798 ± 0.13842

Table E.3: Prefit and postfit parameter values and uncertainties.

Parameter	***PreFit***	***PostFit***
SKNuModeNumu0	1.0 ± 0.10255	1.012 ± 0.059199
SKNuModeNumu1	1.0 ± 0.10177	1.0333 ± 0.053822
SKNuModeNumu2	1.0 ± 0.092573	1.0164 ± 0.046599
SKNuModeNumu3	1.0 ± 0.084265	0.97575 ± 0.04375
SKNuModeNumu4	1.0 ± 0.10227	0.9291 ± 0.055734
SKNuModeNumu5	1.0 ± 0.084528	0.95065 ± 0.050403
SKNuModeNumu6	1.0 ± 0.066909	1.021 ± 0.04356
SKNuModeNumu7	1.0 ± 0.072355	1.0379 ± 0.045617
SKNuModeNumu8	1.0 ± 0.085299	1.0289 ± 0.043839
SKNuModeNumu9	1.0 ± 0.096725	0.98928 ± 0.044167
SKNuModeNumu10	1.0 ± 0.11411	0.96922 ± 0.053331
SKNuModeNumub0	1.0 ± 0.10313	0.97924 ± 0.07523
SKNuModeNumub1	1.0 ± 0.078327	0.9693 ± 0.049141
SKNuModeNumub2	1.0 ± 0.082367	0.98238 ± 0.058624
SKNuModeNumub3	1.0 ± 0.082121	1.0319 ± 0.063217
SKNuModeNumub4	1.0 ± 0.085123	1.0971 ± 0.066473
SKNuModeNue0	1.0 ± 0.090918	1.0161 ± 0.048301
SKNuModeNue1	1.0 ± 0.087065	1.0171 ± 0.044337
SKNuModeNue2	1.0 ± 0.082527	1.0157 ± 0.043157
SKNuModeNue3	1.0 ± 0.076514	1.0058 ± 0.041025
SKNuModeNue4	1.0 ± 0.075773	1.0245 ± 0.042331
SKNuModeNue5	1.0 ± 0.082078	1.0249 ± 0.044485
SKNuModeNue6	1.0 ± 0.092882	1.0344 ± 0.061478
SKNuModeNueb0	1.0 ± 0.071921	1.0436 ± 0.054925
SKNuModeNueb1	1.0 ± 0.12898	1.0838 ± 0.11501

Table E.4: Prefit and postfit parameter values and uncertainties.

Parameter	***PreFit***	***PostFit***
SKANuModeNumu0	1.0 ± 0.093954	0.98279 ± 0.067164
SKANuModeNumu1	1.0 ± 0.076369	0.98905 ± 0.050203
SKANuModeNumu2	1.0 ± 0.0749	1.003 ± 0.047121
SKANuModeNumu3	1.0 ± 0.078108	1.0502 ± 0.050704
SKANuModeNumu4	1.0 ± 0.077505	1.0431 ± 0.0465
SKANuModeNumub0	1.0 ± 0.10859	0.99926 ± 0.066429
SKANuModeNumub1	1.0 ± 0.10191	1.0134 ± 0.054275
SKANuModeNumub2	1.0 ± 0.092787	0.99398 ± 0.046643
SKANuModeNumub3	1.0 ± 0.082669	0.97346 ± 0.042743
SKANuModeNumub4	1.0 ± 0.10209	0.97181 ± 0.053869
SKANuModeNumub5	1.0 ± 0.087732	0.98659 ± 0.048507
SKANuModeNumub6	1.0 ± 0.068117	1.029 ± 0.044329
SKANuModeNumub7	1.0 ± 0.069902	1.0583 ± 0.048501
SKANuModeNumub8	1.0 ± 0.091711	1.0633 ± 0.065275
SKANuModeNumub9	1.0 ± 0.084736	1.0388 ± 0.058505
SKANuModeNumub10	1.0 ± 0.11549	0.99739 ± 0.094353
SKANuModeNue0	1.0 ± 0.066204	1.043 ± 0.048071
SKANuModeNue1	1.0 ± 0.082645	1.0378 ± 0.066228
SKANuModeNueb0	1.0 ± 0.095453	1.0052 ± 0.053129
SKANuModeNueb1	1.0 ± 0.088889	1.0042 ± 0.045099
SKANuModeNueb2	1.0 ± 0.085644	1.0025 ± 0.045486
SKANuModeNueb3	1.0 ± 0.078536	1.0068 ± 0.041601
SKANuModeNueb4	1.0 ± 0.075246	1.035 ± 0.05292
SKANuModeNueb5	1.0 ± 0.086384	1.0377 ± 0.065989
SKANuModeNueb6	1.0 ± 0.15251	1.0751 ± 0.13391

Table E.5: Prefit and postfit parameter values and uncertainties.

Parameter	***PreFit***	***PostFit***
FSI_INEL_LO	0.0 ± 0.41	-0.32332 ± 0.081129
FSI_INEL_HI	0.0 ± 0.34	-0.0086159 ± 0.12846
FSI_PI_PROD	0.0 ± 0.5	0.040936 ± 0.18706
FSI_PI_ABS	0.0 ± 0.41	-0.34771 ± 0.14731
FSI_CEX_LO	0.0 ± 0.57	-0.088986 ± 0.30907
FSI_CEX_HI	0.0 ± 0.28	0.022924 ± 0.10475
MAQE(GeV/c^2)	1.2 ± 0.03	1.1314 ± 0.079024
pF_C(MeV/c)	217.0 ± 13.0	224.16 ± 13.295
pF_O(MeV/c)	225.0 ± 13.0	204.98 ± 15.083
2p2h_norm_nu	1.0 ± 1.0	1.5018 ± 0.1955
2p2h_norm_nubar	1.0 ± 1.0	0.726 ± 0.23125
2p2h_normCtoO	1.0 ± 0.2	0.96392 ± 0.16657
2p2h_shape_C(%)	100.0 ± 300.0	200.22 ± 20.606
2p2h_shape_O(%)	100.0 ± 300.0	199.71 ± 34.746
BeRPA_A	0.59 ± 0.118	0.6878 ± 0.057308
BeRPA_B	1.05 ± 0.21	1.5993 ± 0.11727
BeRPA_D	1.13 ± 0.1695	0.96248 ± 0.13445
BeRPA_E	0.88 ± 0.352	0.8749 ± 0.35332
BeRPA_U	1.2 ± 0.1	1.2 ± 0.1
CA5	0.96 ± 0.15	0.97601 ± 0.064304
MARES(GeV/c^2)	1.07 ± 0.15	0.806 ± 0.044916
ISO_BKG	0.96 ± 0.4	1.3147 ± 0.25594
nue_numu	1.0 ± 0.028284	1.0 ± 0.028284
nuebar_numubar	1.0 ± 0.028284	1.0 ± 0.028284
CC_DIS	0.0 ± 0.4	0.38541 ± 0.19726
CC_Coh_C	1.0 ± 0.3	0.87408 ± 0.28178
CC_Coh_O	1.0 ± 0.3	0.87406 ± 0.28179
NC_Coh	1.0 ± 0.3	0.93795 ± 0.29744
NC_1gamma	1.0 ± 1.0	1.0 ± 1.0
NC_other_near	1.0 ± 0.3	1.208 ± 0.25613
NC_other_far	1.0 ± 0.3	1.0 ± 0.3

Appendix F

Near Detector Distribution After Near Detector Fit

F.1 FGD1 distribution

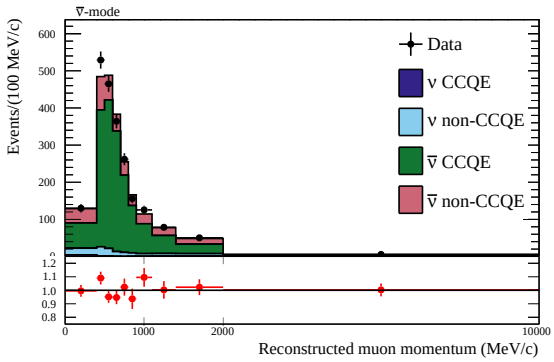

PRELIMINARY

(a) RHC ACC1track momentum distribution

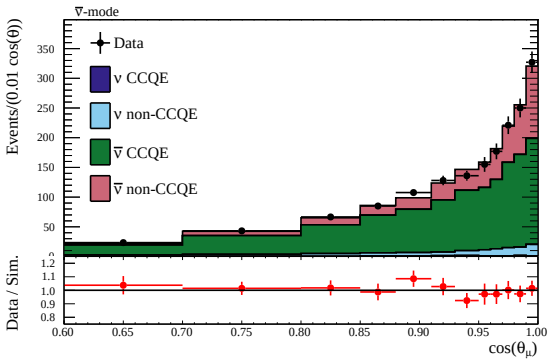

PRELIMINARY

(b) RHC ACC1track $\cos\theta$ distribution

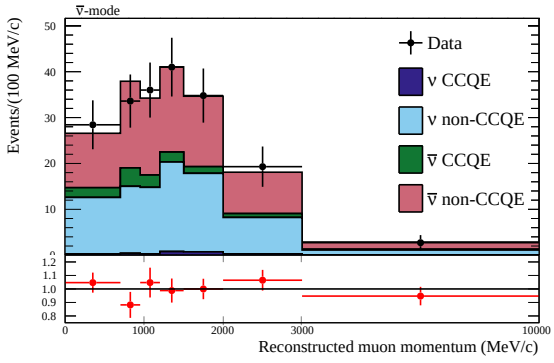

PRELIMINARY

(c) RHC ACCNtrack momentum distribution

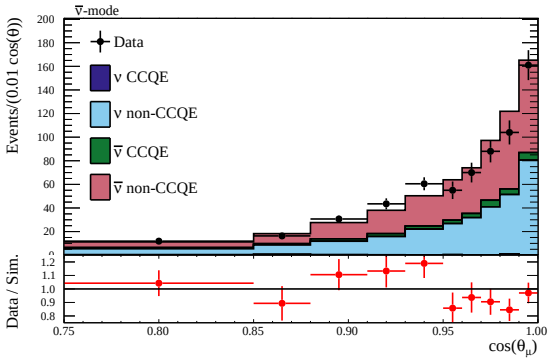

PRELIMINARY

(d) RHC ACCNtrack $\cos\theta$ distribution

Figure F.1: FGD1 momentum and $\cos\theta$ distribution for each sample (ACC1track, ACCNtrack)

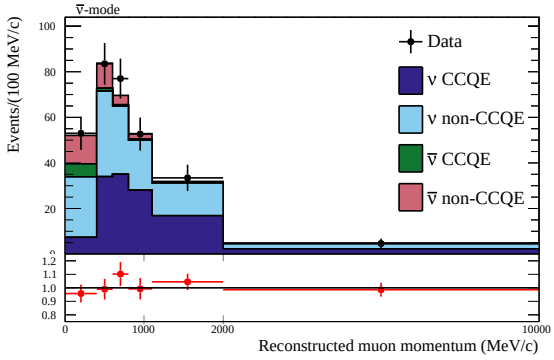

PRELIMINARY

(a) RHC CC1track momentum distribution

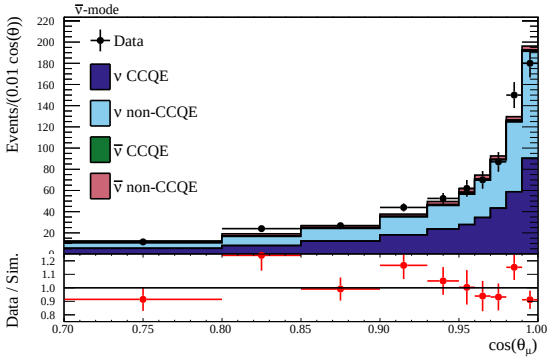

PRELIMINARY

(b) RHC CC1track $\cos\theta$ distribution

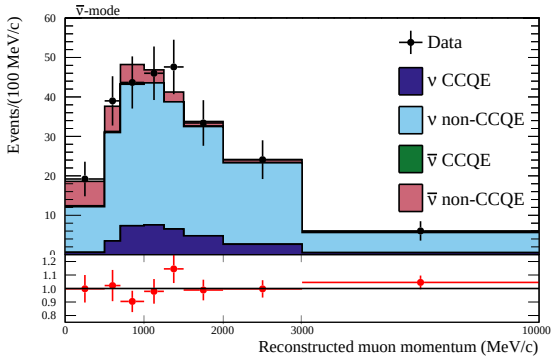

PRELIMINARY

(c) RHC CCNtrack momentum distribution

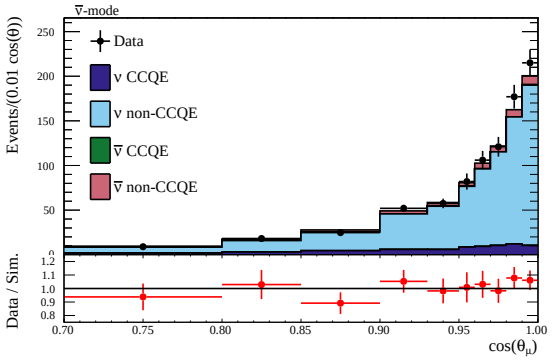

PRELIMINARY

(d) RHC CCNtrack $\cos\theta$ distribution

Figure F.2: FGD1 momentum and $\cos\theta$ distribution for each sample (CC1track, CCNtrack)

F.2 FGD2 distribution

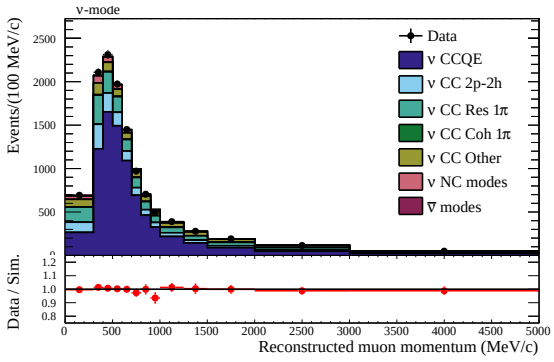

PRELIMINARY

(a) FHC CC0pi momentum distribution

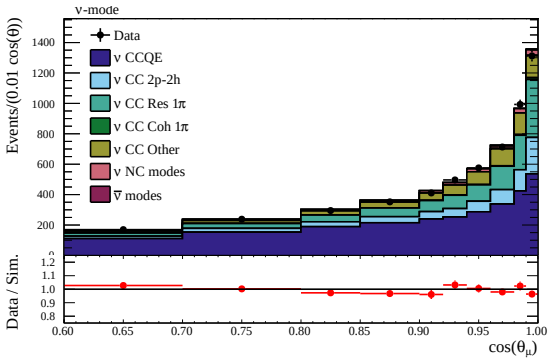

PRELIMINARY

(b) FHC CC0pi $\cos\theta$ distribution

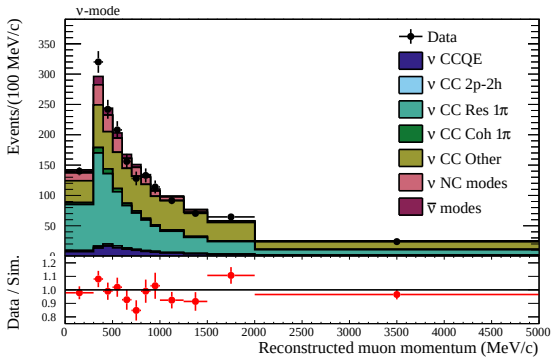

PRELIMINARY

(c) FHC CC1pi momentum distribution

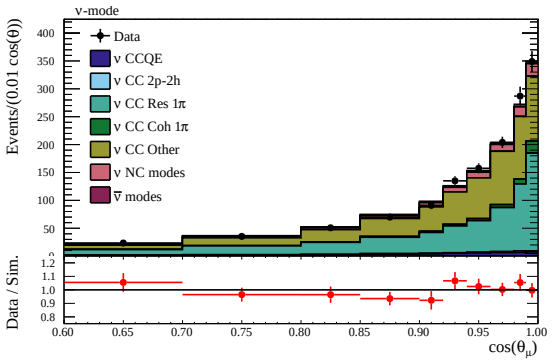

PRELIMINARY

(d) FHC CC1pi $\cos\theta$ distribution

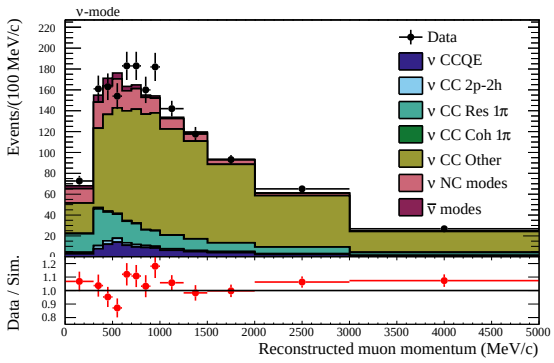

PRELIMINARY

(e) FHC CCOther momentum distribution

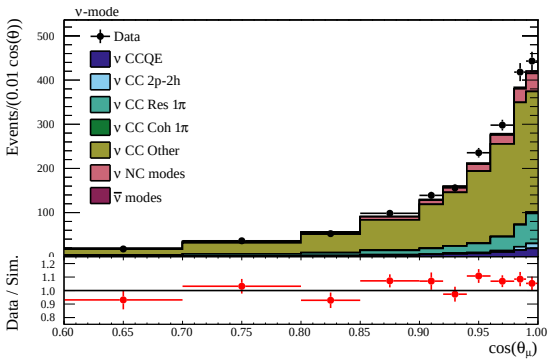

PRELIMINARY

(f) FHC CCOther $\cos\theta$ distribution

Figure F.3: FGD2 momentum and $\cos\theta$ distribution for each sample (CC0π, CC1π, CCOther)

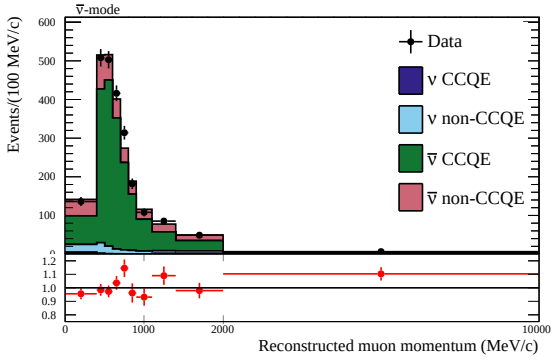

PRELIMINARY

(a) RHC ACC1track momentum distribution

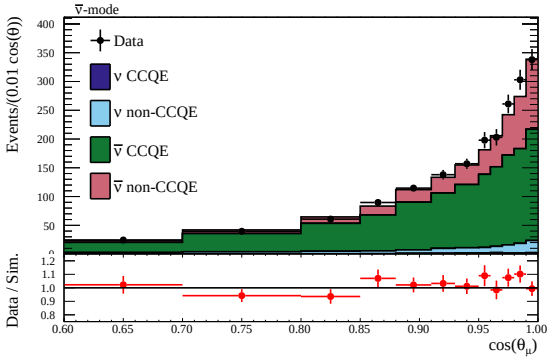

PRELIMINARY

(b) RHC ACC1track $\cos\theta$ distribution

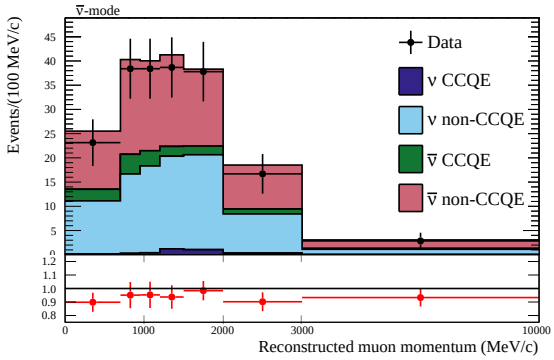

PRELIMINARY

(c) RHC ACCNtrack momentum distribution

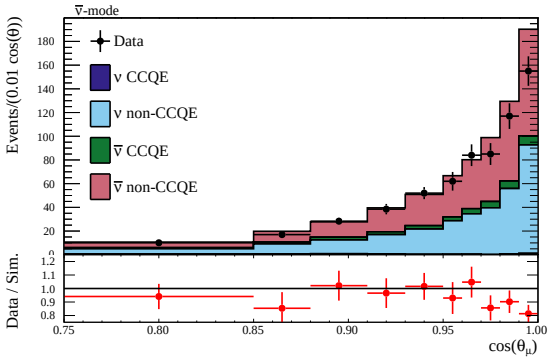

PRELIMINARY

(d) RHC ACCNtrack $\cos\theta$ distribution

Figure F.4: FGD2 momentum and $\cos\theta$ distribution for each sample (ACC1track, ACCNtrack)

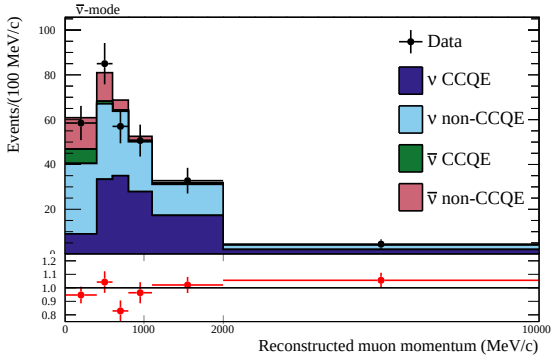

PRELIMINARY

(a) RHC CC1track momentum distribution

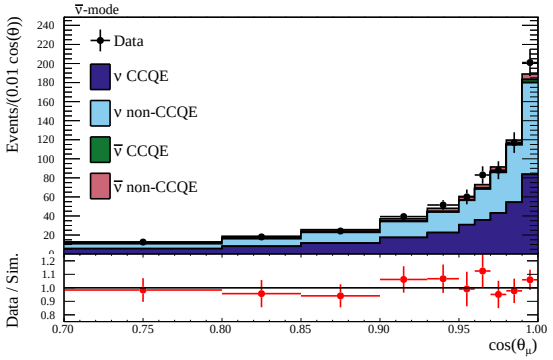

PRELIMINARY

(b) RHC CC1track $\cos\theta$ distribution

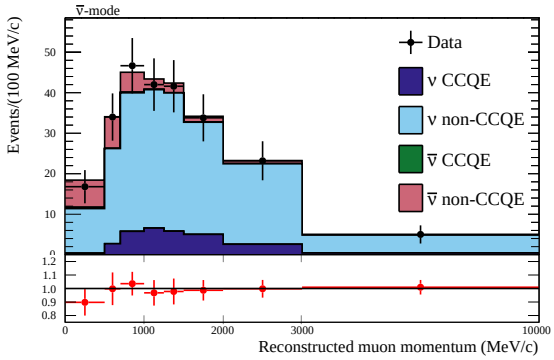

PRELIMINARY

(c) RHC CCNtrack momentum distribution

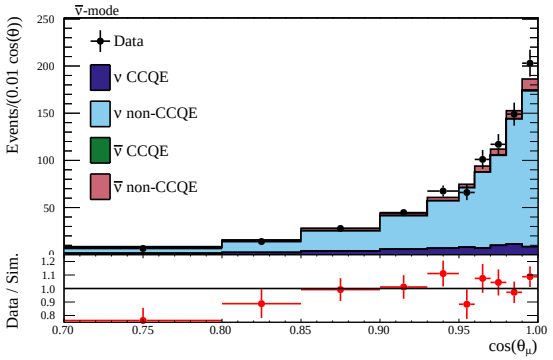

PRELIMINARY

(d) RHC CCNtrack $\cos\theta$ distribution

Figure F.5: FGD2 momentum and $\cos\theta$ distribution for each sample (ACC1track, ACCNtrack)

Appendix G

Sensitivities of Oscillation Parameter Set B

G.1 Sensitivity before smearing

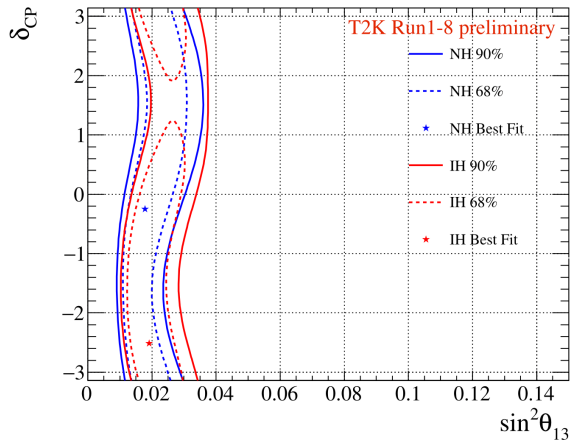

(a) $\sin^2\theta_{13} - \delta_{CP}$ without reactor constraint

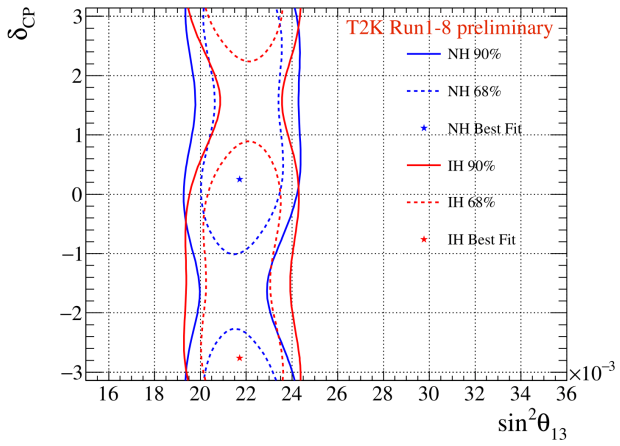

(b) $\sin^2\theta_{13} - \delta_{CP}$ with reactor constraint

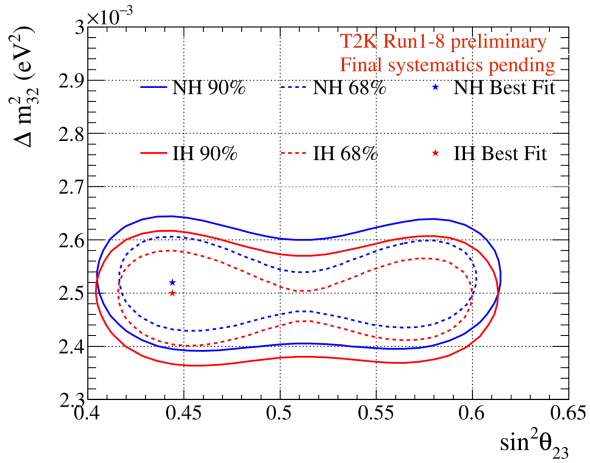

(c) $\sin^2\theta_{23} - \Delta m^2_{32}$ without reactor constraint

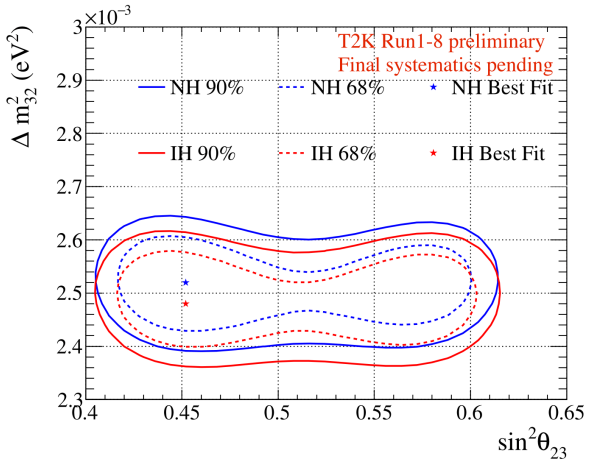

(d) $\sin^2\theta_{23} - \Delta m^2_{32}$ with reactor constraint

Figure G.1: Sensitivity for Asimov B (2D contours)

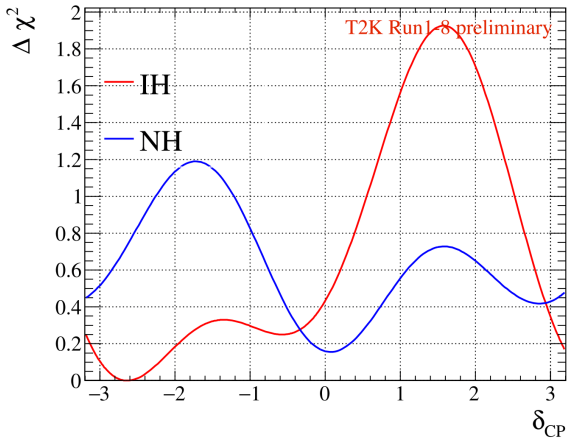

(a) 1D δ_{CP} without reactor constraint

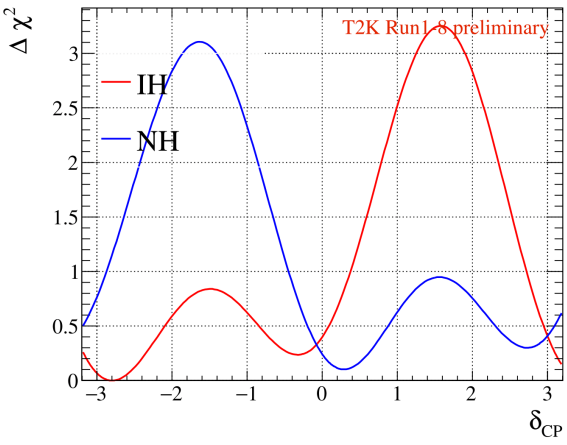

(b) 1D δ_{CP} with reactor constraint

Figure G.2: δ_{CP} Sensitivity for Asimov B

G.2 Sensitivity after the smearing

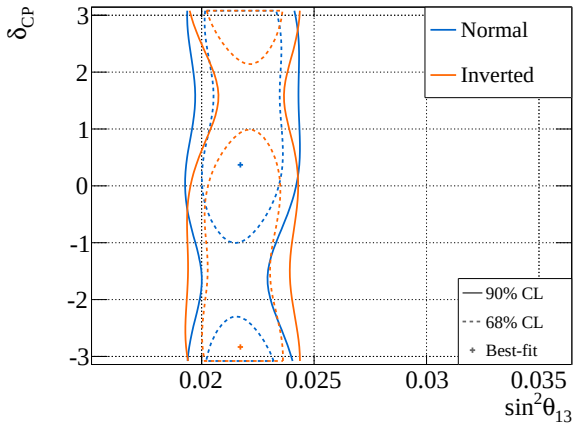

(a) $\sin^2\theta_{13} - \delta_{CP}$ with reactor constraint

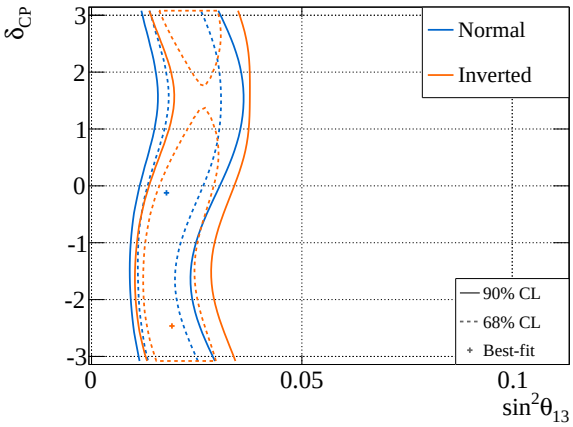

(b) $\sin^2\theta_{13} - \delta_{CP}$ without reactor constraint

Figure G.3: Sensitivity for Asimov B after the smearing method is applied

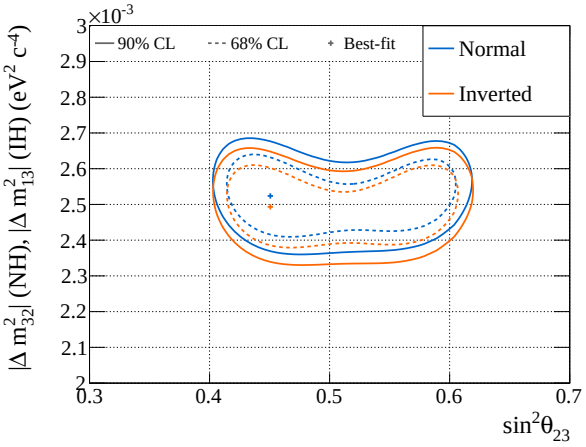

(a) $\sin^2\theta_{23} - \Delta m^2_{32}$ with reactor constraint

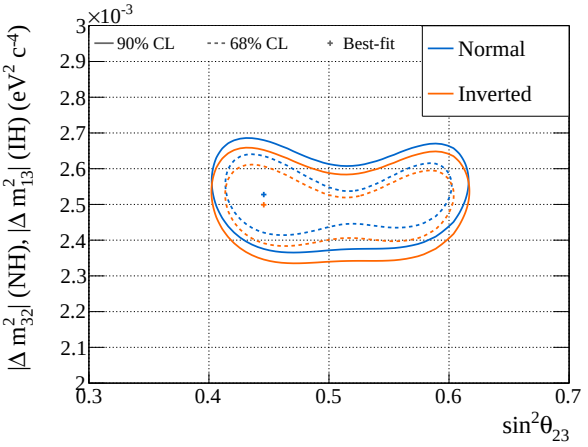

(b) $\sin^2\theta_{23} - \Delta m^2_{32}$ without reactor constraint

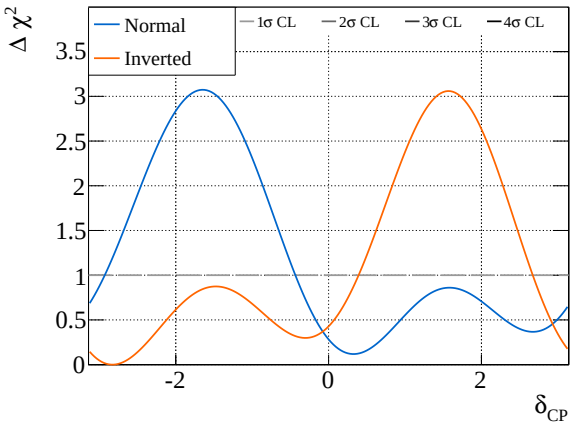

(c) 1D δ_{CP} with reactor constraint

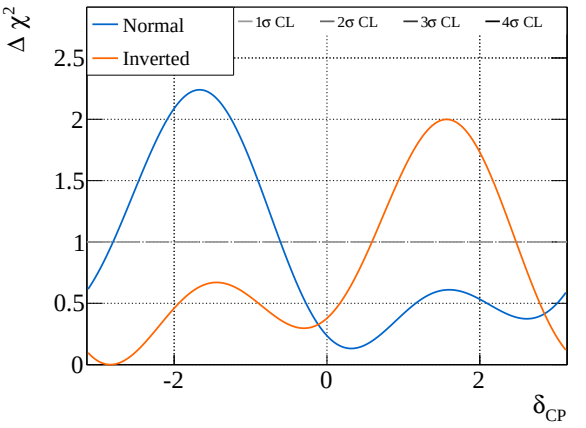

(d) 1D δ_{CP} without reactor constraint

Figure G.4: Sensitivity for Asimov B after the smearing is applied

Appendix H

The Data-Driven Simulated Data Results for 1p1h and 2p2h non PDD-like

H.1 Fit results of Data-driven 1p1h simulated data

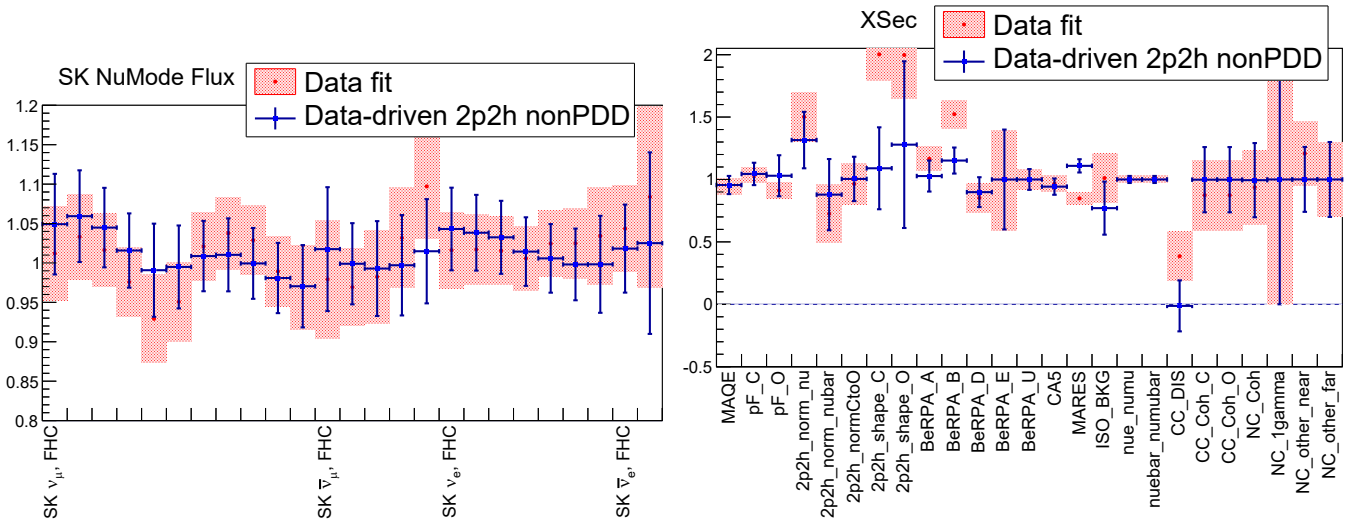

(a) SK flux

(b) Cross-section

Figure H.1: Best-fit parameters from the near detector fit to the ND280 data-driven 2p2h PDD-like simulated data.

The best-fit parameter values with the 1p1h simulated data, compared to those from the actual data fit are shown in Fig. H.1. There are some difference especially in the 2p2h shape parameter compared to the actual data fit. The data fit has PDD-like 2p2h shape, while the parameter stays around nominal for the data-driven simulated data. BeRPA_ A and BeRPA_ B are shifted differently from the actual data fit.

A comparison of the ND280 data-driven 1p-1h simulated data and the prediction from the near detector fit at Super-K is shown in Fig. H.2.

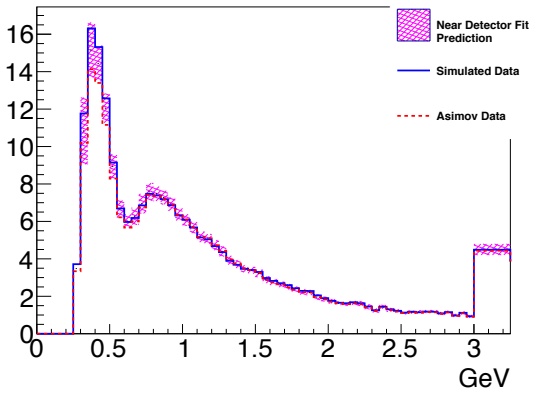

(a) FHC 1Rμ sample

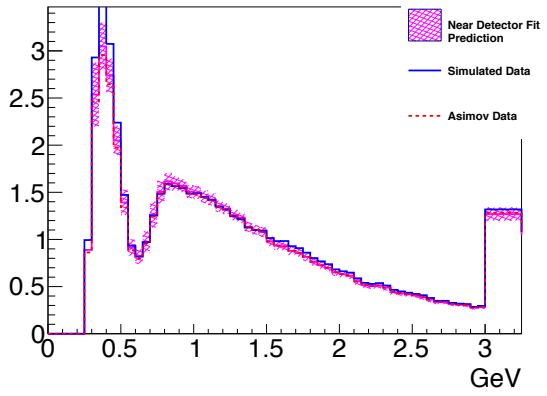

(b) RHC 1Rμ sample

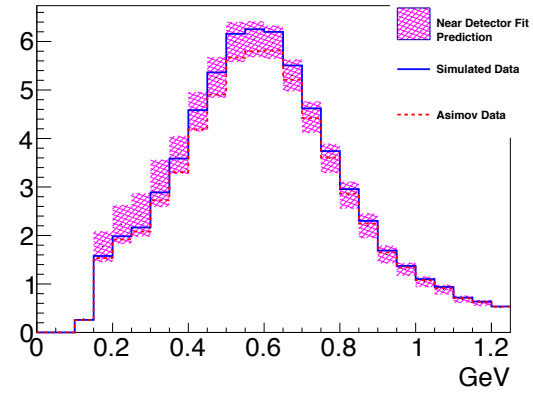

(c) FHC 1Re sample

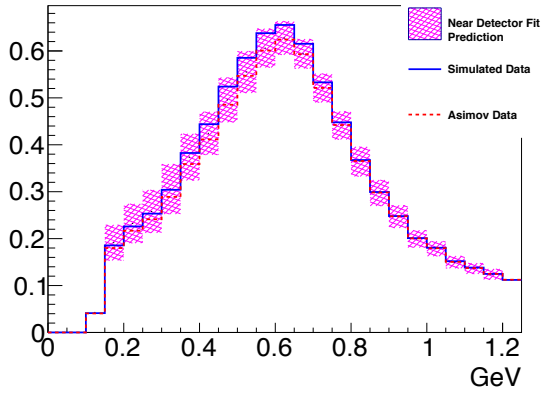

(d) RHC 1Re sample

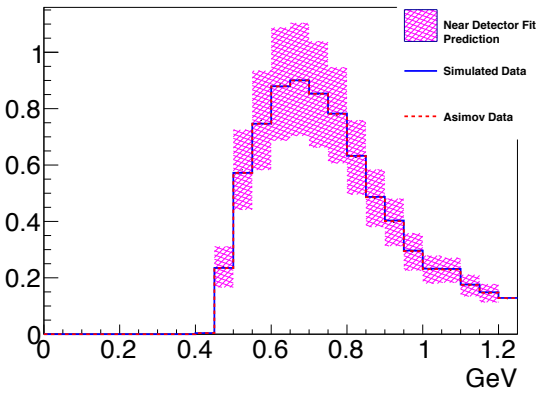

(e) FHC 1Re+1 d.e. sample

Figure H.2: Comparison between the Asimov data (dotted Black), the simulated data expectation (Blue), and the predi ction from the near detector fit to the simulated data (Magenta).

The near detector fit slightly underestimates the events of all samples. The 2D 68% and 90% C.L contours for the simulated data fit results and the Asimov data fit results are shown in Fig. H.3.

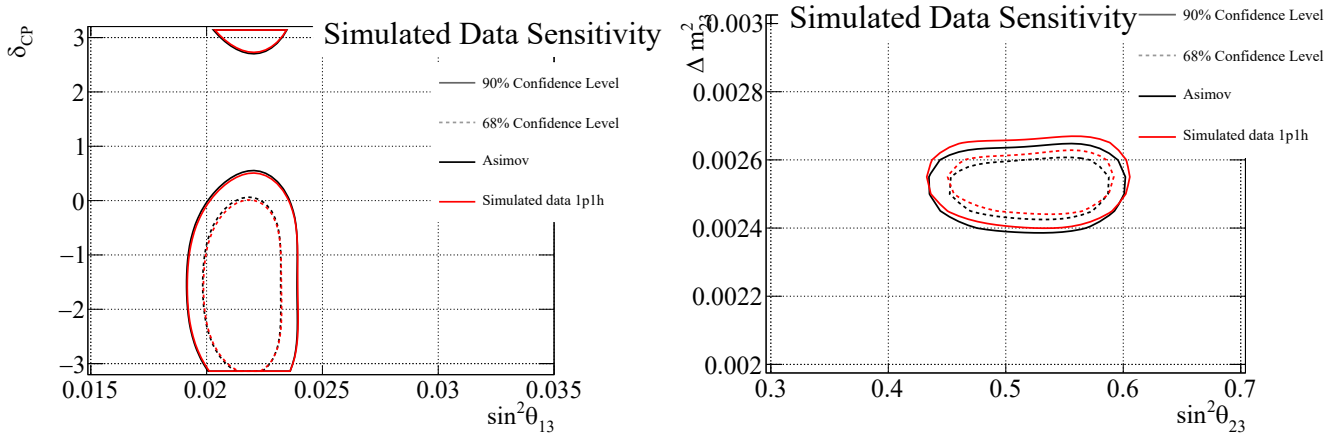

(a) $\delta_{CP} - \sin^2\theta_{13}$ (b) $\Delta m^2_{32} - \sin^2\theta_{23}$

Figure H.3: 2D 68% and 90% contours for Data-driven 2p2h PDD-like simulated data fits including the reactor constraint on $\sin^2\theta_{13}$, assuming normal hierarchy and using the Asimov A oscillation parameter set

The $\sin^2\theta_{13} - \delta_{CP}$ contours are almost same as the Asimov contours. The contours for $\Delta m^2_{32} - \sin^2\theta_{23}$ show the small shifts relative to the Asimov contours.

H.2 Fit results of Data-driven 2p2h non PDD-like simulated data

The best-fit parameter values, compared to those from the actual data fit are shown in Fig. H.5. There are some difference especially in the 2p2h shape parameter. The data fit has PDD-like 2p2h shape, while they becomes non PDD-like for the simulated data. BeRPA_ A and BeRPA_ B stays around the nominal values.

A comparison of the ND280 data-driven 2p2h non PDD-like simulated data and the prediction from the near detector fit at Super-K is shown in Fig. H.6.

The near detector fit slightly underestimate the event rates but within the error in all cases. The 2D 68% and 90% C.L contours for the simulated data fit results and the Asimov data fit results are shown in Fig. H.7.

The fit results for $\sin^2\theta_{13} - \delta_{CP}$ contours are almost same as the Asimov sensitivity. There are small shifts along Δm^2_{32} direction but the size seems small compared with the other data-driven simulated data results.

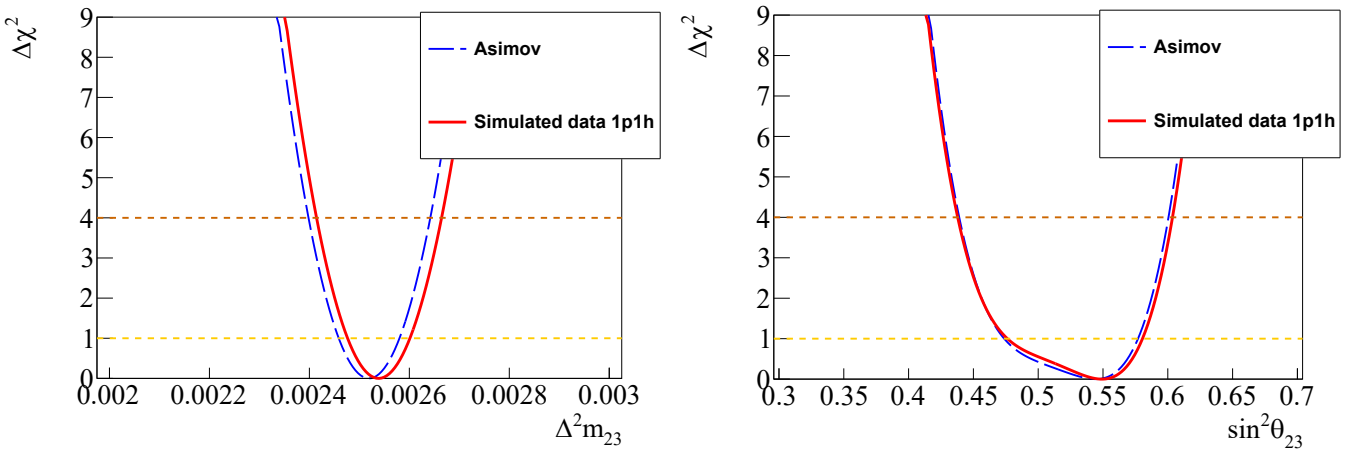

(a) Δm^2_{32} (b) $\sin^2\theta_{23}$

Figure H.4: The 2D 68% and 90% contours for Data-driven 1p1h simulated data fit and Asimov data fit

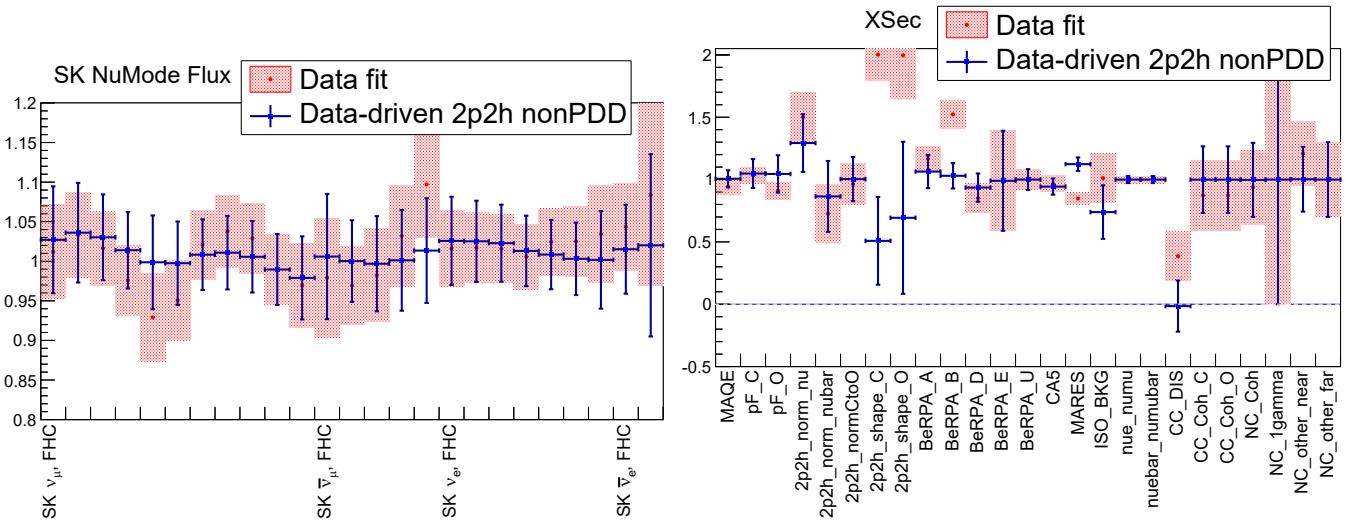

(a) SK flux (b) Cross-section

Figure H.5: Best-fit parameters from the near detector fit to the ND280 data-driven 2p2h non PDD-like simulated data.

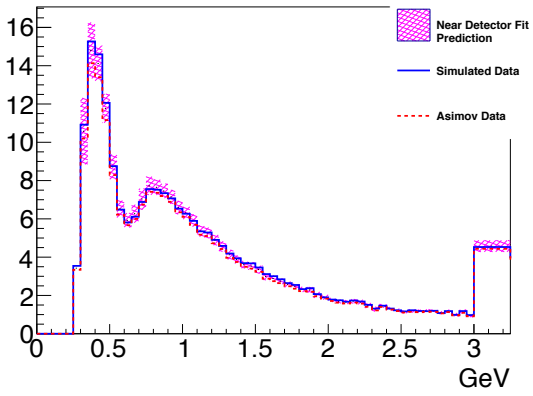

(a) ν_μ sample

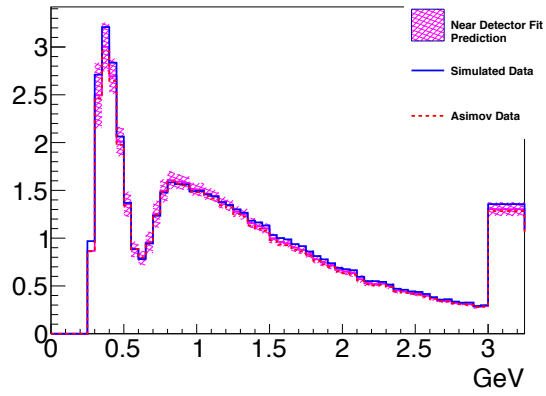

(b) $\bar{\nu}_\mu$ sample

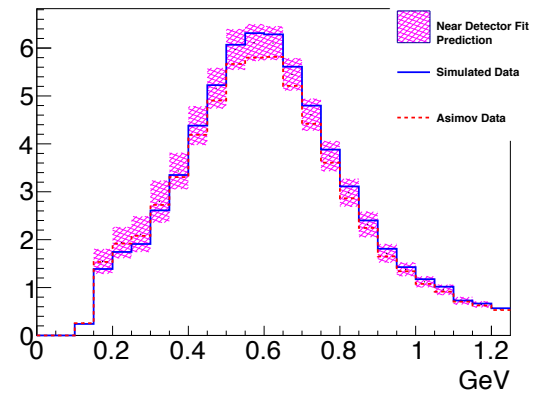

(c) ν_e sample

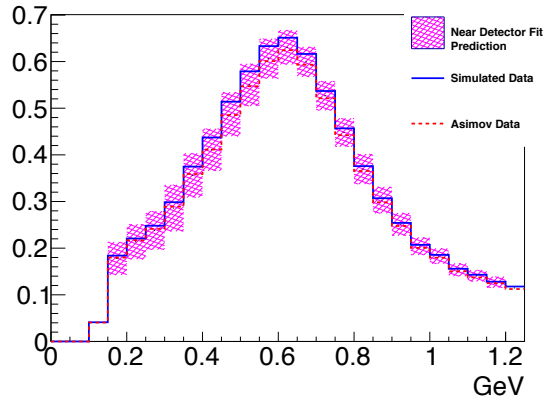

(d) $\bar{\nu}_e$ sample

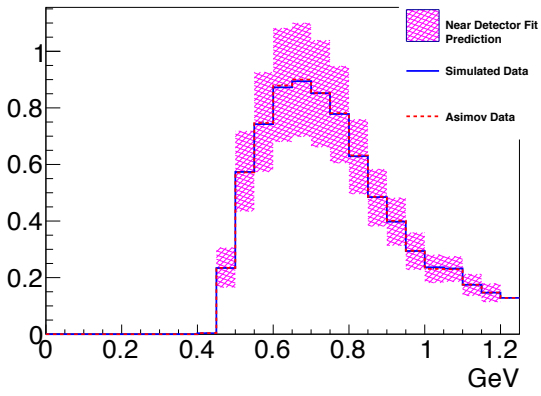

(e) ν_e 1 d.e. sample

Figure H.6: Comparison between the Asimov data (dotted Black), the simulated data expectation (Blue), and the predi ction from the near detector fit to the simulated data (Magenta).

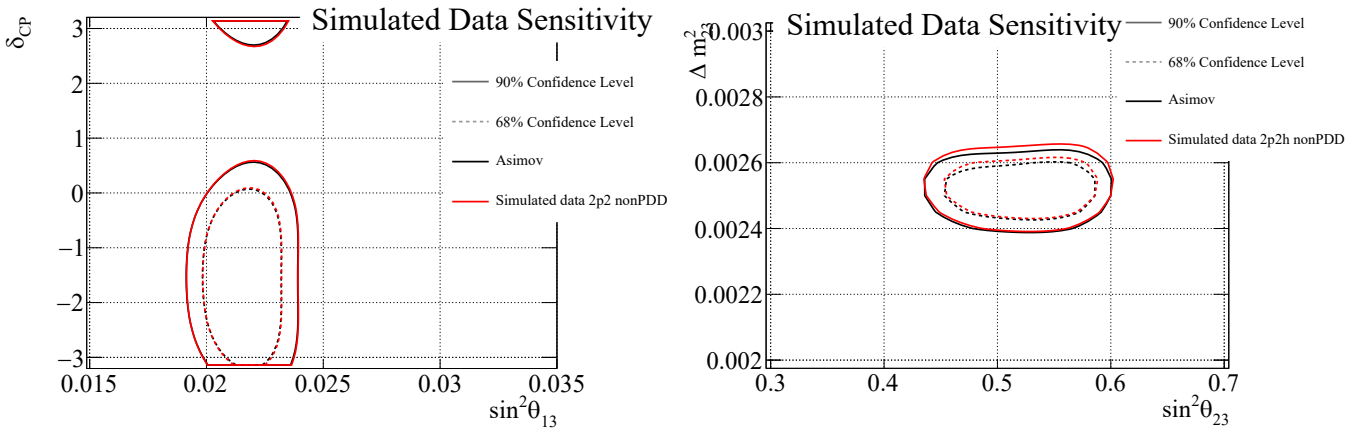

(a) $\delta_{CP} - \sin^2\theta_{13}$ (b) $\Delta m^2_{32} - \sin^2\theta_{23}$

Figure H.7: 2D 68% and 90% contours for Data-driven 2p2h PDD-like simulated data fit and Asimov data fit results

Appendix I

The Data-Driven Simulated Data Results with p-cos θ Weighting

I.1 data-driven 1p1h like simulated data

The fit results of the simulated data and comparison to the data fit is shown in Fig. I.1.

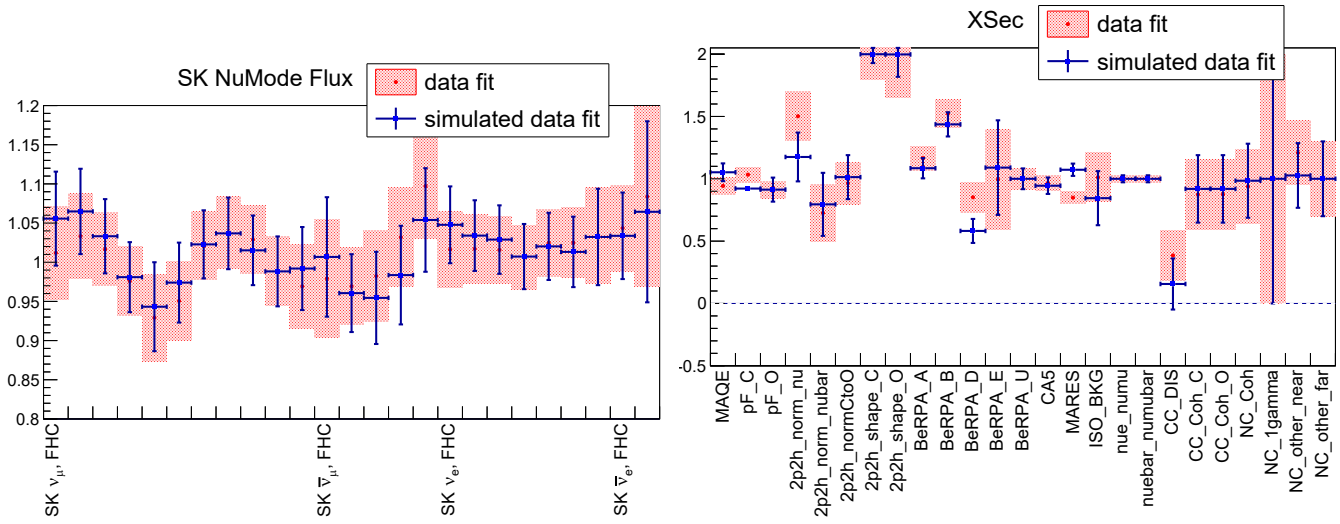

(a) SK flux

(b) Cross-section

Figure I.1: Best-fit parameters from the near detector fit to the ND280 data-driven 1p1h simulated data.

A comparison of the ND280 data-driven 1p-1h simulated data and the ND280-tuned prediction at Super-K is shown in Fig. I.2.

Fig. I.2 shows that the simulated data spectrum at SK increases relative to the nominal prediction at the low energy region in ν_e samples and dip region in ν_μ samples. Near detector extrapolation tends to over-estimate the events in both cases.

The 2D 68% and 90% C.L contours for the simulated data fit results and the nominal model

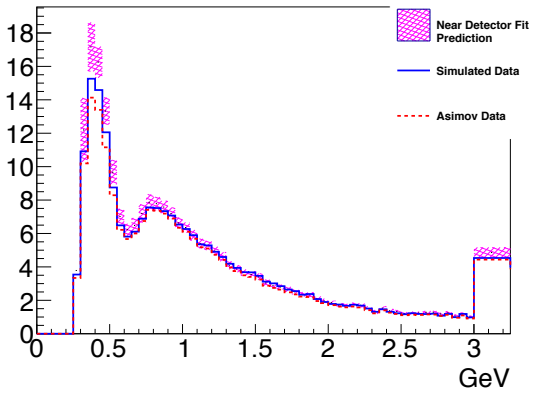

(a) ν_μ sample

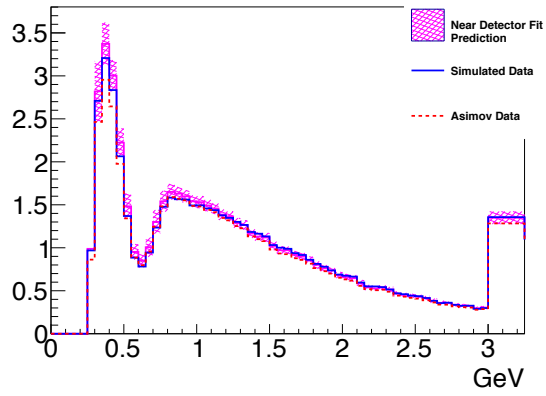

(b) $\bar{\nu}_\mu$ sample

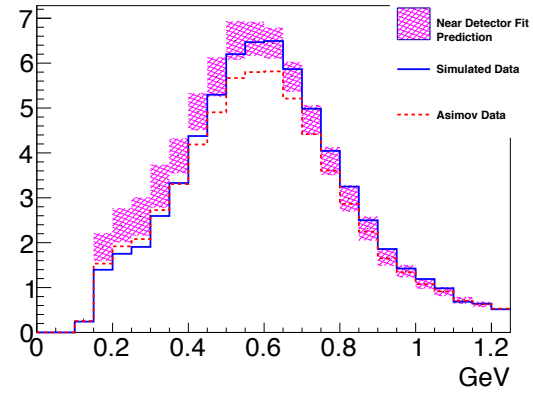

(c) ν_e sample

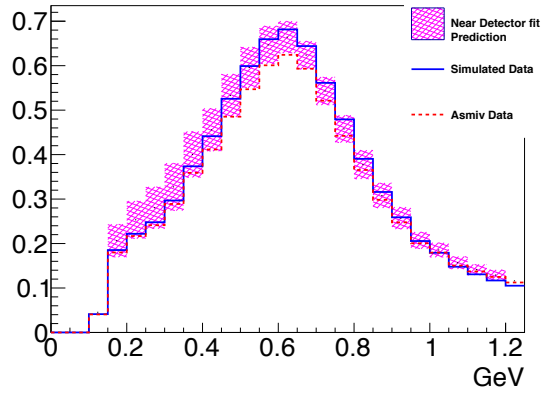

(d) $\bar{\nu}_e$ sample

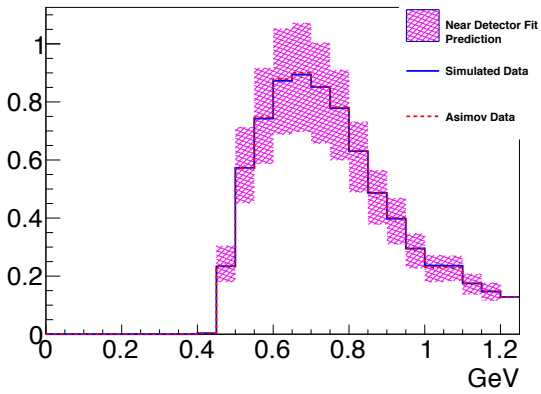

(e) ν_e 1 d.e. sample

Figure I.2: Comparison between the Asimov data (dotted Black), the simulated data expectation (Blue), and the prediction from the near detector fit to the simulated data (Magenta).

results of parameter set A are shown in Fig. I.3. In all case, reactor constraint and Normal hierarchy is assumed.

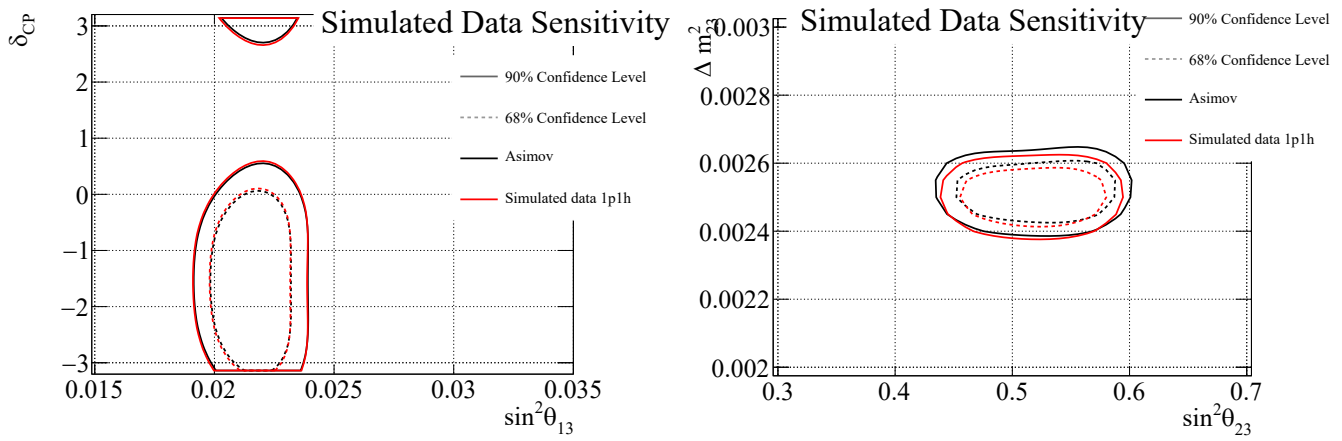

(a) $\delta_{CP} - \sin^2\theta_{13}$ (b) $\Delta m^2_{32} - \sin^2\theta_{23}$

Figure I.3: 2D 68% and 90% contours for Data-driven 1p1h simulated data fits including the reactor constraint on $\sin^2\theta_{13}$, assuming normal hierarchy and using the Asimov A oscillation parameter set

The fit results for $\sin^2\theta_{13} - \delta_{CP}$ contours are almost same as the Asimov sensitivity while $\sin^2\theta_{23} - \Delta m^2_{32}$ contours are smaller than the Asimov sensitivity. The 1D sensitivity curve for $\sin^2\theta_{23}$ and Δm^2_{32} is shown in Fig. I.4.

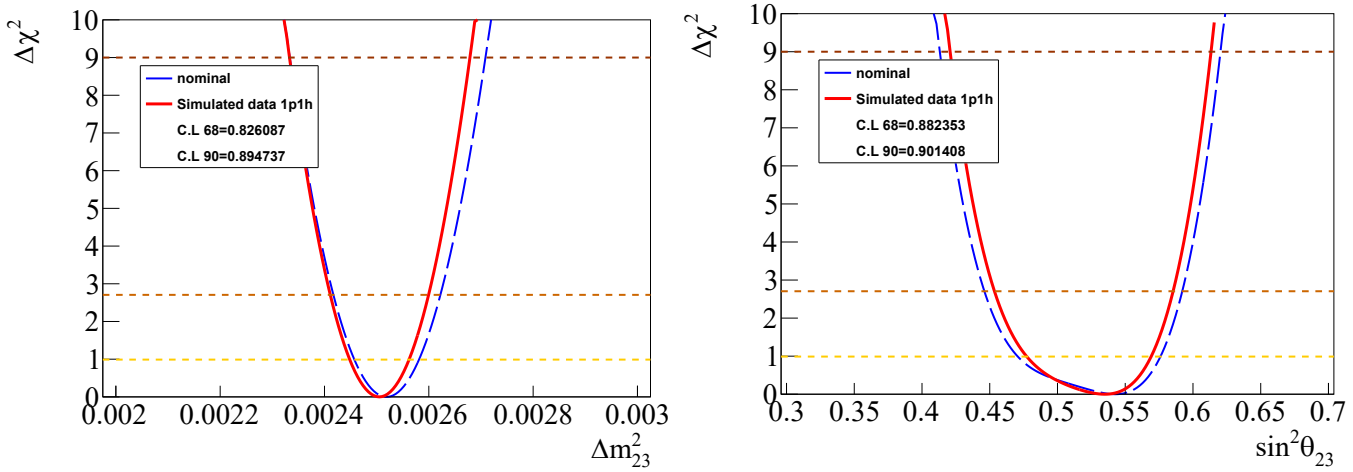

(a) Δm^2_{32} (b) $\sin^2\theta_{23}$

Figure I.4: 2D 68% and 90% contours for Data-driven 1p1h simulated data fits including the reactor constraint on $\sin^2\theta_{13}$, assuming normal hierarchy and using the Asimov A oscillation parameter set

The data-driven 1p1h simulated data fit result has the tighter constraint on the $\sin^2\theta 23$ sensitivity curve. The best fit point of Δm^2_{32} is slightly shifted to the right side. Similar tendency is also observed in the fit results with parameter set B.

I.2 data-driven 2p2h PDD like simulated data

The fit results of the simulated data and comparison to the data fit is shown in Fig. I.5.

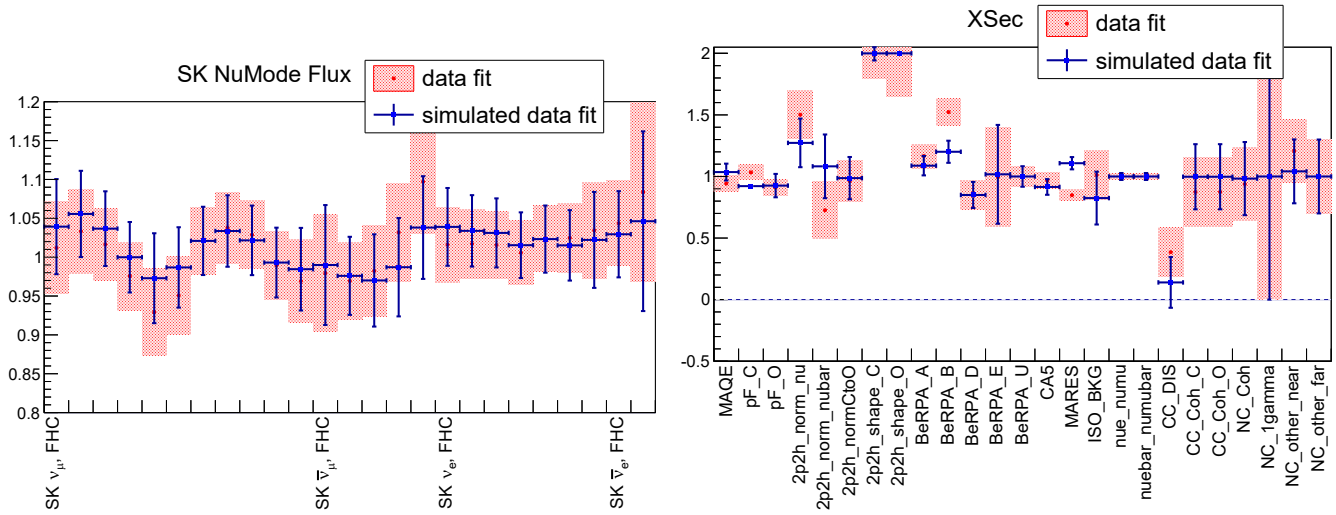

(a) SK flux

(b) Cross-section

Figure I.5: Best-fit parameters from the near detector fit to the ND280 data-driven 2p2h PDD-like simulated data.

A comparison of the ND280 data-driven 1p-1h simulated data and the ND280-tuned prediction at Super-K is shown in Fig. I.6.

Fig. I.6 shows that the simulated data spectrum at SK increases relative to the nominal prediction at the low energy region in ν_e samples and dip region in ν_μ samples. Near detector extrapolation tends to over-estimate the events in both cases.

The 2D 68% and 90% C.L contours for the simulated data fit results and the nominal model results of parameter set A are shown in Fig. I.7. In all case, reactor constraint and Normal hierarchy is assumed.

The fit results for $\sin^2\theta_{13} - \delta_{CP}$ contours are almost same as the Asimov sensitivity while $\sin^2\theta_{23} - \Delta m^2_{32}$ contours are smaller than the Asimov sensitivity. The 1D sensitivity curve for $\sin^2\theta_{23}$ and Δm^2_{32} is shown in Fig. I.8.

The data-driven 2p2h PDD-like simulated data fit result has the tighter constraint on the $\sin^2\theta 23$ sensitivity curve. The best fit point of Δm^2_{32} is slightly shifted to the right side. Similar tendency is also observed in the fit results with parameter set B.

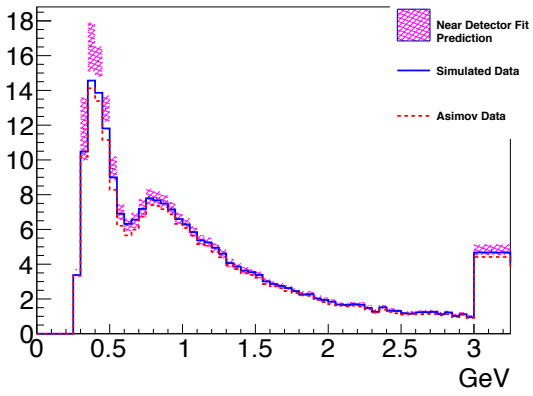

(a) ν_μ sample

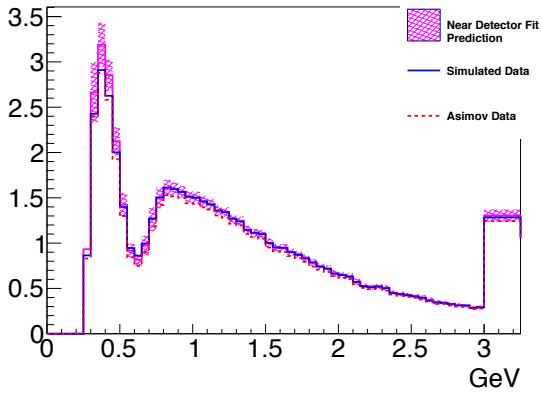

(b) $\bar{\nu}_\mu$ sample

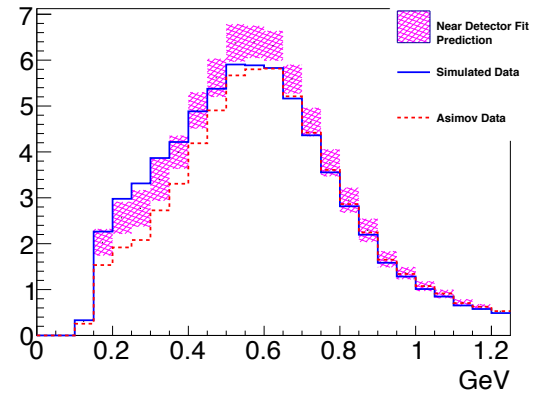

(c) ν_e sample

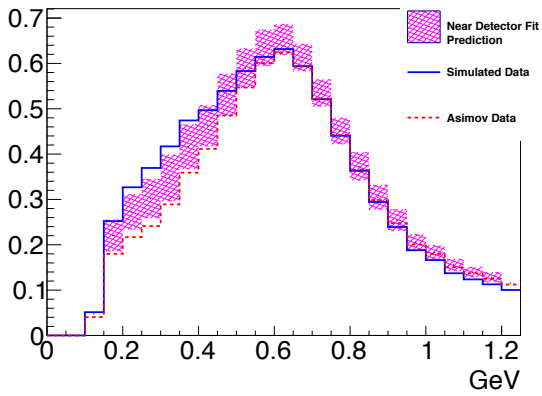

(d) $\bar{\nu}_e$ sample

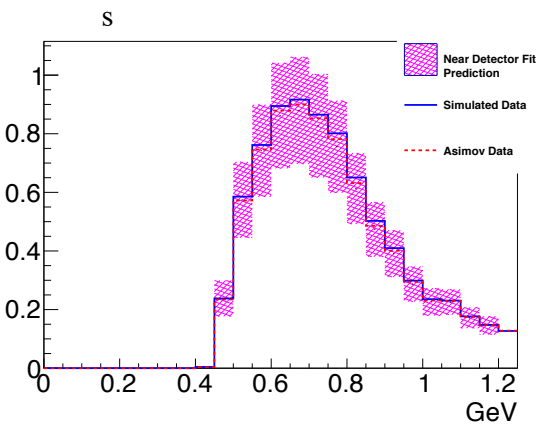

(e) ν_e 1 d.e. sample

Figure I.6: Comparison between the Asimov data (dotted Black), the simulated data expectation (Blue), and the prediction from the near detector fit to the simulated data (Magenta).

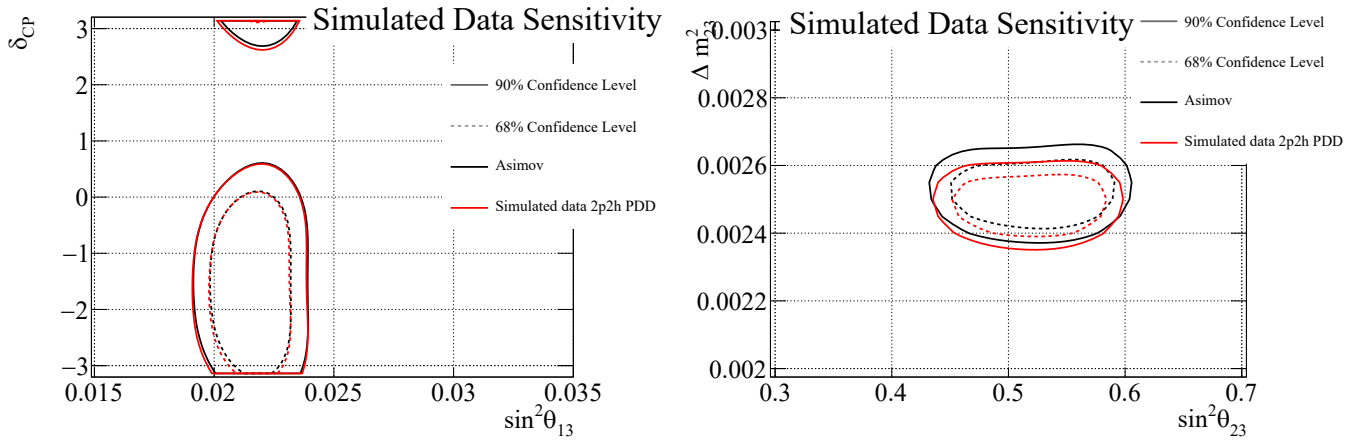

(a) $\delta_{CP} - \sin^2\theta_{13}$ (b) $\Delta m^2_{32} - \sin^2\theta_{23}$

Figure I.7: 2D 68% and 90% contours for Data-driven 2p2h PDD-like simulated data fits including the reactor constraint on $\sin^2\theta_{13}$, assuming normal hierarchy and using the Asimov A oscillation parameter set

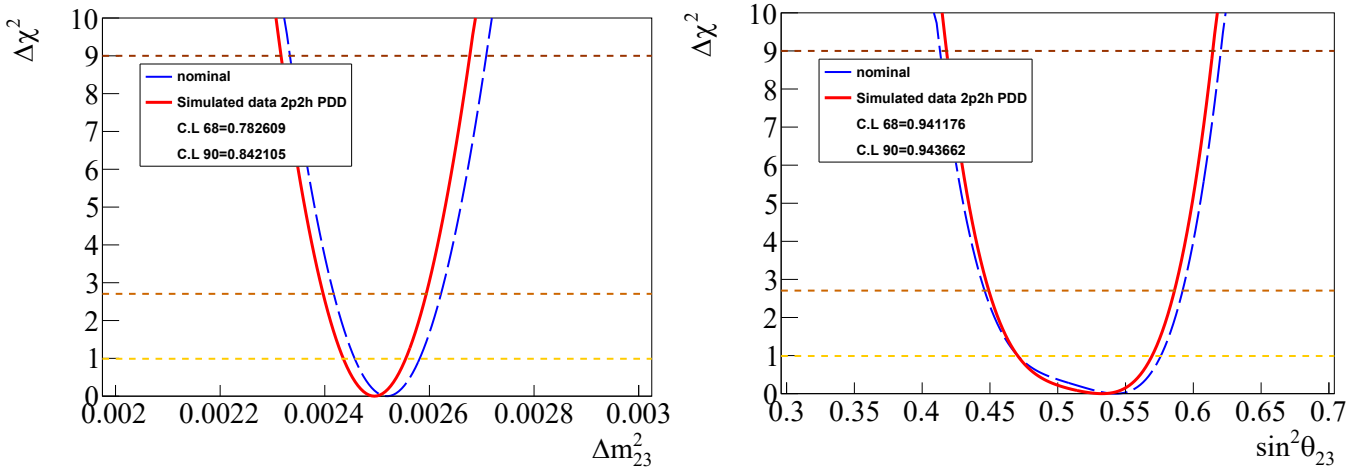

(a) Δm^2_{32} (b) $\sin^2\theta_{23}$

Figure I.8: 2D 68% and 90% contours for Data-driven 2p2h PDD-like simulated data fits including the reactor constraint on $\sin^2\theta_{13}$, assuming normal hierarchy and using the Asimov A oscillation parameter set

I.3 data-driven 2p2h nonPDD like simulated data

The fit results of the simulated data and comparison to the data fit is shown in Fig. I.9.

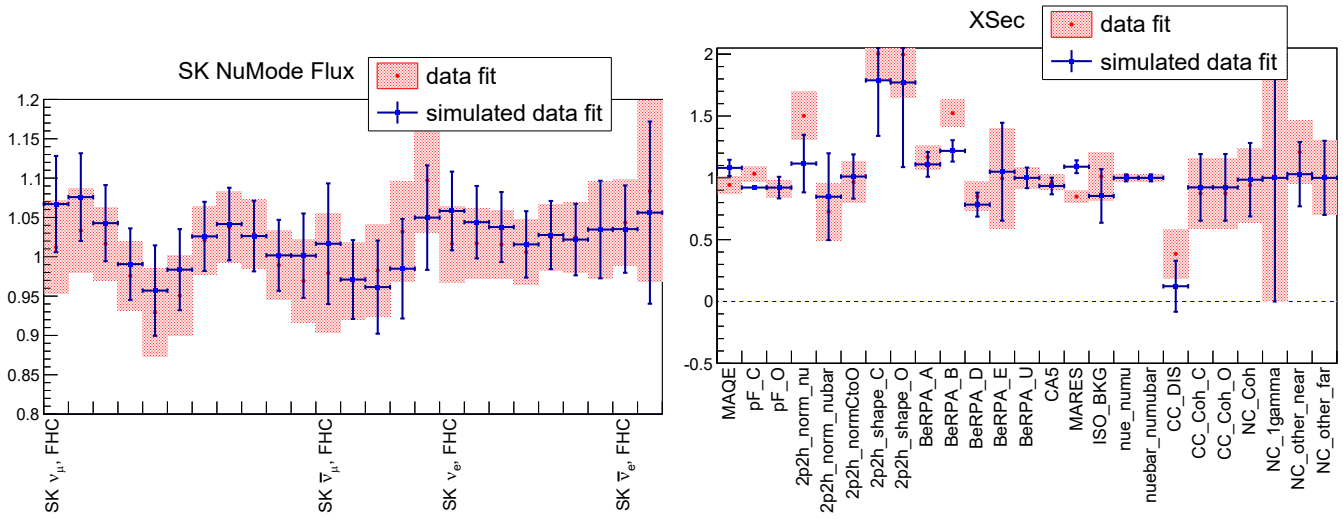

(a) SK flux

(b) Cross-section

Figure I.9: Best-fit parameters from the near detector fit to the ND280 data-driven 2p2h non PDD-like simulated data.

A comparison of the ND280 data-driven 1p-1h simulated data and the ND280-tuned prediction at Super-K is shown in Fig. I.10.

Fig. I.10 shows that the simulated data spectrum at SK increases relative to the nominal prediction at the low energy region in ν_e samples and dip region in ν_μ samples. Near detector extrapolation tends to over-estimate the events in both cases.

The 2D 68% and 90% C.L contours for the simulated data fit results and the nominal model results of parameter set A are shown in Fig. I.11. In all case, reactor constraint and Normal hierarchy is assumed.

The fit results for $\sin^2\theta_{13} - \delta_{CP}$ contours are almost same as the Asimov sensitivity while $\sin^2\theta_{23} - \Delta m^2_{32}$ contours are smaller than the Asimov sensitivity. The 1D sensitivity curve for $\sin^2\theta_{23}$ and Δm^2_{32} is shown in Fig. I.12.

The data-driven 2p2h PDD-like simulated data fit result has the tighter constraint on the $\sin^2\theta 23$ sensitivity curve. The best fit point of Δm^2_{32} is slightly shifted to the right side. Similar tendency is also observed in the fit results with parameter set B.

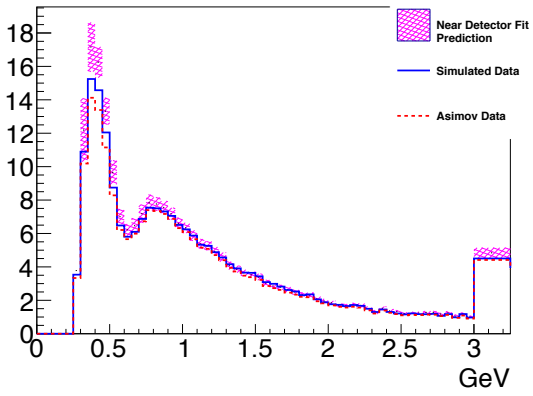

(a) ν_μ sample

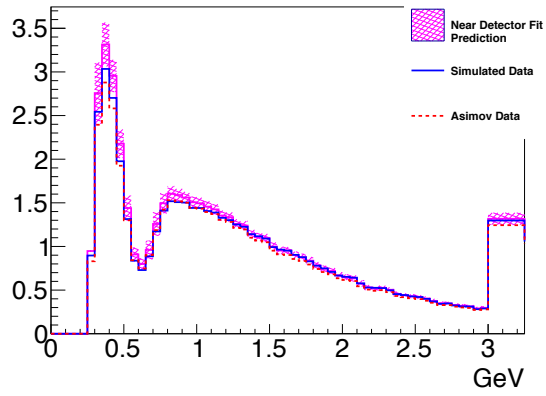

(b) $\bar{\nu}_\mu$ sample

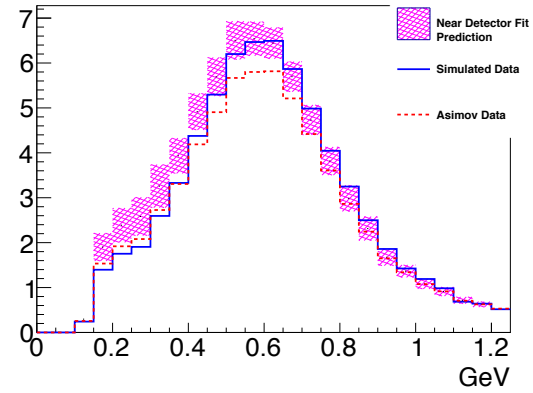

(c) ν_e sample

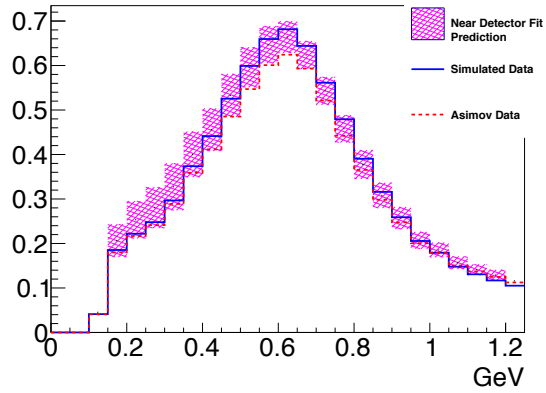

(d) $\bar{\nu}_e$ sample

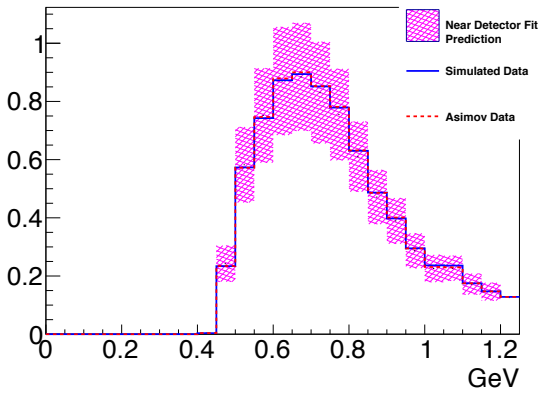

(e) ν_e 1 d.e. sample

Figure I.10: Comparison between the Asimov data (dotted Black), the simulated data expectation (Blue), and the prediction from the near detector fit to the simulated data (Magenta).

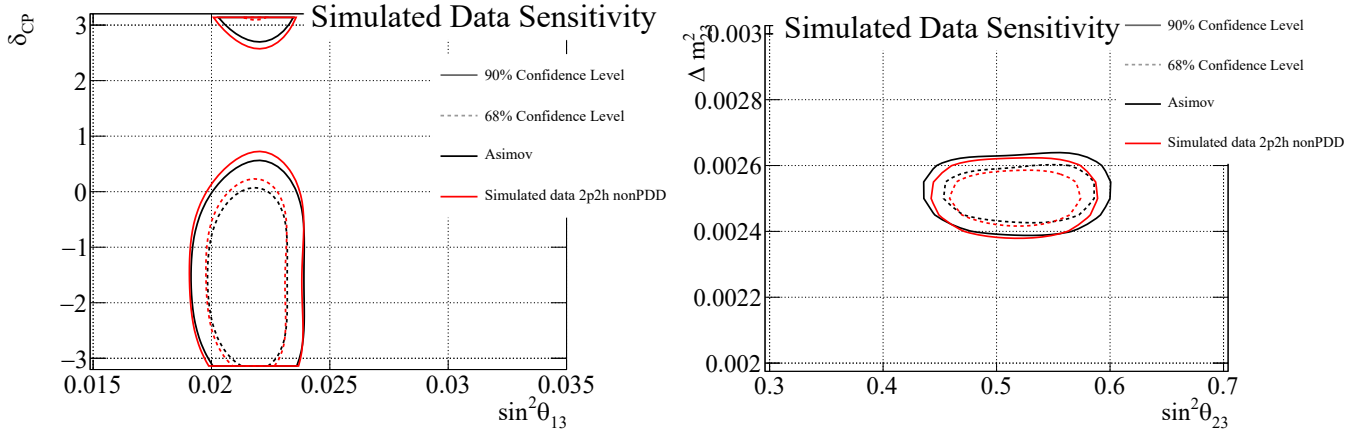

(a) $\delta_{CP} - \sin^2\theta_{13}$ (b) $\Delta m^2_{32} - \sin^2\theta_{23}$

Figure I.11: 2D 68% and 90% contours for Data-driven 2p2h non PDD-like simulated data fits including the reactor constraint on $\sin^2\theta_{13}$, assuming normal hierarchy and using the Asimov A oscillation parameter set

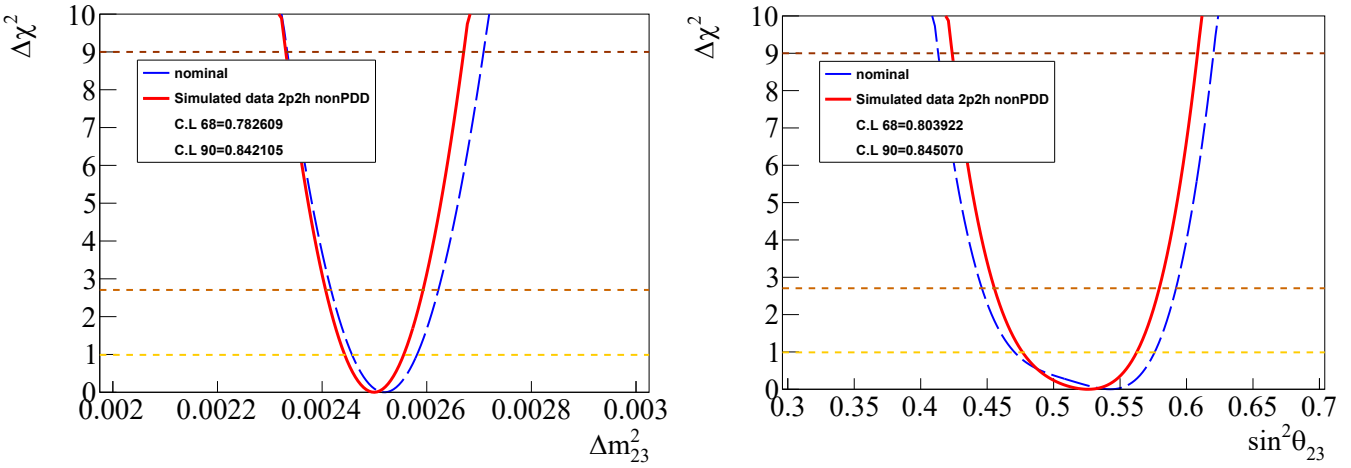

(a) Δm^2_{32} (b) $\sin^2\theta_{23}$

Figure I.12: 2D 68% and 90% contours for Data-driven 2p2h non-PDD-like simulated data fits including the reactor constraint on $\sin^2\theta_{13}$, assuming normal hierarchy and using the Asimov A oscillation parameter set

Table I.1: Fractional shift and width ratio of the intervals after apply $\Delta\chi^2_{diff}(\delta_{cp})$ from the data-driven 1p-1h study.

Type of Interval	Midpoint Shift	Width Ratio
Confidence Interval (NH)	-0.009	0.997
Confidence Interval (IH)	0.039	0.915
Credible Interval (flat δ_{cp})	0	1
Credible Interval (flat $\sin(\delta_{cp})$)	0	1.01

I.4 Effect on δ_{cp} Intervals

We can investigate how much the data intervals for δ_{cp} are changed if the data $\Delta\chi^2$ curves change by an amount that is equal to the difference between the $\Delta\chi^2$ curve from the Asimov fit and the $\Delta\chi^2$ curve from the simulated data fit. We first define the $\Delta\chi^2$ difference in the simulated data study:

$$\Delta\chi^2_{diff}(\delta_{cp}) = \Delta\chi^2_{Asimov}(\delta_{cp}) - \Delta\chi^2_{simulated}(\delta_{cp}). \tag{I.1}$$

Here $\Delta\chi^2_{Asimov}(\delta_{cp})$ and $\Delta\chi^2_{simulated}(\delta_{cp})$ are the $\Delta\chi^2$ curves in the Asimov and simulated data fits respectively. Using this function, we make a shifted $\Delta\chi^2$ curve for the data:

$$\Delta\chi^2_{shift}(\delta_{cp}) = \Delta\chi^2_{data}(\delta_{cp}) + \Delta\chi^2_{diff}(\delta_{cp}). \tag{I.2}$$

Here $\Delta\chi^2_{data}(\delta_{cp})$ is the $\Delta\chi^2$ curve from the fit to the data. The confidence or credible intervals are then calculated with $\Delta\chi^2_{shift}(\delta_{cp})$ and the intervals are compared to those from data. If the change to intervals is small, we can say that the magnitude of $\Delta\chi^2$ difference observed in the simulated data studies are small enough to not significantly impact the intervals extracted from data. We calculate three types of intervals: In this analysis we focus on the presentation of the impact on the 2σ intervals since the boundary of these intervals are closest to the CP conserving values of δ_{cp} and similar results are seen for the 90% intervals.

I.4.1 Data-driven 1p-1h simulated Data

The $\Delta\chi^2_{diff}(\delta_{cp})$ applied and interval comparisons for the data-driven 1p-1h simulated data study are shown in Fig. I.13. The midpoint shifts and width ratios for the 95% intervals are listed in Table I.1. The maximum shift to the interval is by 3.9% for the inverted hierarchy confidence interval. The inverted hierarchy width changes by -8.5%. Given that only a small fraction of the points in the 95% confidence interval are inverted hierarchy, this level of change is acceptably small.

I.4.2 Data-driven non-Δ 2p-2h simulated Data

The $\Delta\chi^2_{diff}(\delta_{cp})$ applied and interval comparisons for the data-driven non PDD-like 2p2h simulated data study are shown in Fig. I.14. The midpoint shifts and width ratios for the 95% intervals are listed in Table I.2. The maximum shift to the interval is by -1.2% for the credible interval with flat δ_{cp} prior. The inverted hierarchy width changes by -7.1%. Given that only a small fraction of the points in the 95% confidence interval are inverted hierarchy, this level of change is acceptably small.

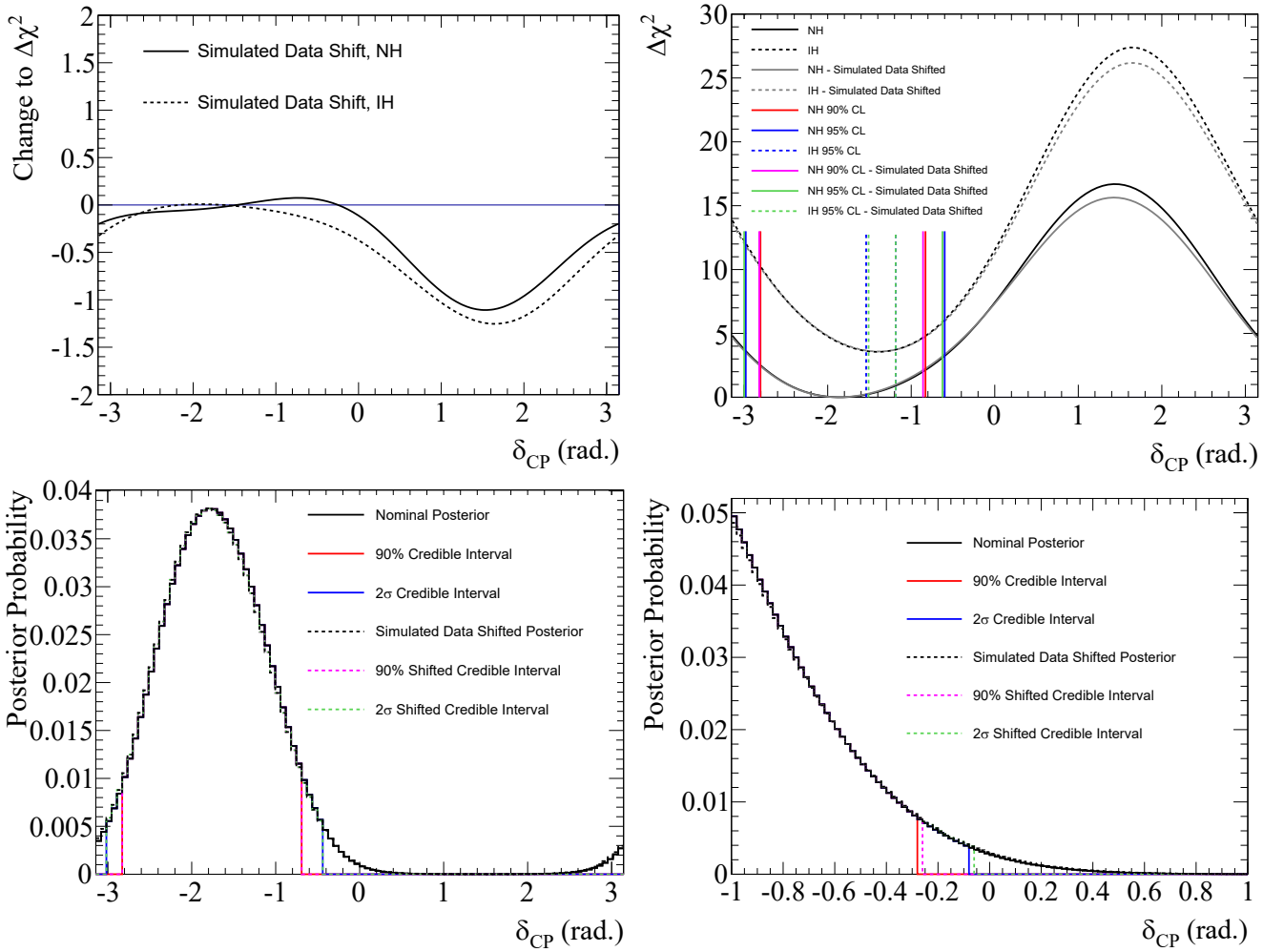

Figure I.13: $\Delta\chi^2_{diff}(\delta_{cp})$ from the data-driven 1p-1h simulated data study (top left), comparison of the confidence intervals (top right), comparison of credible intervals with a flat prior on δ_{cp} (bottom left) and comparison of credible intervals with a flat prior on $\sin(\delta_{cp})$ (bottom right) .

Table I.2: Fractional shift and width ratio of the intervals after apply $\Delta\chi^2_{diff}(\delta_{cp})$ from the data-driven non PDD-like 2p2h study.

Type of Interval	Midpoint Shift	Width Ratio
Confidence Interval (NH)	-0.005	0.977
Confidence Interval (IH)	-0.004	0.929
Credible Interval (flat δ_{cp})	-0.012	0.976
Credible Interval (flat $\sin(\delta_{cp})$)	0	0.987

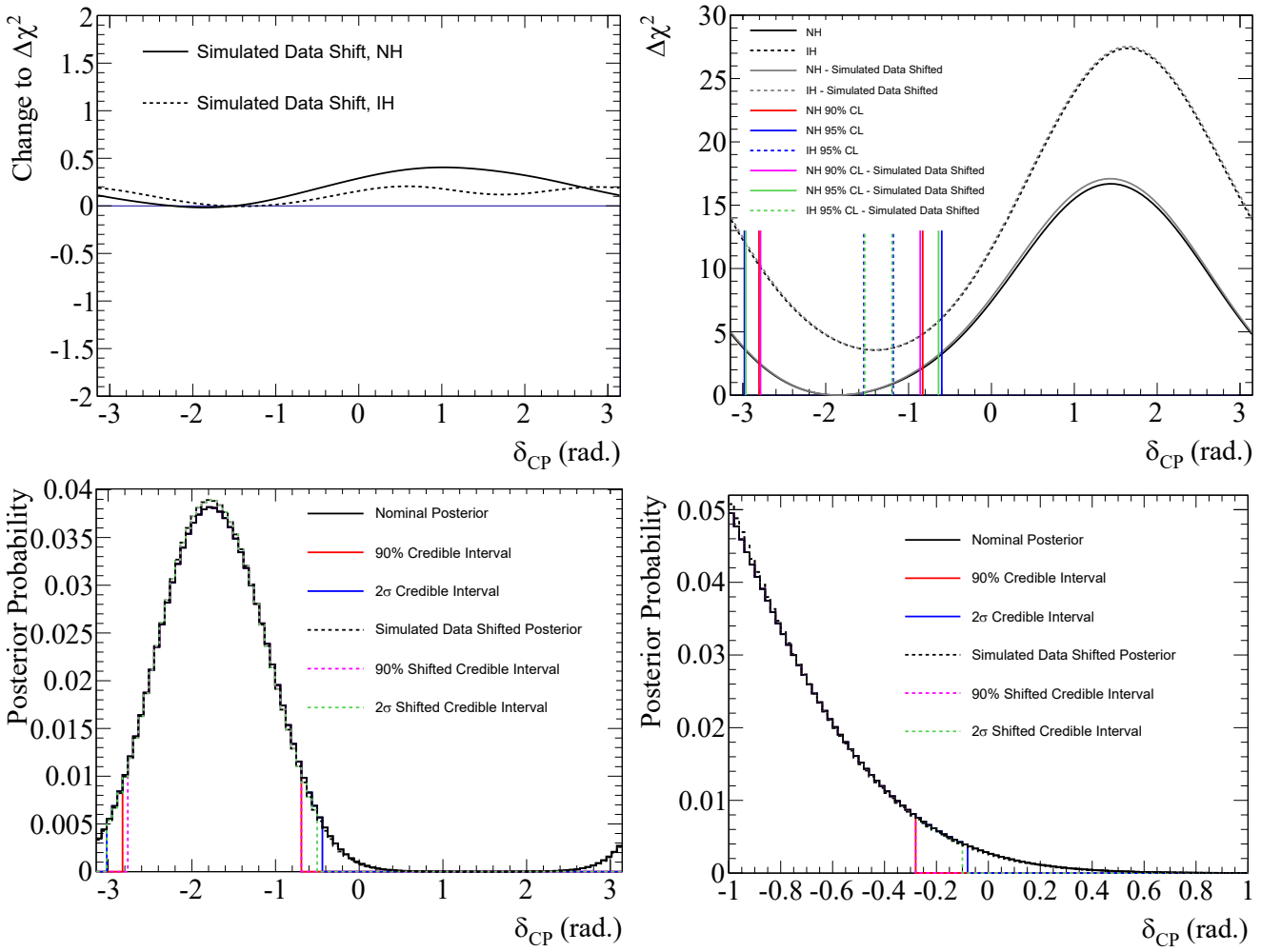

Figure I.14: $\Delta\chi^2_{diff}(\delta_{cp})$ from the data-driven non PDD-like 2p-2h simulated data study (top left), comparison of the confidence intervals (top right), comparison of credible intervals with a flat prior on δ_{cp} (bottom left) and comparison of credible intervals with a flat prior on $\sin(\delta_{cp})$ (bottom right) .

I.4.3 Data-driven PDD-like 2p2h simulated Data

The $\Delta\chi^2_{diff}(\delta_{cp})$ applied and interval comparisons for the data-driven Δ 2p-2h simulated data study are shown in Fig. I.15. The midpoint shifts and width ratios for the 95% intervals are listed in Table I.3. The maximum shift to the interval is by -7.3% for the confidence interval in inverted hierarchy. The inverted hierarchy width changes by -9.6%. Given that only a small fraction of the points in the 95% confidence interval are inverted hierarchy, this level of change is acceptably small.

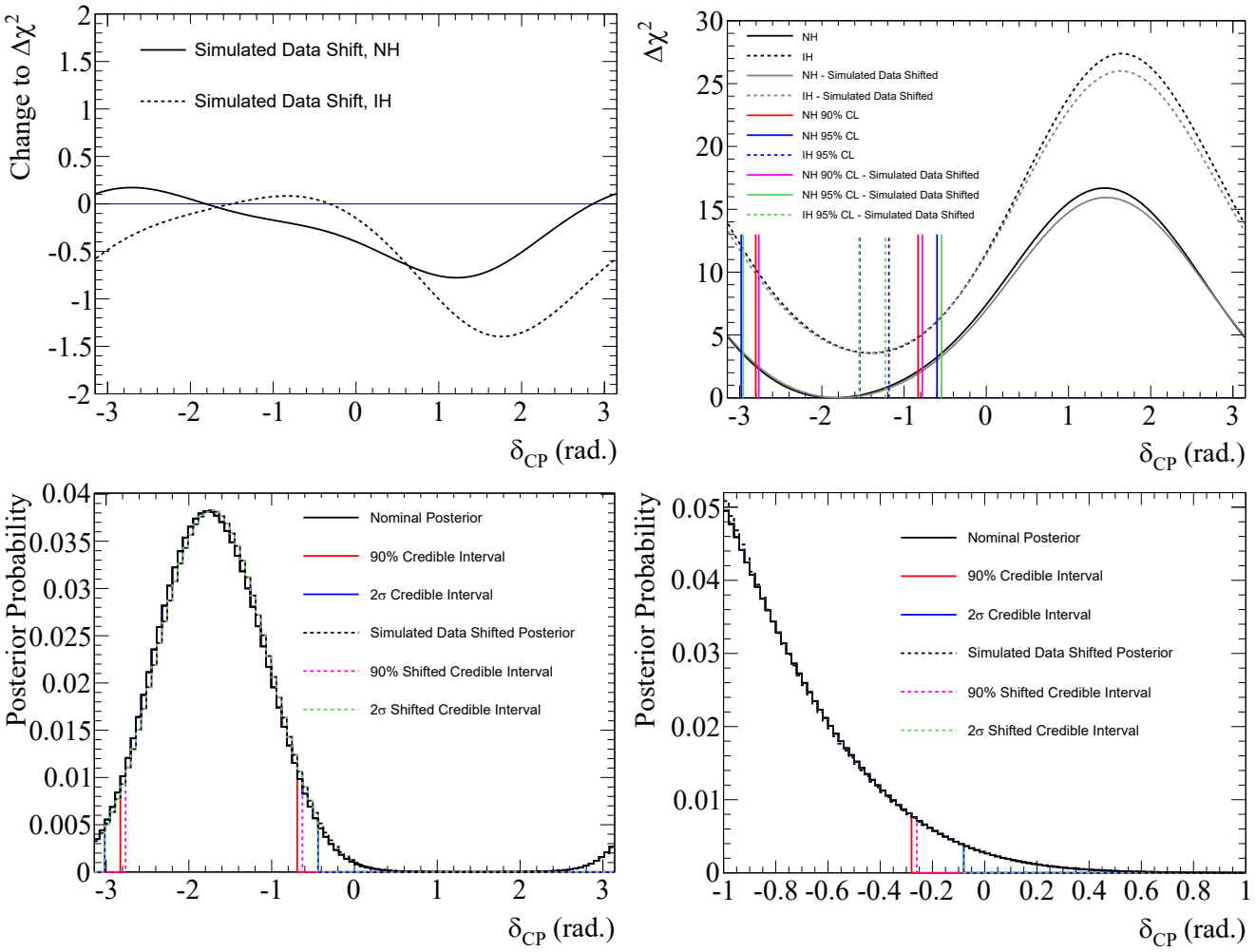

Figure I.15: $\Delta\chi^2_{diff}(\delta_{cp})$ from the data-driven PDD-like 2p2h simulated data study (top left), comparison of the confidence intervals (top right), comparison of credible intervals with a flat prior on δ_{cp} (bottom left) and comparison of credible intervals with a flat prior on $\sin(\delta_{cp})$ (bottom right) .

I.4.4 Data-driven Pion Momentum Simulated Data

The $\Delta\chi^2_{diff}(\delta_{cp})$ applied and interval comparisons for the data-driven pion momentum simulated data study are shown in Fig. I.16. The midpoint shifts and width ratios for the 95% intervals are listed in Table I.4. The maximum shift to the interval is by -0.2% for the confidence interval in normal hierarchy. The inverted hierarchy width changes by -4.3%. This level of change is acceptably small.

Table I.3: Fractional shift and width ratio of the intervals after apply $\Delta\chi^2_{diff}(\delta_{cp})$ from the data-driven PDD-like 2p2h study.

Type of Interval	Midpoint Shift	Width Ratio
Confidence Interval (NH)	0.017	1.013
Confidence Interval (IH)	-0.073	0.904
Credible Interval (flat δ_{cp})	0	1
Credible Interval (flat $\sin(\delta_{cp})$)	0	1

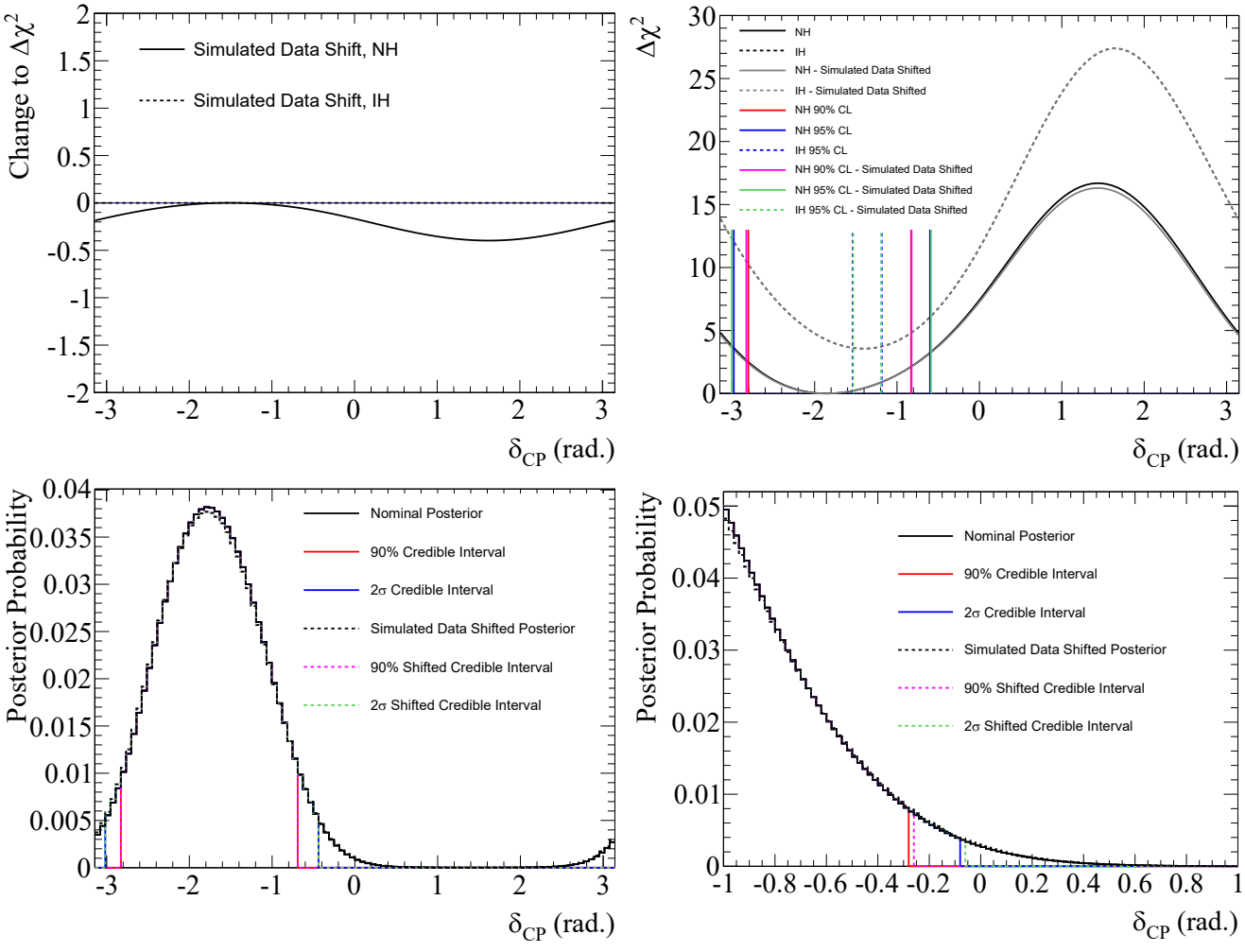

Figure I.16: $\Delta\chi^2_{diff}(\delta_{cp})$ from the data-driven pion momentum data study (top left), comparison of the confidence intervals (top right), comparison of credible intervals with a flat prior on δ_{cp} (bottom left) and comparison of credible intervals with a flat prior on $\sin(\delta_{cp})$ (bottom right) .

Table I.4: Fractional shift and width ratio of the intervals after apply $\Delta\chi^2_{diff}(\delta_{cp})$ from the data-driven pion momentum study.

Type of Interval	Midpoint Shift	Width Ratio
Confidence Interval (NH)	-0.002	1.016
Confidence Interval (IH)	0	0.957
Credible Interval (flat δ_{cp})	0	1
Credible Interval (flat $\sin(\delta_{cp})$)	0	1.013

Table I.5: Largest fractional shift and width changes of the 95% δ_{cp} intervals.

Type of Interval	Midpoint Shift	Width Ratio
Confidence Interval (NH)	0.017 (PDD-like 2p-2h)	0.977 (non PDD-like 2p-2h)
Confidence Interval (IH)	-0.073 (PDD-like 2p-2h)	0.904 (PDD-like 2p-2h)
Credible Interval (flat δ_{cp})	-0.12 (non PDD-like 2p-2h)	0.976 (non PDD-like 2p-2h)
Credible Interval (flat $\sin(\delta_{cp})$)	0	1.013 (Pion momentum)

I.4.5 Summary of impact on δ_{cp} intervals

The impact of simulated data $\Delta\chi^2_{diff}(\delta_{cp})$ on the 95% intervals derived from the data has been shown. In no case, does the shift introduced by the simulated data change any statement about whether the CP conserving values are in the 95% confidence or credible intervals. The maximum changes in the variations for the midpoint and width of the intervals in this study are listed in Table I.5. The largest effects are seen for the 95% confidence interval of inverted hierarchy points. The maximum effect is still less than 10% and we consider this to be acceptably small. For the other intervals, all effects are less than 3%.

Appendix J

Results of the Simulated Data Fit for Parameter Set B

Table J.1: Calculated bias for the ND280 data-driven 2p2h PDD-like simulated data

		θ_{23}	Δm^2_{32} (GeV^2)	δ_{CP}
Asimov B	Mean of the 1σ interval	0.467 and 0.558	2.508e-3	1.540
	1σ interval size	0.035 and 0.034	6.56e-5	1.136
	Bias computed with the 1σ mean and interval	Not defined	**39.56%**	**4.67%**
	Bias relative to σ_{Syst} computed with the 1σ mean and interval	Not defined	**183.35%**	**13.06%**
	Mean of the 2σ interval	0.51122	2.508e-3	Not defined
	2σ interval size	0.101	1.29e-4	Not defined
	Bias computed with the 2σ mean and interval	**4.24%**	**17.32%**	Not defined
	Bias relative to σ_{Syst} computed with the 2σ mean and interval	**13.21%**	**62.80%**	Not defined

Table J.2: Calculated bias for the ND280 data-driven 1p1h simulated data

		θ_{23}	Δm^2_{32} (GeV^2)	δ_{CP}
Asimov B	Mean of the 1σ interval	0.468 and 0.558	2.534e-3	1.444
	1σ interval size	0.036 and 0.033	6.3e-5	1.876
	Bias computed with the 1σ mean and interval	Not defined	**1.76%**	**9.73%**
	Bias relative to σ_{Syst} computed with the 1σ mean and interval	Not defined	**8.17%**	**27.18%**
	Mean of the 2σ interval	0.51122	2.529e-3	Not defined
	2σ interval size	0.103	1.29e-4	Not defined
	Bias computed with the 2σ mean and interval	**4.24%**	**2.85%**	Not defined
	Bias relative to σ_{Syst} computed with the 2σ mean and interval	**13.21%**	**10.33%**	Not defined

Table J.3: Calculated bias for the ND280 data-driven 2p2h non PDD-like simulated data

		θ_{23}	Δm^2_{32}	δ_{CP}
Asimov B	Mean of the 1σ interval	0.467 and 0.558	2.529e-3	1.476
	1σ interval size	0.036 and 0.031	6.04e-5	1.844
	Bias computed with the 1σ mean and interval	Not defined	**6.50%**	**8.04%**
	Bias relative to σ_{Syst} computed with the 1σ mean and interval	Not defined	**8.17%**	**27.18%**
	Mean of the 2σ interval	0.5112	2.529e-3	Not defined
	2σ interval size	0.101	1.29e-4	Not defined
	Bias computed with the 2σ mean and interval	**4.24%**	**2.85%**	Not defined
	Bias relative to σ_{Syst} computed with the 2σ mean and interval	**13.21%**	**10.33%**	Not defined

Table J.4: Calculated bias for the Kabirnezhad model simulated data

		θ_{23}	Δm^2_{32} (GeV^2)	δ_{CP}
Asimov B	Mean of the 1σ interval	0.509	2.487e-3	1.428
	1σ interval size	0.071	6.038e-5	1.764
	Bias computed with the 1σ mean and interval	**54.69%**	**72.63%**	**10.57%**
	Bias relative to σ_{Syst} computed with the 1σ mean and interval	Not defined	**336.64%**	**29.52%**
	Mean of the 2σ interval	0.51122	2.487e-3	Not defined
	2σ interval size	0.096	1.23e-4	Not defined
	Bias computed with the 2σ mean and interval	**4.24%**	**31.80%**	Not defined
	Bias relative to σ_{Syst} computed with the 2σ mean and interval	**13.21%**	**115.3%**	Not defined

Table J.5: Calculated bias for the binding energy simulated data

		θ_{23}	Δm^2_{32} (GeV^2)	δ_{CP}
Asimov B	Middle of the 1σ interval	0.5112	2.476e-3	1.563
	1σ interval size	0.06498	6.75e-05	1.792
	1σ interval ratio to Asimov	1.97	1.06	0.92
	Change in the 1σ interval ratio to syst interval	Not defined	29%	-25%
	Bias computed with the 1σ middle and interval (lower octant θ_{23})	**144%**	**90%**	**1.5%**
	Bias relative to σ_{Syst} computed with the 1σ middle and interval	Not defined	**415%**	**3.1%**
	Middle of the 2σ interval	0.5131	2.478e-3	Not defined
	2σ interval size	0.09766	1.485e-4	Not defined
	2σ interval ratio to Asimov	0.87	1.01	Not defined
	Bias computed with the 2σ middle and interval	**5.0%**	**77%**	Not defined
	Bias relative to σ_{Syst} computed with the 2σ middle and interval	**15%**	**242%**	Not defined

Table J.6: Bias table of the simulated data with the binding energy parameter and the smearing applied to Δm^2_{32}. The values in parentheses are fit results without the binding energy parameter nor the smearing as reference. The smearing procedure is applied to Asimov, and therefore included in the systematic only error. The largest bias from either the upper or lower octant minimum is shown.

Asimov B		θ_{23}	Δm^2_{32}	δ_{CP}
Martini 2p2h	Bias computed with the 1σ middle and interval	**30%**(27%)	**10%**(9%)	-
	Bias relative to σ_{Syst} computed with the 1σ middle and interval	-	**15%**(37%)	-
SF	Bias computed with the 1σ middle and interval	**11%**(7%)	**19%**(26%)	-
	Bias relative to σ_{Syst} computed with the 1σ middle and interval	-	**30%**(107%)	-
Nieves 1p1h	Bias computed with the 1σ middle and interval	**17%**(21%)	**17%**(28%)	-
	Bias relative to σ_{Syst} computed with the 1σ middle and interval	-	**26%**(117%)	-
Kabirnezhad model	Bias computed with the 1σ middle and interval	**6%**(13%)	**25%**(37%)	-
	Bias relative to σ_{Syst} computed with the 1σ middle and interval	-	**39%**(153%)	-
data-driven 1p1h	Bias computed with the 1σ middle and interval	**8%**(8%)	**34%**(35%)	-
	Bias relative to σ_{Syst} computed with the 1σ middle and interval	-	**53%**(143%)	-
Data-driven 2p2hnD	Bias computed with the 1σ middle and interval	**8%**(8%)	**19%**(28%)	-
	Bias relative to σ_{Syst} computed with the 1σ middle and interval	-	**29%**(117%)	-
data-driven 2p2hD	Bias computed with the 1σ middle and interval	**0%**(7%)	**25%**(26%)	-
	Bias relative to σ_{Syst} computed with the 1σ middle and interval	-	**39%**(107%)	-

Appendix K

Effects of the Binding Energy Parameter and Smearing

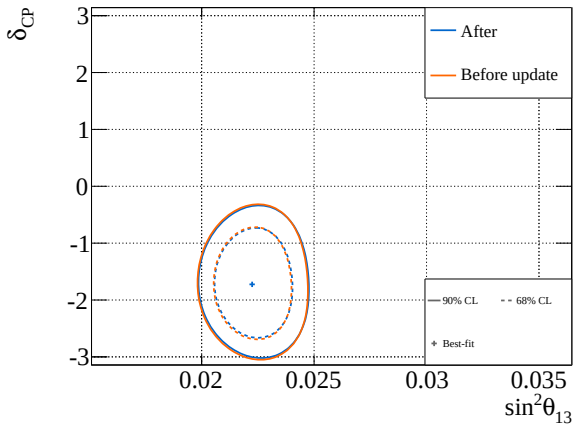

(a) $\sin^2\theta_{13} - \delta_{CP}$ with reactor constraint assuming Normal hierarchy.

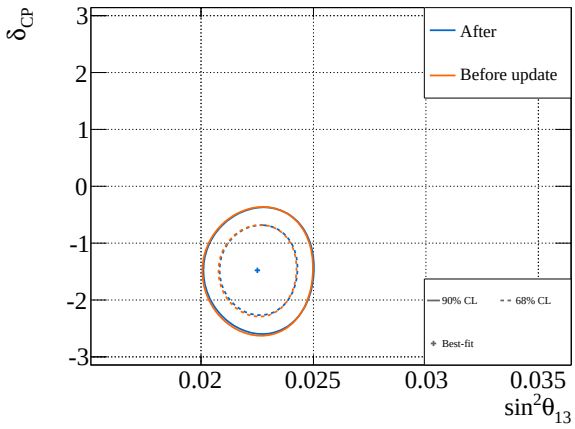

(b) $\sin^2\theta_{13} - \delta_{CP}$ with reactor constraint assuming Inverted hierarchy.

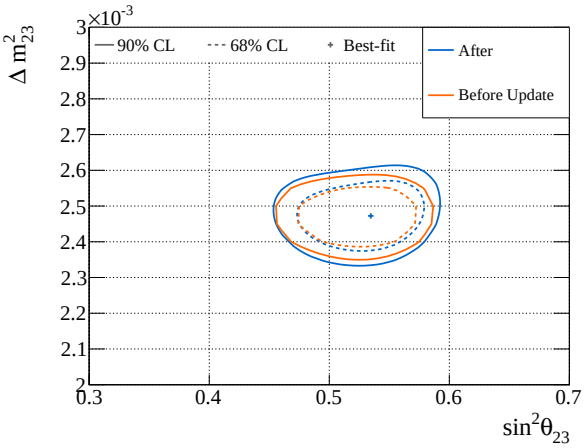

(c) $\sin^2\theta_{23} - \Delta m^2_{32}$ with reactor constraint

Figure K.1: Comparison between the data fit with and without smearing method is applied.

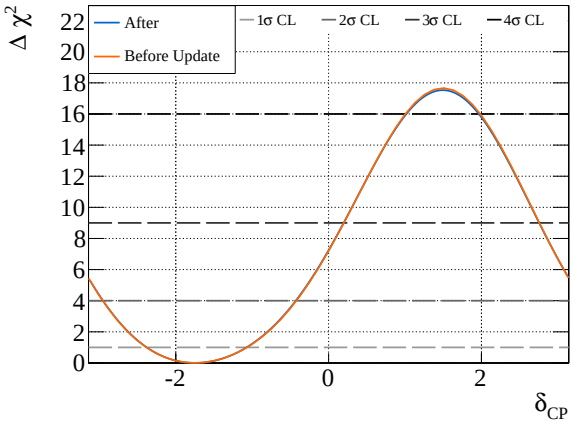

(a) δ_{CP} with reactor constraint assuming normal hierarchy

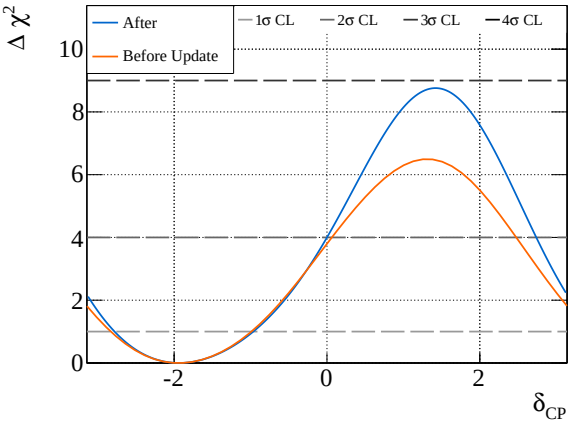

(b) δ_{CP} without reactor constraint assuming normal hierarchy

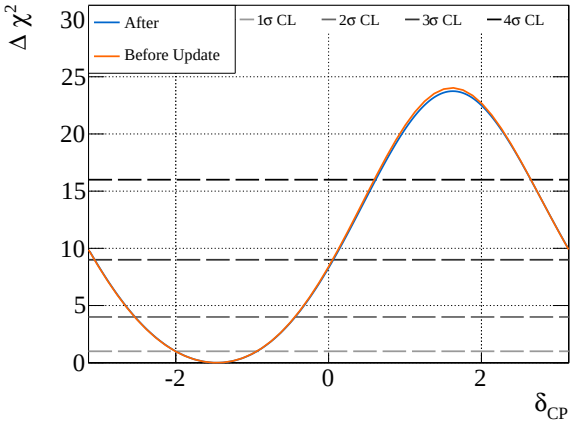

(c) δ_{CP} with reactor constraint assuming inverted hierarchy

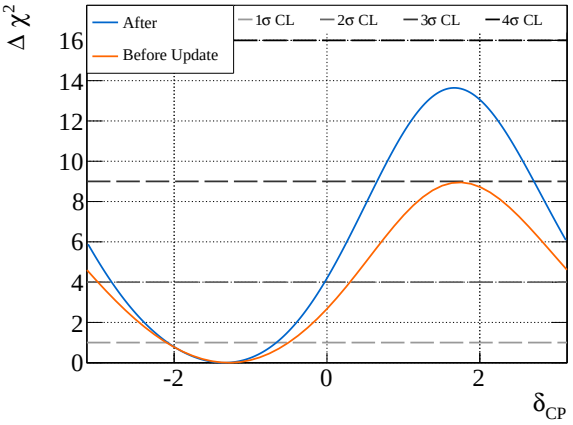

(d) δ_{CP} without reactor constraint assuming inverted hierarchy

Figure K.2: Comparison of δ_{CP} sensitivity between the data fit with and without smearing method is applied.

Bibliography

[1] C. D. Ellis, W. A. Wooster. The average energy of disintegration of radium e. *Proceedings of the Royal Society of London A: Mathematical, Physical and Engineering Sciences*, 117(776):109–123, 1927.

[2] W. Pauli. Dear radioactive ladies and gentlemen. *Phys. Today*, 31N9:27, 1978.

[3] E. Fermi. Versuch einer Theorie der β-Strahlen. I. *Zeitschrift für Physik*, 88(3):161–177, Mar 1934.

[4] F. Reines, C. L. Cowan. Detection of the Free Neutrino. *Phys. Rev.*, 92:830–831, Nov 1953.

[5] R. Davis, Jr., D. S. Harmer. Attempt to observe the $Cl^{37}(\bar{\nu}e^-)Ar^{37}$ reaction induced by reactor antineutrinos. *Bull. Am. Phys. Soc.*, 4:217, 1959.

[6] T. D. Lee, C. N. Yang. Parity Nonconservation and a Two-Component Theory of the Neutrino. *Phys. Rev.*, 105:1671–1675, Mar 1957.

[7] C. S. Wu *et al.* Experimental Test of Parity Conservation in Beta Decay. *Phys. Rev.*, 105:1413–1415, Feb 1957.

[8] R. L. Garwin, L. M. Lederman, M. Weinrich. Observations of the Failure of Conservation of Parity and Charge Conjugation in Meson Decays: the Magnetic Moment of the Free Muon. *Phys. Rev.*, 105:1415–1417, Feb 1957.

[9] M. Goldhaber, L. Grodzins, A. W. Sunyar. Helicity of Neutrinos. *Phys. Rev.*, 109:1015–1017, Feb 1958.

[10] R. P. Feynman, M. Gell-Mann. Theory of the Fermi Interaction. *Phys. Rev.*, 109:193–198, Jan 1958.

[11] E. C. G. Sudarshan, R. E. Marshak. Chirality Invariance and the Universal Fermi Interaction. *Phys. Rev.*, 109:1860–1862, Mar 1958.

[12] S. Weinberg. A Model of Leptons. *Phys. Rev. Lett.*, 19:1264–1266, Nov 1967.

[13] A. Salam. Weak and Electromagnetic Interactions. *Conf. Proc.*, C680519:367–377, 1968.

[14] S. L. Glashow. Partial-symmetries of weak interactions. *Nuclear Physics*, 22(4):579 – 588, 1961.

[15] M. Y. Han, Y. Nambu. Three-Triplet Model with Double SU(3) Symmetry. *Phys. Rev.*, 139:B1006–B1010, Aug 1965.

[16] O. W. Greenberg. Spin and Unitary-Spin Independence in a Paraquark Model of Baryons and Mesons. *Phys. Rev. Lett.*, 13:598–602, Nov 1964.

[17] F. Englert, R. Brout. Broken Symmetry and the Mass of Gauge Vector Mesons. *Phys. Rev. Lett.*, 13:321–323, Aug 1964.

[18] P. W. Higgs. Broken Symmetries and the Masses of Gauge Bosons. *Phys. Rev. Lett.*, 13:508–509, Oct 1964.

[19] G. S. Guralnik, C. R. Hagen, T. W. B. Kibble. Global Conservation Laws and Massless Particles. *Phys. Rev. Lett.*, 13:585–587, Nov 1964.

[20] J. Goldstone. Field theories with « Superconductor » solutions. *Il Nuovo Cimento (1955-1965)*, 19(1):154–164, Jan 1961.

[21] F. Hasert *et al.* Observation of neutrino-like interactions without muon or electron in the gargamelle neutrino experiment. *Physics Letters B*, 46(1):138 – 140, 1973.

[22] G. Arnison *et al.* Experimental observation of isolated large transverse energy electrons with associated missing energy at $s = 540$ GeV. *Physics Letters B*, 122(1):103 – 116, 1983.

[23] G. Arnison *et al.* Experimental observation of lepton pairs of invariant mass around 95 GeV/c^2 at the CERN SPS collider. *Physics Letters B*, 126(5):398 – 410, 1983.

[24] S. Chatrchyan *et al.* Observation of a new boson at a mass of 125 GeV with the CMS experiment at the LHC. *Physics Letters B*, 716(1):30 – 61, 2012.

[25] G. Danby *et al.* Observation of High-Energy Neutrino Reactions and the Existence of Two Kinds of Neutrinos. *Phys. Rev. Lett.*, 9:36–44, Jul 1962.

[26] M. L. Perl *et al.* Evidence for Anomalous Lepton Production in $e^+ - e^-$ Annihilation. *Phys. Rev. Lett.*, 35:1489–1492, Dec 1975.

[27] K. Kodama *et al.* Observation of tau neutrino interactions. *Physics Letters B*, 504(3):218 – 224, 2001.

[28] D. DeCamp *et al.* Determination of the number of light neutrino species. *Physics Letters B*, 231(4):519 – 529, 1989.

[29] N. Aghanim et al. Planck 2018 results. VI. Cosmological parameters. 2018.

[30] R. Davis, D. S. Harmer, K. C. Hoffman. Search for Neutrinos from the Sun. *Phys. Rev. Lett.*, 20:1205–1209, May 1968.

[31] J. N. Bahcall, N. A. Bahcall, G. Shaviv. Present Status of the Theoretical Predictions for the ^{37}Cl Solar-Neutrino Experiment. *Phys. Rev. Lett.*, 20:1209–1212, May 1968.

[32] Y. Fukuda *et al.* Solar Neutrino Data Covering Solar Cycle 22. *Phys. Rev. Lett.*, 77:1683–1686, Aug 1996.

[33] W. Hampel *et al.* GALLEX solar neutrino observations: results for GALLEX IV. *Physics Letters B*, 447(1):127 – 133, 1999.

[34] M. Altmann *et al.* GNO solar neutrino observations: results for GNO I. *Physics Letters B*, 490(1):16 – 26, 2000.

[35] A. I. Abazov *et al.* Search for neutrinos from the Sun using the reaction $^{71}\mathrm{Ga}(\nu_e,e^-)^{71}\mathrm{Ge}$. *Phys. Rev. Lett.*, 67:3332–3335, Dec 1991.

[36] S. Fukuda *et al.* Determination of solar neutrino oscillation parameters using 1496 days of Super-Kamiokande-I data. *Physics Letters B*, 539(3):179 – 187, 2002.

[37] Q. R. Ahmad *et al.* Direct Evidence for Neutrino Flavor Transformation from Neutral-Current Interactions in the Sudbury Neutrino Observatory. *Phys. Rev. Lett.*, 89:011301, Jun 2002.

[38] Y. Fukuda *et al.* Atmospheric vÎijve ratio in the multi-GeV energy rane. *Physics Letters B*, 335(2):237 – 245, 1994.

[39] K. Hirata *et al.* Experimental study of the atmospheric neutrino flux. *Physics Letters B*, 205(2):416 – 420, 1988.

[40] R. Becker-Szendy *et al.* Electron- and muon-neutrino content of the atmospheric flux. *Phys. Rev. D*, 46:3720–3724, Nov 1992.

[41] W. Allison *et al.* Measurement of the atmospheric neutrino flavour composition in Soudan 2. *Physics Letters B*, 391(3):491 – 500, 1997.

[42] Y. Fukuda *et al.* Evidence for Oscillation of Atmospheric Neutrinos. *Phys. Rev. Lett.*, 81:1562–1567, Aug 1998.

[43] M. H. Ahn *et al.* Measurement of neutrino oscillation by the K2K experiment. *Phys. Rev. D*, 74:072003, Oct 2006.

[44] N. Agafonova *et al.* Final Results of the OPERA Experiment on ν_τ Appearance in the CNGS Neutrino Beam. *Phys. Rev. Lett.*, 120:211801, May 2018.

[45] Z. Maki, M. Nakagawa, S. Sakata. Remarks on the Unified Model of Elementary Particles. *Progress of Theoretical Physics*, 28(5):870–880, 1962.

[46] B. Pontecorvo. Inverse beta processes and nonconservation of lepton charge. *Sov. Phys. JETP*, 7:172–173, 1958. [Zh. Eksp. Teor. Fiz.34,247(1957)].

[47] L. Wolfenstein. Neutrino oscillations in matter. *Phys. Rev. D*, 17:2369–2374, May 1978.

[48] S. P. Mikheyev, A. Yu. Smirnov. Resonance Amplification of Oscillations in Matter and Spectroscopy of Solar Neutrinos. *Sov. J. Nucl. Phys.*, 42:913–917, 1985. [,305(1986)].

[49] J. Arafune, M. Koike, J. Sato. CP violation and matter effect in long baseline neutrino oscillation experiments. *Phys. Rev. D*, 56:3093–3099, Sep 1997.

[50] K. Abe et al. Proposal for an Extended Run of T2K to 20×10^{21} POT. 2016.

[51] B. T. Cleveland *et al.* Measurement of the Solar Electron Neutrino Flux with the Homestake Chlorine Detector. *The Astrophysical Journal*, 496(1):505, 1998.

[52] K. Abe *et al.* Solar neutrino results in Super-Kamiokande-III. *Phys. Rev. D*, 83:052010, Mar 2011.

[53] G. Bellini *et al.* Measurement of the solar ^{8}B neutrino rate with a liquid scintillator target and 3 MeV energy threshold in the Borexino detector. *Phys. Rev. D*, 82:033006, Aug 2010.

[54] T. Araki *et al.* Measurement of Neutrino Oscillation with KamLAND: Evidence of Spectral Distortion. *Phys. Rev. Lett.*, 94:081801, Mar 2005.

[55] I. Esteban *et al.* Updated fit to three neutrino mixing: exploring the accelerator-reactor complementarity. *Journal of High Energy Physics*, 2017(1):87, Jan 2017.

[56] K. Abe *et al.* Atmospheric neutrino oscillation analysis with external constraints in Super-Kamiokande I-IV. *Phys. Rev. D*, 97:072001, Apr 2018.

[57] M. G. Aartsen *et al.* Measurement of Atmospheric Neutrino Oscillations at 6–56 GeV with IceCube DeepCore. *Phys. Rev. Lett.*, 120:071801, Feb 2018.

[58] K. Abe *et al.* Measurement of Neutrino Oscillation Parameters from Muon Neutrino Disappearance with an Off-Axis Beam. *Phys. Rev. Lett.*, 111:211803, Nov 2013.

[59] K. Abe *et al.* Precise Measurement of the Neutrino Mixing Parameter θ_{23} from Muon Neutrino Disappearance in an Off-Axis Beam. *Phys. Rev. Lett.*, 112:181801, May 2014.

[60] K. Abe *et al.* Measurements of neutrino oscillation in appearance and disappearance channels by the T2K experiment with 6.6×10^{20} protons on target. *Phys. Rev. D*, 91:072010, Apr 2015.

[61] P. Adamson *et al.* "first measurement of muon-neutrino disappearance in noνa". *Phys. Rev. D*, 93:051104, Mar 2016.

[62] P. Adamson *et al.* Measurement of the Neutrino Mixing Angle θ_{23} in NOvA. *Phys. Rev. Lett.*, 118:151802, Apr 2017.

[63] M. A. Acero *et al.* New constraints on oscillation parameters from ν_e appearance and ν_μ disappearance in the NOνA experiment. *Phys. Rev. D*, 98:032012, Aug 2018.

[64] P. Adamson *et al.* Measurement of Neutrino and Antineutrino Oscillations Using Beam and Atmospheric Data in MINOS. *Phys. Rev. Lett.*, 110:251801, Jun 2013.

[65] Tzanankos *et al.* MINOS+: a Proposal to FNAL to run MINOS with the medium energy NuMI beam. 5 2011.

[66] K. Abe *et al.* Indication of Electron Neutrino Appearance from an Accelerator-Produced Off-Axis Muon Neutrino Beam. *Phys. Rev. Lett.*, 107:041801, Jul 2011.

[67] F. P. An *et al.* Observation of Electron-Antineutrino Disappearance at Daya Bay. *Phys. Rev. Lett.*, 108:171803, Apr 2012.

[68] J. K. Ahn *et al.* Observation of Reactor Electron Antineutrinos Disappearance in the RENO Experiment. *Phys. Rev. Lett.*, 108:191802, May 2012.

[69] Y. Abe *et al.* Indication of Reactor $\overline{\nu}_e$ Disappearance in the Double Chooz Experiment. *Phys. Rev. Lett.*, 108:131801, Mar 2012.

[70] K. Abe *et al.* Observation of Electron Neutrino Appearance in a Muon Neutrino Beam. *Phys. Rev. Lett.*, 112:061802, Feb 2014.

[71] K. Abe *et al.* Measurement of neutrino and antineutrino oscillations by the T2K experiment including a new additional sample of ν_e interactions at the far detector. *Phys. Rev. D*, 96:092006, Nov 2017.

[72] S. Pascoli, S. Petcov. The SNO solar neutrino data, neutrinoless double beta-decay and neutrino mass spectrum. *Physics Letters B*, 544(3):239 – 250, 2002.

[73] V. N. Aseev *et al.* Upper limit on the electron antineutrino mass from the Troitsk experiment. *Phys. Rev. D*, 84:112003, Dec 2011.

[74] C. Kraus et al. Final results from phase II of the Mainz neutrino mass search in tritium beta decay. *Eur. Phys. J.*, C40:447–468, 2005.

[75] A. Aguilar *et al.* Evidence for neutrino oscillations from the observation of $\overline{\nu}_e$ appearance in a $\overline{\nu}_\mu$ beam. *Phys. Rev. D*, 64:112007, Nov 2001.

[76] A. A. Aguilar-Arevalo *et al.* Improved Search for $\overline{\nu}_\mu \to \overline{\nu}_e$ Oscillations in the MiniBooNE Experiment. *Phys. Rev. Lett.*, 110:161801, Apr 2013.

[77] B. Armbruster *et al.* Upper limits for neutrino oscillations $\overline{\nu}_\mu \to \overline{\nu}_e$ from muon decay at rest. *Phys. Rev. D*, 65:112001, Jun 2002.

[78] E. Majorana. Teoria simmetrica dell'elettrone e del positrone. *Il Nuovo Cimento*, 14:171–184, April 1937.

[79] P. Minkowski. $\mu \to e\gamma$ at a rate of one out of 109 muon decays? *Physics Letters B*, 67(4):421 – 428, 1977.

[80] M. Gell-Mann, P. Ramond, R. Slansky. Complex Spinors and Unified Theories. *Conf. Proc.*, C790927:315–321, 1979.

[81] T. Yanagida. Horizontal Symmetry and Masses of Neutrinos. *Progress of Theoretical Physics*, 64(3):1103–1105, 1980.

[82] Mohapatra, Rabindra N. and Senjanović, Goran. Neutrino mass and spontaneous parity nonconservation. *Phys. Rev. Lett.*, 44:912–915, Apr 1980.

[83] J. Schechter, J. W. F. Valle. Neutrino masses in SU(2) $\bigotimes$ U(1) theories. *Phys. Rev. D*, 22:2227–2235, Nov 1980.

[84] M. Agostini *et al.* Improved Limit on Neutrinoless Double-β Decay of ^{76}Ge from GERDA Phase II. *Phys. Rev. Lett.*, 120:132503, Mar 2018.

[85] A. Gando *et al.* Search for Majorana Neutrinos Near the Inverted Mass Hierarchy Region with KamLAND-Zen. *Phys. Rev. Lett.*, 117:082503, Aug 2016.

[86] G. Aad et al. Search for heavy Majorana neutrinos with the ATLAS detector in pp collisions at $\sqrt{s} = 8$ TeV. *JHEP*, 07:162, 2015.

[87] V. Khachatryan et al. Search for heavy Majorana neutrinos in $\mu^\pm\mu^\pm$+ jets events in proton-proton collisions at $\sqrt{s} = 8$ TeV. *Phys. Lett.*, B748:144–166, 2015.

[88] M. Kobayashi, T. Maskawa. CP-Violation in the Renormalizable Theory of Weak Interaction. *Progress of Theoretical Physics*, 49(2):652–657, 1973.

[89] M. Tanabashi *et al.* Review of Particle Physics. *Phys. Rev. D*, 98:030001, Aug 2018.

[90] P. Harrison, D. Perkins, W. Scott. Tri-bimaximal mixing and the neutrino oscillation data. *Physics Letters B*, 530(1):167 – 173, 2002.

[91] S. King. Tri-bimaximal-Cabibbo mixing. *Physics Letters B*, 718(1):136 – 142, 2012.

[92] L. Hall, H. Murayama, N. Weiner. Neutrino Mass Anarchy. *Phys. Rev. Lett.*, 84:2572–2575, Mar 2000.

[93] A. D. Sakharov. Violation of CP Invariance, C asymmetry, and baryon asymmetry of the universe. *Pisma Zh. Eksp. Teor. Fiz.*, 5:32–35, 1967. [Usp. Fiz. Nauk161,no.5,61(1991)].

[94] M. Yoshimura. Unified Gauge Theories and the Baryon Number of the Universe. *Phys. Rev. Lett.*, 41:281–284, Jul 1978.

[95] M. Fukugita, T. Yanagida. Barygenesis without grand unification. *Physics Letters B*, 174(1):45 – 47, 1986.

[96] M. Wascko. T2K Status, Results, and Plans, June 2018.

[97] M. Sanchez. NOvA Results and Prospects, June 2018.

[98] D. Casper. The nuance neutrino physics simulation, and the future. *Nuclear Physics B - Proceedings Supplements*, 112(1):161 – 170, 2002.

[99] K. Abe et al. The T2K Experiment. *Nucl. Instrum. Meth.*, A659:106–135, 2011.

[100] P. Adamson et al. Measurement of the neutrino mixing angle θ_{23} in NOνA. *Phys. Rev. Lett.*, 118(15):151802, 2017.

[101] T. Nakamoto *et al.* Construction of Superconducting Magnet System for the J-PARC Neutrino Beam Line. *IEEE Transactions on Applied Superconductivity*, 20(3):208–213, June 2010.

[102] S. van der Meer. A Directive Device for Charged Particles and Its use in an Enhanced Neutrino Beam. 1961.

[103] A. Ichikawa. Design concept of the magnetic horn system for the T2K neutrino beam. *Nuclear Instruments and Methods in Physics Research Section A: Accelerators, Spectrometers, Detectors and Associated Equipment*, 690:27 – 33, 2012.

[104] T. Sekiguchi *et al.* Development and operational experience of magnetic horn system for T2K experiment. *Nuclear Instruments and Methods in Physics Research Section A: Accelerators, Spectrometers, Detectors and Associated Equipment*, 789:57 – 80, 2015.

[105] T. E. Tubes, L. Devices Co. http://www.toshiba-tetd.co.jp/eng/index.htm., 2008.

[106] S. Bhadra *et al.* Optical transition radiation monitor for the T2K experiment. *Nuclear Instruments and Methods in Physics Research Section A: Accelerators, Spectrometers, Detectors and Associated Equipment*, 703:45 – 58, 2013.

[107] K. Matsuoka *et al.* Design and performance of the muon monitor for the T2K neutrino oscillation experiment. *Nuclear Instruments and Methods in Physics Research Section A: Accelerators, Spectrometers, Detectors and Associated Equipment*, 624(3):591 – 600, 2010.

[108] K. Suzuki *et al.* Measurement of the muon beam direction and muon flux for the T2K neutrino experiment. *Progress of Theoretical and Experimental Physics*, 2015(5):053C01, 2015.

[109] D. Beavis, A. Carroll, I. Chiang. Long baseline neutrino oscillation experiment at the AGS. Technical report, April 1995.

[110] S. Assylbekov *et al.* The T2K ND280 off-axis pi-zero detector. *Nuclear Instruments and Methods in Physics Research Section A: Accelerators, Spectrometers, Detectors and Associated Equipment*, 686:48 – 63, 2012.

[111] N. Abgrall *et al.* Time projection chambers for the T2K near detectors. *Nuclear Instruments and Methods in Physics Research Section A: Accelerators, Spectrometers, Detectors and Associated Equipment*, 637(1):25 – 46, 2011.

[112] P.-A. Amaudruz *et al.* The T2K fine-grained detectors. *Nuclear Instruments and Methods in Physics Research Section A: Accelerators, Spectrometers, Detectors and Associated Equipment*, 696:1 – 31, 2012.

[113] D. Allan *et al.* The electromagnetic calorimeter for the T2K near detector ND280. *Journal of Instrumentation*, 8(10):P10019, 2013.

[114] S. Aoki *et al.* The T2K Side Muon Range Detector (SMRD). *Nuclear Instruments and Methods in Physics Research Section A: Accelerators, Spectrometers, Detectors and Associated Equipment*, 698:135 – 146, 2013.

[115] K. Abe *et al.* Measurements of the T2K neutrino beam properties using the INGRID on-axis near detector. *Nuclear Instruments and Methods in Physics Research Section A: Accelerators, Spectrometers, Detectors and Associated Equipment*, 694:211 – 223, 2012.

[116] Y. Fukuda et al. The Super-Kamiokande detector. *Nucl. Instrum. Meth.*, A501:418–462, 2003.

[117] K. Hirano *et al.* Development of RF chopper system at J-PARC LINAC. In *Proceedings of the 12th annual meeting of Particle Accelerator Society of Japan*, Tsuruga, Japan, 2015. in Japanese.

[118] T. Sugawara, editor. *Proceedings of the International Symposium on Future of Accelerator-Driven System*. JAEA, 2012. in Japanese.

[119] I. Sugai *et al.* Development of thick hybrid-type carbon stripper foils with high durability at 1800K for RCS of J-PARC. *Nuclear Instruments and Methods in Physics Research Section A: Accelerators, Spectrometers, Detectors and Associated Equipment*, 561(1):16 – 23, 2006. Proceedings of the 22nd World Conference of the International Nuclear Target Development Society.

[120] C. Ohmori *et al.* DEVELOPMENTS OF MAGNETIC ALLOY CORES WITH HIGHER IMPEDANCE FOR J-PARC UPGRADE. In *Proceedings of IPACâĂŹ1*, Kyoto, Japan, 2010.

[121] H. Harada *et al.* THE PAINTING INJECTION AT J-PARC 3GeV RCS. 05 2018.

[122] H. Hotchi *et al.* Beam commissioning and operation of the Japan Proton Accelerator Research Complex 3-GeV rapid cycling synchrotron. *Progress of Theoretical and Experimental Physics*, 2012(1):02B003, 2012. and references therein.

[123] T. Koseki *et al.* Beam commissioning and operation of the J-PARC main ring synchrotron. *Progress of Theoretical and Experimental Physics*, 2012(1):02B004, 2012. and references therein.

[124] Y. Sato *et al.* RECENT COMMISSIONING AND PROSPECT OF HIGH POWER BEAM OPERATION OF THE J-PARC MAIN RING . In *Proceedings of the 12th Annual Meeting of Particle Accelerator Society of Japan*, Tsuruga, Japan, 2015. In Japanese.

[125] Y.Hashimoto, et. al. Two-Dimensional and Wide Dynamic Range Profile Monitor Using OTR / Fluorescence Screens for Diagnosing Beam Halo of Intense Proton Beams. In *Proceedings of HB2014*, East Lansing, MI, USA, 2014.

[126] C. Ohmori *et al.* THE SECOND HARMONIC RF SYSTEM FOR J-PARC MR UPGRADE. In *Proceedings of IPAC2016*, Busan, Korea, 2016.

[127] F. Tamura *et al.* Multiharmonic rf feedforward system for beam loading compensation in wideband cavities of a rapid cycling synchrotron. *Phys. Rev. ST Accel. Beams*, 14:051004, May 2011.

[128] S. Igarashi *et al.* TRANSVERSE RESONANCES AND CORRECTIONS IN J-PARC MR. In *Proceedings of the 14th Annual Meeting of Particle Accelerator Society of Japan*, Sapporo, Japan, 2017.

[129] Y. Kurimoto *et al.* THE BUNCH BY BUNCH FEEDBACK SYSTEM IN J-PARC MAIN RING. In *Proceedings of DIPAC2011*, Hamburg Germany, 2011.

[130] Y. Chin *et al.* HEAD-TAIL INSTABILITIES OBSERVED AT J-PARC MR AND THEIR SUPPRESSION USING A FEEDBACK SYSTEM. In *Proceedings of the 11th Annual Meeting of Particle Accelerator Society of Japan*, Osaka, Japan, 2012.

[131] T. P. R. Linnecar. The high frequency longitudinal and transverse pick-ups used in the SPS. *IEEE Trans. Nucl. Sci.*, 26(CERN-SPS-ARF-78-17):3409–3411. 99 p, Aug 1978.

[132] K. Nakamura *et al.* FABRICATION OF TAPERED COUPLER FOR INTRA-BUNCH FEEDBACK SYSTEM IN J-PARC MAIN RING. In *Proceedings of the 11th Annual Meeting of Particle Accelerator Society of Japan*, Aomori, Japan, 2014. in Japanese.

[133] A. Chao, M. Tigner, editors. *Handbook of Accelerator Physics and Engineering*, page 570. World Scientific, Singapore, 1998.

[134] K. Nakamura. Development of Intra-bunch Feedback system in J-PARC MR for the intensity upgrade of T2K neutrino beam. Master's thesis, Kyoto University, 2015. In Japanese.

[135] Y. Shobuda *et al.* Triangle and concave pentagon electrodes for an improved broadband frequency response of stripline beam position monitors. *Phys. Rev. Accel. Beams*, 19:021003, Feb 2016.

[136] K. Nakamura *et al.* DEVELOPMENT OF WIDEBAND BPM FOR PRECISE MEASUREMENT OF INTERNAL BUNCH MOTION. In *Proceedings of IPAC2015*, Richmond, USA, 2015.

[137] Dimtel inc. home page. `https://www.dimtel.com`.

[138] Superkekb project home page. `http://www-superkekb.kek.jp/index.html`.

[139] Sirius light source home page. `https://www.lnls.cnpem.br/sirius-en/`.

[140] M. Okada, T. Toyama. DEVELOPMENT OF THE DLC COATED BEAM EXCITER. In *Proceedings of the 11th Annual Meeting of Particle Accelerator Society of Japan*, Aomori, Japan, 2014. In Japanese.

[141] M.Okada, T.Toyama. THE KICK ANGLE CALIBRATION OF THE EXCITER IN THE J-PARC MR. In *Proceedings of the 13th Annual Meeting of Particle Accelerator Society of Japan August 8-10, 2016, Chiba, Japan*, Chiba, Japan, 2017. In Japanese.

[142] T. Sugimoto *et al.* Performance of Injection Kicker Magnet for the J-PARC Main Ring. In *Proceedings of the 10th Annual Meeting of Particle Accelerator Society of Japan*, Tsukuba ,Japan, 2014. In Japanese.

[143] T. Sugimoto *et al.* UPGRADE OF THE COMPENSATION KICKER MAGNET FOR J-PARC MAIN RING. In *Proceedings of the 13th Annual Meeting of Particle Accelerator Society of Japan*, Chiba, Japan, 2016. in Japanese.

[144] K. Nakamura et al. Transverse Intra-bunch Feedback in the J-PARC MR. In *Proc. of International Particle Accelerator Conference (IPAC'14), Dresden, Germany, June 15-20, 2014*, number 5 in International Particle Accelerator Conference, pages 2786–2788, Geneva, Switzerland, July 2014. JACoW. https://doi.org/10.18429/JACoW-IPAC2014-THOAA03.

[145] K. Nakamura *et al.* PERFORMANCE EVALUATION OF THE INTRA-BUNCH FEEDBACK SYSTEM AT J-PARC MAIN RING. In *Proceedings of IBIC2014*, Monterey CA, USA, 2014.

[146] T. Toyama *et al.* STATUS OF THE INTRABUNCH-FEEDBACK FEEDBACK AT J-PARC MR. In *Proceedings of the 12th Annual Meeting of Particle Accelerator Society of Japan*, Tsuruga, Japan, 2015. In Japanese.

[147] S. Igarashi *et al.* OPTICS MEASUREMENT AND CORRECTION IN J-PARC MR. In *Proceedings of the 8th Annual Meeting of Particle Accelerator Society of Japan*, Tsukuba, Japan, 2011. In Japanese.

[148] K. Nakamura, Y. Kurimoto. MEASUREMENT BETATRON AMPLITUDE FUNCTION DURING ACCELERATION IN J-PARC MAIN RING. In *Proceedings of the 12th Annual Meeting of Particle Accelerator Society of Japan*, Tsuruga, Japan, 2015.

[149] Y. Kurimoto, K. Nakamura. Development and applications of a multi-purpose digital controller with a System-on-Chip FPGA for accelerators. *Nuclear Instruments and Methods in Physics Research Section A: Accelerators, Spectrometers, Detectors and Associated Equipment*, 840(21):160–167, 2016.

[150] T. Toyama *et al.* TRANSVERSE RESONANCES AND CORRECTIONS IN J-PARC MR. In *Proceedings of the 14th Symposium on Accelerator Science and Technology*, Tsukuba, Japan, 2003. In Japanese.

[151] Y. Sato. High Power Beam Operation of the J-PARC RCS and MR. In *Proc. 9th International Particle Accelerator Conference (IPAC'18), Vancouver, BC, Canada, April 29-May 4, 2018*, number 9 in International Particle Accelerator Conference, pages 2938–2942, Geneva, Switzerland, June 2018. JACoW Publishing. https://doi.org/10.18429/JACoW-IPAC2018-THYGBF1.

[152] H. Nakagawa *et al.* THE ACCELERATOR PROTECTION SYSTEM BASED ON EMBEDDED EPICS FOR J-PARC. In *Proceedings of ICALEPCS2009*, Kobe, Japan, 2009.

[153] C. Yong Ho. Beam instability of the high intensity proton beam. "`http://accwww2.kek.jp/oho/OHOtxt3.html`", 2005. in Japanese.

[154] T. Shimogawa *et al.* FIRST NEW POWER SUPPLY OF MAIN MAGNET FOR J-PARC MAIN RING UPGRADE. In *Proceedings of the 14th Annual Meeting of Particle Accelerator Society of Japan*, Sapporo, Japan, 2017. In Japanese.

[155] T. Koseki. Upgrade Plan of J-PARC MR - Toward 1.3 MW Beam Power. In *Proc. 9th International Particle Accelerator Conference (IPAC'18), Vancouver, BC, Canada, April 29-May 4, 2018*, number 9 in International Particle Accelerator Conference, pages 966–969, Geneva, Switzerland, June 2018. JACoW Publishing. https://doi.org/10.18429/JACoW-IPAC2018-TUPAK005.

[156] K. Abe *et al.* T2K neutrino flux prediction. *Phys. Rev. D*, 87:012001, Jan 2013.

[157] Y. Hayato. A neutrino interaction simulation program library NEUT. *Acta Phys. Polon.*, B40:2477–2489, 2009.

[158] S. Agostinelli et al. GEANT4: A Simulation toolkit. *Nucl. Instrum. Meth.*, A506:250–303, 2003.

[159] Y. Fukuda et al. The Super-Kamiokande detector. *Nucl. Instrum. Meth.*, A501:418–462, 2003.

[160] P. Gregory. *Bayesian Logical Data Analysis for the Physical Sciences: A Comparative Approach with Mathematica Support.* Cambridge University Press, 2005.

[161] G. Battistoni *et al.* "the fluka code: description and benchmarking". *AIP Conference Proceedings*, 896(1):31–49, 2007.

[162] R. Brun *et al.* GEANT3. 1987.

[163] M. Gazdzicki, Z. Fodor, G. Vesztergombi. Study of Hadron Production in Hadron-Nucleus and Nucleus-Nucleus Collisions at the CERN SPS. Technical Report SPSC-P-330. CERN-SPSC-2006-034, CERN, Geneva, Nov 2006. revised version submitted on 2006-11-06 12:38:20.

[164] C. Zeitnitz, T. Gabriel. The geant-calor interface and benchmark calculations of zeus test calorimeters. *Nuclear Instruments and Methods in Physics Research Section A: Accelerators, Spectrometers, Detectors and Associated Equipment*, 349(1):106 – 111, 1994.

[165] N. Abgrall *et al.* Measurements of cross sections and charged pion spectra in proton-carbon interactions at 31 GeV/c. *Phys. Rev. C*, 84:034604, Sep 2011.

[166] N. Abgrall *et al.* Measurement of production properties of positively charged kaons in proton-carbon interactions at 31 GeV/c. *Phys. Rev. C*, 85:035210, Mar 2012.

[167] J. Nieves, J. E. Amaro, M. Valverde. Inclusive quasielastic charged-current neutrino-nucleus reactions. *Phys. Rev. C*, 70:055503, Nov 2004.

[168] C. H. Llewellyn Smith. Neutrino Reactions at Accelerator Energies. *Phys. Rept.*, 3:261–379, 1972.

[169] S. L. Adler. Tests of the Conserved Vector Current and Partially Conserved Axial-Vector Current Hypotheses in High-Energy Neutrino Reactions. *Phys. Rev.*, 135:B963–B966, Aug 1964.

[170] M. Gourdin. Weak and electromagnetic form factors of hadrons. *Physics Reports*, 11(2):29 – 98, 1974.

[171] D. Mund *et al.* Determination of the weak axial vector coupling $\lambda=g_A/g_V$ from a measurement of the β-asymmetry parameter a in neutron beta decay. *Phys. Rev. Lett.*, 110:172502, Apr 2013.

[172] V. Bernard, L. Elouadrhiri, U.-G. Meißner. Axial structure of the nucleon. *Journal of Physics G: Nuclear and Particle Physics*, 28(1):R1, 2002.

[173] R. Gran *et al.* Measurement of the quasielastic axial vector mass in neutrino interactions on oxygen. *Phys. Rev. D*, 74:052002, Sep 2006.

[174] X. Espinal, F. Sanchez. Measurement of the axial vector mass in neutrino–Carbon interactions at K2K. *AIP Conference Proceedings*, 967(1):117–122, 2007.

[175] A. A. Aguilar-Arevalo *et al.* Measurement of muon neutrino quasielastic scattering on carbon. *Phys. Rev. Lett.*, 100:032301, Jan 2008.

[176] A. A. Aguilar-Arevalo *et al.* First measurement of the muon neutrino charged current quasielastic double differential cross section. *Phys. Rev. D*, 81:092005, May 2010.

[177] M. Dorman. Preliminary Results for CCQE Scattering with the MINOS Near Detector. *AIP Conference Proceedings*, 1189(1):133–138, 2009.

[178] V. Lyubushkin *et al.* A study of quasi-elastic muon neutrino and antineutrino scattering in the nomad experiment. *The European Physical Journal C*, 63(3):355–381, Oct 2009.

[179] A. Bodek *et al.* Vector and axial nucleon form factors: A duality constrained parameterization. *The European Physical Journal C*, 53(3):349–354, Feb 2008.

[180] D. Rein, L. M. Sehgal. Neutrino-excitation of baryon resonances and single pion production. *Annals of Physics*, 133(1):79 – 153, 1981.

[181] R. P. Feynman, M. Kislinger, F. Ravndal. Current matrix elements from a relativistic quark model. *Phys. Rev.*, D3:2706–2732, 1971.

[182] C. Berger, L. M. Sehgal. Lepton mass effects in single pion production by neutrinos. *Phys. Rev. D*, 76:113004, Dec 2007.

[183] K. M. Graczyk, J. T. Sobczyk. Form factors in the quark resonance model. *Phys. Rev. D*, 77:053001, Mar 2008.

[184] L. Tiator *et al.* Electroproduction of nucleon resonances. *The European Physical Journal A - Hadrons and Nuclei*, 19(1):55–60, Feb 2004.

[185] A. Aguilar-Arevalo et al. Measurement of Neutrino-Induced Charged-Current Charged Pion Production Cross Sections on Mineral Oil at $E_\nu \sim 1$ GeV. *Phys. Rev. D*, 83, 2011.

[186] A. A.-A. et al. Measurement of ν_μ-induced charged-current neutral pion production cross sections on mineral oil at $E_\nu \in$ 0.5-2.0 GeV. *Phys. Rev. D*, 83, 2011.

[187] A. Aguilar-Arevalo et al. Measurement of ν_μ and $\bar{\nu_\mu}$ induced neutral current single π^0 production cross sections on mineral oil at $E_\nu \sim \mathcal{O}(1$ GeV). *Phys. Rev. D*, 81, 2010.

[188] K. Collaboration. Measurement of single charged pion production in the charged-current interactions of neutrinos in a 1.3 GeV wide band beam. *Phys. Rev. D*, 78, 2008.

[189] J. Nieves, I. R. Simo, M. J. V. Vacas. Inclusive charged-current neutrino-nucleus reactions. *Phys. Rev. C*, 83:045501, Apr 2011.

[190] C. Albright, C. Jarlskog. Neutrino production of m+ and e+ heavy leptons (i). *Nuclear Physics B*, 84(2):467 – 492, 1975.

[191] M. Glück, E. Reya, A. Vogt. Dynamical parton distributions revisited. *The European Physical Journal C - Particles and Fields*, 5(3):461–470, Sep 1998.

[192] A. Bodek, U. K. Yang. Modeling neutrino and electron scattering inelastic cross- sections in the few GeV region with effective LO PDFs TV Leading Order. In *2nd International Workshop on Neutrino-Nucleus Interactions in the Few GeV Region (NuInt 02) Irvine, California, December 12-15, 2002*, 2003.

[193] T. Sjöstrand *et al.* An Introduction to PYTHIA 8.2. *Comput. Phys. Commun.*, 191:159–177, 2015.

[194] A. Kayis-Topaksu et al. Charged Particle Multiplicities in Charged-Current Neutrino and Anti-Neutrino Nucleus Interactions. *Eur. Phys. J.*, C51:775–785, 2007.

[195] D. Rein, L. M. Sehgal. Coherent π^0 production in neutrino reactions. *Nuclear Physics B*, 223(1):29 – 44, 1983.

[196] C. Berger, L. M. Sehgal. PCAC and coherent pion production by low energy neutrinos. *Phys. Rev.*, D79:053003, 2009.

[197] A. Higuera *et al.* Measurement of Coherent Production of $\pi^{\pm}$ in Neutrino and Antineutrino Beams on Carbon from E_{ν} of 1.5 to 20 GeV. *Phys. Rev. Lett.*, 113:261802, Dec 2014.

[198] R. A. Smith, E. J. Moniz. NEUTRINO REACTIONS ON NUCLEAR TARGETS. *Nucl. Phys.*, B43:605, 1972. [Erratum: Nucl. Phys.B101,547(1975)].

[199] M. Martini *et al.* A Unified approach for nucleon knock-out, coherent and incoherent pion production in neutrino interactions with nuclei. *Phys. Rev.*, C80:065501, 2009.

[200] C. Wilkinson *et al.* Testing charged current quasi-elastic and multinucleon interaction models in the NEUT neutrino interaction generator with published datasets from the MiniBooNE and MINERνA experiments. *Phys. Rev. D*, 93:072010, Apr 2016.

[201] Salcedo et al. COMPUTER SIMULATION OF INCLUSIVE PION NUCLEAR REACTIONS. *Nuclear Physics A*, 484:557, 1988.

[202] K. Nakamura et al. Review of Particle Physics. *J. Phys. G*, 37:075021, 2010.

[203] O. Benhar *et al.* Electron- and neutrino-nucleus scattering in the impulse approximation regime. *Phys. Rev. D*, 72:053005, Sep 2005.

[204] L. Pickering. *Examining Nuclear Effects in Neutrino Interactions with Transverse Kinematic Imbalance.*

[205] N. Rocco. Comparison to electron scattering, 2016. from talk slides.

[206] K. L. Miller et al. STUDY OF THE REACTION $\nu_{\mu} d \to \mu^- p p_s$. *Phys. Rev.*, D26:537–542, 1982.

[207] S. J. Barish et al. Study of Neutrino Interactions in Hydrogen and Deuterium: Description of the Experiment and Study of the Reaction $\nu + d \to \mu^- + p + p_s$. *Phys. Rev.*, D16:3103, 1977.

[208] N. J. Baker *et al.* Quasielastic Neutrino Scattering: A Measurement of the Weak Nucleon Axial Vector Form-Factor. *Phys. Rev.*, D23:2499–2505, 1981.

[209] T. Kitagaki et al. High-Energy Quasielastic $\nu_{\mu} n \to \mu^- p$ Scattering in Deuterium. *Phys. Rev.*, D28:436–442, 1983.

[210] D. Allasia et al. Investigation of exclusive channels in neutrino / anti-neutrino deuteron charged current interactions. *Nucl. Phys.*, B343:285–309, 1990.

[211] J. E. Amaro, E. Ruiz Arriola. Axial-vector dominance predictions in quasielastic neutrino-nucleus scattering. *Phys. Rev. D*, 93:053002, Mar 2016.

[212] A. S. Meyer *et al.* Deuterium target data for precision neutrino-nucleus cross sections. *Phys. Rev. D*, 93:113015, Jun 2016.

[213] C. Adamuscin *et al.* Two-component model for the axial form factor of the nucleon. *Phys. Rev.*, C78:035201, 2008.

[214] B. Bhattacharya, R. J. Hill, G. Paz. Model independent determination of the axial mass parameter in quasielastic neutrino-nucleon scattering. *Phys. Rev.*, D84:073006, 2011.

[215] M. Kabirnezhad. Single pion production in neutrino-nucleon interactions. *Phys. Rev. D*, 97:013002, Jan 2018.

[216] D. Rein. Angular distribution in neutrino-induced single pion production processes. *Zeitschrift fÃijr Physik C Particles and Fields*, 35(35):43–64, Mar 1987.

[217] M. KABIRNEZHAD. *Improvement of Single Pion Production for T2K experiment simulation tools.* PhD thesis, National Center for Nuclear Research, 2017.

[218] J. Nieves, I. R. Simo, M. J. V. Vacas. Inclusive charged-current neutrino-nucleus reactions. *Phys. Rev. C*, 83:045501, Apr 2011.

[219] K. Nakamura. The T2K cross-section results and prospects from the oscillation perspective. In *The 19th International Workshop on Neutrinos from Accelerators-NUFACT2017*, Uppsala, Sweden, 2017.

[220] P. A. Rodrigues *et al.* Identification of nuclear effects in neutrino-carbon interactions at low three-momentum transfer. *Phys. Rev. Lett.*, 116:071802, Feb 2016.

[221] R. Gran *et al.* Neutrino-nucleus quasi-elastic and 2p2h interactions up to 10 GeV. *Phys. Rev. D*, 88:113007, Dec 2013.

[222] G. Radecky et al. Study of single-pion production by weak charged currents in low-energy νd interactions. *Phys. Dev. D*, 25(5), 1982.

[223] M. Derrick et al. Study of single-pion production by weak neutral current in low-energy νd interactions. *Phys. Dev. D*, 23(3), 1981.

[224] T. Kitagaki et al. Charged-current exclusive pion production in neutrno-deuterium interactions. *Phys. Dev. D*, 34(9), 1986.

[225] N. J. Baker et al. Study of the isospin structure of single-pion production in charged-current neutrino interactions. *Phys. Dev.*, D23(11), 1981.

[226] K. Furuno. BNL 7-foot Bubble Chamber Experiment – Neutrino Deuterium Interactions. *NuInt02 proc.*, KEK Preprint 2003-48, 2003.

[227] A. Cervera-Villanueva, J. Gomez-Cadenas, J. Hernando. Recpack a reconstruction toolkit. *Nuclear Instruments and Methods in Physics Research Section A: Accelerators, Spectrometers, Detectors and Associated Equipment*, 534(1):180 – 183, 2004. Proceedings of the IXth International Workshop on Advanced Computing and Analysis Techniques in Physics Research.

[228] H. Maesaka. *Evidence For Muon Neutrino Oscillation In An Accelerator-based Experiment.* PhD thesis, Kyoto University, 2005.

[229] F. James, M. Roos. Minuit - a system for function minimization and analysis of the parameter errors and correlations. *Computer Physics Communications*, 10(6):343 – 367, 1975.

[230] R. Patterson *et al.* The extended-track event reconstruction for MiniBooNE. *Nuclear Instruments and Methods in Physics Research Section A: Accelerators, Spectrometers, Detectors and Associated Equipment*, 608(1):206 – 224, 2009.

[231] C. Patrignani, P. D. Group. Review of Particle Physics. *Chinese Physics C*, 40(10):100001, 2016.

[232] A. M. Ankowski, C. Mariani. Systematic uncertainties in long-baseline neutrino-oscillation experiments. *Journal of Physics G: Nuclear and Particle Physics*, 44(5):054001, 2017.

[233] P. A. Rodrigues et al. Identification of nuclear effects in neutrino-carbon interactions at low three-momentum transfer. *Phys. Rev. Lett.*, 116:071802, 2016.

[234] T. Katori. Meson Exchange Current (MEC) Models in Neutrino Interaction Generators. *AIP Conf. Proc.*, 1663:030001, 2015.

[235] G. J. Feldman, R. D. Cousins. Unified approach to the classical statistical analysis of small signals. *Phys. Rev. D*, 57:3873–3889, Apr 1998.

[236] M. Friend. J-PARC accelerator and neutrino beamline upgrade programme. *Journal of Physics: Conference Series*, 888(1):012042, 2017.

[237] Y. Ashida *et al.* A new electron-multiplier-tube-based beam monitor for muon monitoring at the T2K experiment. 2018.

[238] M. Friend. J-PARC Neutrino Beamline Monitor R&D, 2018. from talk slides.

[239] K. Abe *et al.* Physics potentials with the second Hyper-Kamiokande detector in Korea. *Progress of Theoretical and Experimental Physics*, 2018(6):063C01, 2018.

[240] R. Acciarri et al. Long-Baseline Neutrino Facility (LBNF) and Deep Underground Neutrino Experiment (DUNE). 2015.

[241] C. Andreopoulos et al. The GENIE Neutrino Monte Carlo Generator. *Nucl. Instrum. Meth.*, A614:87–104, 2010.

[242] T. Golan, C. Juszczak, J. T. Sobczyk. Effects of final-state interactions in neutrino-nucleus interactions. *Phys. Rev. C*, 86:015505, Jul 2012.

[243] O. Buss *et al.* Transport-theoretical description of nuclear reactions. *Physics Reports*, 512(1):1 – 124, 2012. Transport-theoretical Description of Nuclear Reactions.

[244] A. A. G. Soto. *Study of the ν_μ interactions via charged current inthe T2K near detector.* PhD thesis, Institut de Física dÁltes Energies Universitat Auòonoma de Barceona, 2017.

[245] A. Blondel, M. Yokoyama, M. Zito. The T2K-ND280 upgrade proposal. Technical Report CERN-SPSC-2018-001. SPSC-P-357, CERN, Geneva, Jan 2018. This proposal is the follow-up of the Expression of Interest EOI-15 submitted to SPSC in January 2017.

[246] D. Sgalaberna. The upgrade project of the T2K near detector. *PoS*, EPS-HEP2017:518, 2017.

[247] A. Blondel *et al.* A fully-active fine-grained detector with three readout views. *Journal of Instrumentation*, 13(02):P02006, 2018.

[248] T. Koga *et al.* Water/CH Neutrino Cross Section Measurement at J-PARC (WAGASCI Experiment). In *Proceedings of the 2nd International Symposium on Science at J-PARC. Unlocking the Mysteries of Life, Matter and the Universe.*

[249] X.-G. Lu *et al.* Measurement of nuclear effects in neutrino interactions with minimal dependence on neutrino energy. *Phys. Rev. C*, 94:015503, Jul 2016.

[250] K. Abe *et al.* Characterization of nuclear effects in muon-neutrino scattering on hydrocarbon with a measurement of final-state kinematics and correlations in charged-current pionless interactions at T2K. *Phys. Rev. D*, 98:032003, Aug 2018.

[251] C. Adams et al. Comparison of ν_μ-Ar multiplicity distributions observed by MicroBooNE to GENIE model predictions. *Submitted to: Phys. Rev. D*, 2018.

[252] K. Partyka. Exclusive ν_μ+Np topologies with ArgoNeuT. In *American Institute of Physics Conference Series*, volume 1663 of *American Institute of Physics Conference Series*, page 080007, May 2015.

[253] B. Eberly et al. Charged Pion Production in ν_μ Interactions on Hydrocarbon at $E_\nu = 4.0$ GeV. *Phys. Rev.*, D(92), 2015.

[254] T. Fukuda *et al.* First neutrino event detection with nuclear emulsion at J-PARC neutrino beamline. *Progress of Theoretical and Experimental Physics*, 2017(6):063C02, 2017.

[255] C. Rubbia *et al.* Underground operation of the ICARUS T600 LAr-TPC: first results. *Journal of Instrumentation*, 6(07):P07011, 2011.

[256] R. Acciarri *et al.* Design and construction of the microboone detector. *Journal of Instrumentation*, 12(02):P02017, 2017.

[257] M. Antonello et al. A Proposal for a Three Detector Short-Baseline Neutrino Oscillation Program in the Fermilab Booster Neutrino Beam. 2015.

[258] H. Hochi. Beam Dynamics of High Intensity Proton Accelerator 1. "`http://accwww2.kek.jp/oho/OHOtxt4.html`", 2010. in Japanese.